Improvement of the global precision of sea level and sea state estimates from radar altimetry

Habilitation Thesis

Marcello Passaro[1]

May 12, 2021

[1]Deutsches Geodaetisches Forschungsinstitut der Technischen Universitaet Muenchen

Preface

The development of remote sensing techniques in the ocean has given a significant boost to the discipline of oceanography. We are now able to characterise the mean state of the ocean and its variability relying on regular observations taken at hundreds of km of distance by active and passive sensors on board satellites.

Among these techniques, radar altimetry has the special fascination of providing information characterising not only the surface ocean (wave height), but also volume and mass of the full water coloumn (sea level), and even the ocean depths (bathymetry, by means of gravity gradients).

Satellite altimetry was born as a way to measure large scale circulation in the open ocean. Its success meant that soon new applications became available: the global mean sea level curve and the provision of wave heights to forecasting models are two paramount examples. But the development of the technique is pushing the limits of our knowledge towards new challenges, such as the understanding of scales of variability below 100 km and the study of regional and local sea level variability.

In general, I strongly believe that the way forward in satellite altimetry is to improve the precision and the accuracy of the measurement where it is more needed and where the societal impact is higher. This means of course the provision of high quality data in the coastal zone, where people, cities and infrastructures are located, and at the same time where oceanography is particularly challenging due to the high variability of waves, currents, bathymetry and tides. This means also to fill the gaps of knowledge at the high latitudes, those latitudes in which climate change is acting at an even quicker pace and which are of key importance to understand how the changing situation can affect the global climate.

This need for improvement has been my motivation and the line connecting the work leading my research. The "precision" mentioned in the title of the work is to be therefore interpreted in the wider sense of a measurement of quality, including the accuracy and the exactness of the different levels of processing and analysis that this work explores.

In this manuscript I make a selection of the most relevant publications proposed in the context of the Habilitation. This preface in particular has the objective to introduce to the reader the main achievements of my re-

search, distinguished into the three different topics that were recognised as the focus of my work. Hereafter, after each topic title, the corresponding selected publications are listed. The achievements are then shortly summarised and finally the publications provided within this manuscript after this preface.

In the concluding remarks, an overview of the other studies that I co-authored in connection with the topics of the Habilitaton is presented. Those manuscripts are available as well in the Appendix of this dissertation.

- Processing and exploitation of the new Delay-Doppler radar altimetry data, also in combination with other remotely sensed variables and sensors.

  Passaro M., Müller F., Dettmering D.: Lead Detection using Cryosat-2 Delay-Doppler Processing and Sentinel-1 SAR images. 62(6), pp. 1610–1625, Advances in Space Research, 2018

- Development of homogenous signal processing strategies for radar altimetry returns from surfaces with different characteristics

  Passaro M., Rose S.K., Andersen O.B., Boergens E., Calafat F.M., Dettmering D., Benveniste J.: ALES+: Adapting a homogenous ocean retracker for satellite altimetry to sea ice leads, coastal and inland waters. Remote Sensing of Environment, 211, 456-471, 2018

  Passaro M., Zulfikar Adlan N., Quartly G.D.: Improving the precision of sea level data from satellite altimetry with high-frequency and regional sea state bias corrections. Remote Sensing of Environment, 245-254, 2018

- Study of the variability of sea level and sea state time series for climate research

  Rose S.K., Andersen O.B., Passaro M., Ludwigsen C.A., Schwatke C.: Arctic Ocean Sea Level Record from the Complete Radar Altimetry Era: 1991–2018. Remote Sensing, 11(14), 1672, 2019

  Benveniste J., Birol F., Calafat F., Cazenave A., Dieng H., Gouzenes Y., Legeais J.F., Léger F., Niño F., Passaro M., Schwatke C., Shaw A. (The Climate Change Initiative Coastal Sea Level Team): Coastal sea level anomalies and associated trends from Jason satellite altimetry over 2002–2018. Nature Scientific Data, 7, 357, 2020

  Passaro M., Müller F.L., Oelsmann J., Rautiainen L., Dettmering D., Hart-Davis M.G., Abulaitijiang A., Andersen O.B., Høyer J.L., Madsen K.S., Ringgaard I.M., Särkkä J., Scarrott R., Schwatke S., Seitz F., Tuomi L., Restano M., Benveniste J.: Absolute Baltic Sea Level Trends in the Satellite Altimetry Era: A Revisit, Frontiers in Marine Science, In Press (2021)

Passaro M., Hemer M., Quartly G.D., Schwatke C., Dettmering D., Seitz F.: Global coastal attenuation of wind-waves observed with radar altimetry. Nature Communications, ACCEPTED (2021)

Synergetic processing and exploitation of the Delay-Doppler radar altimetry

In the high latitudes, the possibility to observe the polar ocean dynamics from remote sensing is undermined by the presence of sea ice and the consequent scarcity of sea level data. The only possibility we have is to detect the backscatter from leads, long and narrow openings of the sea ice. This backscatter is different from the shape of the return dominated by sea ice, but can influence signals that are located even over a km away from the nadir view of the satellite, causing significant biases in the sea level record.

In the literature there are a number of techniques developed to classify the returns and spot the leads. But once a technique over the area is proposed, it is particularly difficult to validate it, given the absence of in-situ observations. The synergetic use of different remote sensing techniques is therefore our only resource to improve our detection and consequently the quality of the sea level dataset in the polar ocean.

In Passaro et al. (2018a) we have proposed a way to exploit the Delay-Doppler radar altimetry technique, which is onboard Cryosat-2, in order to improve the lead detection. The Delay-Doppler allows for multiple observations of the same segment of the satellite footprint spanning different lines of sight. In terms of data availability it means that we can observe a waveform stack, which means a 2D waveform in which each line corresponds to a different look of the same area. The study demonstrates that the current stack analysis methods are not sufficient to isolate the signal echo corresponding to the moment in which the satellite overflies a lead located in the nadir position. Instead, a new index is proposed for this purpose, named stack peakiness, based on the fact that the strongest mirror-like backscatter coming from the lead would show up as a peak in the returned power.

The other innovation of the paper is the synergetic use of SAR-imaging from Sentinel-1 to validate different classification methodologies analysed in the paper. The comparison with SAR-imaging or optical images was already introduced in previous studies, but here we propose a set of defined processing steps and analysis tools to quantitatively assess the amount of leads that are correctly or incorrectly detected.

Development of homogeneous signal processing strategies

Even if we are tempted to place borders in our definition of a problem, the techniques employed by satellite altimetry to generate the emitted pulse are essentially always the same, regardless of the targets. The methods

adopted to analyse the returned signals instead have diverged considerably in the most challenging areas such as high latitudes, coastal zones and inland waters. As a consequence, the precision and the accuracy of the dataset strongly vary depending on the domain, and biases are inevitable when trying to match, for example, sea level retrievals coming from sea-ice covered areas with the ones obtained during the ice-free summer over the same zone.

In Passaro et al. (2018b) we have developed ALES+, a fitting technique of the altimetric signal that is tuned to any water return. This matches very well the previous study, since for example in the seasonally sea-ice covered areas we have been able to retrieve sea level and sea state in the coastal zone, in the open ocean, and in addition from the very strong and peaky backscattering from leads, using one single algorithm. This is possible thanks to two main features: A very careful detection of the main part of the returned signal (the "leading edge"); and an adapting window that selects the width of the signal that we have to consider in order to avoid interference, but at the same time provides enough information to keep a good level of precision.

The study required also a notable validation effort which, for the first time, had to cover all the different domains that ALES+ aims to unveil. Interestingly, ALES+ demonstrated to be so flexible that it can be used to obtain data from rivers, whose signal analysis shares indeed several challenges with the sea ice and coastal domain.

In Passaro et al. (2018c) my work was focused on the sea state bias, a correction to the sea level that strongly depends on the estimation of the wave height. In the study, we demonstrate that this correction is a mixture of a physical relation between these two parameters and a numerical relation due to the fact that both parameters are estimated from the altimetric waveform. We also show that current global sea state bias models are not able to efficiently correct for the effect, since a regional recomputation is able to improve the precision of the local sea level dataset.

This analysis, which we further developed in Quartly et al. (2019a), paves the way for the homogenisation of the correction. The study identifies a way to eliminate the dependence of the sea state bias from the numerical fitting of the signal, which is what makes the sea state bias unique to every satellite mission. The application of a high-rate correction to the sea level estimate with respect to the wave height shall highlight the underlying physical low-frequency physical relationship between the two variables. The latter should be in fact independent from the methodology adopted to fit the signal.

Study of sea level and sea state time series

The reliability of the developed strategy brought to the use of ALES+ in the context of the Sea Level Climate Change Initiative and the analysis of 25 years of sea level data in the Arctic Ocean (Rose et al., 2019). Here,

two climatic-change signals were highlighted right from the most challenging areas for the observations: the sinking of the sea level along the Greenland because of the diminishing gravitational attraction of the ice masses; and a bulge of sea level in the Beaufort Gyre due increased wind stress on the open water because of the disappearing sea ice.

An effort was then done to apply the lesson learned in the Arctic Ocean to an even more challenging basin: the Baltic Sea. The latter, with its thousands of islands, its rugged coasts, its small scales of variability, the presence of sea-ice and the advantage of a rich in-situ coastal observing system, can be considered a laboratory for enhanced satellite altimetry. In the context of the ESA Baltic Sea Level (Baltic SEAL) project, in which I was involved as principal investigator, the techniques previously developed for the older generation of altimeters were extended to include the Delay-Doppler altimetry missions. The resulting sea level product allowed for sub-basin analysis of interannual sea level variability during winter times. Through synergetic analysis with wind data and Ekman currents, it was shown that the differences in sea level anomalies during winter between the North of the basin (Bothnian Bay) and the South-West are driven by the strength and direction of the large scale wind field and coincides with the different phases of the North Atlantic Oscillation. The methodology and results of this analysis are reported in Passaro et al. (2021a).

In the coastal zone, two other milestones were reached in the analysis of sea level and sea state time series. In Benveniste et al. (2020), the reprocessing of the signals from satellite altimetry was combined with advanced strategies in terms of corrections and quality control to generate a novel altimetry-based coastal sea level data record. It consists of high-resolution (approximately 300 m) monthly sea level data along the satellite tracks, at distances of less than 3-4 km from the coastlines in general, sometimes even closer, within 1-2 km from the coast. It provides coastal sea level trends over 2002-2018 at 429 coastal sites located in six regions (Northeast Atlantic, Mediterranean Sea, West Africa, North Indian Ocean, Southeast Asia and Australia). The study provides the first answer to the important question on whether the sea level very close to the coast is subjected to different linear trends compared to offshore locations. Our study shows that in about 80 % of the investigated sites, the trends seen at the coast do not differ in a statistically significant sense than the ones observe 20 km further away. This has important consequences in terms of the possibility of extending up to the coast the estimated and projected trends from maps and models whose resolution does not cover the coastal zone. Nevertheless future studies will have to analyse which processes are responsible for the significant trend variations in such a short distance, which still affect one fifth of the studied sites.

This manuscript is concluded by the biggest achievement in terms of applications: a global study of the average wave coastal climate in the coastal

zone, recently accepted in Nature Communications (Passaro et al., 2021b). The study analyses 15 years of data of significant wave height from satellite altimetry, reprocessed in order to improve the quality of coastal data. These time series are analysed to extract the mean climate and the annual cycle. Moreover, they are combined with reanalysis data to provide an estimation of the wave energy flux, an essential quantity for coastal engineering, from coastal security to the exploitation of waves as a source of renewable energy. Through this analysis we are able to observe typical coastal phenomena such as the sheltering effect of islands and the depth induced dissipation of wave energy. The results quantify the coastal attenuation of these parameters at an unprecedented resolution that could so far only been achieved using dedicated high-resolution models for regional and local downscalings. This shall constitute a new milestone in terms of global wave power analysis, demonstrating the need to updated the assessment studies that typically use resolutions of one-fourth of degree or coarser (such as the latest assessment of the World Energy Council).

Lead detection using Cryosat-2 delay-doppler processing and Sentinel-1 SAR images

Marcello Passaro*, Felix L. Müller, Denise Dettmering

Deutsches Geodätisches Forschungsinstitut der Technischen Universität München, Arcisstraße 21, 80333 Munich, Germany

Abstract

In the Arctic and Antarctic Ocean, where part of the sea surface is seasonally or continuously covered by sea ice, the sea level monitoring from satellite altimetry relies on the localisation of open water areas, especially on the detection of leads: long and narrow fractures in the sea ice, which dominate the radar echoes even if hundreds of meters away from nadir.

The Cryosat-2 altimetry mission is based on the Delay-Doppler processing, in which the averaged waveform is formed by summing up several looks acquired at different look angles and stacked together. This imaging technique and the resulting improved along-track resolution are here exploited to evaluate different lead identification schemes.

In particular, stack and power statistics of Cryosat-2 waveforms are used to classify leads on a subset of 12 tracks in which the altimetry-based classification is compared to a classification based on Sentinel-1A SAR images. For this scope, a dedicated SAR-image automated processing is proposed to avoid the manual classification.

Results show that the adoption of a single new stack parameter (the Stack Peakiness) can perform equally well as the use of multiple stack parameters currently available. Moreover, a multi-waveform analysis of the Stack Peakiness helps to isolate the point where narrow leads cross the tracks at nadir.

For all the tested strategies, the number of altimetry-detected leads that are unidentified by SAR is comparable to the number of detections from both sensors. This could be due to presence of narrow leads, not detected by SAR due to resolution limits, but still dominant in the radar altimeter return due to the high backscatter.

© 2017 COSPAR. Published by Elsevier Ltd. All rights reserved.

Keywords: Leads detection; Delay-Dopper altimetry; Cryosat-2 stack data; Sentinel-1; SAR image processing

1. Introduction

The measurement of sea level variability in the global ocean is considered among the most important climatic indices. It relies on in situ observations provided by a wide but unevenly distributed set of tide gauges and, since more than 20 years, on measurements collected by the radar altimeters on board of several satellite missions.

The coverage of satellite altimetry over the ocean cannot completely be defined as global, since a large part of the Arctic and Antarctic oceans is excluded. On one side this is due to the limited latitude extent of most of the altimetric missions due to their orbit configuration. On the other side the ocean in the northernmost latitudes is partially covered by sea ice, which reflects the radar signal before it hits the sea surface, preventing the possibility to measure sea level. The estimation in the sea-ice covered regions is limited to the leads, narrow cracks in the sea ice that can be several tens of kms long. Since these ocean patches are very smooth and do not have a developed wave field, the signal

returned to the satellite is much stronger than the one reflected from the surrounding ice and can dominate the registered waveforms even if the lead is not located at nadir. In particular, Armitage and Davidson (2014) have shown that a lead can be the dominant return in the waveform up to about 1.5 km away from the sub-satellite point (nadir). Such off-nadir returns, if not properly spotted, result in erroneous estimations of the sea level.

Cryosat-2 (CS-2) offers ways for improving the sea level records in these regions. With its orbit configuration, it provides coverage up to 88° in latitude. Thanks to the Delay-Doppler processing of its echoes (when operating in the so-called "SAR mode" over sea ice, not to be confused with SAR imaging from Sentinel-1 used in this study), it stores the signal registered by the satellite looking at the same resolution cell on the ground from different look angles. In particular, the beam-limited along-track footprint size (305 m, Scagliola, 2013) should guarantee a more precise determination of the lead position. Nevertheless, due to the size of the pulse-limited across-track footprint (1.65 km), the distinction of a lead return at nadir from an off-nadir reflection is still challenging. Most of the leads have width of less then a km (Lindsay and Rothrock, 1995; Kwok et al., 2009), while Cryosat-2 has a sampling interval of roughly 300 m (using the 20-Hz rate): in most of the cases, only one range measurement per lead will correspond to the distance at nadir. Being able to correctly identify the nadir echoes of these narrow, but numerous open water openings can increase the amount of sea level measurements and therefore improve the records.

Previous studies on past altimetry missions have used lead-detection algorithms that distinguish leads from sea ice based on the shape of the received signal: Empirical thresholds were assigned in order to classify the waveforms based on the "pulse peakiness" (Peacock and Laxon, 2004). Laxon et al. (2013), Ricker et al. (2014) and Rinne and Similä (2014) have classified CS-2 signals using a combination of different waveform parameters (including the pulse peakiness) available in the European Space Agency (ESA) Baseline C Product files or computable from the waveforms. Recently, Wernecke and Kaleschke (2015) argued that it is possible to obtain an efficient lead classification only based on the absolute value of the maximum waveform power.

Leads can be also determined using thermal infrared sensors (Willmes and Heinemann, 2015), microwave radiometers (Röhrs and Kaleschke, 2012) and SAR images (Ivanova et al., 2016). SAR images have the advantage of being independent from weather conditions, while providing a good resolution (40 m for Sentinel 1A). They can be therefore used for comparison with the altimetry-based lead classification, but the time difference between the acquisition of the two different data sources needs to be taken in consideration, since sea ice moves on average from 4 km/day in winter up to over 9 km/day in summer (as measured by buoys in Rampal et al. (2009)) and leads can quickly refreeze and close (Weeks, 2010).

The objective of this study is to provide a first assessment of the lead-classification methodologies based on the Delay-Doppler processing of Cryosat-2 echoes in comparison to SAR images from Sentinel-1A. Our classification, based on a new parameter computed using the Delay-Doppler processing of CS-2 (in particular from the full stack information) and on a multi-waveform analysis to isolate the nadir return, is compared with the methodologies derived from the recent literature. A SAR-image processing chain is proposed to provide a reference for validation and, for the first time, is used to provide an objective comparison that is not based on a visual recognition of lead-like features.

A description of the dataset and the area of study is provided in Section 2. Section 3 describes the methodology used to analyse the altimetry and SAR dataset and to classify the leads. In Section 4 the results of the comparison are presented and discussed. Section 5 draws the conclusions and the outlook for future research.

2. Dataset

2.1. Cryosat-2 L1B-S data

By exploiting the Doppler frequency and the coherence of consecutive pulses, Delay-Doppler altimeters are able to perform multi-looked acquisitions, i.e. to associate to a resolution cell a certain number of looks (variable depending on the processing settings) acquired at different look angles as the satellite moves over the imaged area (Raney, 1998).

Using processing techniques inherited from the SAR processing, such as Range compression and Range migration correction, all the returns corresponding to the resolution cell (a 20-Hz sampling of the illuminated surface, i.e. one measurement every 300 m roughly) are aligned in a 2D-stack (Figs. 1a and 2a). The Cryosat-2 multilooked radar waveforms, such as the one in Fig. 1c and 2c, are obtained by the incoherent sum of all the echoes in the stack. By summing up the returns in the across-track (Range) dimension (Fig. 1b and 2b), the so-called Range Integrated Power (RIP) waveform, can be generated. It contains information concerning the backscattering properties of the illuminated surface, but it also reveals details of the distribution of the scatterers as the satellite spans different look angles passing over the nadir position (Wingham et al., 2006).

When the satellite moves over a very smooth surface, such as for small lakes or leads (Fig. 1), the signal will be specularly reflected back and the RIP will be peaky. On the opposite, when flying over areas containing scatterers with different orientation, such as for wavy seas or ice, the backscattered power will be more normally distributed (Fig. 2).

L1B products provide statistical parameters that describe the RIP behaviour, but do not provide the full stack, limiting therefore the possibilities of analysis. The ESA Grid Processing on Demand (G-POD) service
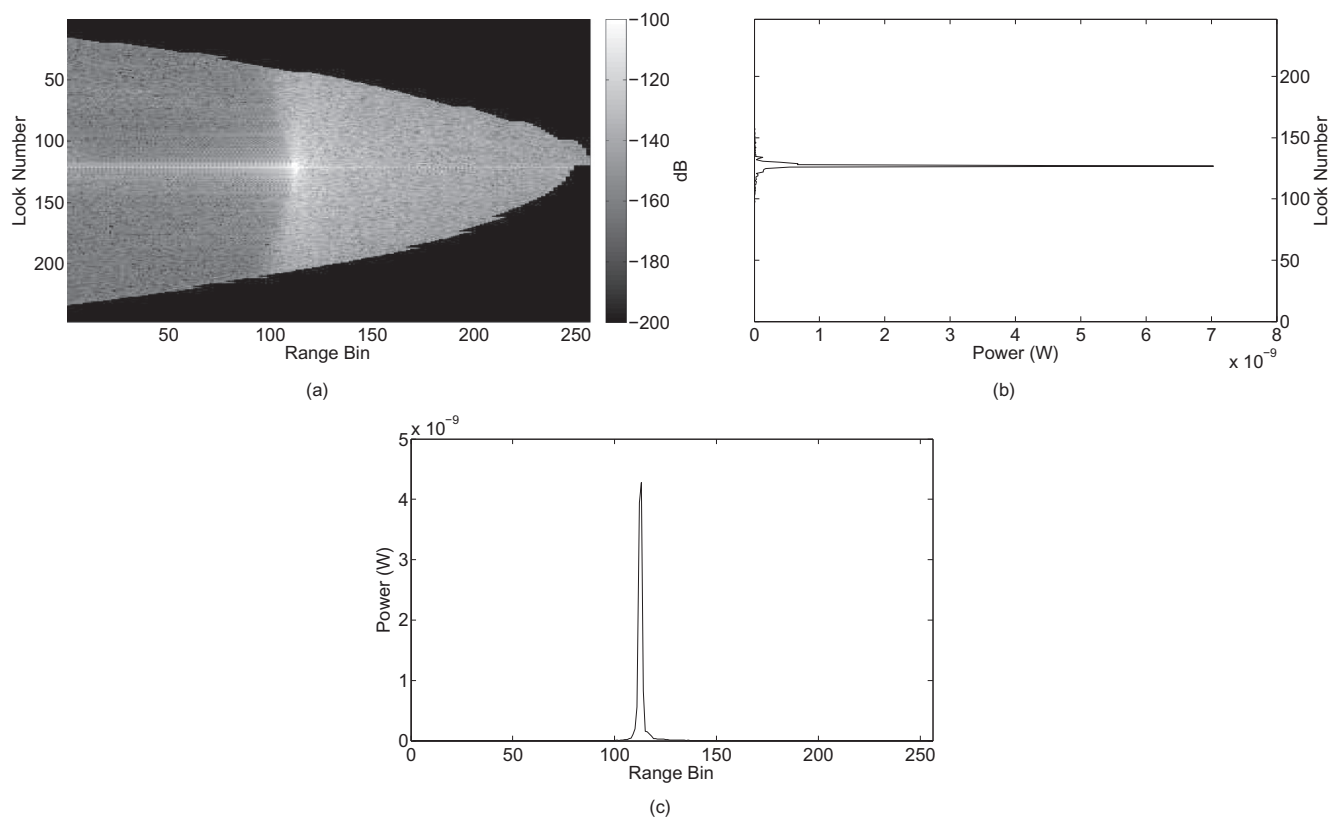
(a)

(b)

(c)

Fig. 1. Example of a stack (a), a RIP (b) and a multilooked waveform (c) acquired by Cryosat-2 over a lead.
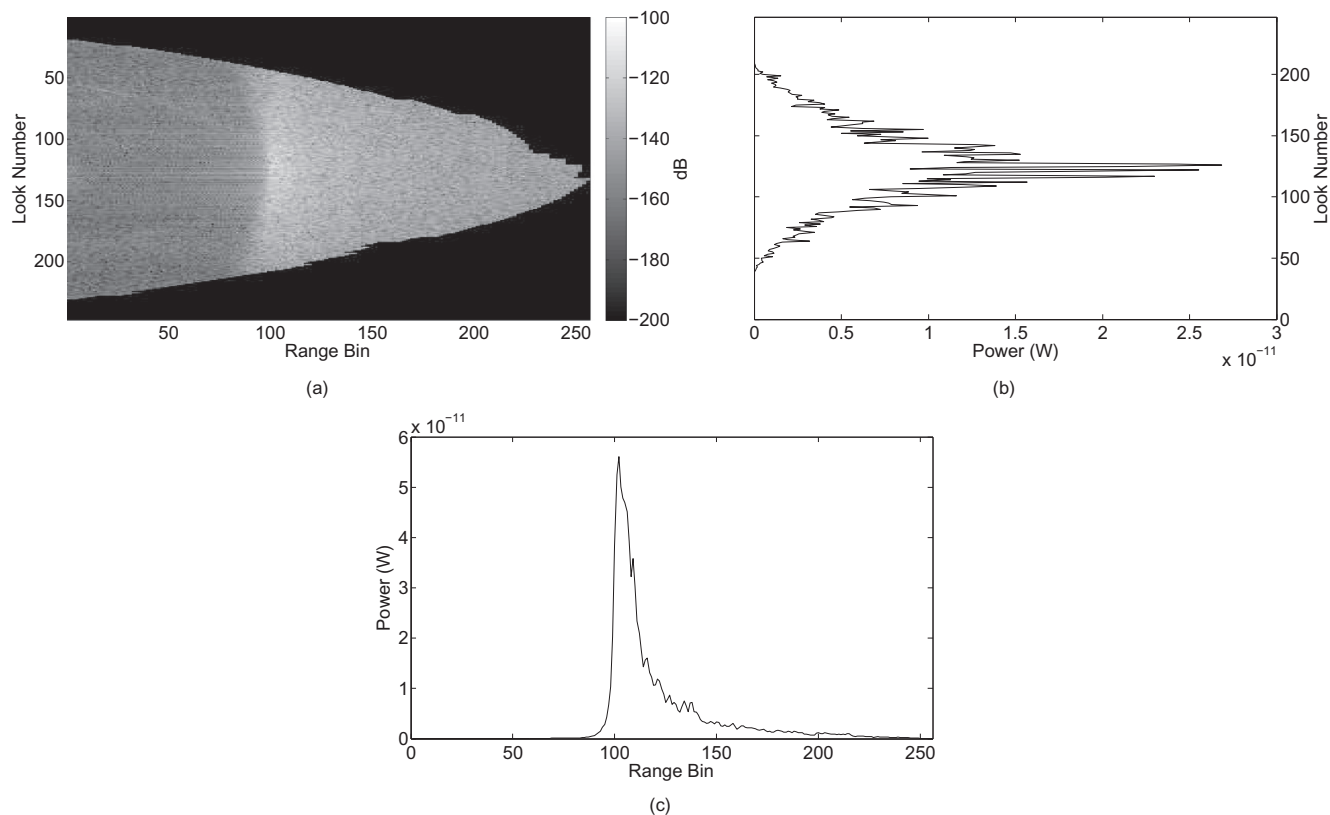

(a)

(b)

(c)

Fig. 2. Example of a stack (a), a RIP (b) and a multilooked waveform (c) acquired by Cryosat-2 over sea ice.
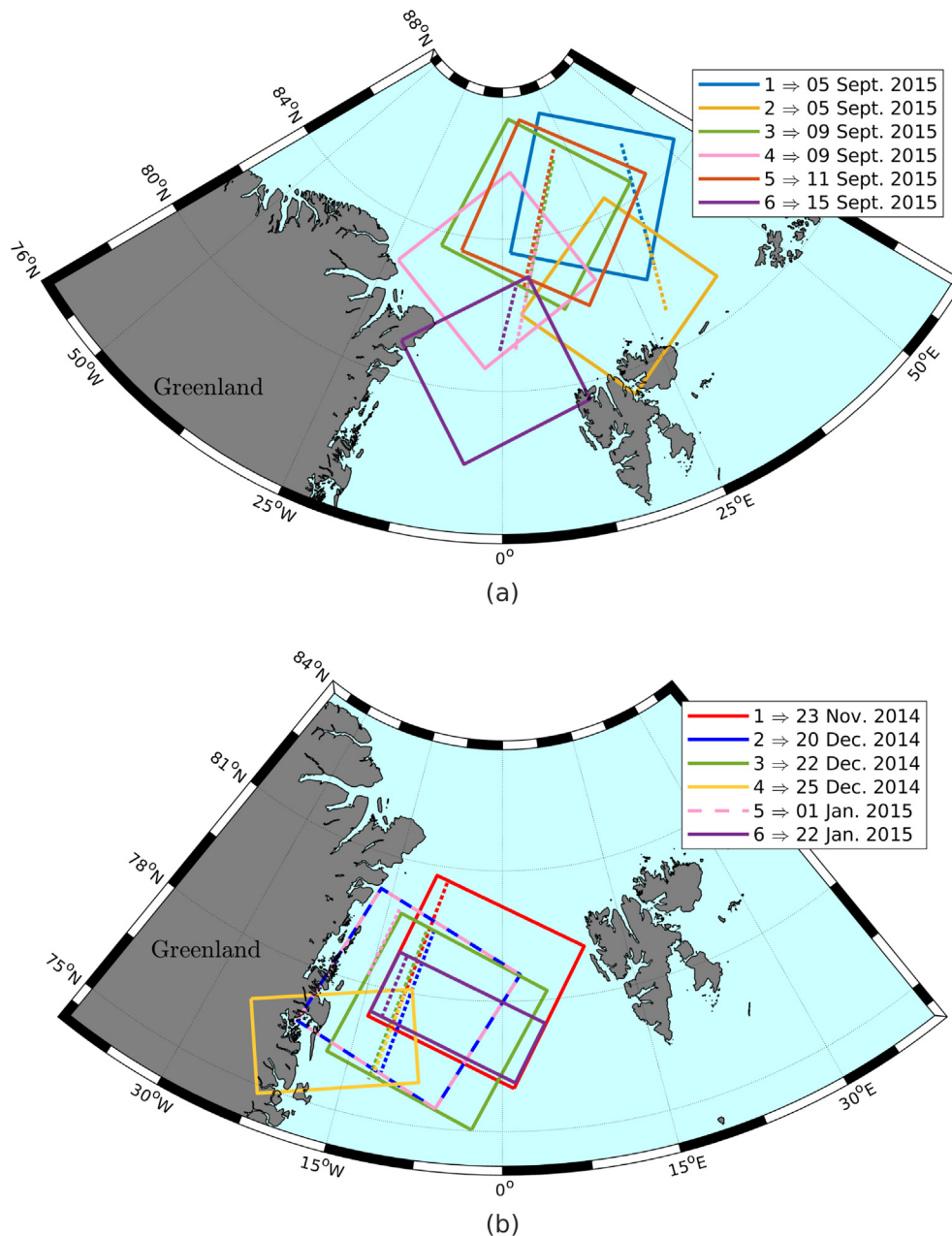
Fig. 3. Location and date of the SAR-images in the two control datasets. Dashed lines are the corresponding segments of CS2 tracks on which the classification is applied.

(see acknowledgements) is currently the only freely and easily available source to access these data. The ESA Baseline C version of this L1B stack (L1B-S) data set is used in this study (Scagliola and Fornari, 2015).

2.2. Sentinel-1A SAR images

One of the ways to verify the classification of altimetric echoes is the comparison with satellite SAR images. These have been used for lead detection, since very smooth water areas reflect electromagnetic waves like a mirror: consequently the slant incident radar waves reflect away from the spacecraft and flat water areas appear dark (Dierking, 2013). Sentinel-1A SAR images are provided with two polarization modes HH and HV (where "H" indicates horizontal and "V" vertical). HH- and HV-polarization are particularly suitable for ice versus open water discrimination because of decreasing ocean clutter and smaller sensitivity to wind and wave scattering.

In the present investigation Level-1 dual-polarized SAR Sentinel-1A extra-wide-swath mode data at medium resolution (S1A-EW-GRDM-1SDH) are employed. The images are ground-range detected showing a 40-meter spatial resolution and a 400-km swath width, which allows a wide spatial coverage and a short revisit time. The images were pre-processed using the following standard
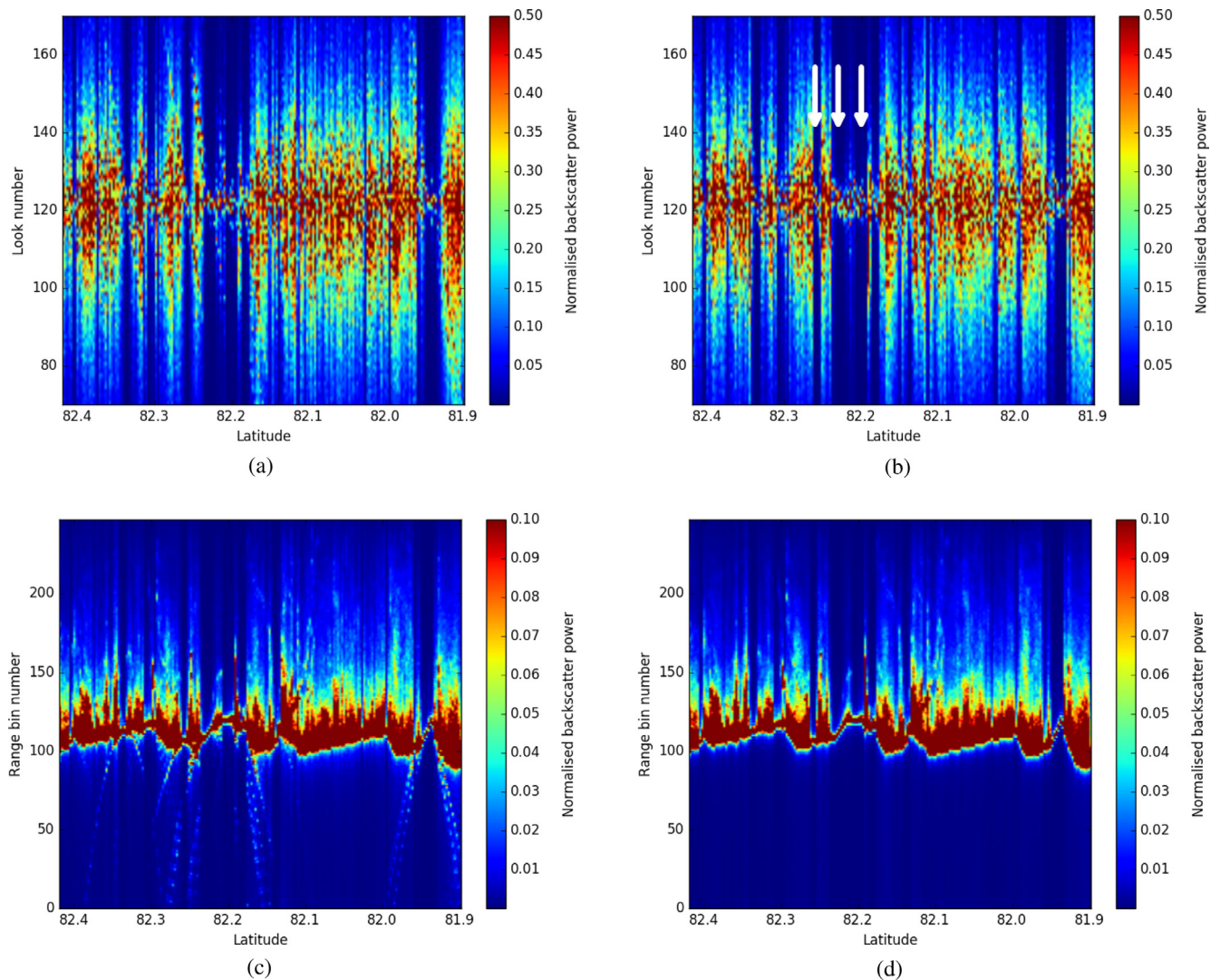
Fig. 4. Multilooked waveform (c and d) and RIP (a and b) radargrams from a CS-2 pass over sea ice acquired on the 5th September 2015 (see Fig. 3 for track location). All plots correspond to the same pass, but Hamming windowing has been applied in b and d. The arrows highlight residual sidelobe effects also despite the Hamming windowing. The normalised power has been saturated in order to visually show the sidelobe effect.

procedures: (1) Thermal noise removal, (2) Radiometric calibration, (3) Range Doppler terrain correction (Veci, 2016). The latter includes a coordinate transformation into an azimuthal equal area map projection to provide the same coordinate background as the sea ice motion vectors used to relate the images to the time of the altimetry over-flight (see 2.3). In a last step, a type conversion to *uint8* is performed in order to get grayscaled values and to reduce disk space.

In this study, two sets of control data of Sentinel-1A HH-polarised images are used (see Fig. 3): Set 1 comprises six images from September 2015 from the Arctic Ocean north of the Fram Strait. They are taken as a reference for comparison between the classification proposed in this study and the one described in Ricker et al. (2014). Set 2 includes six additional images taken between the north-east coast of Greenland and the Fram Strait. They are exploited as a further comparison using a different area

at various times of the year (November 2014 to January 2015).

All images were selected because of the time proximity with collocated Cryosat-2 tracks (never more than four hours of time difference) to reduce the influence of sea ice motion between the acquisition date of the imaging SAR and the altimetry record.

2.3. Sea ice velocities

Since sea ice can move significantly even in short time periods, it is desirable to take the ice velocity into account when comparing altimetry results with SAR images. For this purpose daily sea ice motion vectors provided by the National Snow and Ice Data Center (NSIDC) are used. At the time of writing, daily NSIDC ice motion vector fields are only available until 31 May 2015: therefore, the sea ice motion vectors are not applied to Set 1. The "Polar
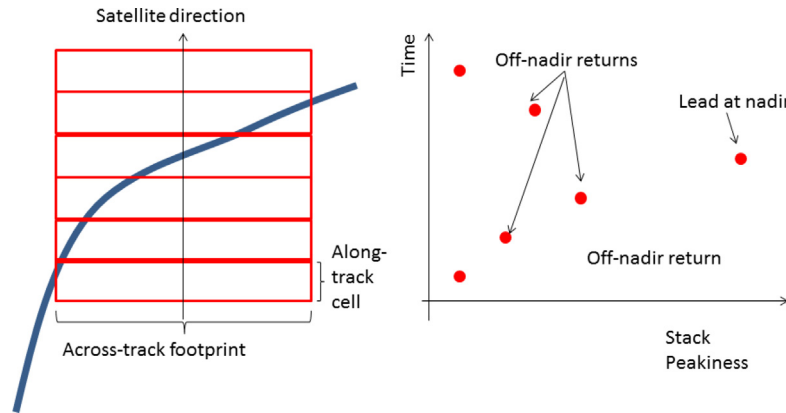
Fig. 5. Modelled lead (blue line) crossing over a CS-2 track (left) and expected SP behaviour (right). (For interpretation of the references to colour in this figure legend, the reader is referred to the web version of this article.)

Pathfinder Daily 25 km EASE-Grid Sea Ice Motion Vectors, Version 3" are based on data derived from different active and passive satellite sensors as well as in situ data. The data are provided at 25-km spatial resolution (Tschudi et al., 2016). The ice motion information is provided as zonal and meridional velocity grids.

Based on these data a mean velocity (magnitude and direction) is estimated by averaging all points in a ±35 km rectangle box around each Cryosat-2 track. The SAR image, i.e., each of its pixel coordinates, is then shifted taking the acquisition time difference between SAR and CS-2 into account.

3. Methodology

3.1. Processing of Delay-Doppler altimetry data

3.1.1. Application of the Hamming window

When using L1B-S data in G-POD, it is possible to exploit different Delay-Doppler processing configurations. In order to apply the lead classification derived in this study, the Hamming-windowing step before the along-track Fast Fourier Transform is selected, which is currently the baseline of the distributed Cryosat-2 product (Bouzinac, 2012). Although this slighlty lowers the along-track resolution and therefore creates some degree of dependence between consecutive echoes, it is needed in order to cut the energy coming from the sidelobes of the antenna.

Fig. 4 shows the so-called "radargrams" of a CS-2 track in a sea-ice covered region for the multilooked waveforms and for the RIP, without (a and c) and with (b and d) the Hamming window application. Each column corresponds to a 20-Hz RIP (a and b) or multilooked waveform (c and d). Before and after the peaky echoes typical of lead-like backscatter, high-power features are seen preceding the leading edge in the multilooked waveform radargram and in the non-zero look angles of the RIP radargram. In fact, the return coming from a sidelobe that sees a lead at nadir when the main lobe is side-looking has a shorter

range and therefore is registered before the leading edge corresponding to the resolution cell.

The sidelobe effects create false leading edges, influence the statistical analysis of the RIP and add backscattering of the same order of magnitude of the nadir return in the look angles closer to zero. These features mostly disappear after the application of the Hamming window, although residual signatures are visible, as highlighted by the arrows in Fig. 4b.

3.1.2. Definition of Stack Peakiness

In order to characterise the RIP shape, the Stack Standard Deviation (SSD) and the Stack Kurtosis (SK) are already given in the ESA Baseline C product. These two indices, although useful to classify the kind of waveform, are not sufficient to isolate the nadir return of a group of waveforms influenced by a lead backscatter. The SSD is based on a gaussian fitting of the RIP, which is a poor approximation for peaky returns such as in Fig. 1b. The SK is highly influenced by remaining sidelobes effects in the looks that are close to the zero look, which can have a similar power. In order to compare the power at the zero look angle with the backscatter registered in the other looks, a new parameter called Stack Peakiness (SP) is defined in this study from the RIP normalised by its maximum value in the following way:

$$SP = \frac{1}{\overline{RIP_{l,r}}} \tag{1}$$

with

$$\overline{RIP_{l,r}} = \frac{\sum_{i=1}^{N} RIP(i)_{l,r}}{N} \tag{2}$$

where N is the number of looks excluding the nadir look and $RIP(i)_{l,r}$ is the power from the look angle i, excluding the nadir look (i.e., at its right or left). A similar index of peakiness of the main return in comparison with the rest of echo was already defined in Ricker et al. (2014). Nevertheless this statistics was computed on the multilooked waveform, which is actually a time series of the received
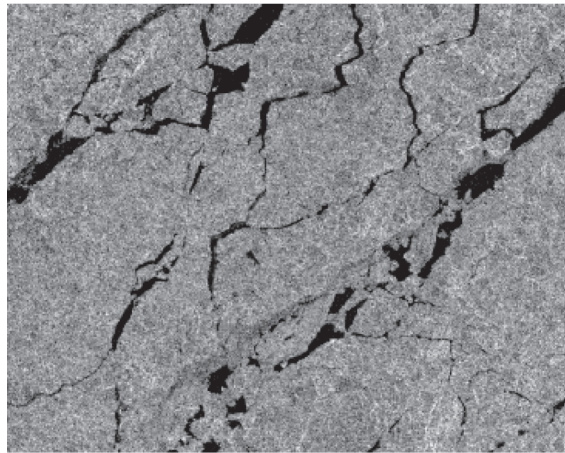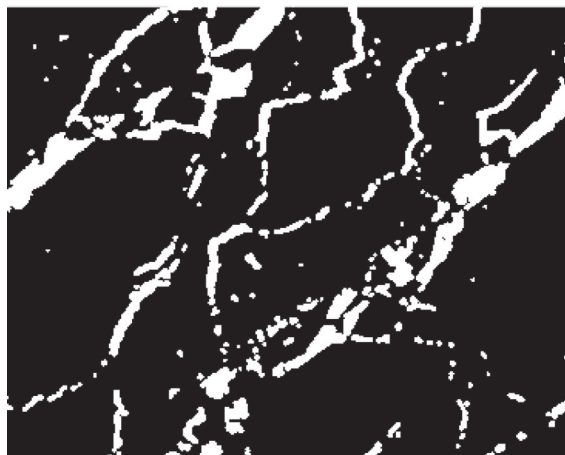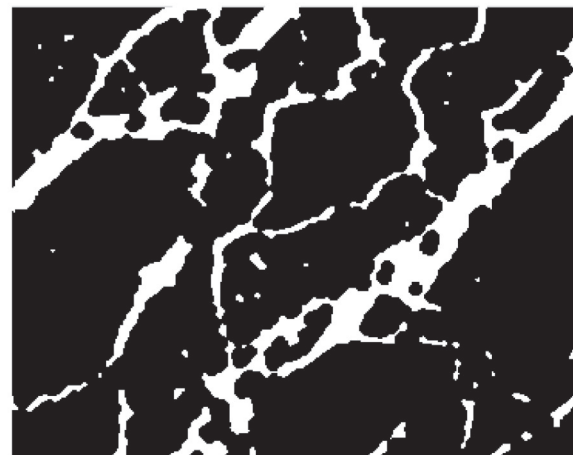
(a) Sentinel-1A image after SAR pre-processing
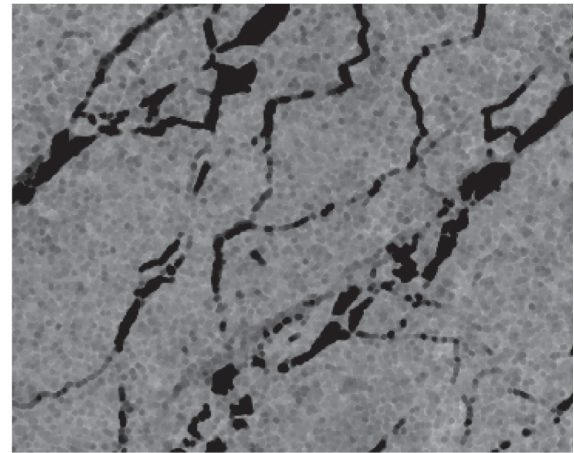
(b) Sentinel-1A image after median and minimum filtering

(c) Sentinel-1A image after segmentation

(d) Sentinel-1A image after morphological closing operation

(e) Octagon kernel for minimum filtering

Fig. 6. Sentinel-1A image subset of about 24 × 24 km: (a) the original grayscaled SAR image after SAR pre-processing; (b) the same image after 5 × 5 median and minimum filtering; (c) the binary image after segmentation by adaptive thresholding; (d) final image after closing operation giving open water in white and sea ice areas in black. Plot (e) shows the octagon kernel with radius 3 around center pixel applied for the minimum filtering.

signal, while SP is able to compare the power reflected from the same resolution cell at different view angles.

The expected behaviour of SP in the case of a narrow lead crossing the CS-2 track is sketched in Fig. 5 and a verification with real data is provided in Section 4.1. When a lead enters the across-track pulse-limited footprint, the SP will be higher than a purely diffusive backscatter event, since the lead will scatter more energy back to the satellite. Nevertheless, the lead will still be slightly off-nadir in the across-track direction: Part of the incoming power will be specularly reflected away. Off-nadir leads are usually characterised by lower levels of backscatter power compared to leads at nadir (Wernecke and Kaleschke, 2015). Consequently, a lead located off-nadir in the across-track direction will scatter less power back to the satellite, if compared with the same lead illuminated at nadir. The maximum SP, i.e. the time when the power at the zero look angle is strongest in comparison with the backscatter received at the other look angles, is therefore expected to correspond to the position in which the lead is at nadir.
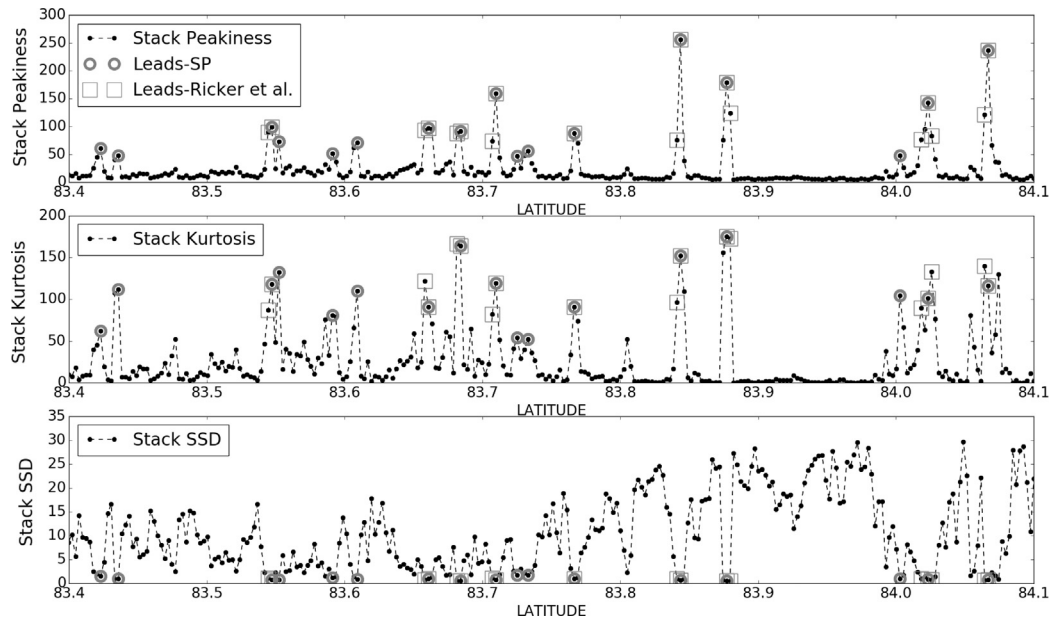
Fig. 7. SP behaviour along a CS-2 track acquired over sea ice (top plot). The figure shows the points that are recognized as leads by the SP-based classification described in this study (circles) and the results of the classification based on Ricker et al. (2014) (squares). The lower plots show Stack Kurtosis and Stack SSD for comparison.
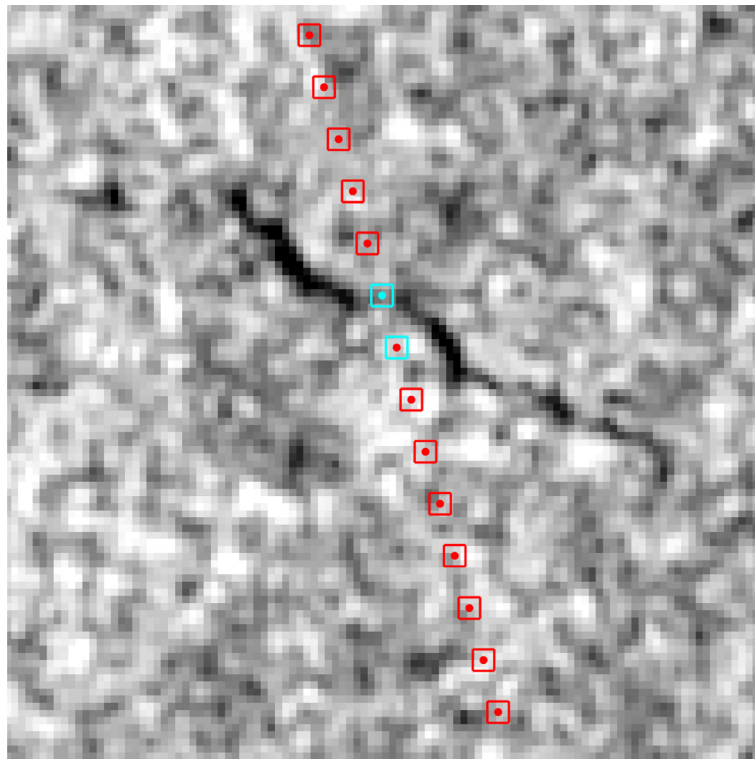

Fig. 8. 4.25 by 4.25 km zoom on a lead seen by Sentinel-1 image from 05/09/2015 at 12:46 (Image 1 of Set 1, see Fig. 3 for location), with Cryosat-2 crossing the area at 16.36. No ice motion correction is applied due to high variation in the ice flow direction. SP (dots) in comparison with classification results of Ricker (squares) showing in cyan lead detections.

3.2. Lead classification based on Cryosat-2

3.2.1. Use of Stack Peakiness

In this study, a local maxima of SP, such as the one in Fig. 5, is considered a potential lead waveform. The SP is almost constant over sea ice, but peaks in presence of a

lead, as shown in Section 4.1. Two additional criteria are used to identify the nadir leads:

- Median SP: The analysis of SP over all CS-2 tracks used for the validation with Set 1 and Set 2 (considering the whole length of each track over the Delay-Doppler geo-

graphical box) shows a median value of $SP_{median} = 8.67$ with a Median Absolute Deviation (MAD) of $SP_{MAD} = 8.72$. In order for a local maxima of SP to be classified as lead, the SP of the RIP before and after the local maxima has to be higher than $SP_{median} + SP_{MAD} \simeq 17$. This is done in order to avoid false detections, by utilising the fact that a lead that crosses the altimeter track influences the SP value also when not yet at nadir.

- Minimum SP: An empirical threshold $SP_{minlead} = 40$ is identified as the minimum SP of the RIP local maxima to be classified as lead. The threshold has been set by empirical observations of the locations of CS-2 points characterised by low SP values on the corresponding SAR images. This additional criteria is added in order to limit the recognition of leads that enter the field of view of the satellite, but never cross the nadir position. Their SP maxima is therefore expected to be lower than the SP maxima of nadir-crossing leads.

In the following sections, SP will be also used as acronym of the corresponding classification method.

3.2.2. Use of received power

Each Delay-Doppler waveform is characterised by a received power. The received power depends on the backscattering characteristic of the surface: flat surfaces such as the still water of small leads or melting ponds specularly scatter most of the incoming radar signal back in the same direction, while ice surfaces are characterised by diffuse scattering, which decreases the amount of power reflected back to the altimeter. In this study (Section 4.3) the adoption of an absolute threshold on received power to identify leads is verified and discussed. The applied threshold is $2.58 \times 10^{-11} \, \text{W}$, as proposed by Wernecke and Kaleschke (2015).

3.2.3. External lead classification

As previously mentioned, the classification proposed in Ricker et al. (2014) is used for comparison. The results of the classification were provided by the Alfred Wegener Institut (see Acknowledgements) for Set 1. The method consists on the use of thresholds set on three waveform-derived parameters (pulse peakiness, peakiness right of the power maximum, peakiness left of the power maximum), two RIP-derived parameters (SK and SSD) and a sea-ice concentration index. The peakiness right and left of the power maximum was directly computed from the waveform, while all the other parameters are provided in the raw data.

3.3. Lead classification based on Sentinel-1 SAR images

A set of image processing algorithms is applied to the Sentinel-1A scenes that should be used as a reference for the lead identification based on CS-2, aimed at extracting open water areas, i.e. black or near black surface areas,

by converting the SAR images into binary format. Leads or polynyas are represented by ones, while ice is coded with zeros. In order to replace the common visual classification an automated SAR image processing is proposed that enables quantitative comparisons with altimetry classification results. The following steps are applied to the SAR images (previously shifted considering the ice motion as described in Section 2.3):

- Noise reduction: To reduce noise in the image due to interfering scattering, a median filter is applied to the grayscaled image. For this purpose a window size of 5×5 pixels (equal to $200 \, \text{m} \times 200 \, \text{m}$ spatial scale) has been chosen to emphasize the transition between ice and water pixels and to minimize a false detection of open water pixels. The filter size is a compromise between noise reduction and compliance with the original image and was experimentally determined.
- Dark pixel emphasizing: After median filtering the grayscale image undergoes a minimum, non-linear filtering emphasizing dark pixel values. This is necessary to compensate uncertainties of the image shifting due to the ice motion (Section 2.3). To control the effect of the minimum filtering a convolution matrix or kernel is needed. Considering the linear and circular shape of openings in the ice, reliable results are reached by using an octagon kernel with a radius of 3 pixels around the center pixel. In Fig. 6, a SAR image before (a) and after median and minimum filtering (b) as well as the used kernel (e) are shown.
- Conversion to binary map: To convert the filtered grayscale image into binary values, a segmentation based on thresholding is applied. For this purpose an adaptive threshold algorithm is employed to compensate spatial variations in contrast and illumination. We follow the approach of Bradley and Roth (2007) that divides the SAR image in foreground and background pixels. In a first step the integral image, a summation of pixel values from top left to bottom right, is computed. The next step computes the average of every pixel in a given neighborhood. The last processing step separates the SAR image in background and foreground by comparing the averaged pixel to the integral image.
- Interconnection of lead fragments: The spatial extent and the shape of a lead can vary very quickly from one meter to over $500 \, \text{m}$ due to persistent ice motion and refreezing (Onstott and Shuchman, 2004). In SAR images leads can show different pattern and pixel values. For example if the leads are refrozen or covered by frost flowers, the pixel values brighten up. Furthermore open water SAR signatures are sensitive to wind conditions. If there are calm conditions, leads appear small and disconnected and could be obscured by surrounding ice (Onstott and Shuchman, 2004). Additionally leads can be segmented due to limited resolution of the SAR image and inaccuracies of the thresholding. In order to reconnect these leads, a morphological closing operation

is applied to the binary images. The closing operator is a consecutive execution of a morphological dilatation followed by a morphological erosion. It enlarges pixel areas by mainly keeping the original boundary shape, thus it fills gaps and connects objects in a specific range. More details regarding the effect of closing operation on binary images can be found in Gonzalez and Woods (2008). As a closing operator, an octagonal kernel with radius of 12 pixels around the center pixel has been chosen based on empirical tests. Fig. 6 visualizes the effect of the closing operation on the segmented binary image (from c to d). The thin adjacent lead fragments are connected by mainly preserving their natural linear spatial extent. As a downside, independent openings that are closely located can be linked, resulting in one widespread open water area.

For the statistical comparison between CS-2 and SAR lead classifications, the binary pixel values of the processed SAR image are interpolated to the altimetry track coordinates, using nearest-neighbor interpolation.

4. Results and discussion

4.1. Analysis of stack parameters

Fig. 7 shows the evolution of the SP over a sea ice covered area in comparison with the Kurtosis and SSD stored in the ESA Baseline C product. Points that are identified as leads by the SP classification described in Section 3.2.1 are highlighted by circles. For comparison, points that are identified as leads using the classification from Ricker et al. (2014) (Ricker from now on) are highlighted by squares.

The evolution of SP in the lead areas closely resembles the scheme of Fig. 5: a peak, which corresponds to the strongest return from the zero look angle compared to the other looks, is easily identifiable, but the lead returns influence also the measurements nearby. The lead areas are also characterized by high Kurtosis and low SSD, but these two indices are often not able to univocally show a

local maximum or minimum: in some cases, the Kurtosis shows multiple peaks in the same sequence of points influenced by a lead, which may be attributed to high power in non-zero look angles due to residual sidelobe effects; the SSD, being based on a Gaussian fitting, is not able to distinguish subtle differences in the power distribution of the very peaky RIP waveforms in the lead areas.

Classifications that are based on these two stack parameters, such as Ricker, tend to classify as leads more points related to the same feature than the SP classification, which performs a sort of multi-waveform approach by looking for local maxima, rather than only considering thresholds on single measurements. In the case of narrow leads, a single-waveform approach can imply that off-nadir returns are being considered as leads. An example is found in Fig. 8, in which the CS-2 track crosses a narrow lead: SP is able to detect the return in which the lead is at nadir, while Ricker classifies as lead also the neighbouring point, in which the lead is seen off-nadir.

4.2. Quantitative comparison with SAR images

The altimetry-based classification is rated considering the following parameters:

- Fraction of False Detections (FFD), i.e. the fraction of points along the CS-2 track that are identified as leads by the altimeter-based method, but identified as ice on the SAR image;
- Fraction of Correctly Classified Leads (FCCL), i.e. the fraction of leads on the SAR image (along the CS-2 track) that are also seen by the CS-2 classification. Note that this statistics concerns the number of leads, therefore two consecutive lead detections are considered as part of the same lead.

The coincidence between CS-2 and SAR lead detection is verified by simply interpolating the SAR binary image generated as in Section 3.3 onto the altimeter track. An along-track tolerance of 400 m is applied in the comparison,

Table 1

Results of the CS-2-based lead classification with the methods described in the study, w.r.t. the SAR images classification. Col 1: name of the SAR images dataset; Col 2: classification method; Col 3: mean and standard deviation of the FFD (defined in 4.2); Col 4: mean and standard deviation of the FCCL (defined in 4.2); Col 5: ratio between FCCL and FFD, taken as final score of the method; Col 6: number of leads seen by each CS-2 lead classification method. For each classification method, the validation against SAR images without the morphological closing operation is identified by the suffix NC (No Closing).

| Validation dataset	Lead detection	Mean(FFD) ± std	Mean(FCCL) ± std	FCCL/FFD	Tot lead
Set 1	Stack Peakiness	0.5444 ± 0.1659	0.6465 ± 0.2121	1.2	472
	Stack Peakiness NC	0.5795 ± 0.1756	0.6065 ± 0.2243	1.0	472
	Ricker et al. (2015)	0.4528 ± 0.1594	0.5496 ± 0.1982	1.2	279
	Ricker et al. (2015) NC	0.4982 ± 0.1758	0.5427 ± 0.2011	1.1	279
	Relative Power Threshold	0.2554 ± 0.2199	0.4269 ± 0.1985	1.7	144
	Relative Power Threshold NC	0.2971 ± 0.2358	0.4276 ± 0.2056	1.4	144
Set 2	Stack Peakiness	0.4472 ± 0.2865	0.5007 ± 0.2217	1.1	507
	Stack Peakiness NC	0.4869 ± 0.2914	0.4392 ± 0.2218	0.9	507
	Relative Power Threshold	0.2885 ± 0.2178	0.4333 ± 0.0728	1.5	188
	Relative Power Threshold NC	0.3349 ± 0.2256	0.4397 ± 0.0994	1.3	188
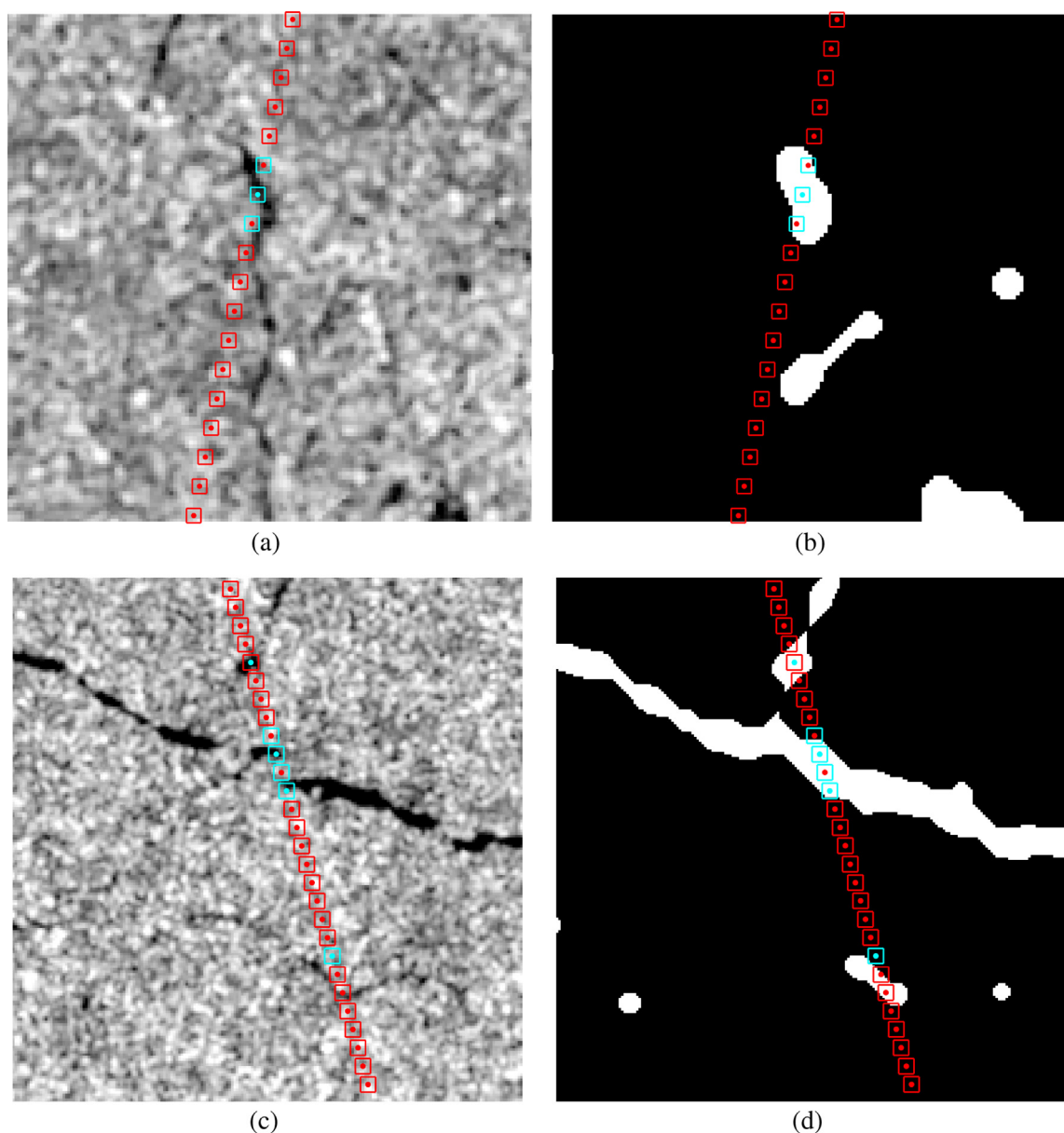
Fig. 9. Examples of lead detection from altimetry against SAR images before (a and c) and after the processing (b and d). a and b show a 5.35 by 5.18 km subset from Image 4 of Set 1, c and d illustrate a 8.11 by 8.34 km zoom from Image 1 of Set 1. Red: ice detection, cyan: lead detection. Squares: Ricker classification, dots: SP classification. (For interpretation of the references to colour in this figure legend, the reader is referred to the web version of this article.)

corresponding to the along-track resolution of CS-2 after the Hamming window application (Scagliola, 2013). The results are summarised in Table 1. The FCCL and the FFD are computed for each SAR image - CS-2 track couple and are shown taking their mean and standard deviation. The total number of leads detected by the SAR images is 232 for September 2015 (Set 1) and 275 for Set 2, while the table reports the total number of detections from the different altimetry-based methods. As a final score for each method, the ratio FCCL/FFD is adopted.

While the Relative Power Threshold and its results will be discussed in the next section, we firstly compare SP with Ricker. The two methods have the same score of 1.2 and

this result is also similar for SP in the control dataset, where the ice motion is applied. The only difference between the two methods is that SP finds 9% more of the leads recognised in the SAR images, but scores 9% worse in the FFD statistics. Essentially, the adoption of the SP index as a criteria is almost equivalent to the use of the 6 indices tuned in Ricker for the purpose of lead detection.

In both methods, the high standard deviation of FCCL and FFD attests the variability of the results depending on the different SAR scenes. We have not found a relationship with the seasonality, since the values are similar in both control data sets. The influence of seasonality cannot be excluded, but to assess it a larger amount of CS-2/SAR
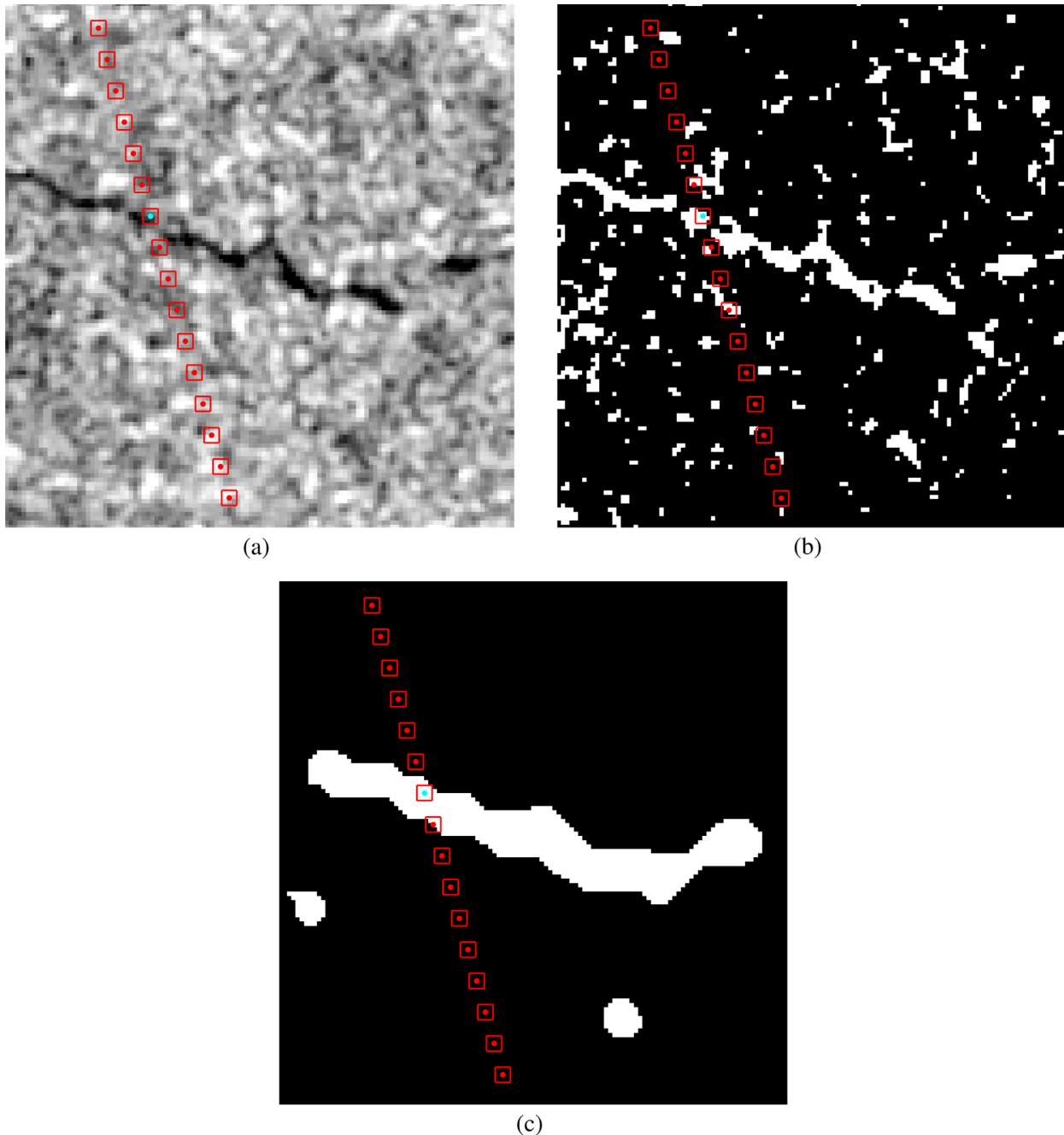
Fig. 10. Examples of lead detection from altimetry against SAR images (4.75 by 4.88 km extract from Image 1 from Set 1) before the processing (a), as a binary map without the filtering and closing (b) and after the full processing (c). Red: ice detection, cyan: lead detection. Squares: Ricker classification, dots: SP classification. (For interpretation of the references to colour in this figure legend, the reader is referred to the web version of this article.)

combinations are needed. This is not trivial, since an archive of these combinations does not exist and since the Stack data are not distributed in the ESA Baseline C CS-2 product and have to be acquired from an external source (G-POD).

Ricker was also validated against MODIS images by Wernecke and Kaleschke (2015). Their True Lead Rate (against MODIS taken as ground truth), essentially equivalent to the FCCL in this research, has a mean value of 60%, in line with our result considering the standard deviation. Despite the different ground truth, the statistics is therefore robust, but the validation here presented can be easily replicable since the lead extraction from the ground truth does not rely on visual criteria such as in the previous studies.

We argue that the reason for which the score of Ricker and SP is equivalent lies in the filtering of the SAR images needed for noise reduction. Fig. 9 shows two examples of the comparison between leads seen through SAR image processing and altimetry-based classification with SP and
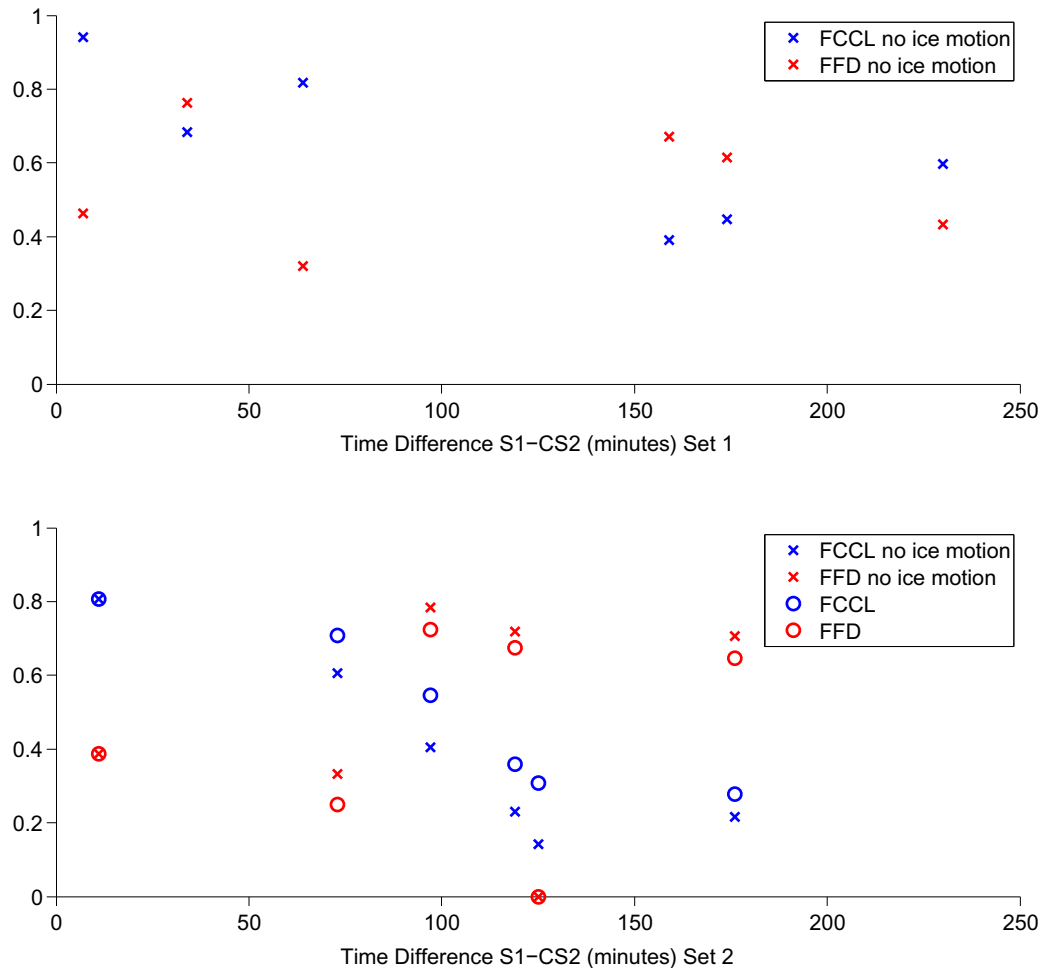
Fig. 11. FCCL (blue) and FFD (red) for each SAR image of Set 1 and Set 2 according to the time difference with the corresponding CS-2 track. In Set 1, the sea ice motion vectors are not applied, as in Table 1. In Set 2, statistics are shown with (circles) and without (crosses) the application of sea ice motion vectors. (For interpretation of the references to colour in this figure legend, the reader is referred to the web version of this article.)

Ricker. The figure shows that the filtering widens the borders of the lead, which has the effect of considering as a correct nadir detection the off-nadir CS-2 points that are classified as leads in Ricker. Nevertheless, the filtering is a necessary step to achieve an authomatic and objective procedure for validation, as shown in Fig. 10: a binary map formed without the noise reduction described in Section 3.3 would result in several incorrect lead-like isolated features and as a consequence would strongly decrease the reliability of the comparison. Even with the filtering, the SAR processing is not always able to extract leads that are very thin, as for example in Fig. 9b. The binary map recognises the wider part of the lead that crosses the CS-2 track, but misses the elongated feature, due to the insufficient contrast between the ice edge and the thin lead.

A validation experiment was also undertaken to observe the effect of the closing operation. The results are listed for each altimetry classification method in Table 1. By comparing altimetry with SAR images without the closing, a general increase of the mean FFD by 3–4% is observed as well as a decrease of the FFCL, which result in a worse score.

The reason is observed in Fig. 10 c: the closing connects a lead that is seen fragmented in the original SAR image, which can be due to partial refreezing or noise. Without the closing, the lead identified by the altimeter would be interpolated on a black (ice) SAR binary pixel, resulting in an apparent false detection.

For the purpose of comparing the lead detection from satellite altimetry with the one applied on SAR images, the latter is considered as a ground truth. This assumption is only meant to provide a common ground for the comparison of different altimetry-based strategy, but it is an approximation of the reality: Despite the high resolution, Sentinel-1 is not able to distinguish leads that are narrower than 40 m, while such cracks in the ice could still be the dominant return in the altimetric waveforms. This difference is even more stringent after the application of the 200 m × 200 m median filter for noise reduction in the SAR image. Moreover, the ability of both the automated SAR technique and the altimetry methods to distinguish between leads and melt ponds, which according to recent studies can occupy as much as 70% of the first-year ice area

in the melting period (Divine et al., 2016), remains hard to verify and further research is needed in this matter.

Finally, the impact of the time difference between S1 and CS-2 and of the application of the sea ice motion vectors in Set 2 is displayed in Fig. 11, considering the SP classification statistics. Regardless of the sea ice motion vectors, in both Sets the best results in terms of FCCL are obtained for S1-CS2 coupling close in time: in particular, only CS-2/SAR comparisons within 90 min show FCCL > 0.4 and the closest CS-2/SAR comparison has the best FCCL score. Moreover, in 4 out of 5 comparisons within 90 min, FCCL is higher than FFD, while the opposite happens in 6 out of 7 comparisons over 90 min, regardless of the sea ice motion vectors application. The latter has nevertheless a limited, but constant positive effect, reducing FFD and improving FCCL.

4.3. Received power as lead classifier

Using the distinction between true leads and false leads on the base of the comparison with SAR images, Fig. 12 shows, for every SAR image of the two datasets, the mean and standard deviation of the received waveform power from the points classified as leads by CS-2. The figure also shows as a dotted line the value of 2.58×10^{-11}, which has been proposed by Wernecke and Kaleschke (2015) as the threshold for the best representation of lead occurence. This threshold is not entirely comparable with the values here presented, since it has been computed using the ESA Baseline B release of the CS-2 data, while at the time of writing this has been substituted with ESA Baseline C: small differences in the Delay-Doppler processing used to build the waveforms can lead to different power output associated to each echo.

Considering the results, the implementation of an absolute threshold to classify the leads does not look feasible. The proposed threshold, although it avoids false detections, does not find leads in three of the tracks from September 2015 and misses almost any lead in Set 2. The return power distribution of false leads and true leads is not constant: for example, the power distribution of false leads in images 1 and 2 from September 2015 is almost coincident with the power distribution of true leads in images 1 and 2 from Set 2. The power backscattered by a lead in fact does not depend only on the off-nadir or nadir view, but also on the presence of sea ice in the illuminated area, on possible refrozen areas of the lead and on its width. In general, the higher is the selected absolute power threshold, the higher is the confidence that the selected points are real leads, but the lower is the number of detections.

Nevertheless, the mean power of the true leads distribution is constantly higher than the one of the false leads distribution. We can use this information in a relative sense by computing the ratio between the power of the CS-2 returns classified as leads and the median of the power in the segment of the track considered (Power Ratio). As a tentative approach in this study, we considered the whole length of

the CS-2 segment downloaded for each corresponding Sentinel-1 image date. These vary between roughly 200 and 800 km. A histogram of the Power Ratio in the two datasets is shown in Fig. 13. Although they refer to different areas at different times, both datasets show that when the Power Ratio is below 10, the False Leads are predominant. Since the results are consistent, we keep the previously defined approach to define the Power Ratio. This relative threshold is therefore used as a "Relative Power Threshold" classification and the results are displayed in Table 1. Although the FCCL is lower than for the other methods, the false lead detections are also considerably less. This brings to an overall score FCCL/FFD of 1.7 in Set 1 and 1.5 in Set 2. The Relative Power Threshold scores therefore best, but it is here derived *a posteriori* and further studies in different locations and at different times of the year are needed in order to understand whether the same threshold can be used systematically. Compared to the use of an absolute threshold, the performances of this method are not dependent on time and location of the track, but, as seen in Table 1, also the Relative Power
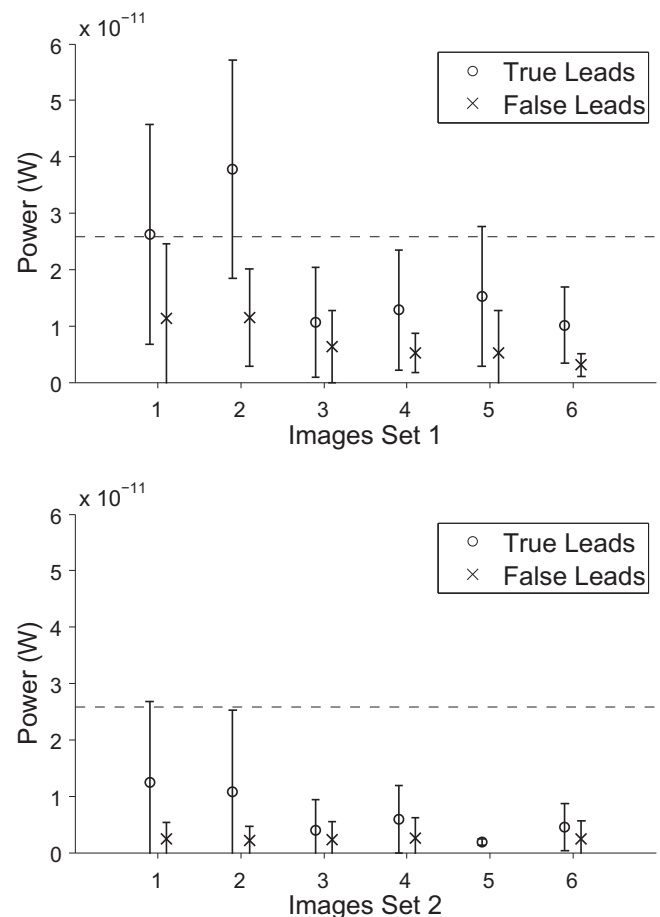

Fig. 12. Mean and standard deviation of the received power of True and False Leads in each image of the two control datasets. True and False Leads are the CS-2 waveforms classified as leads with the Stack Peakiness method and validated by means of comparison with the SAR images. The dashed horizontal line corresponds to the threshold proposed by Wernecke and Kaleschke (2015).
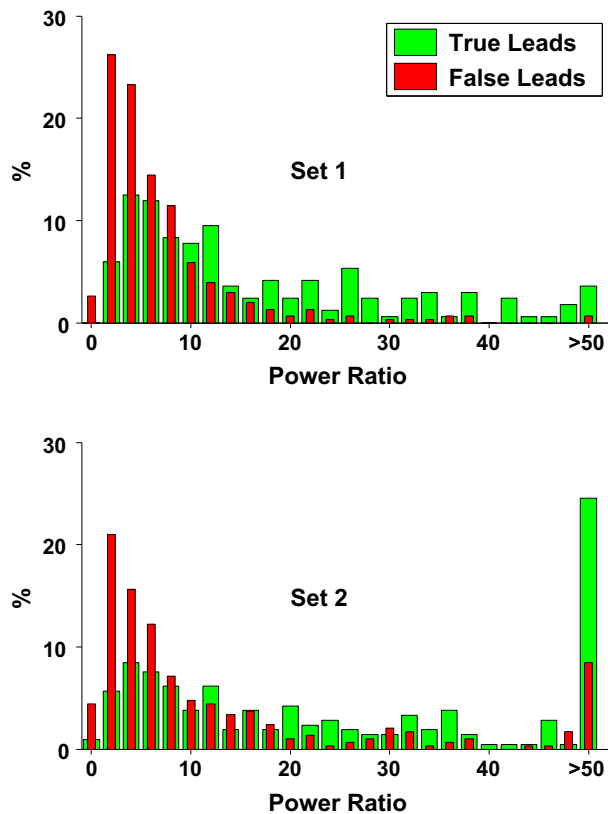
Fig. 13. Histogram of the received power of True and False Leads in both control datasets. True and False Leads are the CS-2 waveforms classified as leads with the Stack Peakiness method and validated by means of comparison with the SAR images.

Threshold brings as a drawback a significant reduction of the number of detected leads, in particular w.r.t. SP.

5. Conclusions

This study aimed at testing different Cryosat-based methods for lead classification taking the SAR images from Sentinel-1 as reference. SAR images have been processed in order to provide an automatic distinction between leads and ice.

A new parameter based on stack data, the Stack Peakiness, has been proposed. A visual analysis of the CS-2 tracks and SAR images has shown how SP can be used to isolate the nadir return from narrow leads crossing the track. The statistics show that in terms of correctly identified leads and false detections, the SP method has comparable results to the method proposed by Ricker et al. (2014), which combines six different waveform indices derivable from the CS-2 returns. The automated SAR processing is not able to highlight significant differences between SP and Ricker, due to the necessary filtering, nevertheless it constitutes a reliable, objective and easily replicable validation method.

In order to quantitavely understand whether SP avoids the off-nadir returns coming from the leads when approaching the altimetry track, an easier and systematic access to CS-2 stack data is needed. In this case, further research could be planned to produce maps of sea surface height in the Arctic region using the identified leads and comparing the sea level variability with previous estimates.

Given the substantial differences of the power distribution of the leads observed in the datasets, the use of an absolute threshold on the return power to classify leads and avoid off-nadir returns, as proposed in previous studies, is not considered reliable. The best performances are nevertheless obtained by using the return power in a relative sense in comparison with the average power of the CS-2 returns in the area considered.

The percentage of false lead detections in comparison with the fraction of correctly classified leads is high for all the tested strategy. If the classification based on SAR images could be taken as the ground truth, this result would undermine the reliability of sea surface estimates in the Arctic Ocean, since it would imply that several reflections from the sea ice are considered for sea level measurements. Nevertheless, given that previous studies on-ground have shown that the width of a lead can be well below 1 km, it is likely that the altimeters spot leads whose width is below the SAR resolution. The time difference between CS-2 and SAR acquisitions plays also a key role and the comparability between the two sources clearly decreases after 60–90 min, despite the attempt of taking in consideration the sea ice velocity.

Although the SAR images do not represent the ground truth in terms of lead classification, given the resolution limits, they represent a well established comparison. The strength of this work is that the automatised validation can be easily reproduced in other areas, if an archive of CS-2 passes and Sentinel-1A images that are sufficiently close in time is provided. Indeed, further validation is needed in different sea-ice covered regions (multi-year and first year ice) and at different times of the year, since the presence of melt ponds and the refreezing of the leads could considerably alter the performances of any classification algorithm.

Future research should also address the exploitation of the SP for classification of the waveforms from the SAR-Interferometric mode of CS-2 (SARIn). In SARIn, the use of a second across-track antenna allows the localisation of different returns using the phase difference between the echoes reaching the two antennas. While the availability of SARIn in the sea ice region is limited to few patches (Armitage and Davidson, 2014) have shown that, combining the classification with an off-nadir ranging correction to characterise the off-nadir leads, the accuracy and the precision of sea ice freeboard measurements can be improved compared to the SAR mode.

References

Armitage, T.W., Davidson, M.W., 2014. Using the interferometric capabilities of the ESA Cryosat-2 mission to improve the accuracy of sea ice freeboard retrievals. IEEE Trans. Geosci. Remote Sens. 52, 529–536.

Bouzinac, C., 2012. CryoSat Product Handbook. European Space Agency, https://earth.esa.int/documents/10174/125272/CryoSat_Product_Handbook.

Bradley, D., Roth, G., 2007. Adaptive thresholding using the integral image. J. Graph. GPU Game Tools 12, 13–21.

Dierking, W., 2013. Sea ice monitoring by synthetic aperture radar. Oceanography 26.

Divine, D.V., Pedersen, C.A., Karlsen, T.I., Aas, H.F., Granskog, M.A., Hudson, S.R., Gerland, S., 2016. Photogrammetric retrieval and analysis of small scale sea ice topography during summer melt. Cold. Reg. Sci. Technol. 129, 77–84.

Gonzalez, R.C., Woods, R.E., 2008. Digital Image Processing. third ed.. Prentice Hall, Upper Saddle River, New Jersey, USA.

Ivanova, N., Rampal, P., Bouillon, S., 2016. Error assessment of satellite-derived lead fraction in the Arctic. Cryosphere 10, 585–595.

Kwok, R., Cunningham, G., Wensnahan, M., Rigor, I., Zwally, H., Yi, D., 2009. Thinning and volume loss of the Arctic Ocean sea ice cover: 2003–2008. J. Geophys. Res.: Oceans 114.

Laxon, S.W., Giles, K.A., Ridout, A.L., Wingham, D.J., Willatt, R., Cullen, R., Kwok, R., Schweiger, A., Zhang, J., Haas, C., et al., 2013. CryoSat-2 estimates of Arctic sea ice thickness and volume. Geophys. Res. Lett. 40, 732–737.

Lindsay, R., Rothrock, D., 1995. Arctic sea ice leads from advanced very high resolution radiometer images. J. Geophys. Res.: Oceans 100, 4533–4544.

Onstott, R.G., Shuchman, R.A., 2004. SAR measurement of sea ice. In: Jackson, Apel (Ed.), Synthetic Aperture Radar: Marine User's Manual, US Department of Commerce, National Oceanic and Atmospheric Administration, National Environmental Satellite, Data, and Information Service, Office of Research and Applications, pp. 81–115.

Peacock, N.R., Laxon, S.W., 2004. Sea surface height determination in the Arctic Ocean from ERS altimetry. J. Geophys. Res.: Oceans 109.

Rampal, P., Weiss, J., Marsan, D., 2009. Positive trend in the mean speed and deformation rate of Arctic sea ice, 1979–2007. J. Geophys. Res.: Oceans 114.

Raney, R.K., 1998. The Delay/Doppler radar altimeter. IEEE Trans. Geosci. Remote Sensing 36, 1578–1588.

Ricker, R., Hendricks, S., Helm, V., Skourup, H., Davidson, M., 2014. Sensitivity of CryoSat-2 Arctic sea-ice freeboard and thickness on radar-waveform interpretation. Cryosphere 8, 1607–1622.

Rinne, E., Similä, M., 2014. Utilisation of CryoSat-2 SAR altimeter in operational ice charting. Cryosphere 10, 121–131.

Röhrs, J., Kaleschke, L., 2012. An algorithm to detect sea ice leads by using AMSR-E passive microwave imagery. Cryosphere 6, 343–352.

Scagliola, M., 2013. CryoSat footprints. Aresys technical note, SAR-CRY2-TEN-6331. Tech. rep., Aresys/ESA, Italy.

Scagliola, M., Fornari, M., 2015. Main evolutions and expected quality improvements in BaselineC Level1b products. Aresys technical note, C2-TN-ARS-GS-5154. Tech. rep., Aresys/ESA, Italy.

Tschudi, M., Fowler, C., Maslanik, J., Stewart, J., Meier, M., 2016. Polar Pathfinder daily 25 km EASE-grid sea ice motion vectors (Last Access: 08/08/2016), Boulder, Colorado USA. NASA National Snow and Ice Data Center Distributed Active Archive Center.

Weeks, W., 2010. On Sea Ice. University of Alaska Press, Fairbanks, USA.

Wernecke, A., Kaleschke, L., 2015. Lead detection in Arctic sea ice from CryoSat-2: quality assessment, lead area fraction and width distribution. Cryosphere 9, 1955–1968.

Willmes, S., Heinemann, G., 2015. Pan-Arctic lead detection from MODIS thermal infrared imagery. Ann. Glaciol. 56, 29–37.

Wingham, D., Francis, C., Baker, S., Bouzinac, C., Brockley, D., Cullen, R., de Chateau-Thierry, P., Laxon, S., Mallow, U., Mavrocordatos, C., et al., 2006. CryoSat: a mission to determine the fluctuations in Earth's land and marine ice fields. Adv. Space Res. 37, 841–871.

Veci, L., 2016. SENTINEL-1 Toolbox SAR Basics Tutorial. Array Systems Computing Inc., http://step.esa.int/main/.

ALES +: Adapting a homogenous ocean retracker for satellite altimetry to sea ice leads, coastal and inland waters

Marcello Passaro[a,*], Stine Kildegaard Rose[b], Ole B. Andersen[b], Eva Boergens[a], Francisco M. Calafat[c], Denise Dettmering[a], Jérôme Benveniste[d]

[a] Deutsches Geodätisches Forschungsinstitut der Technischen Universität München, Arcisstraße 21, Munich 80333, Germany
[b] DTU-Space, National Space Institute, Kgs. Lyngby, Denmark
[c] National Oceanography Centre Liverpool, Liverpool, United Kingdom
[d] European Space Research Institute (ESRIN), European Space Agency, Frascati, Italy

ABSTRACT

Water level from sea ice-covered oceans is particularly challenging to retrieve with satellite radar altimeters due to the different shapes assumed by the returned signal compared with the standard open ocean waveforms. Valid measurements are scarce in large areas of the Arctic and Antarctic Oceans, because sea level can only be estimated in the openings in the sea ice (leads and polynyas). Similar signal-related problems affect also measurements in coastal and inland waters.

This study presents a fitting (also called retracking) strategy (ALES +) based on a subwaveform retracker that is able to adapt the fitting of the signal depending on the sea state and on the slope of its trailing edge. The algorithm modifies the existing Adaptive Leading Edge Subwaveform retracker originally designed for coastal waters, and is applied to Envisat and ERS-2 missions.

The validation in a test area of the Arctic Ocean demonstrates that the presented strategy is more precise than the dedicated ocean and sea ice retrackers available in the mission products. It decreases the retracking open ocean noise by over 1 cm with respect to the standard ocean retracker and is more precise by over 1 cm with respect to the standard sea ice retracker used for fitting specular echoes. Compared to an existing open ocean altimetry dataset, the presented strategy increases the number of sea level retrievals in the sea ice-covered area and the correlation with a local tide gauge. Further tests against in-situ data show that also the quality of coastal retrievals increases compared to the standard ocean product in the last 6 km within the coast.

ALES + improves the sea level determination at high latitudes and is adapted to fit reflections from any water surface. If used in the open ocean and in the coastal zone, it improves the current official products based on ocean retrackers. First results in the inland waters show that the correlation between water heights from ALES + and from in-situ measurement is always over 0.95.

1. Introduction

Sea level is an Essential Climate Variable (ECV) regarded as one of the main indicators of climate variability (Cazenave et al., 2014). For more than 25 years, traditional measurements obtained by means of in-situ pressure gauges have been supported by the repeated global remotely sensed estimations from the radar signals registered onboard satellite altimeters. This has lead to significant advancements in our knowledge of the seasonal and interannual sea level fluctuations (Vinogradov and Ponte, 2010; Ablain et al., 2016), of the regional distribution of trends in a changing climate (Palanisamy et al., 2015) and of the mid to large scales of geostrophic circulation (Pascual et al.,

2006).

The basic concept of this remote sensing technique considers the sea surface height (SSH) as the difference between the height of the satellite referenced to the earth ellipsoid and the distance (range) between the satellite centre of mass and the mean reflecting surface. The SSH has then to be corrected for instrumental, atmospheric and geophysical effects. For a full description of the corrections the reader is referred to Fu and Cazenave (2001). The progress of satellite altimetry has been fostered by the developments in orbit determination (Rudenko et al., 2014), in the corrections (Handoko et al., 2017) and in the range retrieval, based on the fitting of a functional form to the received signal in a procedure called retracking (Cipollini et al., 2017).
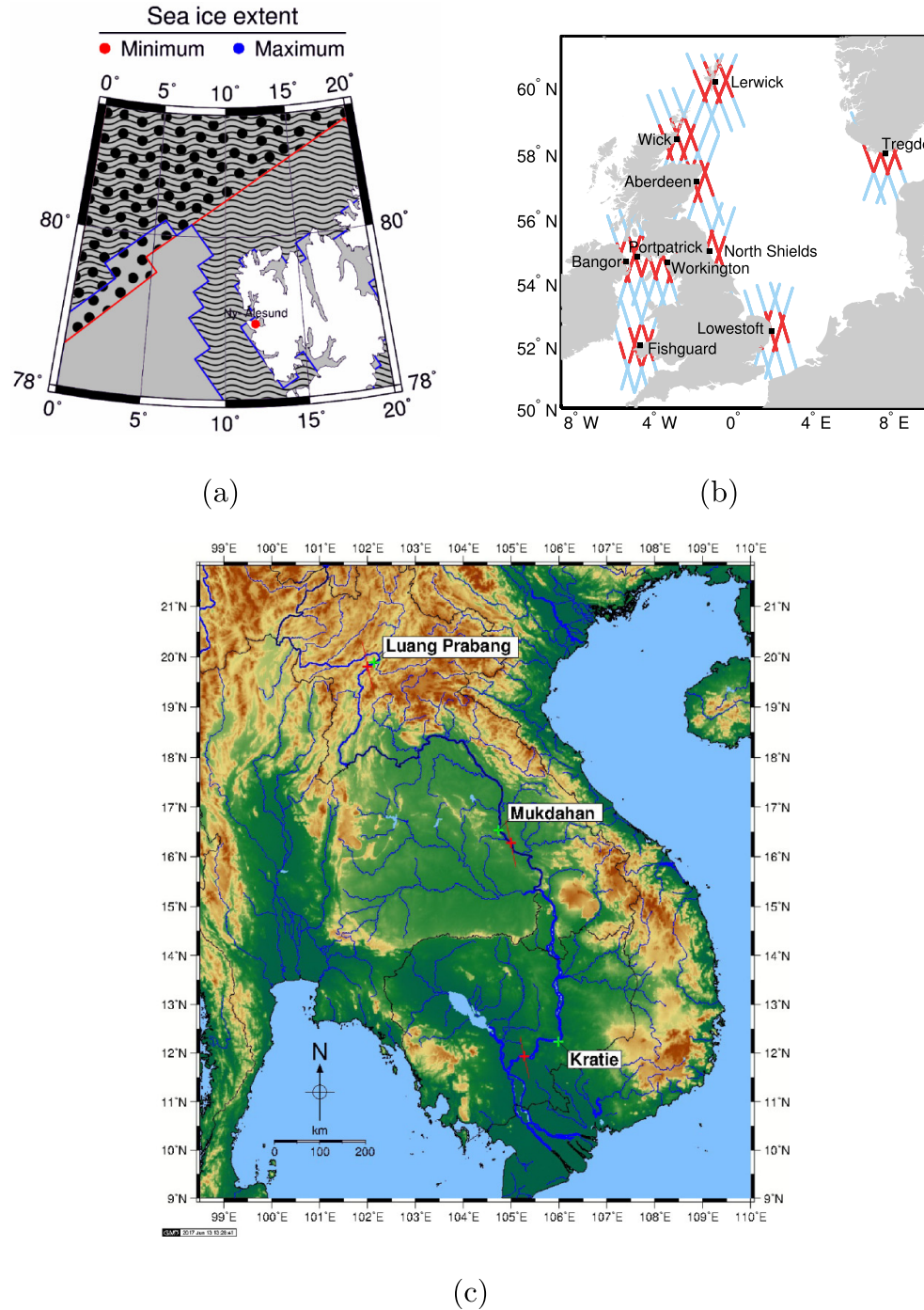
Fig. 1. (a) The Svalbard test area in the Arctic Ocean. The dotted area with red border is the minimum sea ice cover, while the wavy area with blue border is the maximum. The red dot indicates the location of the Ny Ålesund TG used for validation. (b and c) Location of the TGs used for coastal and inland waters validation and (red) along-track extension of nominal Envisat and ERS-2 tracks used for comparison with in-situ data.

The processing of the echoes sent by pulse-limited radar altimeters (i.e. every radar altimeter before the launch of CryoSat-2 in April 2010 and, more recently, Sentinel-3A) is well known in the open ocean, where the shape of the received signal resembles the Brown-Hayne (BH) model (Brown, 1977; Hayne, 1980) perturbed by Rayleigh noise (Quartly et al., 2001), characterised by a steep leading edge and a slowly decaying trailing edge. Departures of the received signal (also called 'waveform', a sampled time series whose resolution cell is called 'gate') from the BH shape are instead found in the presence of sea ice and in the proximity of land (i.e. both in coastal and inland waters)

(Boergens et al., 2016; Laxon, 1994b). The common feature is the presence of the so-called 'bright targets' or 'hyperbolic targets': points with a higher backscatter coefficient that perturb the expected shape travelling along the trailing edge as they appear in the illuminated area, eventually constituting the main leading edge.

These retracking issues, together with the degradation of some corrections in the same areas, have been a major impediment in expanding our knowledge of sea level variability in the coastal ocean and in the Arctic Ocean. These are regions of primary importance, since a growing number of people and infrastructures are located at the coast

(Neumann et al., 2015) and since changes in the Arctic Ocean dynamics significantly affect the global climate (Marshall et al., 2014).

This study is motivated by the need of increasing the quality and the quantity of sea level retrievals in the Arctic Ocean. It focuses on a re-tracking procedure that is able to retrieve the ranges of pulse-limited radar altimeters reflected from the leads (water apertures in sea ice) while improving the retracking in open and coastal ocean as well. Given the similarities of the problem, we aim also at demonstrating the va-lidity of this strategy for the retrieval of water level in inland waters. The result is the definition of a single algorithm that is able to adapt the estimation to any kind of water returns.

Here, our efforts are aimed at improving the times series for 1995–2010 by fitting the signals from the altimeters on two European Space Agency (ESA) missions: ERS-2 and Envisat, which have occupied the same ground tracks of a 35-day repeat cycle between latitudes 82°S and 82°N.

Previous and ongoing studies share the objective of improving the quality of satellite altimetry at high latitudes. Giles et al. (2007) applied a dedicated empirical functional form to lead waveforms, separating the typical peaky shape into a Gaussian and an exponential function. For the open water points though, they used the standard product, which adopts the BH fitting. The use of heterogenous retrackers leads to a significant bias, which was quantified in 15 ± 11 cm. Two different retrackers for ocean and leads and a consequent bias adjustment were also the choice of Peacock and Laxon (2004). More recently, Cheng et al. (2015) edited the Envisat data from the Radar Altimetry Database System (RADS) without applying a specific retracker, while Poisson et al. (2018) are also aiming at a homogenous retracking strategy, as this paper, by using the modified BH proposed by Jackson et al. (1992), in which the peakiness of the waveform is modelled by a surface roughness parameter.

Our starting point is the Adaptive Leading Edge Subwaveform (ALES) retracker by Passaro et al. (2014), which is based on a BH fitting of a portion of the echo in order to avoid bright targets on the trailing edge of the waveforms. The ALES-reprocessed altimetry data have al-ready been validated against in-situ measurements from tide gauges (TGs) and used for coastal sea level variability studies (Passaro et al., 2015a, 2016). The potential for the application to peaky echoes was already identified in a paper by Passaro et al. (2015b), where ALES was applied on the tidal flats in the German Bight, whose still waters pro-duce returns analogous to lead echoes. Here, we develop a new version of the algorithm (ALES +) to improve the fitting of the peaky wave-forms and abate the noise in the open ocean compared to the standard processing.

In the framework of the ESA Sea Level Climate Change Initiative (SL CCI), ALES + is the retracker of choice for Envisat and ERS-2 missions in the DTU/TUM high latitude sea level product. Therefore, the main part of this paper is dedicated to the description and validation of the ALES + solution in a test zone of the Arctic Ocean. We also evaluate the performances at the coast and in the inland waters, in order to exploit ALES + as a homogenous retracker solution for any kind of water sur-faces.

The dataset and the areas of study are defined in Section 2; the ALES + procedure and the methodologies followed to identify leads among the sea ice are described in Section 3; validation and discussion follow in Section 4, while Section 5 derives the conclusions.

2. Areas of study and datasets

2.1. Areas of study

As a main area of study the surroundings of the Svalbard Islands (the Svalbard test area, latitude limits: $78 - 82°N$, longitude limits: $0 - 20°E$) are chosen, in order to validate ALES + in a geographical box that presents both constant open water and sea ice. The presence of a TG, which is very rare at such latitudes, also allows a validation in areas

that are seasonally covered by sea ice. Fig. 1 (a) shows the minimum (September 2007) and maximum (February 1998) extent of the sea ice during the period considered in this study, provided by the Sea Ice Index Data and Image Archive at NSIDC (Fetterer et al., 2016) and is given as a monthly sea ice extent polygon. Also the TG Ny Ålesund used in the validation is shown in Fig. 1 (a).

To validate ALES + as a coastal retracker, the coastal waters of a region in the North-East Atlantic Ocean within 70 km of the coast are considered, due to the availability of local TG data with high temporal resolution. Fig. 1 (b) displays the TGs used in the study and highlights in red the analysed segments of the altimetry tracks.

Finally, the Mekong River is taken as example of an inland water application in order to allow the comparison with previous studies that exploit the synergy between altimetry and in-situ stations, which are shown in Fig. 1 (c).

2.2. Satellite altimetry data

The waveforms and all the additional information needed to apply the ALES + algorithm are taken from the ESA Sensor Geophysical Data Records (SGDR) of ERS-2 REAPER (Femenias et al., 2014) and Envisat version 2.1. For Envisat the entire duration of the phase 2 (May 2002–October 2010) is considered; for ERS-2 the REAPER data cover the period from September 1995 to July 2003. The RADS altimetry database (http://rads.tudelft.nl/) with its default settings is used to provide an alternative sea level anomaly (SLA, see Section 3.3) product for comparison.

2.3. In-situ data

In the sea ice region Revised Local Reference (RLR) TG data of the Ny Ålesund station are downloaded as monthly averages from the Permanent Service for Mean Sea Level (PSMSL) at http://www.psmsl.org/data/obtaining/stations/1421.php. In the coastal region TG re-cords were obtained from the UK National Tide Gauge Network ar-chives at the British Oceanographic Data Centre (BODC) and the University of Hawaii Sea Level Center (UHSLC). The temporal resolu-tion of the sea level data is 15 min for records stored at the BODC and 1 h for those stored at the UHSLC. Here, we use a set of 10 TGs with nearly continuous records of sea level over the period 1995–2010, which have been visually inspected for shifts and outliers. In the Mekong river, telemetric gauge data is provided by the Mekong River Commission (MRC, http://ffw.mrcmekong.org/). The latter has a daily resolution, but no absolute height reference.

This kind of in-situ data are widely used by the Scientific Community as validation means. All types of TG (acoustic, pressure, float, and radar) can measure sea-level variations with an accuracy of at least 1 cm (see the IOC Manual on Sea Level at http://www.psmsl.org/train_and_info/training/manuals), which is significantly better than the accuracy achieved by altimeters. Telemetric river monitoring system is considered to reach a mm accuracy (see http://www.radio-data-networks.com/products/flooding/radar-based-river-level-monitoring-telemetry/).

3. Methodology

3.1. ALES + retracker

3.1.1. The Brown-Hayne model
ALES + inherits the functional form used to fit the waveforms from the BH model. In order to clarify the terminology in use, we report here the corresponding Equations. The return power V_m is

$$V_m(t) = a_\xi P_u \frac{[1 + \text{erf}(u)]}{2} \exp(-v) + T_n \tag{1}$$

where

$$\mathrm{erf}(x) = 2\frac{1}{\sqrt{\pi}}\int_0^x e^{-t^2}dt, \quad a_\xi = \exp\left(\frac{-4\sin^2\xi}{\gamma}\right), \quad \gamma = \sin^2(\theta_0)\frac{1}{2\cdot\ln(2)}$$

$$(2)$$

$$u = \frac{t - \tau - c_\xi \sigma_c^2}{\sqrt{2}\,\sigma_c} \qquad v = c_\xi\left(t - \tau - \frac{1}{2}c_\xi\sigma_c^2\right)$$

$$(3)$$

$$\sigma_c^2 = \sigma_p^2 + \sigma_s^2 \qquad \sigma_s = \frac{SWH}{2c}$$

$$(4)$$

$$c_\xi = b_\xi a, \qquad a = \frac{4c}{\gamma h\left(1 + \frac{h}{R_e}\right)}, \qquad b_\xi = \cos(2\xi) - \frac{\sin^2(2\xi)}{\gamma}$$

$$(5)$$

where c is the speed of light, h the satellite altitude, R_e the Earth radius, ξ the off-nadir mispointing angle, θ_0 the antenna beam width, τ the Epoch with respect to the nominal tracking reference point (linked to the range), σ_c the rise time of the leading edge (depending on a term σ_s linked to the Significant Wave Height (SWH) and on the width of the radar point target response σ_p), P_u the amplitude of the signal (linked to the backscatter coefficient σ_0) and T_n the thermal noise level.

The variables that can alter the slope of the trailing edge in BH are all contained in the term c_ξ. It is important to note that c_ξ has also a small effect on u via the term $c_\xi\sigma_c^2$. This means that changes in c_ξ also slightly affect the position of the retracking point τ along the leading edge. An approach to fit the trailing edge slope was also attempted in other studies, such as in the empirical 5-parameter model by Deng and Featherstone (2006), in which nevertheless a change in the parameter related to the slope of the trailing edge would not cause any change in the location of the retracking point on the leading edge.

In Eqs. (1)–(5), the trailing edge slope variability is constrained by the fact that θ_0 is given and the variations of ξ are slow and must be smaller than 0.3° (Dorandeu et al., 2004). While these constraints correctly model a typical open ocean response, they prevent the fitting of peakier waveforms. Therefore, in order to be able to fit waveforms with a steep trailing edge slope, ALES+ preliminary estimates c_ξ. The steps followed by ALES+ are the following:
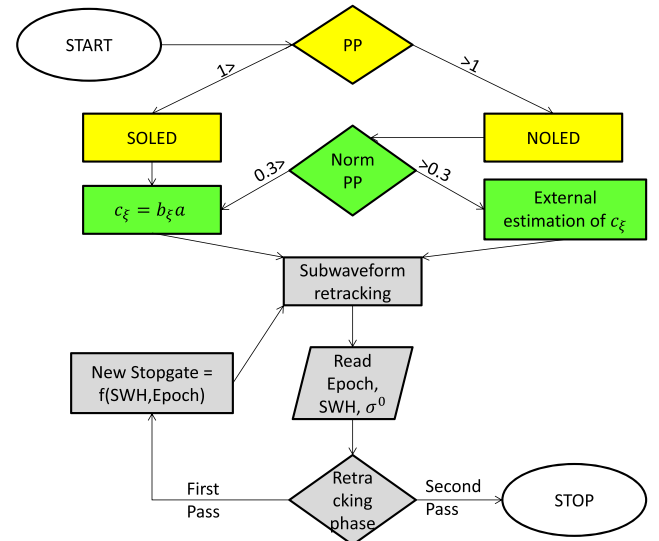
1. Detection of the leading edge
2. Choice of c_ξ
3. First retracking of a subwaveform restricted to the leading edge, i.e. first estimation of the SWH
4. Extension of the subwaveform using a linear relationship between width of the subwaveform and first estimation of the SWH
5. Second retracking of the extended subwaveform, i.e. precise determination of τ, SWH and P_u

Steps 1 and 2 are described respectively in Sections 3.1.2 and 3.1.3. Steps 3 to 5 are unchanged compared to the ALES retracker (Passaro et al., 2014) and they are recalled in Section 3.1.4. A flow diagram of the main steps followed by ALES+ to retrack each waveform is shown in Fig. 2.

3.1.2. Leading edge detection

Since ALES+ is based on the selection of a subwaveform, it is essential that the leading edge, containing the information on the range between satellite and reflecting surface, is correctly detected in all cases. Lead waveforms and ocean/coastal waveforms are characterised in this respect in two different ways: in the first case, the lead return (if at nadir) clearly dominates any other return, but the decay of the trailing edge is extremely quick; in the latter, the leading edge is better characterised, but spurious strong returns can precede (if from icebergs, ships, or targets at a higher height than the water level) or follow (if from areas of the footprint characterised by different backscatter characteristics) the main leading edge, whose trailing edge decreases very slowly.

To distinguish between the two cases, a Pulse Peakiness (PP) index

Fig. 2. Flow diagram of ALES+ retracking procedure for each waveform. PP stands for Pulse Peakiness, Norm PP for Pulse Peakiness computed on the normalised waveforms. SOLED and NOLED are the leading edge detection procedures for standard and non-standard ocean waveforms described in Section 3.1.2. The steps highlighted in green are described in Section 3.1.3 and the ones in grey, analogous to ALES in Passaro et al. (2014), are recalled in Section 3.1.4.

is computed in ALES+ following the formula in Peacock and Laxon (2004). The order of magnitude of PP ranges from 10^{-1} for waveforms in which the peak power is comparable to the average backscatter in the other waveform gates, to over 10^1 for echoes dominated by a strong specular reflector. Waveforms with PP < 1 are sent to the standard ocean leading edge detection (SOLED) procedure, the others are sent to the non-standard ocean leading edge detection procedure (NOLED). This is not a physical classification aimed at detecting leads, but only a way to aid the correct detection of the leading edge; moreover, the retracking (steps 3–5 in Section 3.1.1) remains the same in both cases.

Non-standard ocean waveforms are in our case not only the leads (peaky waveforms), but any waveform whose trailing edge decay is more pronounced than in the standard ocean return. We do not exclude the waveforms coming from sea ice, since these are excluded in the post-processing by the classification of Section 3.2. The aim is therefore different from Peacock and Laxon (2004), in which a strict classification is needed in order to send each kind of waveform to a different retracker and to avoid the detection of false leads, which would cause inconsistencies in the sea level retrieval.

The steps followed by NOLED are the following:

1. The waveform is normalised with normalisation factor N, where N = 1.3 * median(waveform).
2. The temptative starting point of the leading edge, defined as startgate, is assigned to the first gate higher than 0.01 normalised power units compared to the previous gate.
3. If any of the subsequent 4 gates after the selected startgate have a normalised power below 0.1 units, the algorithm goes back to step 2 and a new startgate is found.
4. The end of the leading edge (stopgate) is fixed at the first gate in which the derivative changes sign (i.e. the signal start decreasing and the trailing edge begins), if the change of sign is kept for the following 3 gates.

The steps followed by SOLED are the following:

1. The waveform is normalised with normalisation factor N, where N

= max(waveform).

2. The stopgate is the maximum value of the normalised waveform.
3. Going backwards from stopgate, the startgate is the first gate in which the derivative is lower than 0.001 units.

N = 1.3*median(waveform) was chosen empirically as a reference power whose value is close to the maximum of the leading edge also in case of high trailing edge noise. Note that for NOLED waveforms the maximum of the leading edge does not necessarily correspond to the maximum power registered in the waveform, since it may come from spurious coastal reflections and/or noise in the trailing edge.

3.1.3. Choice of c_ξ

The non-standard ocean waveforms undergo a further preliminary step: c_ξ is estimated externally. Beforehand, a further check on the PP recomputed on the normalised waveform (Norm PP > 0.3) is computed in order to avoid, where possible, the estimation of c_ξ in the presence of other peaks in the trailing edge. Norm PP is useful because by using a normalised waveform it is easier to set up a threshold for all peaky waveforms regardless of their maximum backscatter power, which greatly differ between specular reflections (Passaro et al., 2017). The threshold was determined by empirical observation of waveforms, of which Fig. 3 provides an example.

In the external estimation, the full waveform is fitted using a simplified BH model up to Eq. (4), having 4 unknowns: $\tau, \sigma_c, P_u, c_\xi$. From this result, only c_ξ is kept and used as an input in the remaining steps of the ALES + algorithm.

If Norm PP < 0.3, c_ξ is computed from Eq. (5).

c_ξ can be therefore estimated for all the waveforms that successfully pass through SOLED and if Norm PP > 0.3, i.e. all the peaky waveforms in which one clear leading edge can be identified. Since the estimation of c_ξ is suitable for peaky waveforms, irregular waveforms where no leading edge is identifiable cannot be correctly fitted by ALES + . Fig. 4 shows the estimations of c_ξ for cycle 35 of Envisat (February–March 2005). The areas where c_ξ is estimated are all located in the sea-ice-covered region.

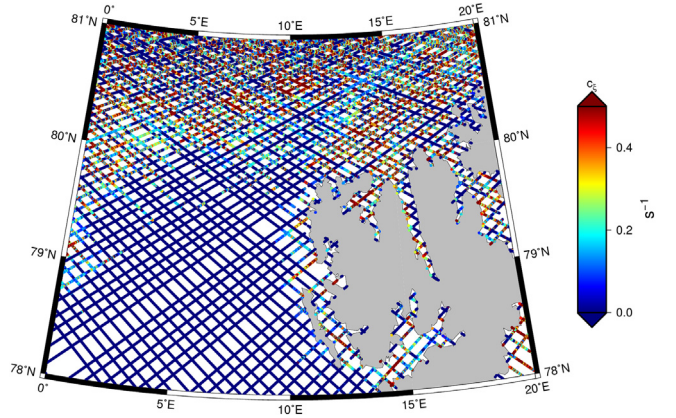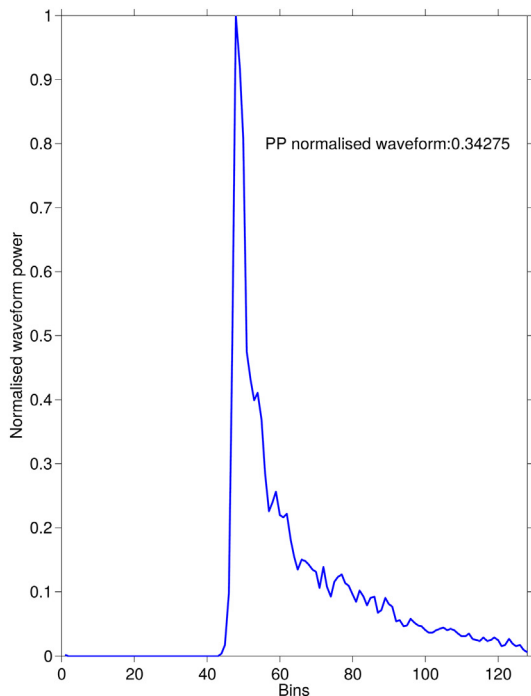**Fig. 4.** Estimations of c_ξ for cycle 35 of Envisat. In the plot, c_ξ is set to 0 for NOLED waveforms and for waveforms in which Norm PP < 0.3, because c_ξ is in these cases not estimated.

3.1.4. Subwaveform retracking

Steps 3 to 5 are analogous to the ALES retracker. In step 3, a first subwaveform from startgate to stopgate is fitted with the BH model having τ, σ_c, P_u as unknowns.

The SWH derived from σ_c and τ are used in step 4 to compute the new stopgate using the following linear relationship:

$$\text{Stopgate} = \text{Ceiling(Tracking point} + 2.4263 + 4.1759 \times \text{SWH)} \tag{6}$$

for Envisat and:

$$\text{Stopgate} = \text{Ceiling(Tracking point} + 3.1684 + 2.3203 \times \text{SWH)} \tag{7}$$

for ERS-2. The Tracking point is the gate corresponding to the estimated Epoch τ.

Finally, in step 5 a new fitting is performed using a subwaveform up to the new stopgate and the final estimations of τ, σ_c and P_u are obtained. Note that in every fitting, the subwaveform is oversampled by means of the Akima interpolation by Akima (1970) in order to increase the redundancy of the information across the leading edge as described in
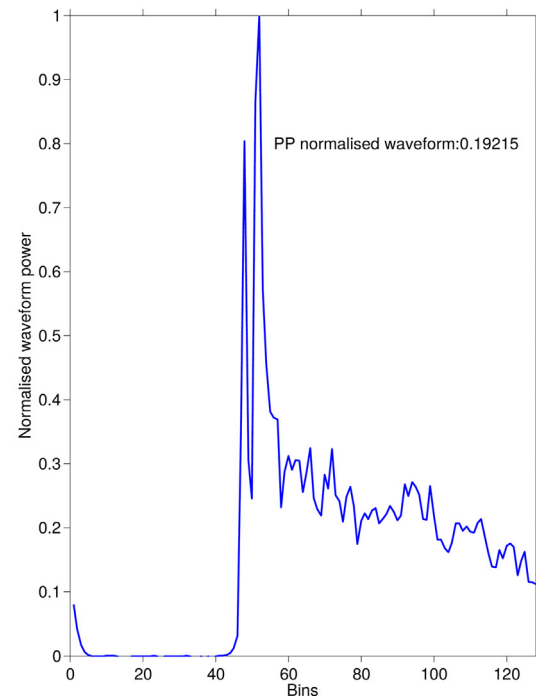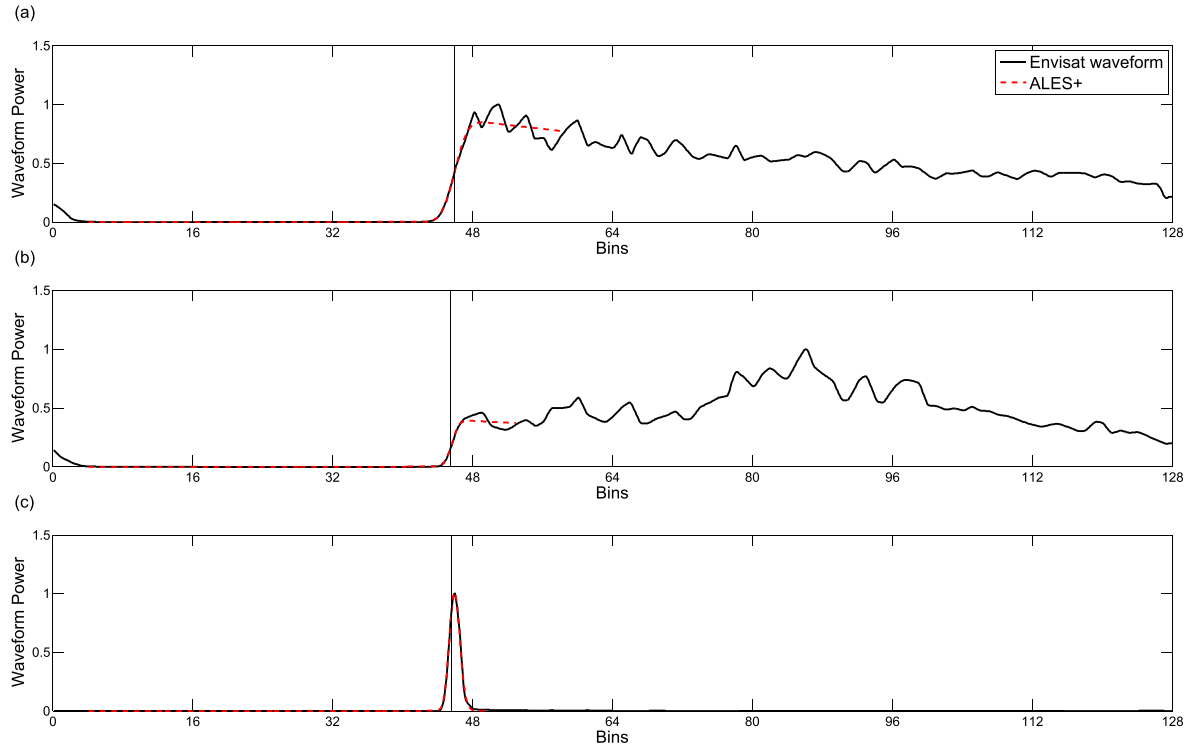

Fig. 3. Normalised waveforms and their pulse peakiness (Norm PP). Left: a peaky waveform in which c_ξ can be estimated by ALES + ; Right: a waveform with a peak following the trailing edge.

Fig. 5. Examples of ALES + waveform fitting for three different trailing edge slope conditions typical of open ocean (a), coast (b) and leads (c). A black vertical line highlights the location of the retracking point estimated by ALES +.

Passaro et al. (2015b); in ALES +, the waveforms are oversampled by a factor of 8 for both Envisat and ERS-2.

Fig. 5 shows three examples of ALES + waveform fitting for three different trailing edge slope conditions typical of open ocean, coast and leads. A black vertical line highlights the location of the retracking point estimated by ALES +. In the lead case (Fig. 5c), it is evident how the retracking point (Epoch) is not located at the mid-point of the visible leading edge, since the retracking point τ and c_ξ are present both in the exponential term v and in the argument of the error function u as described in Section 3.1.1. This effect is not simply empirical, but is related to the mean square slope (MSS) of the sea surface, as shown in Jackson et al. (1992). In the latter, the so-called trailing edge parameter, which has an effect on the retracking point as well, depends explicitly on the MSS and hence on the surface roughness. Indeed, using the mid-point of the 'visible' leading edge as the retracking point of any peaky waveform has no physical meaning, because the waveform, i.e. a discrete time series, is in this case highly undersampled: the information on the position of the true maximum power and consequently the location of the true mid-point of the leading edge cannot be retrieved. ALES + cannot create new information and solve the problem of the undersampled leading-edge, but it can perform a consistent guess of τ given c_ξ, using an existing waveform model and adapting it to a more general case.

3.1.5. Sea State Bias recomputation

The Sea State Bias (SSB) is among the time-variable corrections that are applied to SSH estimates from satellite altimetry. SSB is linked with both the signal processing of the radar echo and the interaction between the latter and the waves. Given the theoretical complexity and the different sources of SSB, the accepted procedure to derive an SSB correction is to infer an empirical relationship between the height error due to SSB, and the SWH and wind speed (derived from σ^0) estimated from the retracking of each altimetry mission. Sandwell and Smith (2015) have studied the relationship between the parameters estimated

by the retracking algorithms (range, SWH and σ^0) and have found significant correlated errors. In the same study, they argue that correlated errors in the retrackers explain a significant part of the SSB. It is therefore fundamental to correct the ranges for the SSB corresponding to SWH and σ^0 values estimated by the same retracker.

The SSB applied to the ALES + data is obtained by bilinear interpolations from a look-up table in which this correction is a function of SWH and Wind Speed (Labroue, 2007). The look-up table could be obtained from the SGDR data by tabulating the values assumed by the given SSB correction for each value of SWH and Wind. In order to be more accurate, the authors have obtained the look-up table with permission from Collecte Localisation Satellite (CLS). When performing the bilinear interpolations, SWH and σ^0 obtained from ALES + were used. σ^0 was converted to wind speed using the algorithm described in Abdalla (2012). This follows the procedure applied and validated against in-situ data for ALES Envisat in Gómez-Enri et al. (2016). For ERS-2, we use the same look-up Table as for Envisat mission, since the one used in the REAPER product has not been published (Gilbert et al., 2014).

3.2. Waveform classification

To allow the validation of the retracking strategy in the sea ice region, lead and open ocean waveforms need to be isolated by means of a classification algorithm. For our purposes, given that sea ice waveforms can be hard to distinguish from open ocean returns (Drinkwater, 1991; Laxon, 1994a), we first separate the ice-covered region from the open ocean using the daily ice concentration grids from the Global Sea Ice Concentration Climate Data Records 1978–2015(v1.2, 2015) of the Norwegian and Danish Meteorological Institutes (available online from EUMETSAT Ocean and Sea Ice Satellite Application Facility http://osisaf.met.no). The sea ice area is defined by all the points in the grid with a sea ice concentration over 15% (Fetterer et al., 2016).

In this study, the following classification criteria are used for both

Envisat and ERS-2:

- The samples within the sea ice area characterised by PP > 20 and σ_c < 3 ns are classified as leads;
- The samples outside the sea ice area characterised by PP < 1.5 and σ^0 < 15 dB are classified as open water.

Any other point is either classified as unknown or as sea ice and is therefore not considered in our analysis. The criterion on σ^0 is applied to remove spurious data near the ice edge and in the ice pack (Chelton and McCabe, 1985). Additional discussion and validation of the classification method will be provided in a separate study.

3.3. Corrections applied to the range

While the retracking technique at the centre of this investigation influences the range and the SSB, as mentioned in the introduction other corrections are needed in order to obtain a sea level that is comparable to external sources for validation. In particular, we define the SSH as follows:

$$
\begin{aligned}
\text{SSH} = \ &\text{Orbit altitude} - \text{Corrected Range} \\
&- (\text{Solid Earth Tide} + \text{Load Tide} + \text{Ocean Tide})
\end{aligned}
\tag{8}
$$

where

$$
\begin{aligned}
\text{Corrected Range} = \ &\text{Range} + \text{Dry tropospheric correction} \\
&+ \text{Wet Tropospheric Correction} + \text{+Sea State Bias} \\
&+ \text{Ionospheric correction}
\end{aligned}
\tag{9}
$$

Note that the correction that eliminates the static and dynamic response of the sea level to the atmospheric wind and pressure forcing (often called Dynamic Atmosphere Correction) is not applied, since the water level measured by pressure gauges used for validation is also subjected to these factors.

We use the corrections for the wet and dry troposphere and for the ionosphere from the models available in the SGDR. The SSB is recomputed for ALES+ as previously described. The sea level is also corrected for tides: the FES2014 model is used in the Svalbard test area, given the improvements brought by the model in the Arctic region (Carrere et al., 2015); the Empirical Ocean Tidal model EOT2011a (Savcenko and Bosch, 2012) is used in the coastal validation, since it has scored best in a recent validation effort against coastal TGs (Stammer et al., 2014). Finally, the Sea Level Anomaly (SLA), i.e. the variation of the SSH with respect to a local mean, is obtained by subtracting the Mean Sea Surface model DTU15 to the SSH (Andersen et al., 2016).

4. Validation and discussion

4.1. Svalbard test area

4.1.1. Comparison among retrackers

The first index that proves the quality of the retracking is the fitting error on the leading edge. The fitting error is a measure of how close the fitted waveform is to the real signal and corresponds to the normalised square root of the difference between the modelled waveform and the real signal along the leading edge. It has already been used in Passaro et al. (2015a) for outliers detection. In Fig. 6, the histogram of the fitting error for the waveforms classified as leads is compared to the one for the open ocean waveforms with low SWH, whose leading edge is therefore more similar to the peaky case. The fitting error of lead waveforms is in the vast majority of instances lower than for the low-SWH ocean case, which proves the capability of ALES+ to fit the leading edge of all the peaky waveforms. The statistics for ERS-2 are slightly worse than for Envisat: this can be attributed to the fact that the

original ERS-2 data are defined on half the number of gates (64) compared to Envisat (128).

Firstly, we compare our retracked data with the SGDR output in the sea ice domain. In particular, concerning SGDR we consider both the ocean retracker and the sea ice retracker, which was specifically designed for the fitting of specular waveforms by Laxon (1994a) and included in the official ESA products from Envisat and ERS-2. This retracker was used to estimate sea level from leads by Peacock and Laxon (2004). Given the absence of a network of high-resolution in-situ data at such latitudes, we validate the retrackers following the procedure of Deng and Featherstone (2006) by means of an independently surveyed reference. We use GOCO5s, the latest release of the GOCOs geoid model, which is independent from altimetry, being based exclusively on satellite gravimetry data (Pail et al., 2010), although as such it is not able to observe the shorter wavelengths (below 100 km) detected by the altimeter. The GOCO5s geoid height are interpolated to the altimetry tracks in the whole area and the differences between SSH and geoid height are computed. These differences of course include the mean dynamic topography and the uncertainties in the corrections to the altimetry data. Nevertheless what matters for our analysis are the differences among the retrackers and the corrections do not have an influence, since exactly the same corrections are applied to every dataset. In order to make our results independent of the performances of the waveform classification, we compute the differences for any point with PP > 1 and we only keep the additional criteria of σ_c < 3 ns, to be sure that we are dealing with peaky echoes. After removing outliers (absolute value of SLA above 2 m), the Median Absolute Deviation (MAD) of the differences is computed for every cycle and the average values are shown in Table 1. For both missions ALES+ is the best performing dataset, improving not only the results of the ocean retracker (more than 7 cm improvement for Envisat, more than 10 cm improvement for ERS-2), which is not able to fit peaky waveforms properly, but also of a dedicated solution (more than 2 cm improvement for Envisat against the sea ice retracker, 2.8 cm for ERS-2).

To further investigate the noise performances of ALES+ compared to a standard ocean retracker, the analysis of repetitive tracks in the open sea is needed. For this purpose, we limit our area of study using only the track segments that are out of the maximum extent of the sea ice, as shown in Fig. 7. As a noise index we use the standard deviation of the high frequency data within a 1-Hz block. For comparison, the same analysis is performed using the SGDR ranges (from the ocean retracker) corrected and processed in the same way as ALES+ ranges. In the figure, the maps in (a) and (b) show for each 1-Hz point in ERS-2 and Envisat the median of the difference between the noise of the ocean retracker (SGDR) and the noise of the ALES+ retracker (ALES+). Positive numbers therefore mean that SGDR is noisier than ALES+. The histograms considering each 1-Hz point are shown in (c) and (d). In both missions, ALES+ is less noisy than SGDR in over 70% of the domain and in 20% of the domain it improves by over 3 cm. The maps show that, although the best improvements are reached at the border with the maximum sea ice extent, ALES+ is superior to the standard ocean retracking also in the open ocean. Overall, the median SGDR noise is 6.23 cm in Envisat and 9.18 cm in ERS-2, while the ALES+ noise is 5.08 cm in Envisat and 7.95 cm in ERS-2, meaning over 1.1 cm of improvement.

This demonstrates that the ALES+ compromise between a sufficient width of the subwaveform to characterise the signal and a limited influence of the noise in the trailing edge in the fitting allows a more precise estimation of the open ocean sea level, if compared with a full-waveform retracker. This clear improvement in the open ocean was not evident in Passaro et al. (2014) for ALES. The reason lies in the recomputation of the SSB correction using the ALES+ SWH and backscatter coefficient. We demonstrate this in Fig. 9, where the standard deviation of the 1-Hz points is plotted against the SWH for ALES+ corrected by the standard SSB and by the recomputed SSB. For comparison, the SGDR statistics are also shown. From the linear fit it is
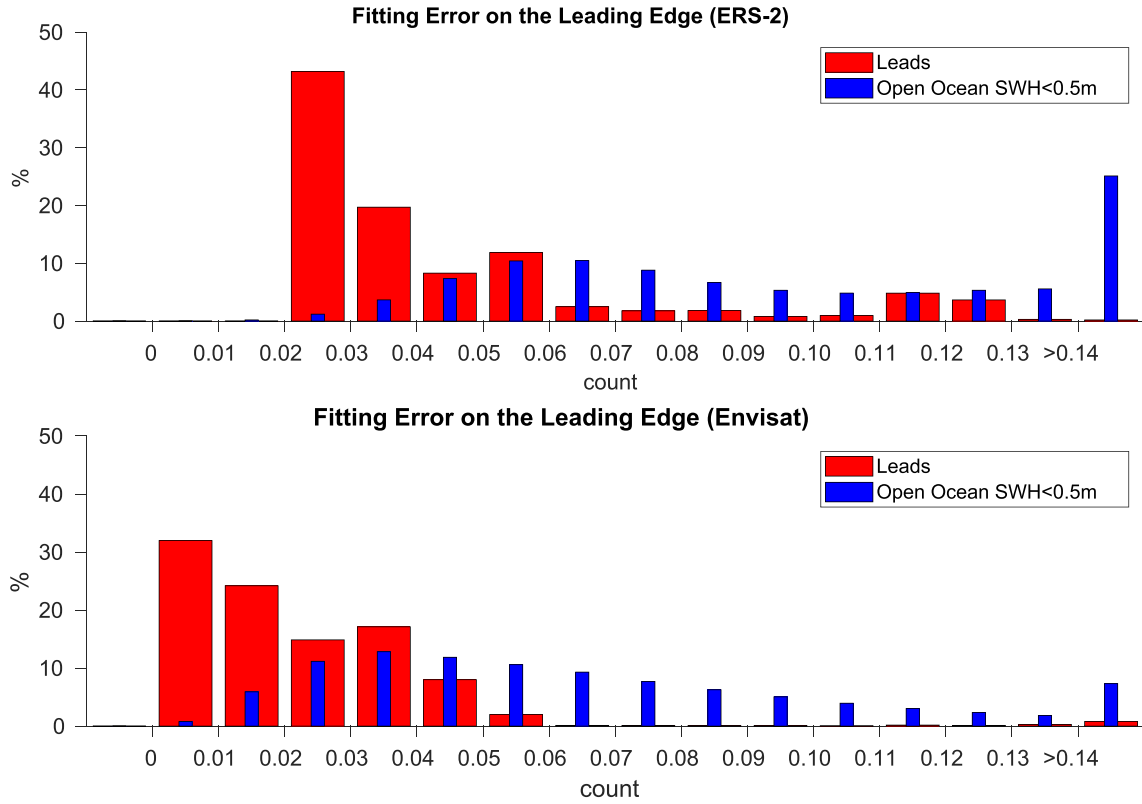
Fig. 6. Error of the leading edge fit computed w.r.t. the normalised waveform for echoes classified as leads (red) and as open water with SWH < 0.5 m (blue) in ERS-2 (upper plot) and Envisat (lower plot).

Table 1
Median Absolute Deviation between GOCO5s geoid heights and SSH data retracked with ALES +, SGDR-Ocean and SGDR-Seaice retracker for peaky waveforms in the Svalbard test area.

	ALES +	SGDR-Ocean	SGDR-Seaice
ERS-2	0.2620 m	0.3659 m	0.2901 m
Envisat	0.2142 m	0.2961 m	0.2364 m

evident that without a recomputed SSB correction ALES + is slightly noisier than SGDR, while the new correction brings a strong improvement.

4.1.2. Comparison of sea level products

The main application of ALES + is the provision of improved ranges that will be used to compute SLA in the SL CCI DTU/TUM high latitude sea level product. We evaluate the improvements in this section. We take RADS as an open ocean sea level reference that flags coastal and sea ice data, with the objective to show what improvements a dataset including these areas can bring to the sea level records.

We apply a gridding procedure to the dataset. First of all, outliers are detected by a MAD filter. The RADS data are per default already post-processed so no further outlier detection to this dataset is applied. Subsequently, for each week the SLA values are gridded using a least squares collocation (kriging) method with a second order Markov covariance function (Andersen, 1999):

$$c(r) = C_0 \left(1 + \frac{r}{\alpha}\right) e^{-r/\alpha} \tag{10}$$

where C_0 is the signal variance, r is the spatial distance, and α is the correlation length. The covariance scale is derived from the data variance, the correlation length is set to 500 km. Each grid cell measures

0.1° latitude × 0.5° longitude. For reference, we process RADS data in the same way. The collocation error is displayed in Fig. 8 (a) –(b), while (c) –(f) show the number of valid measurements used for each grid point. The much higher number of measurements used by ALES + is simply explained by the fact that it uses high-frequency measurements (18 Hz for Envisat, 20 Hz for ERS-2), while RADS is based on 1-Hz averages. This allows ALES + to retrieve much more points in the sea ice-covered regions. Even if the number of measurements is much lower than in the open ocean, the error is kept below 2 cm also in most of the northern and coastal areas of the domain. Overall, the mean error for ALES + in the sea ice covered zone is 2.1 cm (2.7 cm for RADS) while in the open ocean domain the mean error is 0.9 cm (1.3 cm for RADS).

Finally, we verify the accuracy of our sea level estimations by comparison with the Ny Ålesund TG. The location of the TG is visible in Fig. 1 (a). SLA from ALES +, generated from the range using the corrections in Section 3.3 is averaged in space in a radius of 350 km around the TG and in time to generate a monthly time series. The radius of 350 km is needed to perform a regional average that includes both sea ice cover and open ocean areas and the choice was already justified in the same area by Cheng et al. (2015). The agreement of the time series (Fig. 10) is proved by a correlation of 0.85. For comparison, we also build a time series using RADS. Indeed, the better correlation using ALES + is expected, given that RADS is not optimised for the Arctic Ocean: the benefit of the ALES + retracking is particularly evident in the winter months of 1996 and 1998. As mentioned in Section 4.1, the winter of 1998 had the maximum sea ice extent; a significant part of the area considered for the comparison (the coast west of the Svalbard islands) was covered by sea ice and therefore the use of a standard altimetry product is more problematic. In the last decade, most of the area was ice-free during winter as well (not shown, see for example https://nsidc.org/data/seaice_index/archives/image_select.html) and therefore the RADS and ALES + time series are more similar.
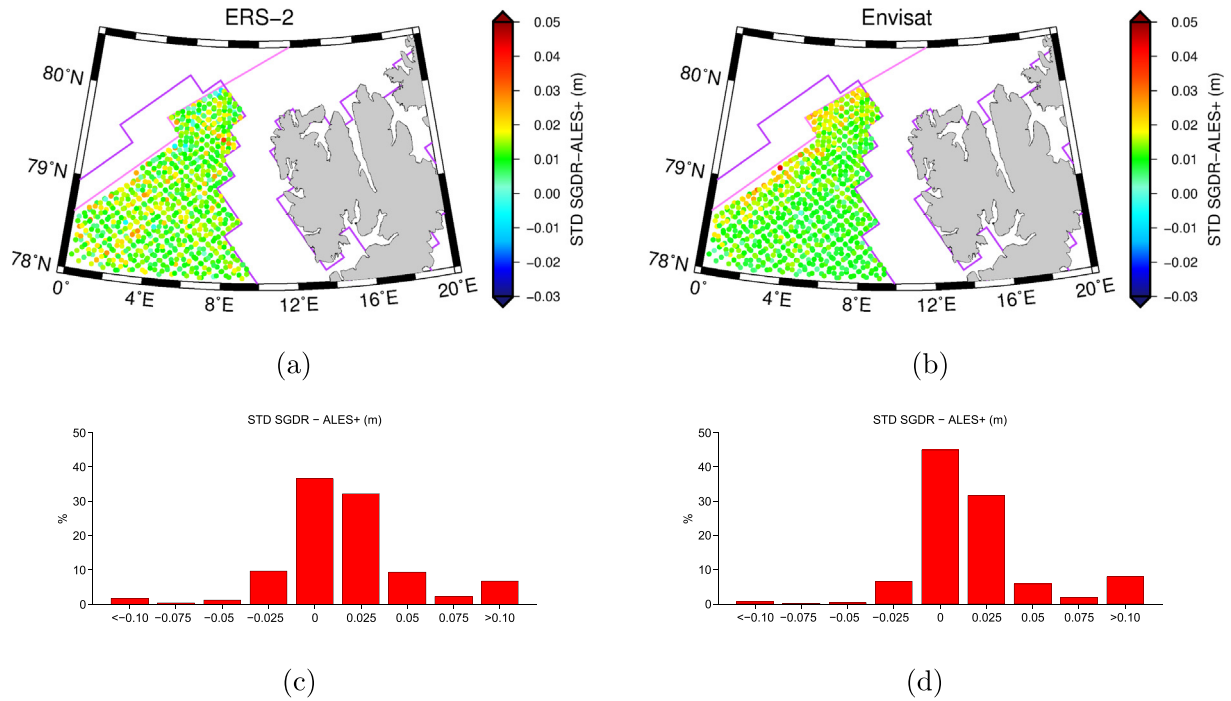
Fig. 7. Difference of high-frequency noise in SGDR and ALES + for ERS-2 (a,c) and Envisat (b,d). The noise is computed as standard deviation of the 1-Hz averages. The maps in (a) and (b) show the median of the noise difference for each 1-Hz point along the satellite tracks considering the entire period of study. Areas characterised by seasonal or multi-year sea ice are masked out.

4.2. Coast

In this Section, the performances of ALES + in the coastal ocean are tested by comparison with the set of TGs in Fig. 1 (b). The comparison is performed for detided time series of sea level. The amplitudes and phases of the tidal constituents in the tide gauge records were estimated on a year-by-year basis by harmonic analysis using the program t-tide (Pawlowicz et al., 2002). Harmonic analysis produces non-tidal residuals that are more representative of the true variability and can then be used as our ground truth against which we assess the altimetry data. Only constituents with a signal-to-noise ratio equal or larger than three were used to reconstruct the tidal signal. This guarantees the estimation of the most important constituents, while less energetic tidal constituents are not well resolved given the observations and their noise level and thus it is better to remove them.

At each tide gauge station, the performance of the altimetry data is assessed as a function of distance from the coast by assigning such data to distance bands of 1 km width starting from the 0–1 km band. As shown in Fig. 1 (b), only data that fall within 70 km of the TG are used. For each altimetry pass we obtain one altimetry value by averaging all the high frequency records falling within the selected distance band. Records with an absolute SLA larger than 2 m or three standard deviations above the mean were rejected prior to computing the average. The corresponding tide gauge matching value is obtained by linearly interpolating the tide gauge observations to the time of the altimetry pass. The corresponding time series for each km-band are then evaluated according to the Percentage of Cycles for High Correlation (PCHC): the maximum percentage of cycles of data that could be retained while guaranteeing a correlation with the TG time series of at least 0.8 (Passaro et al., 2015b). The same procedure is applied to the SGDR ocean retracker and to the ALES retracker as described in Passaro et al. (2014), but with the addition of the recomputed SSB.

Firstly, the results are displayed in Fig. 11 considering each TG-altimetry track couple. The values shown in the figures are the median PCHC in the last 10 km from the coast. Statistics vary considerably

depending on the TG and satellite tracks. For example PCHC is below 20% in 2 cases for Envisat and 4 cases for ERS-2. This is partly related to the general worse performances and loss of altimetry data in land to sea transitions (see for example Gómez-Enri et al. 2016). This is not a problem for our analysis, in which the objective is the comparison between the retrackers. In many cases, the three retrackers have very similar performances. This is well known from previous studies such as Passaro et al. (2014): a different retracking method is not always needed. Nevertheless, SGDR has a better PCHC than ALES + in only 2 cases out of 33 in Envisat (Fishguard-401 and Workington-704) and ERS-2 (Fishguard-160 and Lowenstoff-57). In several cases ALES + and ALES are substantially better than SGDR (for example Tregde-543 in ERS-2 and Wick-143 in Envisat). Nevertheless there are 3 cases in Envisat and 5 cases in ERS-2 in which ALES scores better than ALES + by over 5%. To produce a final rating of the coastal performances with respect to the tide gauges, we looked at the median value of the PCHC considering all the tracks.

The results are displayed in Fig. 12, where a median of the PCHC considering all 33 tracks is highlighted with a continuous line for each dataset. In terms of PCHC, the performances of the three retrackers are indistinguishable until 8 km from the coast. From 8 to 2 km from the coast, ALES is the best-performing dataset, followed by ALES +, while SGDR is the worst-performing. In the last km, where waveforms are extremely irregular, but also where most of the oceanic peaky waveforms are located (Deng and Featherstone, 2006), ALES + is the best performing dataset.

This is expected, since ALES + needs to reach a compromise in the normalisation and leading edge detection, in order to be able to treat peaky waveforms as well, while the objective of ALES is to maximise the number of retracked coastal waveforms, which are normally characterised by strong peaks in the trailing edge.

We further validate and compare the retracking solutions by means of the comparison with the geoid model. The GOCO5s geoid height are interpolated to the altimetry tracks in the whole coastal area of the North Sea (Latitude limits: 50–61, Longitude limits: −11 15). We
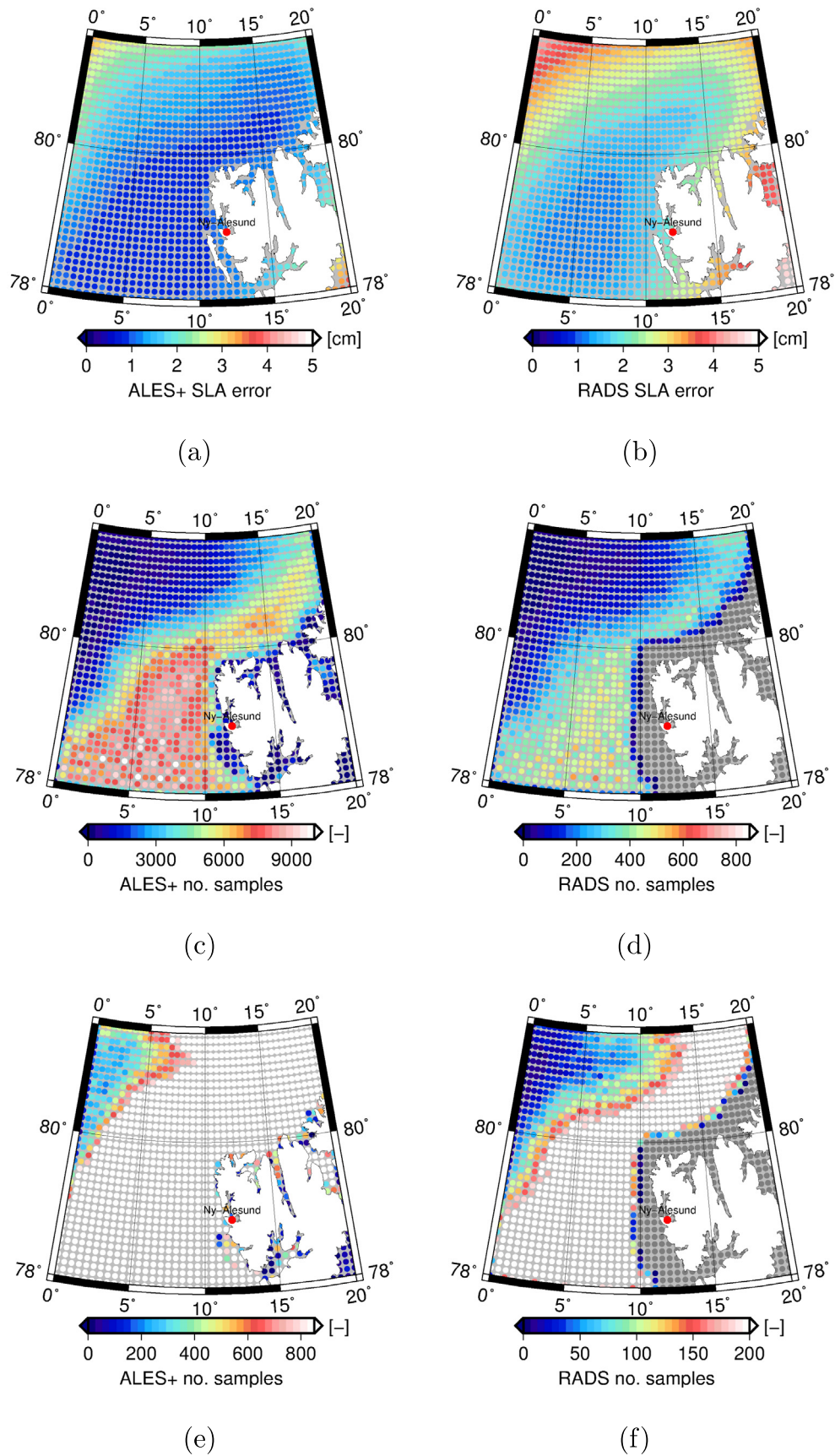
Fig. 8. Collocation error estimate for (a) ALES + and (b) RADS. The error is dependent on the number of samples. Number of samples in each grid cell for (c) ALES +
and (d) RADS. Notice the different colour scales. (e) and (f) are the same as (c) and (d), but with saturated colour scales in order to highlight points in the sea ice-
covered areas.

M. Passaro et al.
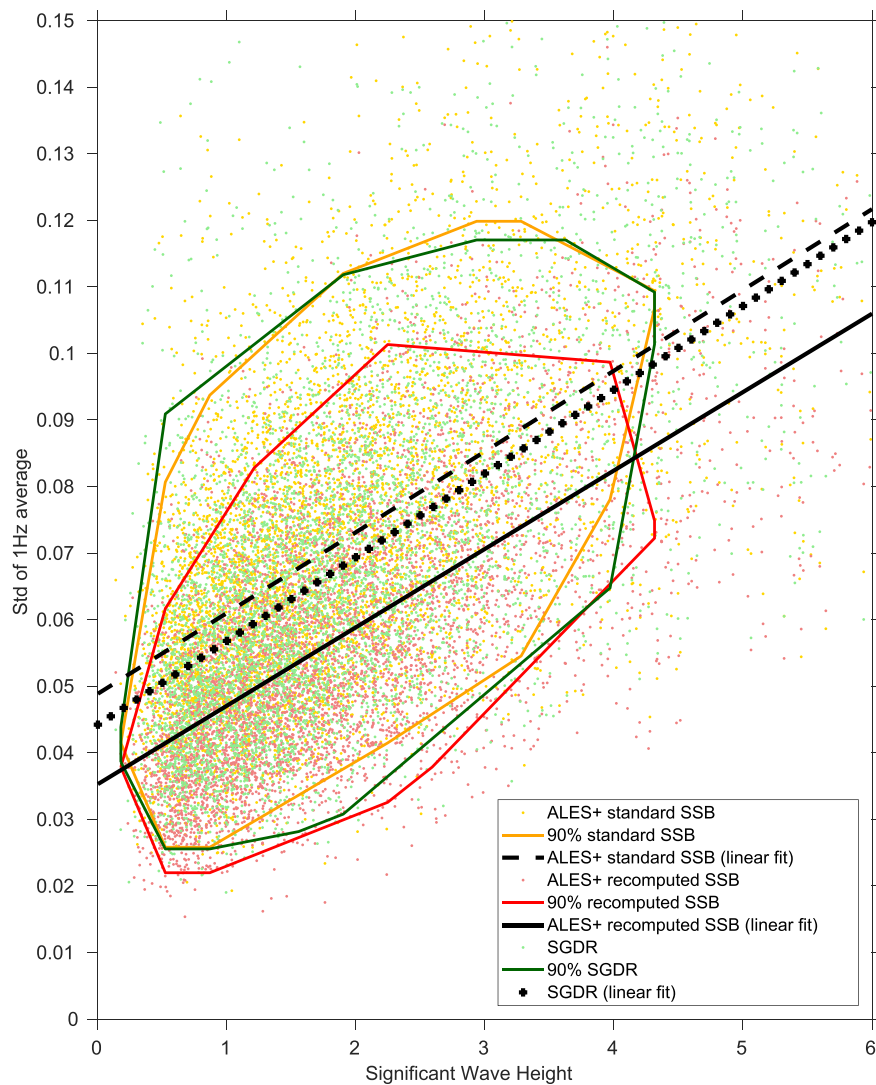
Fig. 9. Scatter plot and linear fit of the standard deviations of the 1-Hz points (used as measurement of high-frequency noise) against the SWH, for ALES+ corrected by the standard SSB and by the recomputed SSB. For comparison, the SGDR statistics are also shown. The contours delimit the location of 90% of the data for each dataset.
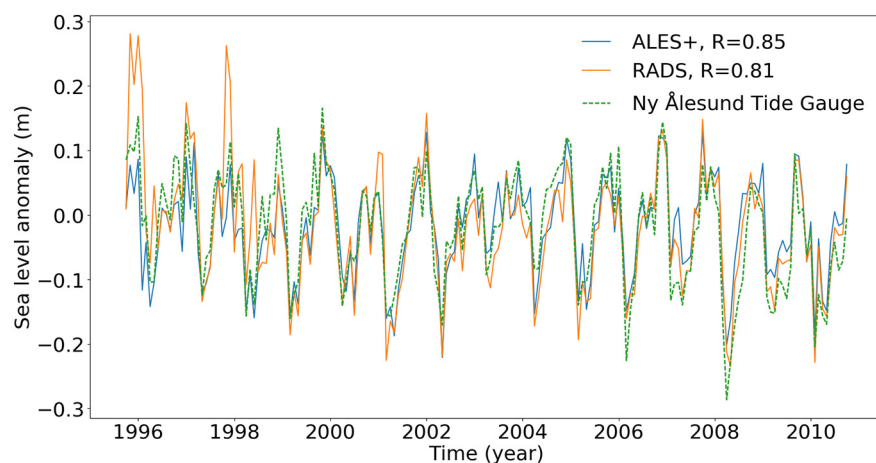
Fig. 10. Time series of SLA of ALES+ and RADS data compared to the Ny Alesund TG. The gridded weekly median data are resampled to monthly SLAs. The inverse barometer effect is excluded to be comparable to the TG. R stands for the value of the correlation coefficient between the corresponding altimetry dataset and the TG.
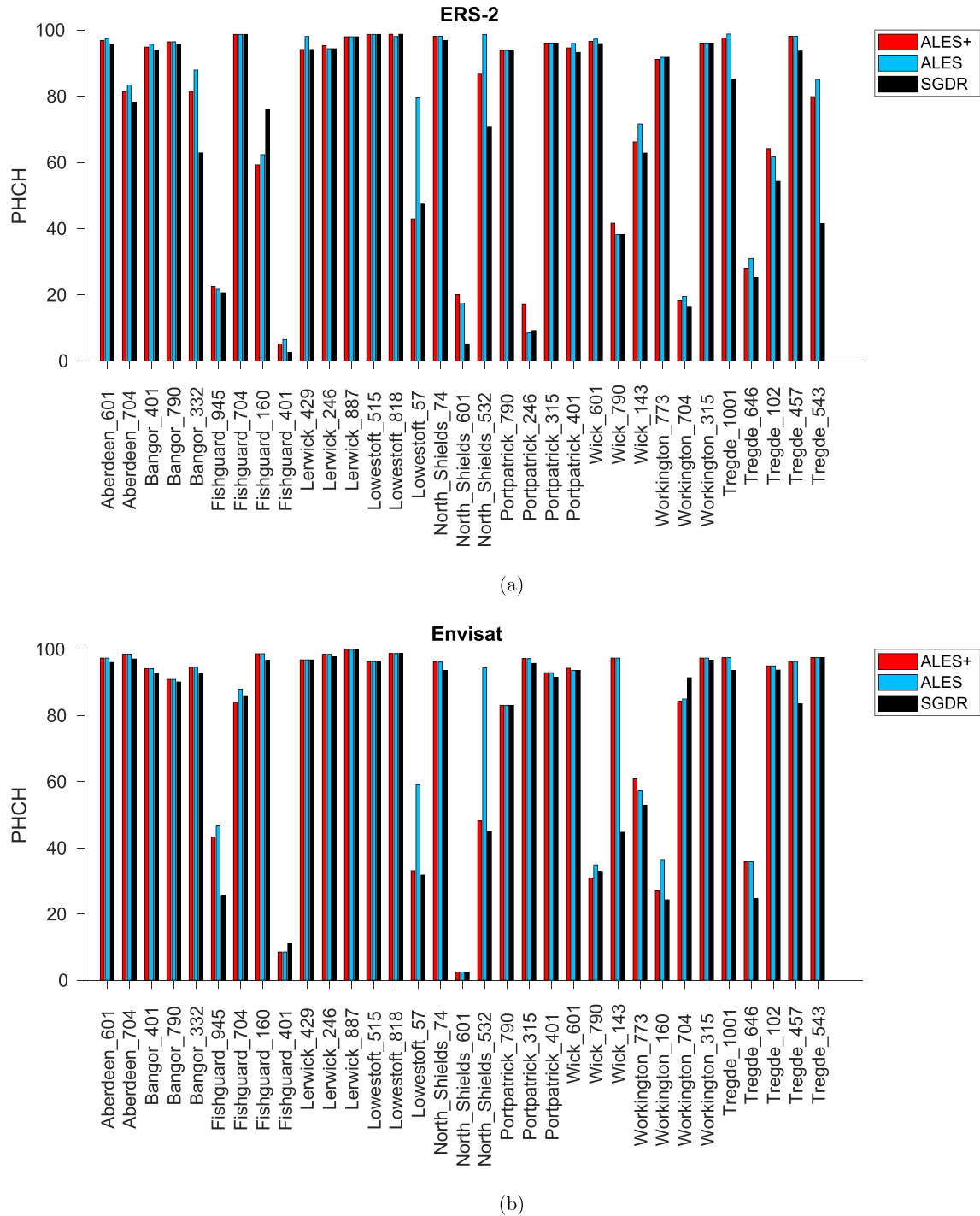
Fig. 11. Median PCHC for ERS-2 tracks (upper plot) and the Envisat tracks (lower plot) within 10 km of the TG for SGDR, ALES + and ALES (with recomputed SSB). On the x axis, the name of each TG and the corresponding satellite track numbers are shown.

divide the domain via 5-km coastal distance bands. For each cycle of Envisat and ERS-2, after excluding unrealistic values of $|SLA| > 2$ m and $SWH > 11$m, we store the MAD of the differences between SSH and geoid height. Fig. 13 show the averages of the results for Envisat and ERS-2. In the last 5 km to the coast, ALES scores better in terms of STD, and ALES + scores second. Both are much better than the original SGDR data, which scores 2.7 cm worse than ALES + for Envisat and 1.6 cm worse than ALES + for ERS-2. ALES and ALES + are of course equivalent going towards the open ocean and their MAD against the geoid is always lower than in SGDR.

We conclude that in the coastal zone ALES is the best choice among the three methods, but ALES + scores constantly better than the current SGDR standard.

4.3. Inland waters

The possibility of using the same retracker to treat altimetry echoes from leads, open and coastal waters can be extended to retrieve water level in inland water bodies. Indeed, it has been shown that waveforms from rivers and small lakes are mostly quasi-specular or quasi-Brown
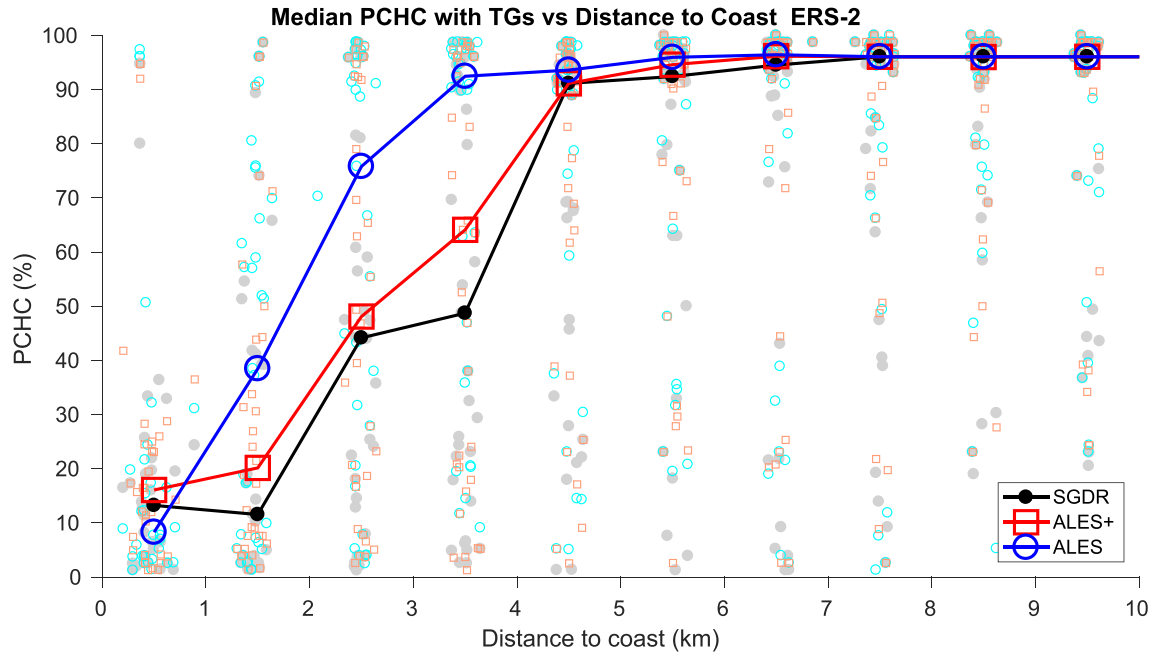
(a)
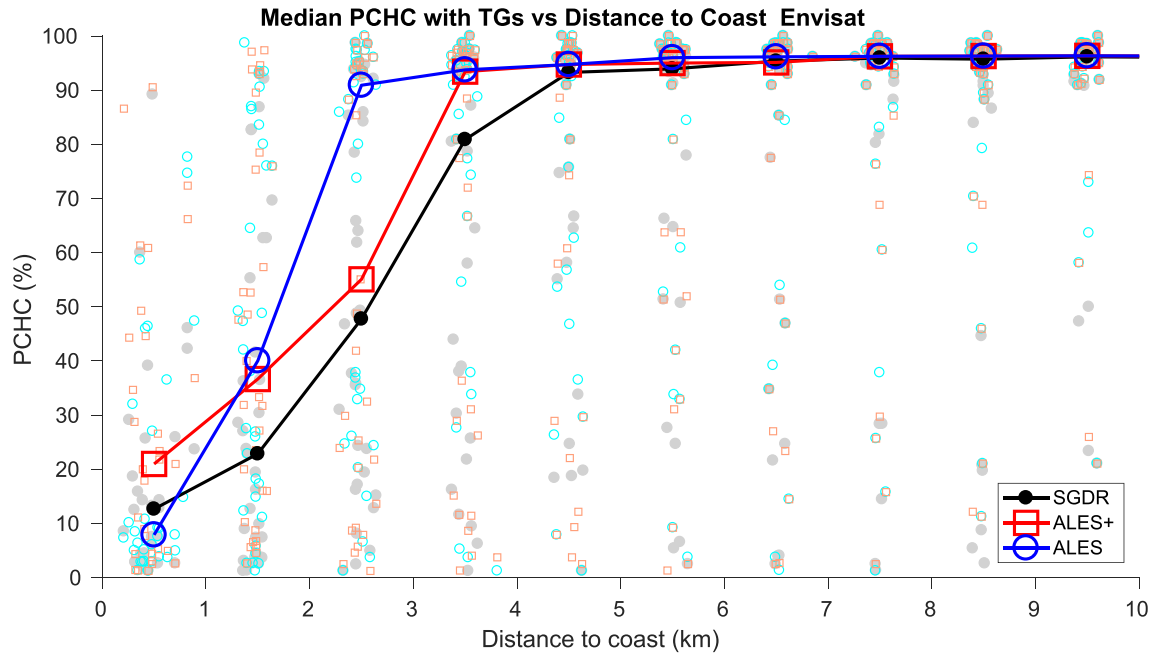
(b)

Fig. 12. PCHC for ERS-2 tracks (upper plot) and the Envisat tracks (lower plot) within 10 km of the TG w.r.t. the distance to the coast for SGDR, ALES + and ALES (with recomputed SSB). Single results are shown as grey dots (SGDR), red squares (ALES +) and cyan circles (SGDR). The continuous lines show the median of the statistics.

(Berry et al., 2005).

For a first investigation, we have integrated the ALES + ranges from Envisat for the Mekong river in the Database for Hydrological Time Series over Inland Waters (DAHITI, processed at the DGFI-TUM), in which altimetric ranges are used to produce water levels for river and lakes using a set of corrections, outlier rejection criteria and Kalman filter processing as described in Schwatke et al. (2015). As a comparison, we use the results from the Improved Threshold Retracker (ITR), implemented selecting a threshold of 50% (Hwang et al., 2006), processed through DAHITI in the same way as ALES +. The ITR is of common use in the reprocessing of inland water data (Hossain et al., 2014) and has already been used in the area of study (Boergens et al., 2016). It references a threshold value to the amplitude of the detected leading edge and determines the range by linearly interpolating
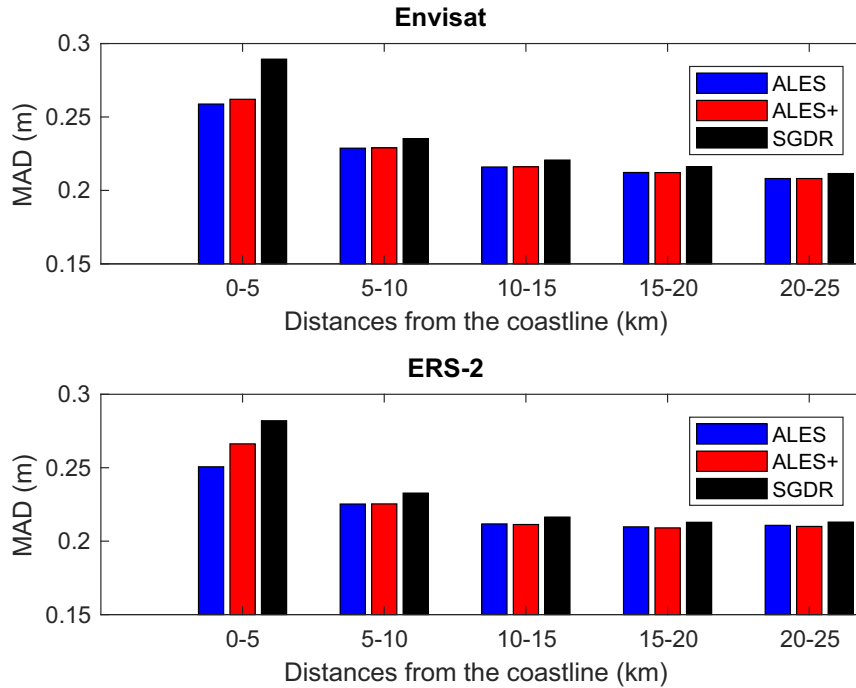

Fig. 13. Median Absolute Deviation between GOCO5s geoid heights and SSH data retracked with ALES, ALES + and SGDR in 5-km wide distance bands.

between adjacent samples (Gommenginger et al., 2011).

The comparison of the water level time series is shown in Fig. 14 and the results in terms of root mean square (RMS) error and correlation coefficient are reported in Table 2, as well as the number of points in each time series. It is observed that none of the retrackers is able to catch the water extremes: this is due to the fact that the temporal resolution of Envisat (one pass every 35 days) is suboptimal compared to an in-situ gauge. The results of the two retrackers are comparable in terms of correlation, while ITR has a better RMS in two of the three stations. In Kratie, if one excludes the clear outlier in the time series in 2003, ALES + RMS scores 1.37 and therefore is inline with the ITR result. Also the number of points in the time series is comparable between both retrackers in two of the three stations, while only in Mukdahan ITR has considerably more points. Unfortunately, the comparison with the gauges is only relative, because the in-situ stations lack an absolute reference. Nevertheless, the average bias between ALES + and ITR changes from 1.8 m in Luang Prabang to slightly more than 0.30 m in Mukdahan and Kratie. The variable bias is due to the fact that, while ITR locates the range using always the same threshold of the waveform amplitude, the location of the retracking point of ALES + varies depending on the estimated c_ξ, as explained in Section 3.1.1. Further validation against absolute water levels are needed to assess whether this improves the accuracy of the altimeter for rivers.

5. Conclusion

In this study, we have presented a homogenous retracking strategy that uses the same functional form to fit signals reflected back from leads in the sea ice pack and open ocean. The algorithm named ALES + is applied to ERS-2 and Envisat missions and is based on modifications to the ALES algorithm described in Passaro et al. (2014). Thanks to a preliminary step aimed at estimating the slope of the trailing edge, it is able to adapt the fitting to specular echoes. As a result of a subwaveform strategy aimed at limiting the impact of the noise in the trailing edge and to a recomputed SSB correction, it is able to decrease the high-frequency noise of the SSH estimations by over 1.1 cm in the open sea unaffected by sea ice. Even considering only peaky waveforms, range retrieval by ALES + is over 2 cm more precise than the available

solution used in previous studies to estimate sea level from leads (the sea ice retracker).

The validation against a TG situated on the Svalbard islands demonstrates that ALES + can improve the quality and the amount of data of the sea level records at high-latitudes. The improvement is brought by the retracking of non-standard ocean waveforms and the use of high-frequency data instead of 1-Hz averages, which are of limited use at high-latitudes given that most of the leads are narrower than 1 km (Lindsay and Rothrock, 1995; Kwok et al., 2009). ALES + is able to decrease the error on the sea level estimation of the sea ice-covered ocean up to a comparable level with the open ocean and therefore should be used in the next steps of the research to update the sea level record in the Arctic and Antarctic ocean.

The lower noise of ALES + in the open ocean could be used to study mesoscale structures and a spectral analysis should be able to reveal if this can be useful to solve at least partially the noise problems that affect standard altimetry at these scales (Dibarboure et al., 2014). The improvements obtained by recomputing the SSB using ALES + estimations could be even higher if a new SSB model is recomputed specifically for this retracker.

A validation against coastal TGs has demonstrated that ALES + improves the quality of sea level retrievals in the last 6 km within the coastline compared to the standard open ocean retracking. For coastal studies, ALES still overperforms ALES + . As a possible improvement to ALES + , future studies will seek a better strategy for the leading edge detection in order to avoid that peaks in the trailing edge, typical of coastal waveforms, could be interpreted as peaky leading edges by the algorithm.

A preliminary validation has shown that ALES + time series of water level of the Mekong River are very highly correlated with in-situ data. Nevertheless, the typical retracker used for inland waters (improved threshold) has better statistics, mainly due to outliers still present in ALES + . Future studies should further validate this application and exploit the seamless transition between inland waters and open sea, in order to study the sea level variations across deltas and estuaries.

In conclusion, ALES + offers the chance to fit the echoes from any water surface without the need to change the retracking strategy and therefore avoiding internal bias corrections and calibrations. It provides

Luang Prabang

Mukdahan

Kratie
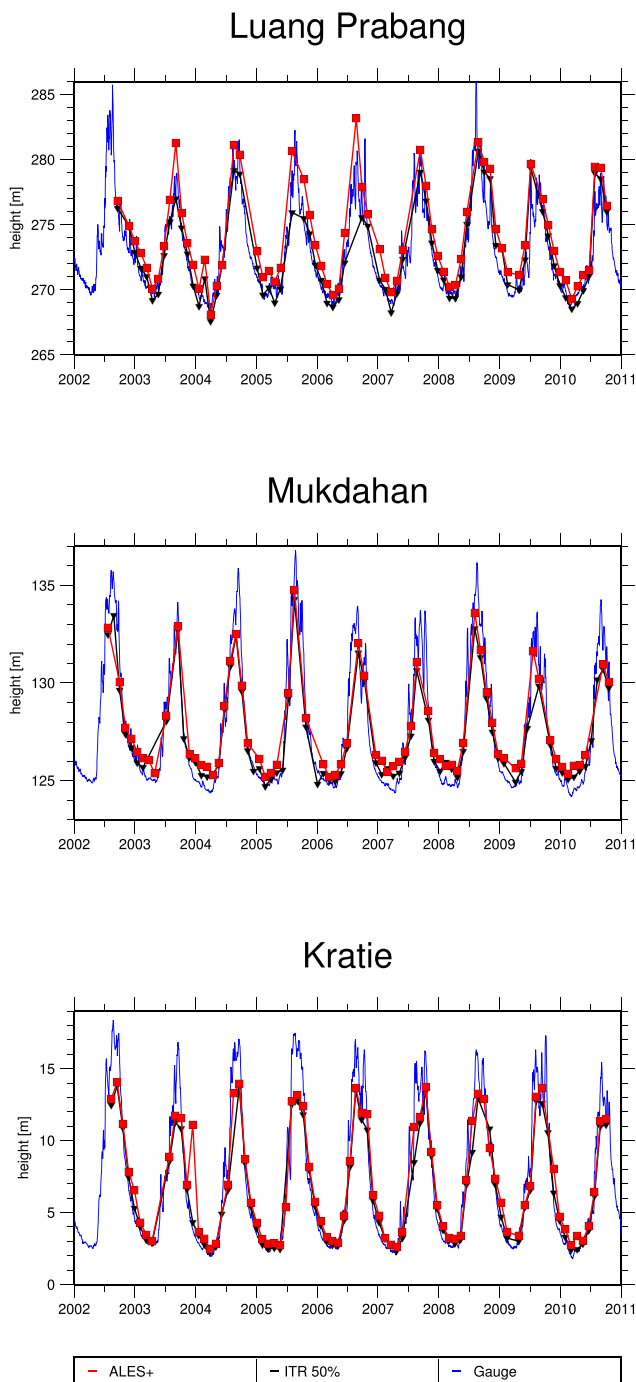
Fig. 14. Visual comparison of water level time series in the Mekong river from Envisat retracked by ALES+ (red squares), Envisat retracked by Improved Threshold Retracker at 50% and data from three gauges.

a more precise and accurate sea level estimation than the available sea ice and ocean retrackers for ERS-2 and Envisat in leads and in open and coastal waters.

Acknowledgements

Table 2
Comparison of water level time series in the Mekong river from Envisat retracked by ALES+ and by Improved Threshold Retracker at 50% w.r.t. data from three TGs. In terms of root mean square (RMS), correlation coefficient and number of points in the time series (Num of points).

		RMS (m)	Correlation coefficient	Num of points
Luang Prabang vs	ALES+	0.87	0.97	72
Envisat pass 651	ITR 50%	0.81	0.97	72
Mukdahan vs Envisat	ALES+	0.79	0.99	69
pass 21	ITR 50%	0.79	0.99	74
Kratie vs Envisat pass	ALES+	1.59	0.96	80
565	ITR 50%	1.33	0.98	79

References

Abdalla, S., 2012. Ku-band radar altimeter surface wind speed algorithm. Mar. Geod. 35, 276–298. http://dx.doi.org/10.1080/01490419.2012.718676.

Ablain, M., Legeais, J., Prandi, P., Marcos, M., Fenoglio-Marc, L., Dieng, H., Benveniste, J., Cazenave, A., 2016. Satellite altimetry-based sea level at global and regional scales. Surv. Geophys. 1–25. http://dx.doi.org/10.1007/s10712-016-9389-8.

Akima, H., 1970. A new method of interpolation and smooth curve fitting based on local procedures. J. ACM 17, 589–602. http://dx.doi.org/10.1145/321607.321609.

Andersen, O.B., 1999. Shallow water tides in the northwest European shelf region from TOPEX/POSEIDON altimetry. J. Geophys. Res. Oceans 104, 7729–7741. http://dx.doi.org/10.1080/01490419.2012.718676.

Andersen, O.B., Stenseng, L., Piccioni, G., Knudsen, P., 2016. The DTU15 MSS (Mean Sea Surface) and DTU15LAT (Lowest Astronomical Tide) reference surface. (presented at the ESA Living Planet Symposium).

Berry, P., Garlick, J., Freeman, J., Mathers, E., 2005. Global inland water monitoring from multi-mission altimetry. Geophys. Res. Lett. 32. http://dx.doi.org/10.1029/2005GL022814.

Boergens, E., Dettmering, D., Schwatke, C., Seitz, F., 2016. Treating the hooking effect in satellite altimetry data: a case study along the Mekong River and its tributaries. Remote Sens. 8, 91. http://dx.doi.org/10.3390/rs8020091.

Brown, G.S., 1977. The average impulse response of a rough surface and its applications. IEEE Trans. Antennas Propag. 25, 67–74. http://dx.doi.org/10.1109/TAP.1977.1141536.

Carrere, L., Lyard, F., Cancet, M., Guillot, A., 2015. Fes 2014, a new tidal model on the global ocean with enhanced accuracy in shallow seas and in the arctic region. In: EGU General Assembly Conference Abstracts. 17. pp. 5481.

Cazenave, A., Dieng, H.-B., Meyssignac, B., von Schuckmann, K., Decharme, B., Berthier, E., 2014. The rate of sea-level rise. Nat. Clim. Change 4, 358–361. http://dx.doi.org/10.1038/nclimate2159.

Chelton, D.B., McCabe, P.J., 1985. A review of satellite altimeter measurement of sea surface wind speed: with a proposed new algorithm. J. Geophys. Res. 90, 4707. http://dx.doi.org/10.1029/JC090iC03p04707.

Cheng, Y., Andersen, O., Knudsen, P., 2015. An improved 20-year arctic ocean altimetric sea level data record. Mar. Geod. 38, 146–162. http://dx.doi.org/10.1080/01490419.2014.954087.

Cipollini, P., Calafat, F.M., Jevrejeva, S., Melet, A., Prandi, P., 2017. Monitoring sea level in the coastal zone with satellite altimetry and tide gauges. Surv. Geophys. 1–25. http://dx.doi.org/10.1007/s10712-016-9392-0.

Dibarboure, G., Boy, F., Desjonqueres, J., Labroue, S., Lasne, Y., Picot, N., Poisson, J., Thibaut, P., 2014. J. Atmos. Ocean. Technol. 31 (6), 1337–1362. http://dx.doi.org/10.1175/JTECH-D-13-00081.1.

Deng, X., Featherstone, W., 2006. A coastal retracking system for satellite radar altimeter waveforms: application to ERS-2 around Australia. J. Geophys. Res. Space 111, C06012. http://dx.doi.org/10.1029/2005JC003039.

Dorandeu, J., Ablain, M., Faugere, Y., Mertz, F., Soussi, B., Vincent, P., 2004. Jason-1 global statistical evaluation and performance assessment: calibration and cross-calibration results. Mar. Geod. 27, 345–372. http://dx.doi.org/10.1080/01490410490889094.

Drinkwater, M.R., 1991. Ku band airborne radar altimeter observations of marginal sea ice during the 1984 Marginal Ice Zone Experiment. J. Geophys. Res. 96, 4555–4572. http://dx.doi.org/10.1080/01490410490889094.

Femenias, P., Baker, S., Brockley, D., Martinez, B., Massmann, F.~H.,Otten, M., Picard, B., Roca, M., Rudenko, S., Scharroo, R., Soulat, F., Visser, P., Paul, F., Fische, P., 2014. Reprocessing of the ERS-1 and ERS-2 altimetry missions. the REAPER project. In: presented at the Ocean Surface Topography Science Team meeting, Konstanz, Germany, http://dx.doi.org/10.13140/2.1.3756.7685.

Fetterer, F., Knowles, K., Meier, W., Savoie, M., 2016. Sea Ice Index. NSIDC: National Snow and Ice Data Center http://dx.doi.org/10.7265/N5736NV7.

Fu, L., Cazenave, A. (Eds.), 2001. Satellite altimetry and earth sciences. A Handbook of Techniques and Applications. 69 Academic, San Diego, CA.

Gilbert, L., Baker, S., Dolding, C., Vernier, A., Brockley, D., Martinez, B., Gaudelli, J., 2014. Reaper: Product Handbook for ERS Altimeters Reprocessed Products v. 3.1. ESA User Manual, ESA.

Giles, K.A., Laxon, S.W., Wingham, D.J., Wallis, D.W., Krabill, W.B., Leuschen, C.J., McAdoo, D., Manizade, S.S., Raney, R.K., 2007. Combined airborne laser and radar altimeter measurements over the Fram Strait in May 2002. Remote Sens. Environ. 111, 182–194. http://dx.doi.org/10.1016/j.rse.2007.02.037.

Gómez-Enri, J., Cipollini, P., Passaro, M., Vignudelli, S., Tejedor, B., Coca, J., 2016. Coastal altimetry products in the Strait of Gibraltar. IEEE Trans. Geosci. Remote Sens. 54, 5455–5466. http://dx.doi.org/10.1038/ngeo1379.

Gommenginger, C., Thibaut, P., Fenoglio-Marc, L., Quartly, G.D., Deng, X., Gómez-Enri, J., Challenor, P.G., Gao, Y., 2011. Retracking altimeter waveforms near the coasts. In: Vignudelli, S., Kostianoy, A., Cipollini, P., Benveniste, J. (Eds.), Coastal Altimetry. Springer-Verlag, Berlin Heidelberg, pp. 61–102. http://dx.doi.org/10.1007/978-3-642-12796-0_4.

Handoko, E.Y., Fernandes, M.J., Lázaro, C., 2017. Assessment of altimetric range and geophysical corrections and mean sea surface models-impacts on sea level variability around the Indonesian seas. Remote Sens. 9. http://dx.doi.org/10.3390/rs9020102.

Hayne, G.S., 1980. Radar altimeter mean return waveforms from near-normal-incidence ocean surface scattering. IEEE Trans. Antennas Propag. 28, 687–692. http://dx.doi.org/10.1109/TAP.1980.1142398.

Hossain, F., Siddique-E-Akbor, A., Mazumder, L.C., ShahNewaz, S.M., Biancamaria, S., Lee, H., Shum, C., 2014. Proof of concept of an altimeter-based river forecasting system for transboundary flow inside Bangladesh. IEEE J. Sel. Top. Appl. Earth Obs. Remote Sens. 7, 587–601. http://dx.doi.org/10.1109/JSTARS.2013.2283402.

Hwang, C., Guo, J., Deng, X., Hsu, H.-Y., Liu, Y., 2006. Coastal gravity anomalies from retracked Geosat/GM altimetry: improvement, limitation and the role of airborne gravity data. J. Geod. 80, 204–216. http://dx.doi.org/10.1007/s00190-006-0052-x.

Jackson, F., Walton, W., Hines, D., Walter, B., Peng, C., 1992. Sea surface mean square slope from Ku-band backscatter data. J. Geophys. Res. Oceans 97, 11411–11427. http://dx.doi.org/10.1029/92JC00766.

Kwok, R., Cunningham, G., Wensnahan, M., Rigor, I., Zwally, H., Yi, D., 2009. Thinning and volume loss of the Arctic Ocean sea ice cover: 2003–2008. J. Geophys. Res. Oceans 114. http://dx.doi.org/10.1029/2009JC005312.

Labroue, S., 2007. RA2 Ocean and MWR Measurement Long Term Monitoring, 2007 Report for WP3, Task 2 NSSB Estimation for RA2 Altimeter. In: Technical Report Contract 17293/03/I-OL, CLS-DOS-NT-07-198, CLS, Ramonville St. Agne, France, . ftp://ftp.esa-sealevel-cci.org/Data/TechnicalRef/PhaseE_envisat_ssb_report_2010.pdf.

Laxon, S., 1994a. Sea ice extent mapping using the ERS-1 radar altimeter. EARSeL Adv. Remote Sens. 3, 112–116. http://www.earsel.org/Advances/3-2-1994/3-2_13_Laxon.pdf.

Laxon, S.W., 1994b. Sea ice altimeter processing scheme at the EODC. Int. J. Remote Sens. 15, 915–924. http://dx.doi.org/10.1080/01431169408954124.

Lindsay, R., Rothrock, D., 1995. Arctic sea ice leads from advanced very high resolution radiometer images. J. Geophys. Res. Oceans 100, 4533–4544. http://dx.doi.org/10.1080/01431169408954124.

Marshall, J., Armour, K.C., Scott, J.R., Kostov, Y., Hausmann, U., Ferreira, D., Shepherd, T.G., Bitz, C.M., 2014. The ocean's role in polar climate change: asymmetric arctic and antarctic responses to greenhouse gas and ozone forcing. Philos. Trans. R. Soc. Lond. A Math. Phys. Eng. Sci. 372, 20130040. http://dx.doi.org/10.1098/rsta.2013.0040.

Neumann, B., Vafeidis, A.T., Zimmermann, J., Nicholls, R.J., 2015. Future coastal population growth and exposure to sea-level rise and coastal flooding-a global assessment. PLoS One 10, e0118571. http://dx.doi.org/10.1371/journal.pone.0118571.

Pail, R., Goiginger, H., Schuh, W.-D., Hoeck, E., Brockmann, J.M., Fecher, T., Gruber, T., Mayer-Guerr, T., Kusche, J., Jaeggi, A., Rieser, D., 2010. Combined satellite gravity field model GOCO01S derived from GOCE and GRACE. Geophys. Res. Lett. 37, L20314. http://dx.doi.org/10.1029/2010GL044906.

Palanisamy, H., Cazenave, A., Delcroix, T., Meyssignac, B., 2015. Spatial trend patterns in the Pacific Ocean sea level during the altimetry era: the contribution of thermocline depth change and internal climate variability. Ocean Dyn. 1–16.

Pascual, A., Faugère, Y., Larnicol, G., Le Traon, P.-Y., 2006. Improved description of the ocean mesoscale variability by combining four satellite altimeters. Geophys. Res. Lett. 33, L02611. http://dx.doi.org/10.1029/2005GL024633.

Passaro, M., Cipollini, P., Benveniste, J., 2015a. Annual sea level variability of the coastal ocean: the Baltic Sea-North Sea transition zone. J. Geophys. Res. Oceans 120, 3061–3078. http://dx.doi.org/10.1002/2014JC010510.

Passaro, M., Cipollini, P., Vignudelli, S., Quartly, G., Snaith, H., 2014. ALES: A multi-mission subwaveform retracker for coastal and open ocean altimetry. Remote Sens. Environ. 145, 173–189. http://dx.doi.org/10.1016/j.rse.2014.02.008.

Passaro, M., Dinardo, S., Quartly, G.D., Snaith, H.M., Benveniste, J., Cipollini, P., Lucas, B., 2016. Cross-calibrating ALES Envisat and Cryosat-2 Delay–Doppler: a coastal altimetry study in the Indonesian Seas. Adv. Space Res. 58, 289–303.

Passaro, M., Fenoglio-Marc, L., Cipollini, P., 2015b. Validation of significant wave height from improved satellite altimetry in the German Bight. IEEE Trans. Geosci. Remote Sens. 53, 2146–2156. http://dx.doi.org/10.1109/TGRS.2014.2356331.

Passaro, M., Mueller, F.L., Dettmering, D., 2017. Lead detection using Cryosat-2 delay-Doppler processing and Sentinel-1 SAR images. Adv. Space Res. http://dx.doi.org/10.1016/j.asr.2017.07.011.

Pawlowicz, R., Beardsley, B., Lentz, S., 2002. Classical tidal harmonic analysis including error estimates in matlab using t_tide. Comput. Geosci. 28, 929–937. http://dx.doi.org/10.1016/j.asr.2017.07.011.

Peacock, N.R., Laxon, S.W., 2004. Sea surface height determination in the Arctic ocean from ERS altimetry. J. Geophys. Res. Oceans 109. http://dx.doi.org/10.1029/2001JC001026.

Poisson, J., Quartly, G.D., Kurekin, A., Thibaut, P., Hoang, D., Nencioli, F., 2018. Extending sea level estimation into the Arctic Ocean using ENVISAT altimetry. accepted for publication in IEEE Trans. Geosci. Remote Sens. http://dx.doi.org/10.1109/TGRS.2018.2813061. in press.

Quartly, G.D., Srokosz, M.A., McMillan, A.C., 2001. Analyzing altimeter artifacts: statistical properties of ocean waveforms. J. Atmos. Ocean. Technol. 18, 2074–2091. http://dx.doi.org/10.1175/1520-0426(2001)018<2074:AAASPO>2.0.CO;2.

Rudenko, S., Dettmering, D., Esselborn, S., Schöne, T., Förste, C., Lemoine, J.-M., Ablain, M., Alexandre, D., Neumayer, K.-H., 2014. Influence of time variable geopotential models on precise orbits of altimetry satellites, global and regional mean sea level trends. Adv. Space Res. 54, 92–118. http://dx.doi.org/10.1016/j.asr.2014.03.010.

Savcenko, R., Bosch, W., 2012. EOT11a - Empirical Ocean Tide Model from Multi-Mission Satellite Altimetry. In: Technical Report DGFI No. 89, . https://epic.awi.de/36001/1/DGFI_Report_89.pdf.

Sandwell, D.T., Smith, W.H.F., 2005. Retracking ERS-1 altimeter waveforms for optimal gravity field recovery. Geophys. J. Int. 163, 79–89. http://dx.doi.org/10.1111/j.1365-246X.2005.02724.x.

Schwatke, C., Dettmering, D., Bosch, W., Seitz, F., 2015. DAHITI–an innovative approach for estimating water level time series over inland waters using multi-mission satellite altimetry. Hydrol. Earth Syst. Sci. 19, 4345–4364. http://dx.doi.org/10.5194/hess-19-4345-2015.

Stammer, D., Ray, R., Andersen, O., Arbic, B., Bosch, W., Carrère, L., Cheng, Y., Chinn, D., Dushaw, B., Egbert, G., et al., 2014. Accuracy assessment of global barotropic ocean tide models. Rev. Geophys. http://dx.doi.org/10.1002/2014RG000450.

Vinogradov, S., Ponte, R., 2010. Annual cycle in coastal sea level from tide gauges and altimetry. J. Geophys. Res. Space 115, C04021. http://dx.doi.org/10.1029/2009JC005767.

Improving the precision of sea level data from satellite altimetry with high-frequency and regional sea state bias corrections

Marcello Passaro[a,*], Zulfikar Adlan Nadzir[a,b], Graham D. Quartly[c]

[a] *Deutsches Geodätisches Forschungsinstitut der Technischen Universität München, Arcisstraße 21, 80333 Munich, Germany*
[b] *Sumatera Institute of Technology (Itera), Indonesia*
[c] *Plymouth Marine Laboratory, UK*

ARTICLE INFO

ABSTRACT

The sea state bias (SSB) is a large source of uncertainty in the estimation of sea level from satellite altimetry. It is still unclear to what extent it depends on errors in parameter estimations (numerical source) or to the wave physics (physical source).

By improving the application of this correction we compute 20-Hz sea level anomalies that are about 30% more precise (i.e. less noisy) than the current standards. The improvement is two-fold: first we prove that the SSB correction should be applied directly to the 20-Hz data (12 to 19% noise decrease); secondly, we show that by recomputing a regional SSB model (based on the 20-Hz estimations) even a simple parametric relation is sufficient to further improve the correction (further 15 to 19% noise decrease).

We test our methodology using range, wave height and wind speed estimated with two retrackers applied to Jason-1 waveform data: the MLE4 retracked-data available in the Sensor Geophysical Data Records of the mission and the ALES retracked-data available in the OpenADB repository (https://openadb.dgfi.tum.de/). The regional SSB models are computed parametrically by means of a crossover analysis in the Mediterranean Sea and North Sea.

Correcting the high-rate data for the SSB reduces the correlation between retracked parameters. Regional variations in the proposed models might be due to differences in wave climate and remaining sea-state dependent residual errors. The variations in the empirical model with respect to the retracker used recall the need for a specific SSB correction for any retracker.

This study, while providing a significantly more precise solution to exploit high-rate sea level data, calls for a re-thinking of the SSB correction in both its physical and numerical component, gives robustness to previous theories and provides an immediate improvement for the application of satellite altimetry in the regions of study.

1. Introduction

Satellite altimetry measures the distance between the sea surface and the satellite (range), but this first estimate needs to be corrected for a number of geophysical effects, prior to being used for sea level estimation. The sea state bias (SSB) is among the time-variable corrections that are applied to sea surface height estimates from satellite altimetry. With a mean of 5 cm and a time-variable standard deviation of 2 to 5 cm in the open ocean (Andersen and Scharroo, 2011), it is currently one of the largest sources of uncertainty linked with the altimetric signal (Pires et al., 2016).

Previous studies have usually identified different effects that play a role in the SSB. The first, the Electromagnetic (EM) bias, is strongly dependent on the significant wave height (SWH) in the viewing area of the altimeter, and is due to the different backscattering of troughs and crests of the waves, which causes the EM range (what the altimeter

actually measures) to be biased towards the troughs in comparison with the mean sea level (Fu and Cazenave, 2001).

The second contribution is known as "Skewness Bias", which is related to the notion that the algorithms (retrackers) that are used to fit the altimetric waveform assume that the vertical distribution of specular reflectors illuminated by a radar altimeter is Gaussian, while their actual probability density function has a non-zero skewness.

The third contribution, historically called Tracker Bias, is actually a sum of errors related to the way the altimeter tracks the returning echoes. This contribution plays a role in the total SSB correction due to the empirical way in which this is estimated. Despite a few attempts to produce a theoretical description of the EM bias, e.g. Elfouhaily et al. (1999), any SSB correction currently used in the production of sea level data is derived by an empirical method that models this correction by expressing sea level residuals as a function of SWH and wind speed

---

estimated by the altimeter itself. More recently, attempts have been made to add a third parameter, namely the mean wave period from a numerical model (Tran et al., 2010a). The empirical nature of the SSB modeling implies that any sea-state dependent error in the residuals will be included in the correction.

Conceptually, only the third term varies with instrument and retracking algorithm, while the first two components should be the same for all Ku-band altimeters. Two fundamental studies have dealt with this contribution. Firstly, Sandwell and Smith (2005) has shown that part of the SSB correction is related to the inherent correlation between arrival time and rise time of the leading edge of the altimetric waveform, from which the physical parameters of SWH and sea level are estimated. Secondly, Zaron and DeCarvalho (2016) developed a correction to de-correlate SWH and sea level estimations based on the analysis of their errors. They derived a correction to be applied to low frequency (LF, i.e. at 1 Hz, corresponding to roughly one measurement every 7 km) data that are already corrected for SSB. Quartly et al. (2016) demonstrated that the correlation of the errors in the estimation process shows up as correlated high frequency (HF, i.e. at 20 Hz for Jason-1, Jason-2 and Jason-3) SWH and SLA estimates within the LF spacing. A term related to issues in the fitting of a waveform cannot be considered as a SSB in a physical sense, since the non-linearities of the ocean waves should not vary at scales smaller than 10 km. Nevertheless, due to the empirical derivation of the SSB models, it does influence any attempt in finding a parametric relation between SLA and SWH. For clarity and in analogy with Zaron and DeCarvalho (2016), we will refer to "retracker-related noise" to discuss the contribution of this term to the total SSB correction.

In the empirical estimation of the SSB, the sea level residuals are analyzed by differencing repeat measurements along collinear tracks (Chelton, 1994) or at orbit crossover points (Gaspar et al., 1994), or directly observing the anomalies with respect to the mean sea level (Vandemark et al., 2002). The residuals are modelled with respect to the variables influencing the sea state either in a parametric formulation (Fu and Glazman, 1991; Pires et al., 2016) or non-parametrically solving a large linear system of observation equations for the SSB taken as unknown (Gaspar et al., 2002).

The motivation of this study is three-fold:

1. The SSB correction in the standard products, as any other geophysical correction, is given at LF, rather than at HF. Lately, the attention of the scientific community and particularly the effort to better observe coastal dynamics at a regional scale has moved to the exploitation of HF data (Cipollini et al., 2017b; Birol and Delebecque, 2014). Gómez-Enri et al. (2016) and Passaro et al. (2018) have successfully applied the SSB model of the Envisat and ERS-2 satellite missions to high-rate estimations of SWH and wind speed from the ALES retracker (Passaro et al., 2014), although no SSB-specific consideration was made in analysing the results.
2. Several retrackers alternative to the standards have been proposed in recent years (Cipollini et al., 2017a). It is likely that different retrackers would bring different errors that play a role in the tracker bias. Nevertheless, for none of these alternative methods has a specific SSB correction been derived.
3. Several dedicated altimetry products during recent years provide region-specific processing (Birol et al., 2017; Passaro, 2017). Also the current phase of the European Space Agency's Sea Level Climate Change Initiative project (SL cci) (Quartly et al., 2017; Legeais et al., 2018) is focused on regional sea level analysis. Residual errors in the sea level, which are mirrored in the SSB model estimation, can also be dependent on the region. Since SSB models are estimated globally, regional predominance of certain wind and wave conditions might not be well enough represented in the realization of a global SSB model. An attempt of a regional SSB derivation was the SSB correction proposed for Cryosat-2 mission in the Indonesian Archipelago by Passaro et al. (2016), but comparison was not possible given that there is no official SSB model for that mission.

For these reasons, we aim in this work at computing a high-frequency, regional and retracker-dependent SSB correction in order to improve the performances of HF altimetry data. This is done in two subsequent steps. Firstly, we show that a simple application of the existing SSB model using HF estimations of two different retrackers is sufficient to reduce the SLA noise level in a comparable way to the correction of Zaron and DeCarvalho (2016). Secondly, a new retracker-specific regional parametric SSB model is derived in two test regions.

The novelty compared with previous studies consists in i) an approach to reduce the retracker-related noise starting from HF data rather than the LF of Zaron and DeCarvalho (2016), ii) the adoption of regionally focused corrections as suggested by Tran et al. (2010b) and iii) the provision of a SSB correction for the ALES retracker, which is the algorithm chosen for the current phase of SL cci.

The test regions are defined together with the data sources in Section 2; the methodology for SSB derivation and analysis is described in Section 3; results are presented and discussed in Section 4; the work and its perspectives are finally summarised in Section 5.

2. Data and region of study

In this study HF observations from the Jason-1 mission are used. By choosing this mission, 7 years of data (January 2002 to January 2009) including cycles 1–259 (before the start of the drifting phase) can be exploited and at the same time comparisons can be made with the latest studies focused on SSB (Tran et al., 2010a; Pires et al., 2016). The HF (20 Hz) data were extracted from the DGFI-TUMs Open Altimeter Database (OpenADB: https://openadb.dgfi.tum.de) and are publicly available upon request. The OpenADB contains data from the original Sensor Geophysical Data Records (SGDR Version E) and from the Adaptive Leading Edge Subwaveform (ALES) reprocessing.

The SGDR product provides the orbital altitude, all the necessary corrections to compute the sea level anomaly and the output of the MLE4 retracker (Amarouche et al., 2004; Thibaut et al., 2010): range, SWH and backscatter coefficient. These are also estimated and given as output of ALES (Passaro et al., 2014). We computed the wind speed starting from the backscatter coefficient from the two retrackers using the processing described in Abdalla (2012).

The sea level anomalies (SLA) are derived from the range measurements using exactly the same orbital altitude and corrections (for tides and atmospheric effects), except, of course, the SSB correction, for both SGDR and ALES. Unrealistic estimations are identified using the outlier rejection suggested by Picot et al. (2003). Moreover, since the MLE4 retracker is not optimised for coastal waveforms, data within 20 km of the coast are excluded from the analysis.

The regions of study are the Mediterranean Sea (Med) and the North Sea (NS) and are shown in Fig. 1. These regions have been selected in the context of the SL cci for the high interest in regional sea level dynamics and the relatively abundant in-situ measurements. Moreover, in the context of this study, these choices provide the opportunity to test the results in two areas characterised by different bathymetry, tidal regime and sea state conditions.

3. Methods

3.1. Different SSB corrections used in the study

Three different SSB corrections are applied to derive the SLA in this study:

- 1-Hz SSB is the SSB correction available at LF in the SGDR product. The correction is derived using the methodology described in Gaspar et al. (2002) and Labroue et al. (2004) and updated in Tran et al. (2010a). This methodology adopts a non-parametric estimation: a statistical technique (kernel smoothing) is used to solve a large system of linear equations based on the observations and on a set of weights.
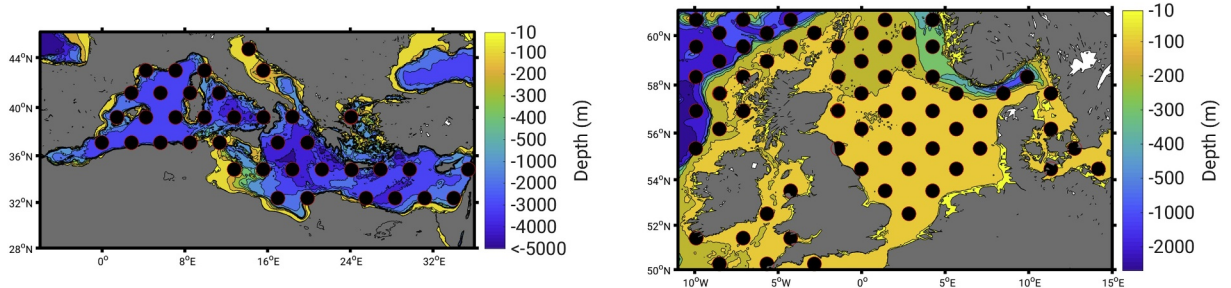
Fig. 1. The two areas of study and their bathymetry. The black circles highlight the crossover locations used for the estimation of the regional SSB corrections.

The result is a 2D map of the SSB against wind speed and SWH.

- 20-Hz SSB is the SSB correction derived by using the same 2D map from Tran et al. (2010a) and obtained courtesy of Ngan Tran from Collecte Localisation Satellites, but computed for each HF point using the HF wind speed and SWH estimations from SGDR and ALES. As previously mentioned, the computation of the current SSB model is based on an empirical relationship between three retracked parameters. While part of it is due to the physics of the waves and will manifest itself at LF, the model contains also a relation that is due to the correlated errors in the estimation, which is performed at HF. This was already noted by Zaron and DeCarvalho (2016), who stated that "the development of the SSB correction involves, in part, removing the correlation between SSH and SWH" and "it will have some impact on the short-wavelength components of these fields". Applying the SSB model at LF therefore means assuming that the error component of the sea level estimation related to the sea state exists only at long wavelengths, reducing its impact on the short-wavelength components. While recomputing a LF SSB model after eliminating the retracker-related noise must be an aim for future work, but goes beyond the scope of this paper, the original SSB model of the SGDR product is here applied at HF to consider its impact on the short wavelengths.

- Reg SSB is the SSB correction derived using the regional parametric models computed using the methodology described in Section 3.2 and then applied to each HF point using the HF wind speed and SWH estimations from SGDR and ALES.

3.2. Derivation of regional SSB corrections

Since the focus of this study is to investigate the improvements brought by the introduction of HF estimations and regional processing in the SSB derivation, we have not investigated the non-parametric modeling strategies, which are more complex to implement and numerically expensive. We chose instead a simple parametric form to model the regional corrections: the Fu-Glazman (FG) model proposed in Fu and Glazman (1991), expressed as

$$SSB = \hat{\alpha} SWH \left(g \frac{SWH}{U_{10}^2} \right)^{-\hat{d}} \tag{1}$$

where U_{10} is the wind speed computed from the backscatter coefficient estimated by each retracker, g is the acceleration due to gravity, $\hat{\alpha}$ and $\hat{d}$ are the two parameters to be estimated.

This model incorporates a non-linear relation involving SWH and wind speed, so that finding $\hat{\alpha}$ and $\hat{d}$ at the same time is a non-linear problem. We linearise the problem by computing the $\hat{\alpha}$ coefficient for a set of $\hat{d}$ as in Gaspar et al. (1994).

Following the latter, the equations needed to compute the regional SSB models are built using HF SLAs at each crossover m:

$$\Delta SLA_m = \hat{\alpha} X_o - \hat{\alpha} X_e + \epsilon \tag{2}$$

where o and e stand for odd and even tracks (indicating ascending and descending tracks respectively), ϵ accounts for residual errors that do

not depend on the missing SSB correction and:

$$X_o = SWH_o \left(g \frac{SWH_o}{U_{10,o}^2} \right)^{-\hat{d}} \qquad X_e = SWH_e \left(g \frac{SWH_e}{U_{10,e}^2} \right)^{-\hat{d}} \tag{3}$$

We have therefore a set on m linear equations, which we can express in vectorial form:

$$\Delta \mathbf{SLA} = \hat{\alpha} \Delta \mathbf{X} + \epsilon \tag{4}$$

Eq. (4) is solved in a linear least square sense, giving one value of $\hat{\alpha}$ for each $\hat{d}$.

Finally, the chosen $\hat{\alpha}$, $\hat{d}$ couple is the one that maximises the variance explained at the crossovers, i.e. the difference between the variance of the crossover difference before and after correcting the SLA for the SSB using the computed FG model.

This derivation is shown in Fig. 2 for SGDR and ALES in the two regions of study. The chosen $\hat{d}$ coefficients are indicated by a vertical line in the panels. $\hat{\alpha}$ is then derived as a function of $\hat{d}$. A discussion of these results is given in Section 4.2.
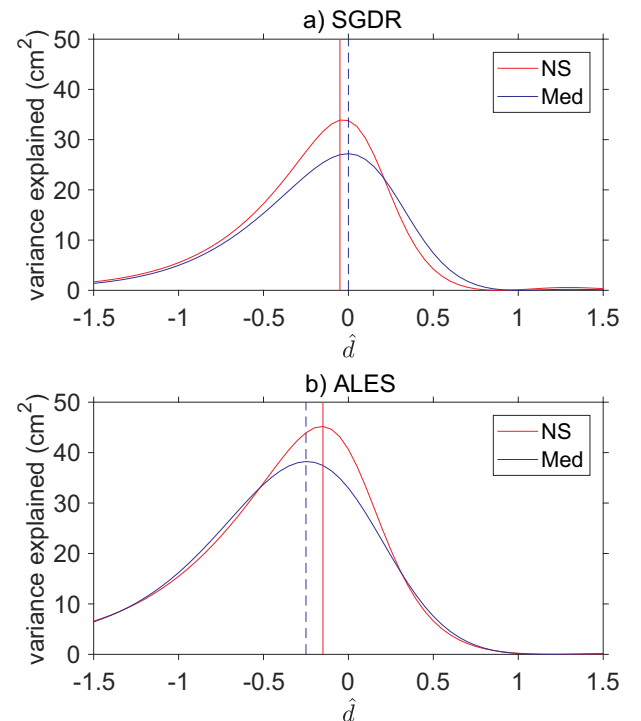
Fig. 2. Parameter estimation for the FG model in the regions of study. Choice of parameter $\hat{d}$ according to the variance explained by the application of the SSB correction at the crossover points for SGDR (a) and ALES (b) dataset. In all the plots, lines referring to the Med (NS) are specified in blue (red). Vertical lines highlight the optimal $\hat{d}$ value. (For interpretation of the references to color in this figure legend, the reader is referred to the web version of this article.)
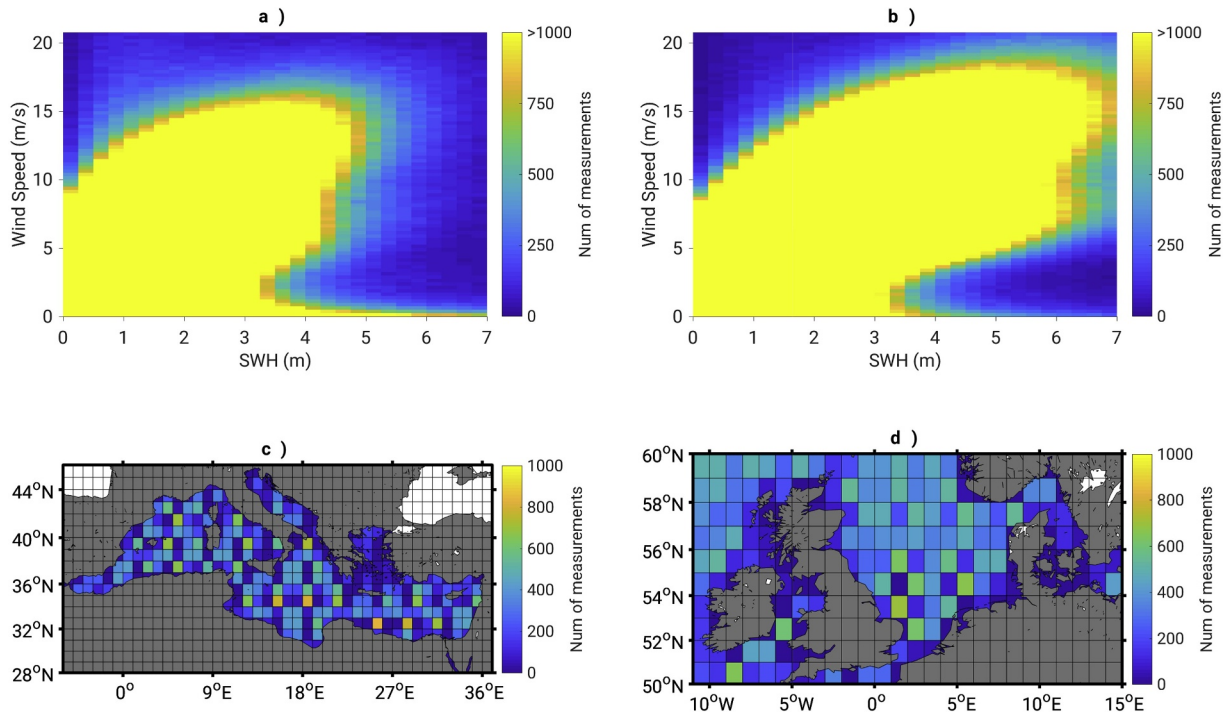
Fig. 3. (a and b): 2d histogram of the number of measurements available for different wind and wave states in Med (a) and NS (b). The color bar is saturated at 1000 to show the limits of validity of the regional SSB corrections derived in this study. c and d show the locations of the valid measurements in a 1-degree grid (For interpretation of the references to color in this figure legend, the reader is referred to the web version of this article.).

3.3. Methods for data analysis

3.3.1. Methods for noise statistics

Two noise statistics are employed to evaluate the precision of the dataset. Firstly, the high-rate noise is computed by considering the differences between consecutive HF SLA values, since SLA is not supposed to change significantly in 300 to 350 m, which is the distance between one measurement and the next. This reference of noise was first used in Passaro et al. (2014) and subsequently employed in other studies, for example by Cipollini et al. (2017b).

Secondly, the difference in SLA variance between different datasets, i.e. SLA dataset corrected with the models in Section 3.1, is computed on a 1-degree grid. Reducing SLA variance, both at global and regional scales, is the most common performance test for corrections applied to range measurements from satellite altimetry, for example wet tropospheric correction (Fernandes et al., 2015), inverse barometer correction (Carrère and Lyard, 2003), dynamic atmosphere correction (Pascual et al., 2008). This metric has also been widely used in evaluation of SSB corrections (Tran et al., 2010a); for our purposes we use the latest formulation proposed by Pires et al. (2016): the scaled SLA variance differences, which illustrate the impact of different SLAs relative to the regional variability, with the following formulation:

$$S = \left[\frac{(var(SLA1) - var(SLA2))}{var(SLA1)} \right] \times 100 \qquad (5)$$

3.3.2. Intra-1 Hz correlation

Waveform data are subject to speckle noise leading to short-scale variations in the derived parameters. As this multiplicative noise is independent from one waveform to its successor, there is no correlation between the anomalies noted for consecutive records; however, any realization of the noise may affect multiple derived parameters in a concerted way. Variations in the trailing edge affect estimates of backscatter strength and mispointing in a highly correlated way (Quartly, 2009); variations on the leading edge have been shown to lead to synchronised errors in SWH and range (Sandwell and Smith, 2005; Quartly et al., 2016).

The real values for SLA and for SWH will, in general, vary slowly over scales of 10 km (although there may be more pronounced changes close to the coast or rapidly shoaling bathymetry). Thus we consider 20 consecutive HF estimates of both parameters and calculate the regression coefficient within that ensemble, following the approach of Quartly et al. (2016). Most geophysical corrections (including the standard SSB model) are only applied at 1 Hz, and so will not affect the connection between these terms. However, by choosing to apply the SSB model at 20 Hz, we can evaluate how this affects the perceived connection between SWH and SLA.

4. Results and discussion

4.1. Robustness of the results

When using a simple parametric model to estimate the SSB correction, its robustness will be influenced by the SWH and wind speed data distribution in the region of study. Fig. 3 gives us the possibility to understand the similarities and differences of the sea state characteristics in Med and NS. Panels a and b show the number of measurements for any wind-wave condition. There are in total over 10^7 measurements in both regions, the color bar is saturated at 10^3 measurements to highlight the conditions that happen rarely. Higher SWH conditions (> 5 m) are seen in NS more often than in Med, as expected, as well as stronger winds. The location of the measurements are reported on a 1-degree grid in c and d, which is of course influenced by the Jason-1

track pattern and by the fact that points closer than 20 km to the coast are not considered. This results in few observations in the Aegean Sea, because of the many islands within it.

4.2. Comparison between models

Fig. 2 shows that the best parameterisation according to the FG model differs considerably between different retrackers (upper panel vs lower panel), while smaller differences are also seen between different regions. The stability and robustness of the solutions was confirmed by separately solving for maximum variance explained using just the first three years' data and also just the last four years' data, and noting that the results were essentially the same as the solution using all seven years' data. By using the best choice of coefficients, chosen as described in Section 3.2, the following Reg SSB models are defined:

$$SSB_{SGDR,Med} = -0.058 \times SWH \left(g\frac{SWH}{U_{10}^2}\right)^{0.00}$$

$$SSB_{SGDR,NS} = -0.058 \times SWH \left(g\frac{SWH}{U_{10}^2}\right)^{0.05}$$

$$SSB_{ALES,Med} = -0.050 \times SWH \left(g\frac{SWH}{U_{10}^2}\right)^{0.25}$$

$$SSB_{ALES,NS} = -0.061 \times SWH \left(g\frac{SWH}{U_{10}^2}\right)^{0.15} \qquad (6)$$

In order to better visualise the application of these models, Fig. 4 displays the SSB correction to be applied according to each model to each HF SLA given a SWH and wind speed estimation. For comparison,

the correction applied to the LF SLA in the official Jason-1 product is shown in panel a. To help the visualisation, SWH and wind speed intervals are restricted to the most frequent cases (SWH < 5 m, wind speed < 17 m/s). Panel b shows the spread between all the different models as standard deviation of the SSB values.

This figure and Eq. (6) show that the set of optimal parameters is considerably different when switching retracker, at least for the parameter $\hat{a}$, which is responsible in the SSB for the influence of the wind speed estimation. The latter is considerably more influential on ALES than on SGDR. The dependence of the crossover differences on the sea state is therefore strongly influenced by correlated errors between the retracked parameters, as postulated in Sandwell and Smith (2005). If the physics of the interaction between the signal and the waves were dominant with respect to the retracker-related noise, then the difference of coefficients and SSB model between ALES and SGDR would not be so marked. Regional differences are also present, although less prominent. On one side, these can be the consequence of the choice to model the SSB in a parametric form, which could influence the solution of the linear system due to the presence of more observations with higher sea states in NS. On the other side, other remaining sea-state dependent residual errors can play a role. In general, regional differences of the wave climate from the global average exist and can justify differences between regional and global SSB models. For example, the prevailing difference between the regional SGDR SSB models of this study and the global model is a higher sensitivity of the former to the SWH, which means that for the same value of SWH the regional SSB will be in absolute value higher than in the global model. A comparable effect was found by Tran et al. (2010b) in the same regions considering
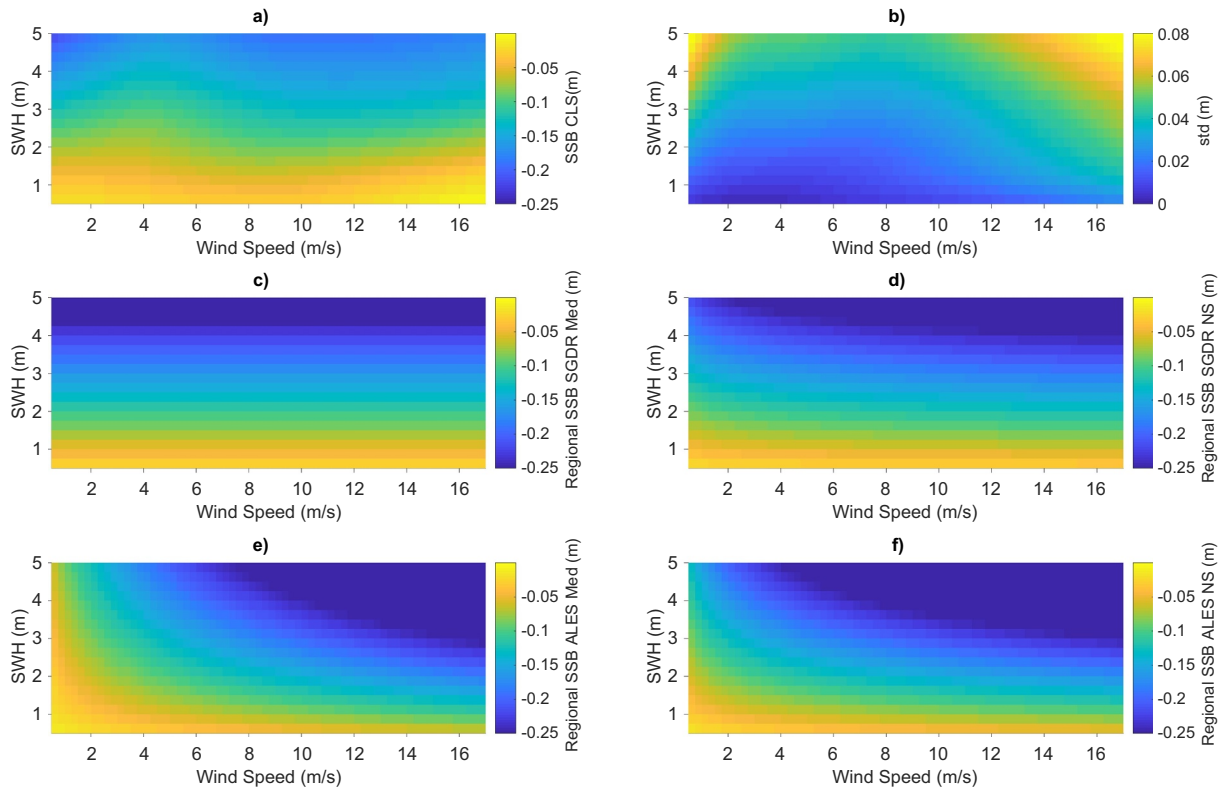

Fig. 4. Different SSB models outputs used in this study for SWH-wind speed domain considering the same dataset and spread between them. (a) SSB model currently in use for Jason-1 SGDR. (b) Spread of the models in these figures, computed as standard deviation. Regional HF FG model for SGDR data in Med (c) and NS (d). Regional HF FG model for ALES data in Med (e) and NS (f).

Table 1

Variance at crossover locations (XO var) before and after the application of the regional sea state bias (Reg SSB) correction based on the derived Fu-Glazman model. The last row provides the corresponding numbers reported in Gaspar et al. (1994) for a global solution using 1 Hz data.

Dataset	XO var before SSB [cm^2]	XO var after SSB [cm^2]
SGDR Med	135.6	108.4
SGDR NS	233.7	199.8
ALES Med	167.8	129.8
ALES NS	246.9	201.8
Gaspar et al. (1994)	127.7	120.4

the mean difference between a 3-D SSB model including a dependence on the wave period and the global SSB model.

In Table 1 the variance at the crossover before and after the application of the SSB corrections is reported, together with the values reported by Gaspar et al. (1994), who estimated the coefficients of FG model on a global scale. The variance in the latter is smaller, since in our study we consider shelf seas and areas that are much more variable than the deep open ocean and since we use HF values at the crossover points, instead of LF as in Gaspar et al. (1994). The higher variance in ALES compared with SGDR corresponds to the known 1 cm difference in RMS for precision of HF estimations, as reported in Passaro et al. (2014). The models computed in this study decrease the variance at the crossover by 15 to 23%. In comparison, the variance after the global LF correction by Gaspar et al. (1994) decreased by 6%. This comparison is only meant to underline the different way in which the same parameterisation is estimated in this study with respect to previous literature. Considerations about precision are instead given in the next sections.

4.3. Noise statistics

In this section we study the performances of the SLA corrected by different SSB models using the statistics described in Section 3.3.1.

Firstly we consider the noise quantified as difference of consecutive HF SLA measurements. We estimate for each cycle the average noise binned in 25-cm intervals of SWH. Then, results are averaged over all the cycles and displayed in Fig. 5 with respect to the SWH. The more irregular lines seen at higher SWH are due to the decrease in available measurements, as reported in the lower panels. The blue curves show the HF SLA noise in Med (a) and NS (b) when correcting ALES (dashed line) and SGDR (continuous line) with the given 1-Hz SSB. For the 1-cm difference between the two retrackers, we refer the readers to the considerations in the previous section. The behaviour of the curves in the Med is much more complicated than in the NS, whose shape is similar to the globally-averaged behaviour, which is shown for example in Garcia et al. (2014). This calls for a dedicated regional approach, in particular when estimating empirical corrections such as the SSB correction, but ultimately leading to a better understanding and parameterization of a global process.

The application of the 20-Hz SSB decreases both the noise at low sea states and the slope of the noise curve. This corresponds to the effect observed by Garcia et al. (2014) when applying a 2-pass retracker to decouple SWH and range estimation and is again proof that SSB should be applied at HF, because it includes retracking errors that are strongly sea-state dependent. On top of that, further improvement of the same kind is brought when the Reg SSB models from Eq. (6) are applied. Notably, the improvement is of a similar magnitude for both SGDR and ALES and therefore it is not only attributable to the need of a specific correction for a different retracker. This means that our regional high-frequency empirical parametrical SSB correction is superior to the global non-parametric SSB model, even if the latter is applied at HF. It
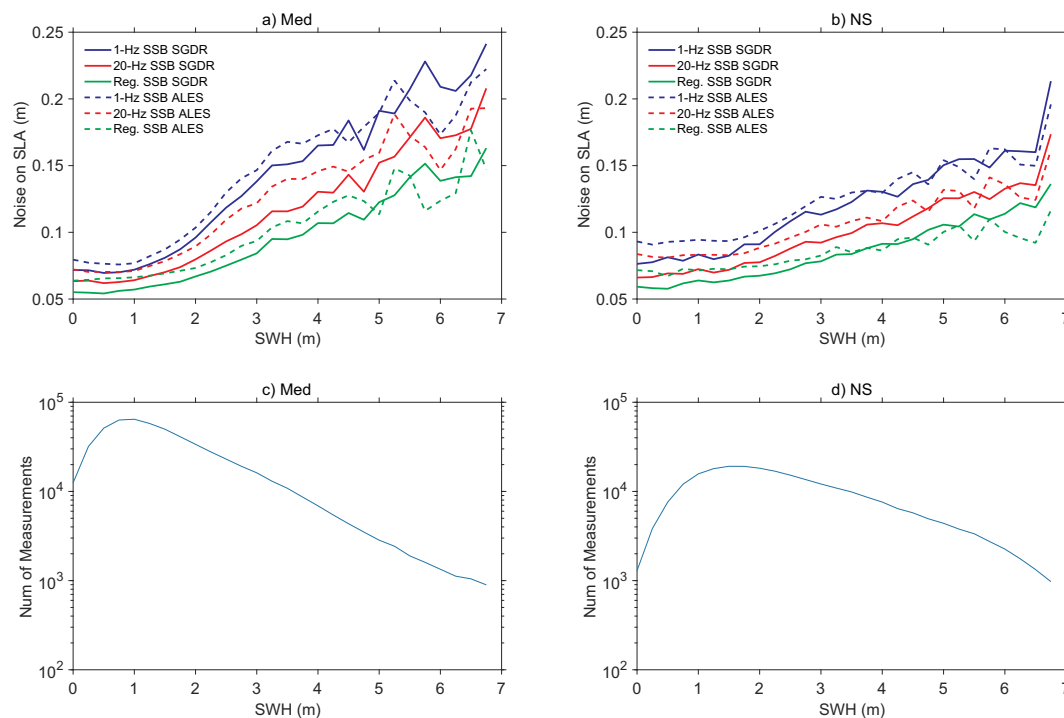
Fig. 5. Noise of the sea level anomalies computed as difference between consecutive high-rate estimations using different SSB corrections analyzed in this study in Med (a) and NS (b). Continuous lines refer to SGDR data, while dashed lines refer to ALES data. The sea level anomalies were corrected with the original 1-Hz SSB correction (blue), with the 20-Hz SSB correction (red) and with the regional SSB correction (green). Number of measurements available with respect to the significant wave height in Med (c) and NS (d). (For interpretation of the references to color in this figure legend, the reader is referred to the web version of this article.)
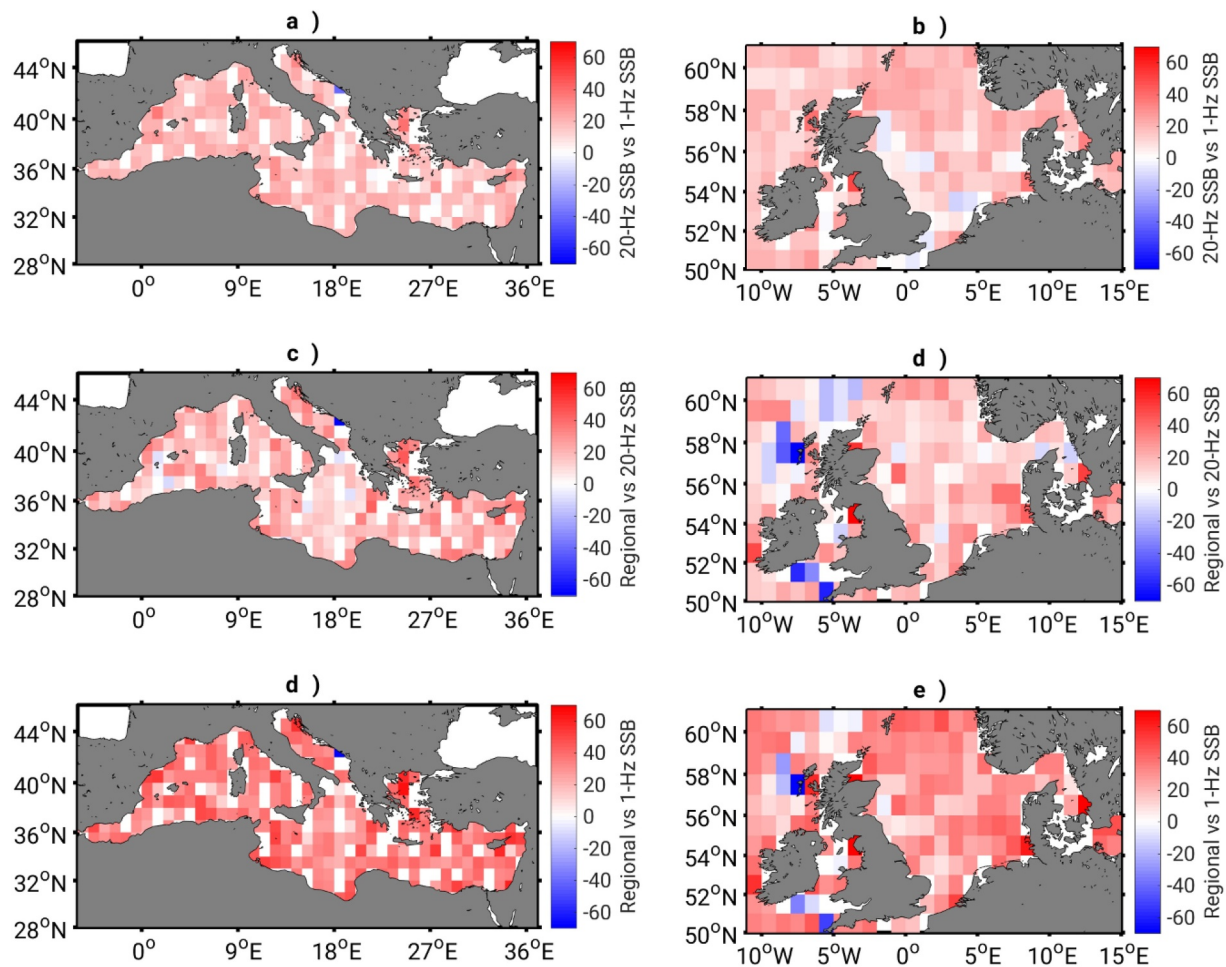
Fig. 6. Percentage of scaled sea level anomalies (SLA) variance differences between a challenger and a reference model. a and b: SLAs computed with 20-Hz SSB correction (challenger) against the ones computed with the original 1-Hz correction (reference). c and d: SLAs computed with 20-Hz SSB correction (challenger) against the ones computed with the regional SSB correction (reference). d and e: SLAs computed with regional SSB correction (challenger) against the ones computed with the original 1-Hz correction (reference). Red squares represent regions with a lower SLA variance for the challenger, i.e. an improvement in the noise statistics with respect to the reference. The dataset used is the SGDR. (For interpretation of the references to color in this figure legend, the reader is referred to the web version of this article.)

must be stressed that the metrics used in this paper, which follow what is done in previous works on the corrections to the range estimated by radar altimetry, are focused on improvements of the precision, i.e. the repeatability of a HF sea level estimate, which can be quantified by a reduction in the HF variance. An evaluation of the improvement in accuracy shall rely on external data, such as tide gauges, and can be the subject of a future validation study involving other regions as well.

To better quantify this improvement, we compute the scaled SLA variance difference in the two regions of study on a 1-degree grid for SGDR in Fig. 6 and for ALES in Fig. 7. The median results are summarised in Table 2. The comparison is performed by choosing a reference and a challenger dataset: in this way, panels a and b show the performances of the 20-Hz SSB taking the 1-Hz SSB as a reference; panels c and d show the performances of the Reg SSB taking the 20-Hz SSB as a reference; finally panels e and f shows the performances of the Reg SSB taking the 1-Hz SSB as a reference and therefore summarise the overall improvement given by this study against the current product. The improvements are of the same amount independently of the region and the variability, as already seen in the crossover statistics of Table 1, with the important addition that the decrease in variance is ubiquitous

also within the domains. A few points present exceptions: they either correspond to locations in which very few observations are available (see Fig. 3) and therefore might present residual outliers with high sea states (and consequently high SSB correction) or, interestingly, to locations characterised by a deep bathymetry in the NS (Fig. 7, panels d and e). The latter point is yet another hint as to the different characteristics of sea-state dependent altimetry errors for shallow areas and the necessity of a dedicated regional processing.

To summarise using the statistics in Table 2, results are very robust. The simple application of an SSB correction based on HF data improves the precision of HF sea level data by 12 to 19%. We notice how the improvement shown by the 20-Hz SSB for SGDR is similar to the one reported by Zaron and DeCarvalho (2016) in their North Pacific test region, which indicates that this application is an alternative method to reduce the retracker-related noise. Subsequently, the recomputation of a parametric regional SSB model improves it overall by 26% to 35%.

4.4. Intra-1 Hz correlations

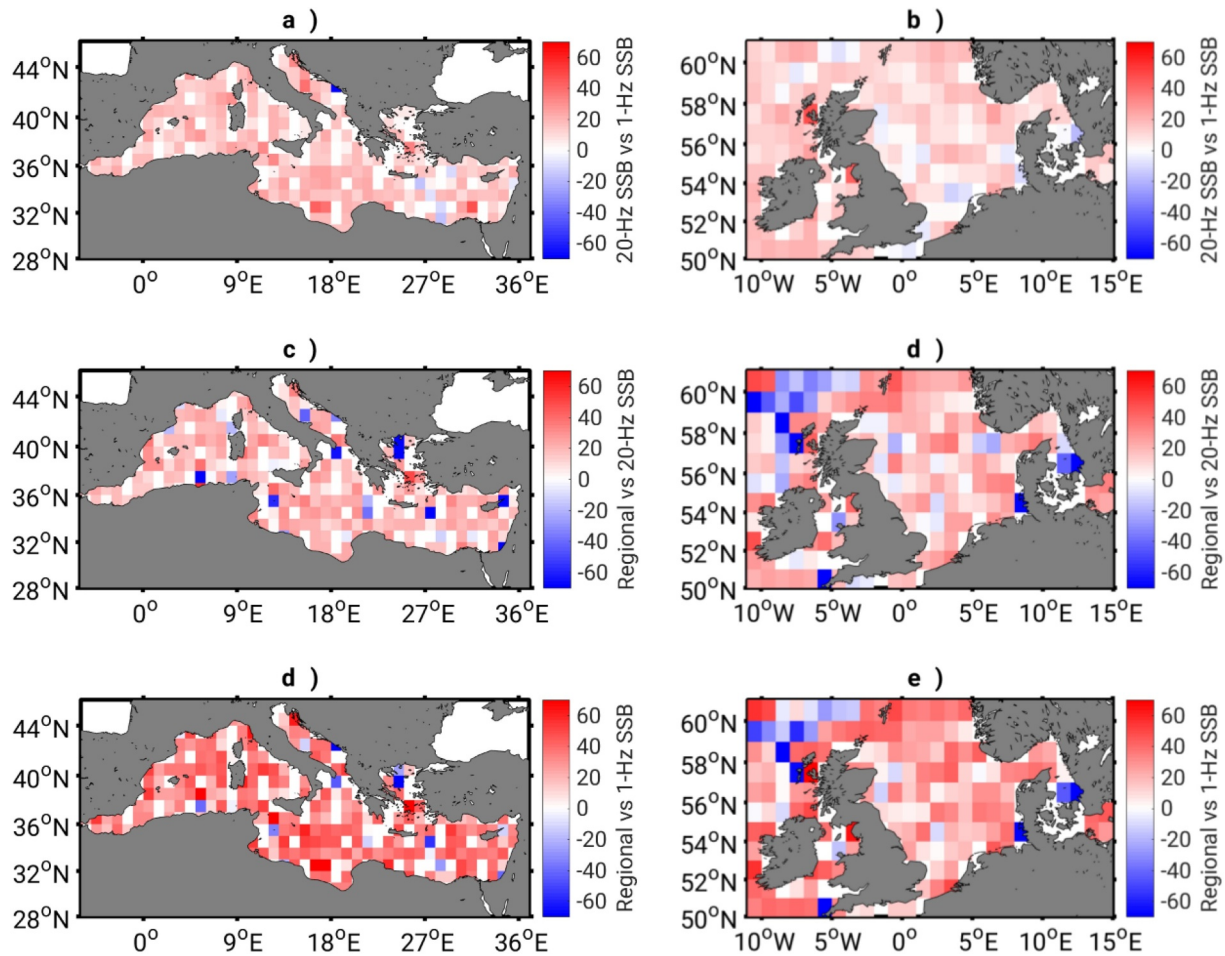The regression coefficient β between the 20-Hz values for SLA and

Fig. 7. As in Fig. 6, but the dataset used is ALES.

Table 2
Median scaled SLA variance improvement in the regions of study. For each column, the reference is the correction of the right and the challenger is the correction on the left. The percentage shows the improvement when using the challenger with respect to the reference.

Dataset	20-Hz vs 1-Hz SSB [%]	Reg vs 20-Hz SSB [%]	Reg vs 1-Hz SSB [%]
SGDR Med	19.18	19.83	34.64
SGDR NS	17.31	15.01	29.93
ALES Med	14.05	18.77	29.34
ALES NS	12.21	16.67	25.81

for SWH from the SGDR has a median value of −0.092, with an interquartile range of −0.100 to −0.064, with the values showing a clear tendency to a larger magnitude at larger wave heights (see Fig. 8). The application of 20-Hz SSB corrections reduces the magnitude of this regression coefficient. A similar pattern is seen for the output of the ALES retracker: with a 1-Hz SSB model applied, the median value of the scaling is −0.102, but there is less variation with SWH in particular for SWH between 2 and 7 m, due to the adaptive retracking window used by this retracker, whose width is tuned on the SWH value. Similar results are noted for the Mediterranean dataset, except that there were fewer observations for the domain SWH > 8 m.

The regression term β represents a residual retracker-related noise, which is partly compensated for by the SSB correction. This analysis shows that applying SSB models at the full data rate and recomputing a regional model as described in this paper reduce the correlation between SLA and SWH estimation.

5. Conclusions

This study demonstrates, using Jason-1 mission as a testbed, that the combination of the use of HF estimations and a regional parametric approach provide a SSB correction that improves the precision of HF sea level data by more than one fourth with respect to the current standard.

We argued and justified that part of the reason lies in the suppression of most of the so-called "tracker bias", which is actually due to correlated errors in the retracking process and is therefore called "retracker-related noise" in this study following Zaron and DeCarvalho (2016). This error is not correctly modelled in a LF SSB correction.

Another improvement is brought by a dedicated regional approach, which showed that the noise in sea level estimation, and consequently the recomputed SSB model, behaves differently in different regions, probably due to residual errors of different nature, which require further investigations.

One drawback of the methodology proposed here could be the following: if one assumes that the SSB estimation is related on one side to
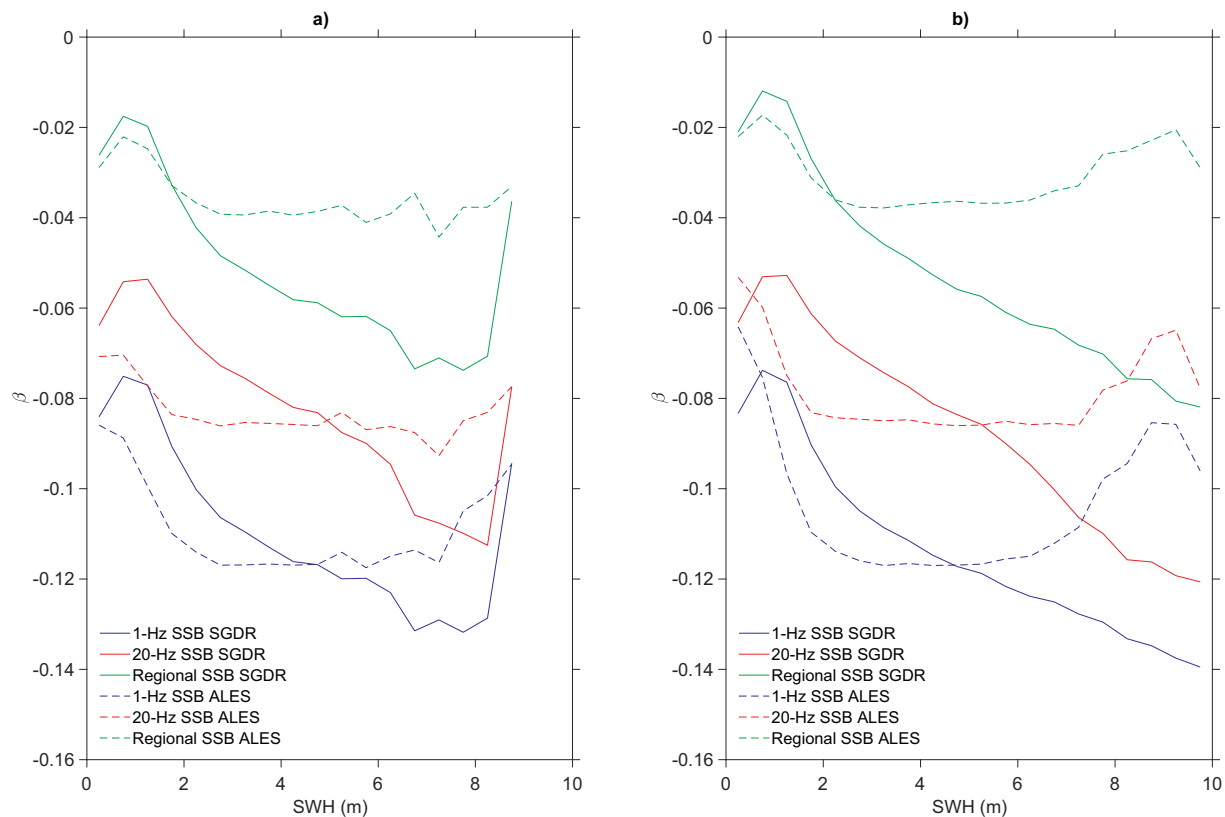
Fig. 8. Variation of the regression coefficient, β as a function of SWH using different SSB corrections analyzed in this study in Med (a) and NS (b). Continuous lines refer to SGDR data, while dashed lines refer to ALES data. The sea level anomalies were corrected with the original 1-Hz SSB correction (blue), with the 20-Hz SSB correction (red) and with the regional SSB correction (green). (For interpretation of the references to color in this figure legend, the reader is referred to the web version of this article.)

the real SWH and wind through a physical low-frequency relation and on the other side to the high-frequency errors in the estimation of SWH and wind, the empirical approach proposed in this work assumes that their combined effect can be modelled together. While this exploratory study demonstrates that this assumption produces more precise estimates than the current SSB model applied at 1-Hz, we cannot exclude that the separate treatment of the two components could generate an even better SSH estimation. The general aim of the research on SSB shall be therefore to work on a retracked dataset that is free from the retracker-related noise, in order to correct for the physical effects of the interaction between the radar signal and the waves. This is therefore one objective of our future work, which shall also further investigate regional differences, understand if the latter are present also when using a non-parametric approach and focus on high sea states, which are poorly represented in our model.

In conclusion, while providing a significantly more precise solution to exploit HF sea level data, this study gives robustness to previous theories on SSB, proposes a method to reduce the retracker-related noise alternative to Zaron and DeCarvalho (2016) and provide an immediate improvement for the application of satellite altimetry in the North Sea and in the Mediterranean Sea.

References

Abdalla, S., 2012. Ku-band radar altimeter surface wind speed algorithm. Mar. Geod. 35, 276–298.

Amarouche, L., Thibaut, P., Zanife, O., Dumont, J.-P., Vincent, P., Steunou, N., 2004. Improving the Jason-1 ground retracking to better account for attitude effects. Mar. Geod. 27, 171–197.

Andersen, O., Scharroo, R., 2011. Range and geophysical corrections in coastal regions and implications for mean sea surface determination. In: Vignudelli, S., Kostianoy, A., Cipollini, P., Benveniste, J. (Eds.), Coastal Altimetry. Springer-Verlag, Berlin Heidelberg, pp. 103–146.

Birol, F., Delebecque, C., 2014. Using high sampling rate (10/20 Hz) altimeter data for the observation of coastal surface currents: a case study over the northwestern Mediterranean Sea. J. Mar. Syst. 129, 318–333.

Birol, F., Fuller, N., Lyard, F., Cancet, M., Nino, F., Delebecque, C., Fleury, S., Toublanc, F., Melet, A., Saraceno, M., et al., 2017. Coastal applications from nadir altimetry: example of the X-TRACK regional products. Adv. Space Res. 59, 936–953.

Carrère, L., Lyard, F., 2003. Modeling the barotropic response of the global ocean to atmospheric wind and pressure forcing-comparisons with observations. Geophys. Res. Lett. 30, 1275.

Chelton, D.B., 1994. The sea state bias in altimeter estimates of sea level from collinear analysis of TOPEX data. J. Geophys. Res. Oceans 99, 24995–25008.

Cipollini, P., Benveniste, J., Birol, F., Fernandes, M., Obligis, E., Passaro, M., Strub, P., Valladeau, G., Vignudelli, S., Wilkin, J., 2017a. Satellite altimetry in coastal regions. In: Stammer, D., Cazenave, A. (Eds.), Satellite Altimetry Over Oceans and Land Surfaces. CRC Press, New York, pp. 343–380.

Cipollini, P., Calafat, F.M., Jevrejeva, S., Melet, A., Prandi, P., 2017b. Monitoring sea level in the coastal zone with satellite altimetry and tide gauges. Surv. Geophys. 1–25. https://doi.org/10.1007/s10712-016-9392-0.

Elfouhaily, T., Thompson, D., Vandemark, D., Chapron, B., 1999. Weakly nonlinear theory and sea state bias estimations. J. Geophys. Res. Oceans 104, 7641–7647.

Fernandes, M.J., Lázaro, C., Ablain, M., Pires, N., 2015. Improved wet path delays for all ESA and reference altimetric missions. Remote Sens. Environ. 169, 50–74.

Fu, L., Cazenave, A. (Eds.), 2001. Satellite Altimetry and Earth Sciences. A Handbook of Techniques and Applications. vol. 69 Academic, San Diego, CA.

Fu, L.-L., Glazman, R., 1991. The effect of the degree of wave development on the sea state bias in radar altimetry measurement. J. Geophys. Res. Oceans 96, 829–834.

Garcia, E.S., Sandwell, D.T., Smith, W.H., 2014. Retracking Cryosat-2, Envisat and Jason-

1 radar altimetry waveforms for improved gravity field recovery. Geophys. J. Int. ggt469.

Gaspar, P., Ogor, F., Le Traon, P.-Y., Zanife, O.-Z., 1994. Estimating the sea state bias of the TOPEX and POSEIDON altimeters from crossover differences. J. Geophys. Res. Oceans 99, 24981–24994.

Gaspar, P., Labroue, S., Ogor, F., Lafitte, G., Marchal, L., Rafanel, M., 2002. Improving nonparametric estimates of the sea state bias in radar altimeter measurements of sea level. J. Atmos. Ocean. Technol. 19, 1690–1707.

Gómez-Enri, J., Cipollini, P., Passaro, M., Vignudelli, S., Tejedor, B., Coca, J., 2016. Coastal altimetry products in the Strait of Gibraltar. IEEE Trans. Geosci. Remote Sens. 54, 5455–5466.

Labroue, S., Gaspar, P., Dorandeu, J., Zanife, O., Mertz, F., Vincent, P., Choquet, D., 2004. Nonparametric estimates of the sea state bias for the Jason-1 radar altimeter. Mar. Geod. 27, 453–481.

Legeais, J.-F., Ablain, M., Zawadzki, L., Zuo, H., Johannessen, J.A., Scharffenberg, M.G., Fenoglio-Marc, L., Fernandes, M.J., Andersen, O.B., Rudenko, S., Cipollini, P., Quartly, G.D., Passaro, M., Cazenave, A., Benveniste, J., 2018. An improved and homogeneous altimeter sea level record from the ESA climate change initiative. Earth Syst. Sci. Data 10, 281.

Pascual, A., Marcos, M., Gomis, D., 2008. Comparing the sea level response to pressure and wind forcing of two barotropic models: validation with tide gauge and altimetry data. J. Geophys. Res. Oceans 113.

Passaro, M., 2017. COSTA v1.0: DGFI-TUM Along Track Sea Level Product for ERS-2 and Envisat (1996–2010) in the Mediterranean Sea and in the North Sea, Links to Data Sets in NetCDF Format. Deutsches Geodaetisches Forschungsinstitut der Technischen Universitaet Muenchen, PANGAEA https://doi.org/10.1594/PANGAEA.871920.

Passaro, M., Cipollini, P., Vignudelli, S., Quartly, G., Snaith, H., 2014. ALES: a multi-mission subwaveform retracker for coastal and open ocean altimetry. Remote Sens. Environ. 145, 173–189.

Passaro, M., Dinardo, S., Quartly, G.D., Snaith, H.M., Benveniste, J., Cipollini, P., Lucas, B., 2016. Cross-calibrating ALES Envisat and Cryosat-2 delay–Doppler: a coastal altimetry study in the Indonesian seas. Adv. Space Res. 58, 289–303.

Passaro, M., Rose, S., Andersen, O., Boergens, E., Calafat, F., Dettmering, D., Benveniste, J., 2018. ALES +: adapting a homogenous ocean retracker for satellite altimetry to sea ice leads, coastal and inland waters. Remote Sens. Environ. 211, 456–471. https://doi.org/10.1016/j.rse.2018.02.074.

Picot, N., Case, K., Desai, S., Vincent, P., 2003. AVISO and PODAAC User Handbook. IGDR and GDR Jason Products. (SMM_MU_M5_OP_13184_CN (AVISO) JPL D_21352 (PODAAC)).

Pires, N., Fernandes, M.J., Gommenginger, C., Scharroo, R., 2016. A conceptually simple modeling approach for Jason-1 sea state bias correction based on 3 parameters exclusively derived from altimetric information. Remote Sens. 8, 576.

Quartly, G.D., 2009. Optimizing σ^0 information from the Jason-2 altimeter. IEEE Geosci. Remote Sens. Lett. 6, 398–402.

Quartly, G., Smith, W., Passaro, M., 2016. Intra-1 Hz Correlations, Presented at the Ocean Surface Topography Science Team Meeting, La Rochelle, France, 1–4 November 2016. Available from. https://mediatum.ub.tum.de/doc/1338249/1338249.pdf.

Quartly, G., Legeais, J.-F., Ablain, M., Zawadzki, L., Fernandes, M., Rudenko, S., Carrère, L., García, P.N., Cipollini, P., Andersen, O., Poisson, J.-C., Mbajon Njiche, S., Cazenave, A., Benveniste, J., 2017. A new phase in the production of quality-controlled sea level data. Earth Syst. Sci. Data 9, 557–572.

Sandwell, D.T., Smith, W.H., 2005. Retracking ERS-1 altimeter waveforms for optimal gravity field recovery. Geophys. J. Int. 163, 79–89.

Thibaut, P., Poisson, J., Bronner, E., Picot, N., 2010. Relative performance of the MLE3 and MLE4 retracking algorithms on Jason-2 altimeter waveforms. Mar. Geod. 33, 317–335.

Tran, N., Labroue, S., Philipps, S., Bronner, E., Picot, N., 2010a. Overview and update of the sea state bias corrections for the Jason-2, Jason-1 and TOPEX missions. Mar. Geod. 33, 348–362.

Tran, N., Vandemark, D., Labroue, S., Feng, H., Chapron, B., Tolman, H.L., Lambin, J., Picot, N., 2010b. Sea state bias in altimeter sea level estimates determined by combining wave model and satellite data. J. Geophys. Res. 115, C03020.

Vandemark, D., Tran, N., Beckley, B., Chapron, B., Gaspar, P., 2002. Direct estimation of sea state impacts on radar altimeter sea level measurements. Geophys. Res. Lett. 29.

Zaron, E.D., DeCarvalho, R., 2016. Identification and reduction of retracker-related noise in altimeter-derived sea surface height measurements. J. Atmos. Ocean. Technol. 33, 201–210.

Arctic Ocean Sea Level Record from the Complete Radar Altimetry Era: 1991–2018

Stine Kildegaard Rose [1,*,†], **Ole Baltazar Andersen** [1], **Marcello Passaro** [2] (ORCID),
Carsten Ankjær Ludwigsen [1] (ORCID) **and Christian Schwatke** [2] (ORCID)

[1] Technical University of Denmark—National Space Institute (DTU Space), 2800 Kgs. Lyngby, Denmark
[2] Deutsches Geodätisches Forschungsinstitut der Technischen Universität München (DGFI-TUM),
   80333 Munich, Germany
* Correspondence: stine@space.dtu.dk; Tel.: +45-45259742
† Current adress: Department of Geodesy, DTU Space—National Space Institute, Elektrovej Build. 228,
   2800 Kgs. Lyngby, Denmark.

check for updates

Abstract: In recent years, there has been a large focus on the Arctic due to the rapid changes of the region. Arctic sea level determination is challenging due to the seasonal to permanent sea-ice cover, lack of regional coverage of satellites, satellite instruments ability to measure ice, insufficient geophysical models, residual orbit errors, challenging retracking of satellite altimeter data. We present the European Space Agency (ESA) Climate Change Initiative (CCI) Technical University of Denmark (DTU)/Technischen Universität München (TUM) sea level anomaly (SLA) record based on radar satellite altimetry data in the Arctic Ocean from the European Remote Sensing satellite number 1 (ERS-1) (1991) to CryoSat-2 (2018). We use updated geophysical corrections and a combination of altimeter data: Reprocessing of Altimeter Product for ERS (REAPER) (ERS-1), ALES+ retracker (ERS-2, Envisat), combination of Radar Altimetry Database System (RADS) and DTUs in-house retracker LARS (CryoSat-2). Furthermore, this study focuses on the transition between conventional and Synthetic Aperture Radar (SAR) altimeter data to make a smooth time series regarding the measurement method. We find a sea level rise of 1.54 mm/year from September 1991 to September 2018 with a 95% confidence interval from 1.16 to 1.81 mm/year. ERS-1 data is troublesome and when ignoring this satellite the SLA trend becomes 2.22 mm/year with a 95% confidence interval within 1.67–2.54 mm/year. Evaluating the SLA trends in 5 year intervals show a clear steepening of the SLA trend around 2004. The sea level anomaly record is validated against tide gauges and show good results. Additionally, the time series is split and evaluated in space and time.

Keywords: radar altimetry; satellite altimetry; arctic ocean; remote sensing of the oceans; sea level rise; polar area

1. Introduction

The Arctic region has warmed faster than any other parts of the Earth, where the sea level of the Arctic Ocean is an important climate indicator. The arctic sea-ice is decreasing, and has since 1997 experienced a steepening in the decrease [1]. In the fifth Intergovernmental Panel on Climate Change (IPCC) report a global total sea level rise of 2.8 ± 0.7 mm/year in the period of 1993–2010 is found [2]. The sea level rise is due to: (1) Thermal expansion [3]. 93% of the atmospheric energy imbalance, which is caused by greenhouse gases, accumulates in the ocean as ocean heat content. Recent models show an increasing ocean warming trend in the upper 2 km of the oceans [4]. (2) Land water storage from human interactions i.e., ground water depletion and reservoir storage [5]. (3) Glacier and ice

sheet mass losses. Outlet glaciers are losing mass more rapidly [6,7], contributing to the sea level rise, changing the oceans freshwater flux, and influencing the ocean thermohaline circulation [8].

The polar oceans are often not included in the global sea level estimations and can be seen as white spots on the global sea level maps. This is because of the challenging polar sea level determination due to; the seasonal to permanent sea-ice cover, the lack of regional coverage of satellites, satellite instruments ability to measure ice, insufficient geophysical models, residual orbit errors and retracking of satellite altimeter data.

The sea-ice cover is in constant change. The sea-ice extent is the largest in March and the smallest in September. The Norwegian and Barents Sea are only seasonally covered by sea-ice while the central part up to the Canadian Archipelago and the North coast of Greenland are permanently ice covered (see Figure 1 for an Arctic Ocean overview). The older ice is pushed against these parts, and additionally, the Canadian Archipelago and the land-fast ice areas are also the part with the fewest leads and consequently the most inaccurate sea level determination [9].
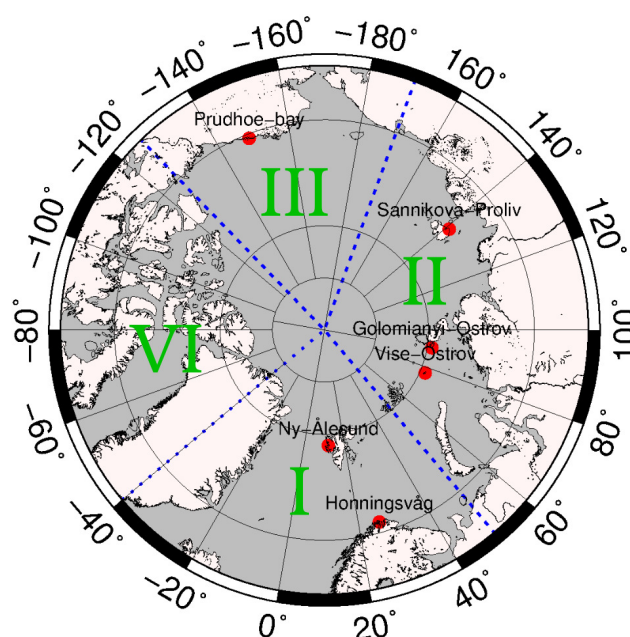
Figure 1. Overview map of the Arctic Ocean. The map show the tide gauges (red dots) used to validate the SLA and the different sectors (divided in blue punctured lines) used to investigate the different Arctic regions. The four regions are: I: Fram Strait, Greenland Sea, Norwegian Sea and Barents Sea. II: The Russian Arctic: Kara Sea and Laptev Sea, III: East Siberian Sea and Beaufort Sea, IV: The Canadian Archipelagos and Baffin Bay.

Sea-ice affects the returned satellite radar signal (or waveform) resulting in a poorer coverage and a lower quality of the return signal. Sea level estimates in the sea-ice covered areas are dependent on gaps in between ice floes (leads or polynyas). From now on we are not separating between leads and polynyas but referring to leads as ocean water surrounded by frozen ice. Leads are often very flat ocean surfaces, where there are almost no scatter from the radar wave. This will be registered as a very peaky waveform in the received echo. If leads are located off-nadir their strong backscatter can substantially decrease the quality of the range retracking, this is also known as snagging [10]. In case of Envisat, the nominal circular footprint of 2 km in diameter [11] can increase up to 10 km [12] for strong off-nadir backscatter sources. Despite its much smaller along-track footprint (1.65 km × 0.30 km), CryoSat-2 can also be affected by off-nadir leads, which will result in erroneous range estimates [13]. Refrozen leads are often seen as normal specular lead waveforms but they can be biased up to a couple of centimeters. Another source of errors can be melt ponds on-top of the ice in Spring/Summer and ice freeze-ups in Autumn.

Also the geophysical range corrections are less accurate in the Arctic due to the sea-ice contamination of the radiometer and the lack of observations. The tides and the inverse barometer effect (IBE) are the most important parameters, but also the most uncertain [9,14].

The satellite altimeter era has completed more than 25 years of measurements distributed over several satellites: ERS-1, ERS-2, Envisat, CryoSat-2, ICESat-1/2, SARAL and Sentinel-3A/B. All these satellites have a geographical coverage suitable for Arctic Ocean research. The T/P and Jason satellite series have proven worthy for mid latitude SLA studies, but do not cover the Arctic region. In this study, we use data from four ESA radar altimeter satellites; ERS-1, ERS-2, Envisat and CryoSat-2. In the earlier altimeter satellite missions (ERS-1, ERS-2 and Envisat) orbit errors up to 5 cm still exists [15].

The Arctic Ocean is lacking in-situ measurements consistent in time and space, mainly due to its harsh environment. Various publications (e.g., [16,17]) of the Arctic sea level from tide gauge data exists, where the sea level are measured along the Russian and Norwegian coasts. There exist few tide gauges in the interior of the Arctic Ocean, and they are all short time series. Several bouys have been deployed in the Arctic Ocean ex. Argo (www.argo.ucsd.edu), Ice-Tethered Profiler (www.whoi.edu /website/itp), UNCLOS and GreenArc [18] The Argo buoys have shown great results in validating altimeter data [19], but are not yet densely deployed in the Arctic Ocean.

The first Sea Surface Height (SSH) studies covering large parts of the Arctic Ocean were computed from the ERS satellites to produce sea-ice thicknesses [20] and gravity anomalies [21]. Peacock and Laxon [22] were the first to construct an ocean product, a mean SSH (MSS), from the Arctic Ocean using ERS-1 and ERS-2 altimeter data from a 10 year period. Since then several e.g., [23–26] have followed. Global MSS products are available from: CNES/CLS (not covering the Arctic) [27], DTU [28], SSALTO/DUACS by AVISO.

In this paper, as part of ESA's Sea level CCI (SL_CCI) and the Sea Level Budget Closure (SLBC_CCI), we use 27 years of radar satellite altimeter data for constructing a new improved monthly sea level record for the Arctic Ocean - the CCI DTU/TUM Arctic Ocean data set. We find a sea level rise of 1.54 mm/year of the Arctic Ocean covering 65°N to 81.5°N latitude and −180° to 180° longitude from September 1991 to September 2018, with a 95% confidence interval of 1.16–1.81 mm/year. The coverage from the ERS-1 satellite is sparse during periods of time and the time series may be more error prone in this period, therefore looking at the time series starting from ERS-2 we get a sea level rise of 2.22 mm/year with a 95% confidence interval within 1.67–2.54 mm/year.

The paper starts by describing the data used (Section 2). We use a combination of tailored level-2 (L2) ERS-1 data together with a new retracking of ERS-2 and Envisat data and with a combination of state-of-the-art altimeter data and retracked data from CryoSat-2. In Section 3, the methods are described in making the SLA product from pre-processing (Section 3.1) and geophysical corrections (Section 3.2) to handling the sea-ice (Section 3.3) and the intermission biases (Section 3.4) between the different satellites. The SLA product resampling and gridding are described (Section 3.6), and finally, in Section 3.7 a bootstrap analysis is described to evaluate the SLA uncertainties. In Section 4, the results are described and validated. The section starts by showing the resulting SLA uncertainty (Section 4.1). The results are described as regional trends (Section 4.2), inter-annual variability (Section 4.3) and regional variability (Section 4.4). The sea level anomalies (SLA) are validated against six tide gauge stations shown in Figure 1. This is described in Section 4.5. The results are discussed in Section 5 and summarized in the conclusion (Section 6).

2. Data

This section describes the data used in this study.

2.1. Altimetry Data

The CCI DTU/TUM Arctic SLA contains data from four ESA radar altimeter satellites ERS-1, ERS-2, Envisat, CryoSat-2. ERS-1, ERS-2 and Envisat are conventional altimetry or low resolution mode (LRM) data sets processed with a single processor, while CryoSat-2 consists of three types: LRM,

Synthetic Aperture Radar (SAR) and SAR Interferometry (SARIn), which are processed with different processors. For satellite specific details see Appendix A. In Section 3.2 the geophysical range correction data are described.

2.2. Ice Concentration Data

In Section 3.3, we use sea-ice concentration data in separating sea-ice data from ocean data. The sea-ice concentration data are derived in an operational product (after 2015) [29] and a reprocessed product (before 2015) [30] by the EUMETSAT Ocean and Sea Ice Satellite Application Facility. Both products are given as sea-ice concentrations in 10 km Polar Stereographic grids for every six hours.

2.3. Tide Gauge Data

In validation of the CCI DTU/TUM SLA data set (Section 4.5), tide gauge data from the Permanent Service for Mean Sea Level (PSMSL) [31,32] are used. The tide gauge data are given as monthly SLAs. Six tide gauges are chosen spread along the coast of the Arctic Ocean (Figure 1).

3. Generation of the Sea Level Product

The Arctic Ocean SLAs are computed by the following steps:

1.　Pre-processing
2.　Adding/removing geophysical corrections
3.　Sea-ice concentration data are used to discriminate between the sea-ice cover and the open ocean
4.　Threshold criterias are used to separate the leads/open ocean from the sea-ice
5.　Inter-satellite biases are determined and corrected
6.　Removing outliers
7.　Resampling and gridding the data to compute the final Arctic SLA
8.　Uncertainty analysis

3.1. Pre-Processing

Pre-processing details for the individual satellites are described in Appendix A.

3.2. Geophysical Corrections

The geophysical corrections were updated to get a more uniform product, suitable to compare the SLAs in between satellites. Table 1 summarizes the corrections used.

Table 1. Data origin and applied geophysical corrections. O, L, LP tides are the Ocean tide, ocean loading tide, long-periodic non-equilibrium ocean tide, LP otide + setide includes the long-periodic ocean tide and the solid earth tide.

	ERS-1	ERS-2	Envisat	CryoSat-2 [33]
Data origin	REAPER L2 [34]	ALES+ [34,35]	ALES+ [35,36]	LARS/RADS [33,37,38]
Wet troposphere	ECMWF [39]	ECMWF [39]	ECMWF [39]	ECMWF [39]
Dry troposphere	Radiometer/ECMWF [39]	Radiometer/ECMWF [39]	ECMWF [39]	ECMWF [39]
Ionosphere	NICO [40]/GIM [41]	NICO [40]/GIM [41]	Doris [36]	GIM [41]/Bent [42]
DAC	ERA-Interim [43]	ERA-Interim [43]	ERA-Interim [43]	DAC-ECMWF [44]
O, L, LP tides	FES2014 [45]	FES2014 [45]	FES2014 [45]	FES2014 [45]
LP otide + setide	Cartwright [46]	Cartwright [46]	Cartwright [46]	Cartwright [46]
Pole tide	Wahr [47]	Wahr [47]	Wahr [47]	Wahr [47]
Sea state bias	Altimetrics [34]	ALES+ [48]	ALES+ [48]	None/RADS [38]
Mean sea surface	DTU18 [49]	DTU18 [49]	DTU18 [49]	DTU18 [49]

The preferred method for estimating the wet tropospheric correction over the Arctic Ocean is to use modeled data, due to the radiometer contamination by the sea-ice [50]. For most of the satellites a model correction is available. For ERS-1 REAPER data the microwave radiometer wet tropospheric

correction is applied over the ocean if valid or else a model correction is applied. The authors were not aware of a way to see which of the corrections were applied, and therefore it was not possible to change this correction.

We use the FES2014 [45] ocean tide model with loading effects. This model is optimized in the Arctic Ocean compared to previous versions. The tide model is limited in coastal areas resulting in a final data set not defined close to the coast. FES2014 was produced by Noveltis, Legos and CLS Space Oceanography Division and distributed by Aviso, with support from CNES (http://www.aviso.altime try.fr/).

The atmospheric correction in the Arctic is very important since amplitudes of the signal can reach 1 m, i.e., greater than the SLA signal. Normally in the Arctic, IBE is favored over the Dynamic Atmosphere Correction (DAC) including high atmospheric fluctuations, because of high latitude issues. For consistency, ERS-1, ERS-2 and Enivsat are reprocessed with the DAC ERA-Interim [43] by linear interpolation in space and time. In consequence, this will give more outliers in the data. The DAC ERA-Interim product are computed in the period of 1991–2015, not covering the total CryoSat-2 period. Therefore, the DAC-ECMWF [44] from CLS is here used from the CryoSat-2 GDR product. Various models were tested, and this was proven to be the one closest to the DAC ERA-Interim model.

The applied sea state bias correction for ERS-1 is taken from the REAPER product. For ERS-2 and Envisat the sea state bias is derived from the ALES+ retracker and applied at 20 Hz [48]. For CryoSat-2 only sea state bias for the LRM mode is applied, which is a hybrid sea state bias from the RADS product. For most cases it is fair to ignore the sea state bias in SAR and SARIn mode, such leads are very flat surfaces, where the sea state bias is very close to zero.

The DTU18 MSS was used as a reference [49]. The new MSS from DTU is improved in the central Arctic region and in coastal zones. It has a bias towards recent years sea level heights including three years of Sentinel-3A and eight years of improved CryoSat-2 data.

3.3. Lead and Ocean Discrimination

The Arctic Ocean SLA record is derived by separating leads in the sea-ice cover and open ocean according to the different classification of their surfaces. Various sea-ice types can mistakenly be associated with open ocean waveforms. The ocean is separated from the sea-ice cover by the ice concentration grids (Section 2.2). For more details see Appendix B.

Sea-ice and mixed surfaces are removed by using the waveform Pulse Peakiness (PP) and the width of the leading edge. Furthermore, for CryoSat-2, the stack standard deviation is used to identify the leads. For removing erroneous data in the open ocean (that could be data from the ice edge or near the coast), the PP and the backscatter coefficient are used. There exists many variations of the PP formula e.g., [13,22,51,52]. The values used in this study for each satellite are shown in Table 2. All references to the PP (in Table 2 and in text) are described as in [13], which is given by the waveform maximum power received multiplied with the sum of all range bin powers. In parenthesis, PP values are described as in [22] which is the same formulation as [13] but multiplied with a constant of 31.5. This formulation was first used for the ERS satellites. The choice of these threshold values are based on several studies [11,13,22,53,54] and adjusted and evaluated for this study.

Table 2. Thresholds used in lead and ocean discrimination. The table columns are PP, stack standard deviation (St. Std), and width for lead discrimination and PP. Backscatter coefficient (σ_0) for the ocean discrimination. The PP values are described as in [13] and in parenthesis as in [22]. The PP is calculated differently for CryoSat-2 (see the details in the text). The two numbers corresponds to SAR and SARIn, respectively. The width in ERS-1 is from the REAPER product and is the OCOG width, for ERS-2 and Envisat the width is the ALES+ leading edge rising time, and for CryoSat-2 the width is the width of the Gaussian fit.

|	Lead			Ocean	
	PP >	**St. Std**	**Width <**	**PP <**	**σ_0 <**
ERS-1	0.60 (19)	-	3	0.048 (1.5)	15
ERS-2	0.65 (20.5)	-	3	0.048 (1.5)	15
Envisat	0.71 (22.5)	-	3	0.048 (1.5)	15
CryoSat-2	0.35/0.25 (11/7.9)	4	0.9	-	-

3.4. Intermission Bias

To get a seamless transition between conventional altimetry (from ERS-1/2, Envisat, CryoSat-2 (LRM)) and SAR/SARIn (CryoSat-2) altimetry can be error prone, especially in the Arctic due to the different data coverage. SAR altimeter data have much more data over the sea-ice cover, while conventional altimetry are having troubles. Conventional and SAR/SARIn altimetry data sets are covering different regional areas and are processed with different strategies and having different retracking corrections.

For CryoSat-2, the best approach of merging the different satellite measurement types (LRM, SAR and SARIn) has proven to be a detailed study of individual satellite tracks (not shown). RADS data are in LRM while LARS data are covering SAR and SARIn, so no data are overlapping in time. We found a retracker bias between RADS and LARS of −12.9 cm.

The transition between the four satellite missions, the intermission biases were estimated and minimized. The following steps were completed to handle the intermission biases:

1. Monthly medians were calculated for each mission, over the entire Arctic Ocean, covered by the data sets
2. For overlapping mission pairs (either ERS-1 and ERS-2, ERS-2 and Envisat, or Envisat and CryoSat-2) coinciding months (only full months considered) were detected and extracted
3. For each overlapping pair, the median difference was calculated and the data sets were aligned
4. The biases between the satellites are: ERS-1/ERS-2 ~0.67 m, ERS-2/Envisat ~0.53 m and Envisat/CryoSat-2 ~0.03 m

Figure 2 shows the monthly median of each overlapping satellite pair. The Pearsons correlation coefficient of the three satellite pairs ERS-1/ERS-2, ERS-2/Envisat and Envisat/CryoSat-2 gives 0.52, 0.96, 0.95, respectively.

(a) ERS-1 and ERS-2
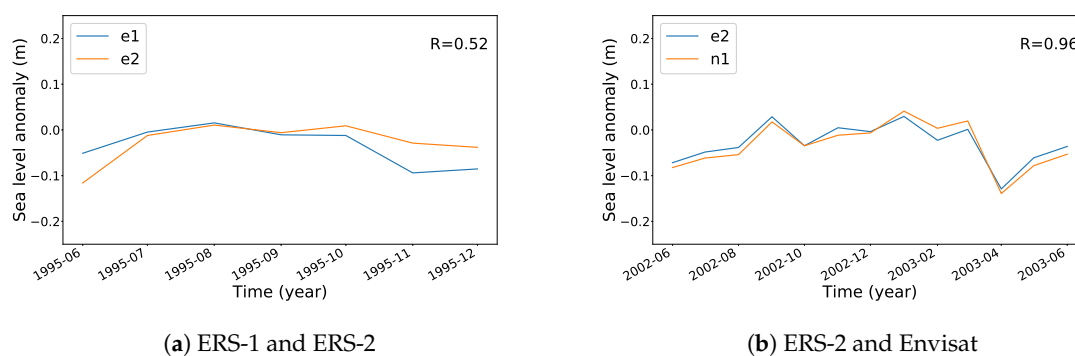
(b) ERS-2 and Envisat

Figure 2. *Cont.*
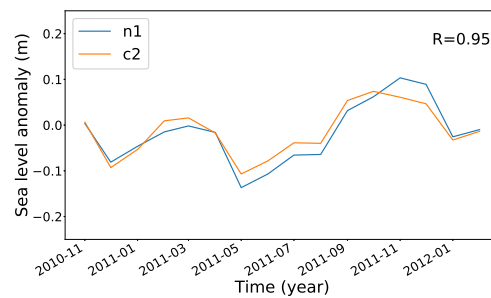
(**c**) Envisat and CryoSat-2

Figure 2. Monthly median of the entire Arctic in the overlapping periods for (**a**) ERS-1 (e1) and ERS-2 (e2), (**b**) ERS-2 and Envisat (n1) and (**c**) Envisat and CryoSat-2 (c2). In the top right corner of each figure the correlation coefficient is shown.

3.5. Removing Outliers

The outlier removal is carried out in two steps. First, as mentioned in Appendix A, outliers are removed from each track with a MAD outlier detector to get rid of the largest outliers. Second, outliers are detected and removed on a monthly basis with a hard cut-off of ±0.3 m from the median. This was done similar to Cheng et al. [24]. The hard cut-off resulted in rejection of 18.05% data for ERS-1, 2.45% data for ERS-2, 0.52% for Envisat and 0.06% of data for CryoSat-2. The large removal of ERS-1 data are due to error-prone orbit estimation and bad data sampling, which are causing bad waveforms, resulting in wrong height estimates.

3.6. The Arctic Sea Level Anomaly Product

First, monthly data are averaged in cells of $0.2° \times 0.2°$ to overcome the sampling dissimilarity in latitude, which would favor high latitude data especially for Cryosat-2, where the data coverage is much larger than for the conventional altimetry satellites. Second, a least squares collocation with second-order Markov covariance function [55] is used to grid the monthly data. The final grid size is $0.25°$ latitude by $0.5°$ longitude using a 500 km correlation length with a RMS noise of 2 cm. The outputs from the collocation are the SLA data record and a interpolation error estimate both given in monthly grids from September 1991 to September 2018, covering $65°N–81.5°N$ and $180°W–179.5°E$ in gridline registration. The mean SLAs are shown in Figure 3 for each satellite: ERS-1 (a), ERS-2 (b), Envisat (c) and CryoSat-2 (d). The mean SLA is slightly higher over the sea-ice cover. This is especially the case for ERS-1. For ERS-2 and CryoSat-2 low SLAs controls the Canadian Arctic and the Beaufort Gyre areas, while we see a large mean SLA for Envisat in the Kara Sea. The SLAs in the Fram Strait and Barents Sea areas are slightly negative for the three first missions, while it is slightly positive for CryoSat-2. These figures will be discussed further in Section 5.1.
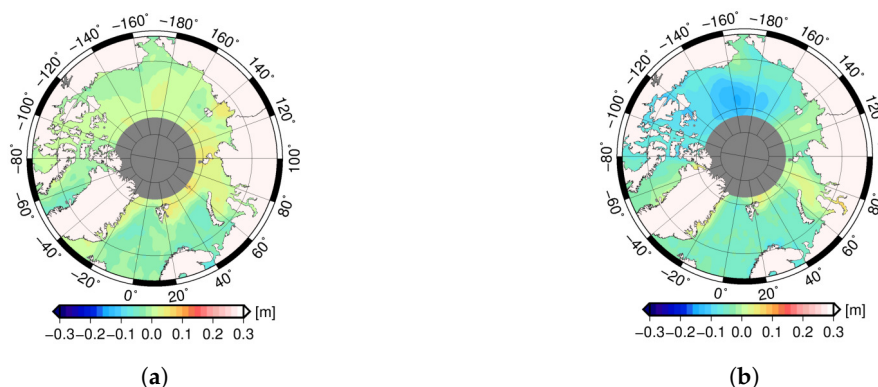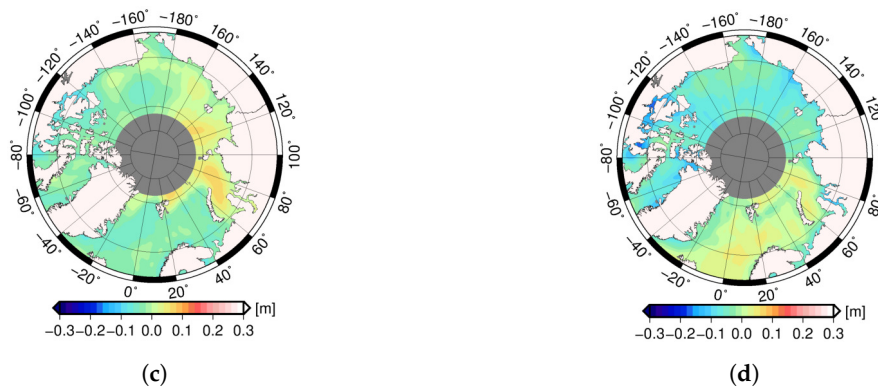

(**a**)

(**b**)

Figure 3. *Cont.*

(c)

(d)

Figure 3. The average SLA in meters for each satellite period: (**a**) ERS-1, (**b**) ERS-2, (**c**) Envisat, (**d**) CryoSat-2.

3.7. Uncertainty Estimates

In Section 1, multiple error sources that contribute to the total uncertainty of the derived SLA are introduced. These are errors on the altimeter instruments, the orbit determination, the retracking of the radar signal, and from this follows the many uncertainties on the geophysical range corrections (Section 3.2). We can now calculate the true SLA including noise. The exact size of this noise coming from the uncertainties described above are not known, but Ablain et al. [56] looked into this error budget. On top of all these uncertainties there can be errors in the discrimination of ocean and leads (Section 3.3), inter-satellite biases (Section 3.4), in making of the SLA grids (Section 3.6), in making of the total SLA time series and trend maps (Section 4.2), and furthermore, uncertainties can arise from: retracker biases, interpolation, filtering, sampling. The size of all these individual uncertainties are, however, not well known, and additionally it is difficult to propagate the uncertainties analytic in the long processing chain. As an alternative we apply a bootstrap approach [57] to estimate the error of the SLA. Bootstrapping embrace all the variations from the various uncertainties. To obtain valid error estimates using bootstrap, the observations must be independent and the bootstrap data sets must resemble the original data set. Hence, to better approximate independent observations, a block bootstrap is used.

The specific bootstrap procedure to derive the error for each monthly data set is carried out as follows: (1) the data are split in n non-overlapping blocks. (2) 1000 bootstrap realizations are created, by sampling with replacement among the blocks. (3) For each bootstrap data set the SLA is derived in the same way as described in Section 3.6. (4) Finally we have 1000 estimates of the SLA for each grid cell from which we can extract error information such as standard deviation and confidence interval. In Appendix C a more thorough review of the bootstrapping procedure is described.

It is only valid to show results with a standard deviation if the results are normal distributed. The Arctic SLA distributions are not normal distributed for all grid cells in the Arctic Ocean (see Figure A1 in Appendix C for more details). Therefore, the uncertainty is expressed in a 95% confidence level. The results are shown with the median and not the mean value, because of the skewness of the distributions (Figure A1, Appendix C).

4. The Arctic Sea Level Anomaly Record

The resulting CCI DTU/TUM Arctic SLA product is analyzed in this section. The SLA product is given by monthly grids from September 1991 to September 2018. These grids are available at DTU: https://ftp.space.dtu.dk/pub/ARCTIC_SEALEVEL/DTU_TUM_V3_2019/ and at ESA SLBC_CCI: (cci.esa.int/data).

Firstly, the total uncertainty of the SLA product is shown. Secondly, we investigate the spatial trend patterns over the entire Arctic region. Thirdly, we show the averaged inter-annual variability. Fourthly, the SLA is validated against tide gauges.

## 4.1. Uncertainty of the Arctic Sea Level Product

The total uncertainty of the Arctic CCI DTU/TUM sea level product from the bootstrapping is summarized (Figure 4). This is given by the monthly median ranges of the 95% confidence interval (i.e., the median of the SLA range between the percentiles 2.5% and 97.5%) from September 1991 to September 2018. We see larger uncertainties in the interior of the Arctic where permanent and seasonal sea-ice appears with a SLA range 50–60 mm compared to the ice-free regions with a SLA range of 10–20 mm.
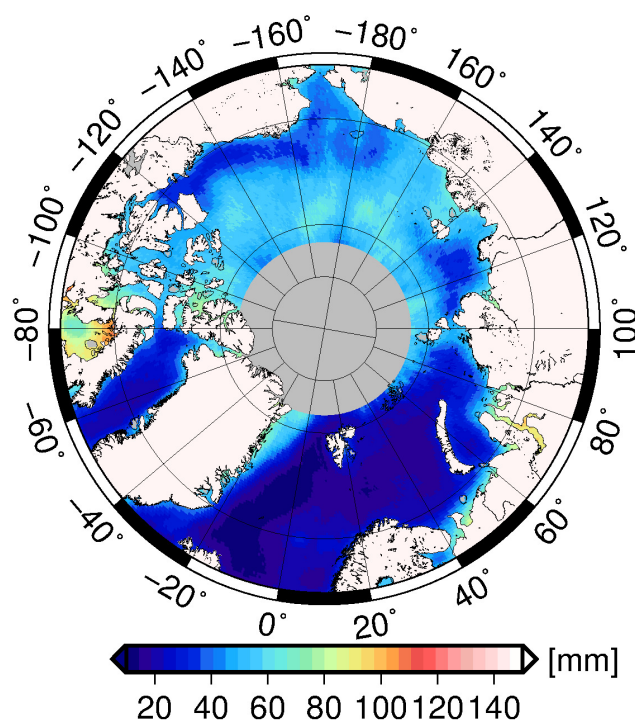
Figure 4. The total uncertainty of SLAs from the bootstrapping, given as the median SLA range between the 2.5% percentile to the 97.5% percentile (i.e., the 95% confidence level interval) of monthly data in the SLA product from September 1991 to September 2018.

4.2. Regional Trends in the ERS-2 to CryoSat-2 Era

We investigate the spatial trend pattern from 65°N to 81.5°N in the entire Arctic Ocean. In Figure 5a the spatial pattern is shown covering the time period from January 1996 to September 2018. Here, the ERS-1 data are dismissed due to too low data distribution in the Eastern sector. Furthermore, all data are eliminated with an interpolation error (from the collocation) above 10 cm. We find a pattern with a high trend >10 mm/year in the Beaufort Gyre, a slightly negative trend or no trend in the Russian sector (−2 to 1 mm/year), trends between 3–7 mm/year in the Barents Sea and in the Fram Strait, and a strong negative trend in the northern Baffin Bay. The regional trend uncertainties are shown as the 2.5% percentile (Figure 5b) and the 97.5% percentile (Figure 5c) corresponding to the 95% confidence level.

(**a**) SLA Trend

(**b**) SLA trend of percentile 2.5%.

(**c**) SLA trend of percentile 97.5%.
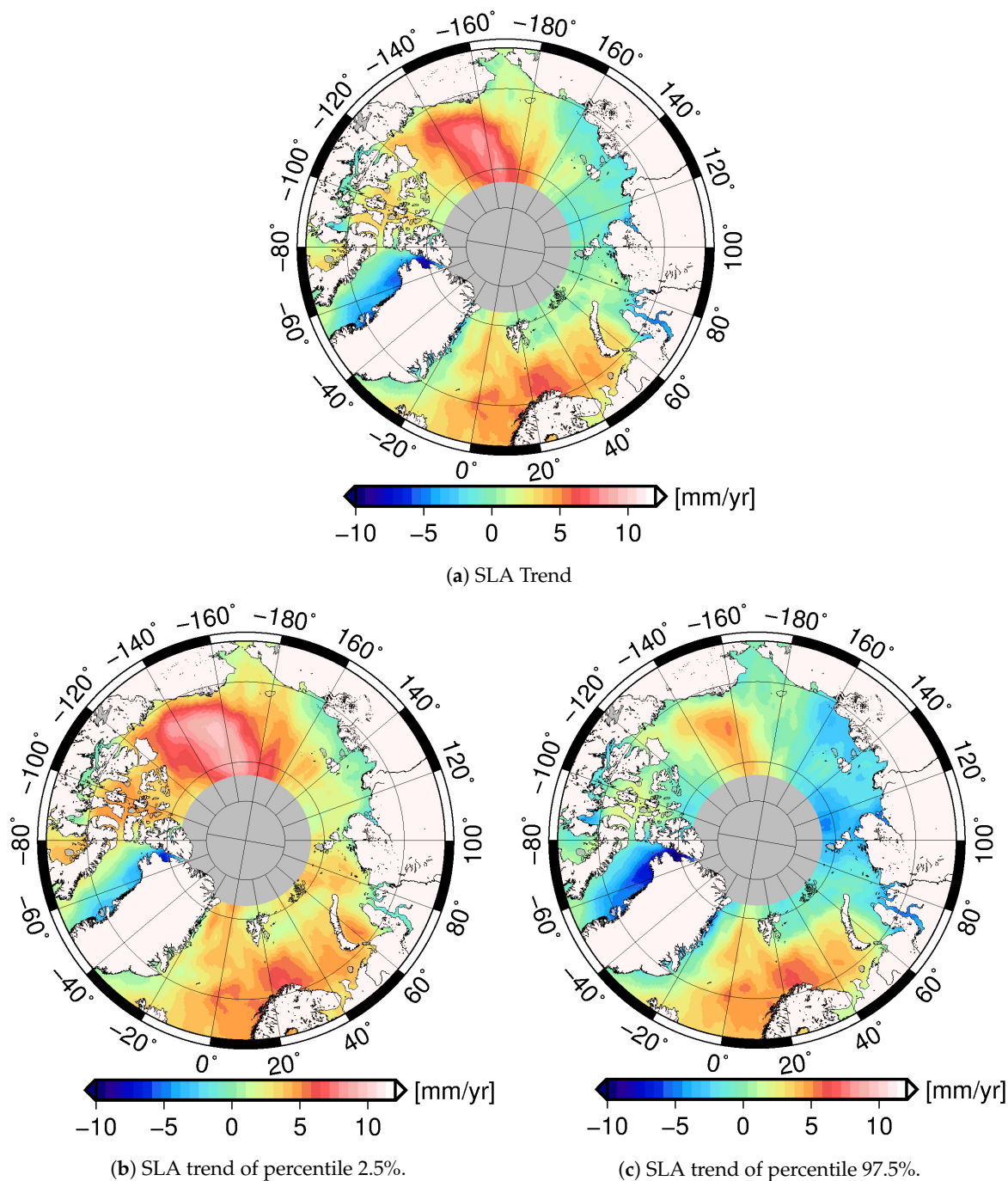
Figure 5. (**a**) The CCI DTU/TUM SLA trends from January 1996 to September 2018 given in mm/year. (**b**,**c**) show the SLA trend uncertainty in the same period. There is found a 95% confidence interval of the SLA trend within (**b**) and (**c**).

4.3. Inter-Annual Variability

The SLA data are averaged for each month with a cosine latitude weighting (Figure 6). The seasonal variability are plotted from September 1991 to September 2018 (27 years) in (Figure 6a) and January 1996 to September 2018 (almost 23 year) in (Figure 6b), respectively. We are investigating the time series with and without ERS-1, because the coverage of the ERS-1 satellite is sparse during periods of time (especially in the ice covered regions), and therefore the time series may be more error prone in this period. Both figures show solutions with and without Glacial Isostatic Ajustment (GIA). The applied GIA model is from Caron et al. [58], which is kindly converted to sea level anomalies and

associated standard deviations by Benjamin D. Gutknecht. Generally, we see a seasonal variability of high sea level in late Autumn and a low sea level in the Spring. Both time series have a positive trend with a sea level rise of 1.54 (1.40) mm/year and 2.22 (2.08) mm/year in the respectively periods with and without (in parenthesis) GIA correction). There is a 95% confidence that data lies within 1.16 (1.01)–1.81 (1.67) mm/year and 1.67 (1.52)–2.54 (2.40) mm/year, respectively.
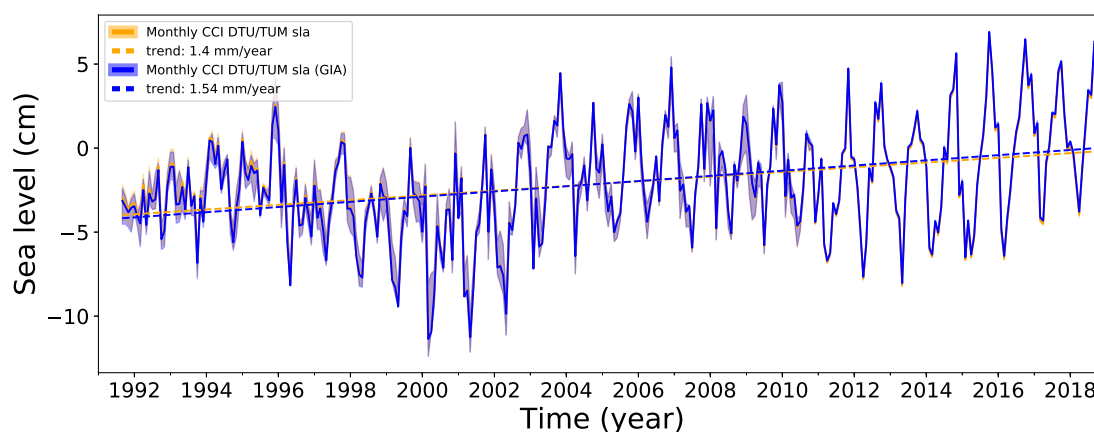
(**a**) Monthly SLA values from September 1991 to September 2018.
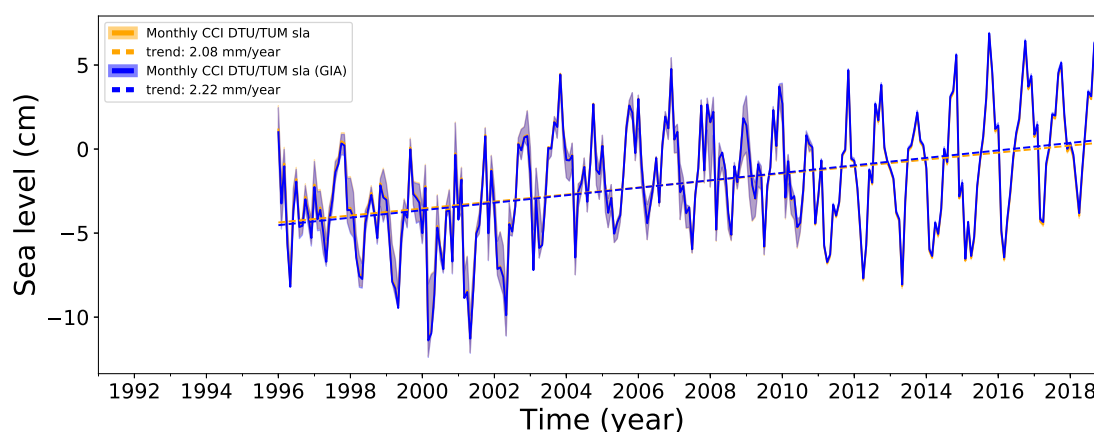
(**b**) Monthly SLA values from January 1996 to September 2018.

Figure 6. Monthly SLA values. (**a**) From September 1991 to September 2018 with a linear trend of 1.54 and 1.40 mm/year with a 95% confidence level of data laying within 1.16 to 1.81 and 1.01 to 1.67 mm/year with and without GIA correction, respectively. (**b**) From January 1996 to September 2018 with a linear trend of 2.22 and 2.08 mm/year with a 95% confidence level of data laying within 1.67 to 2.54 mm/year and 1.52 to 2.40 mm/year with and without GIA correction, respectively. The blue and yellow shadows are the 95% confidence level for measurements with GIA and without GIA, respectively.

The uncertainties expressed in Figure 6 as light yellow (no GIA) and light blue (GIA) shadows are derived by continuing each of the 1000 bootstrap realizations through the same procedure as described in Section 3.6. The uncertainties are given as the median SLA range of the 1000 bootstrap realizations in the 95% confidence level.

4.4. Regional Sea Level Variability

In Figure 7, the CCI DTU/TUM sea level record from 1996–2018 is divided into four sectors (Figure 1). The regional SLAs with and without GIA and the associated uncertainties are summarized in Table 3.

Table 3. SLA trend for each sector and the associated uncertainty. The SLA trend is given with and without GIA correction and the uncertainty is given by a 95% confidence level.

|	SLA Trend (No GIA) mm/year	95% Conf. Level (No GIA) mm/year	SLA (GIA) mm/year	95% Conf. Level (GIA) mm/year
Sector I	3.04	2.96–3.23	3.19	3.10–3.37
Sector II	0.33	−0.58–1.28	0.04	−0.86–1.00
Sector III	4.06	2.41–4.71	5.77	4.12–6.42
Sector IV	0.49	−0.72–1.15	−0.63	−1.84–0.03

Two areas (Sector I (Figure 7a) and III (Figure 7c) have a clear sea level rise in the period. The maximum SLA trend is observed in the Beaufort Gyre (Sector III) up to approximately 10 mm/year. In Sector I (Figure 7a) the highest SLA trend is observed in the southern part towards the Norwegian coast, and smallest along the coast of Greenland and in the upper northeastern part.

Considering the confidence level, Sector II has no or a little positive/negative trend. Sector IV has a positive trend when no GIA is applied, but a negative trend when it is applied. The most negative trend is in the northeastern Baffin Bay of about −10 mm/year. It is unclear if this is due to fresh water flow from the large outlet glaciers or a simple artifact of the LRM to SARIn transition.

(**a**) Sector I

(**b**) Sector II

(**c**) Sector III
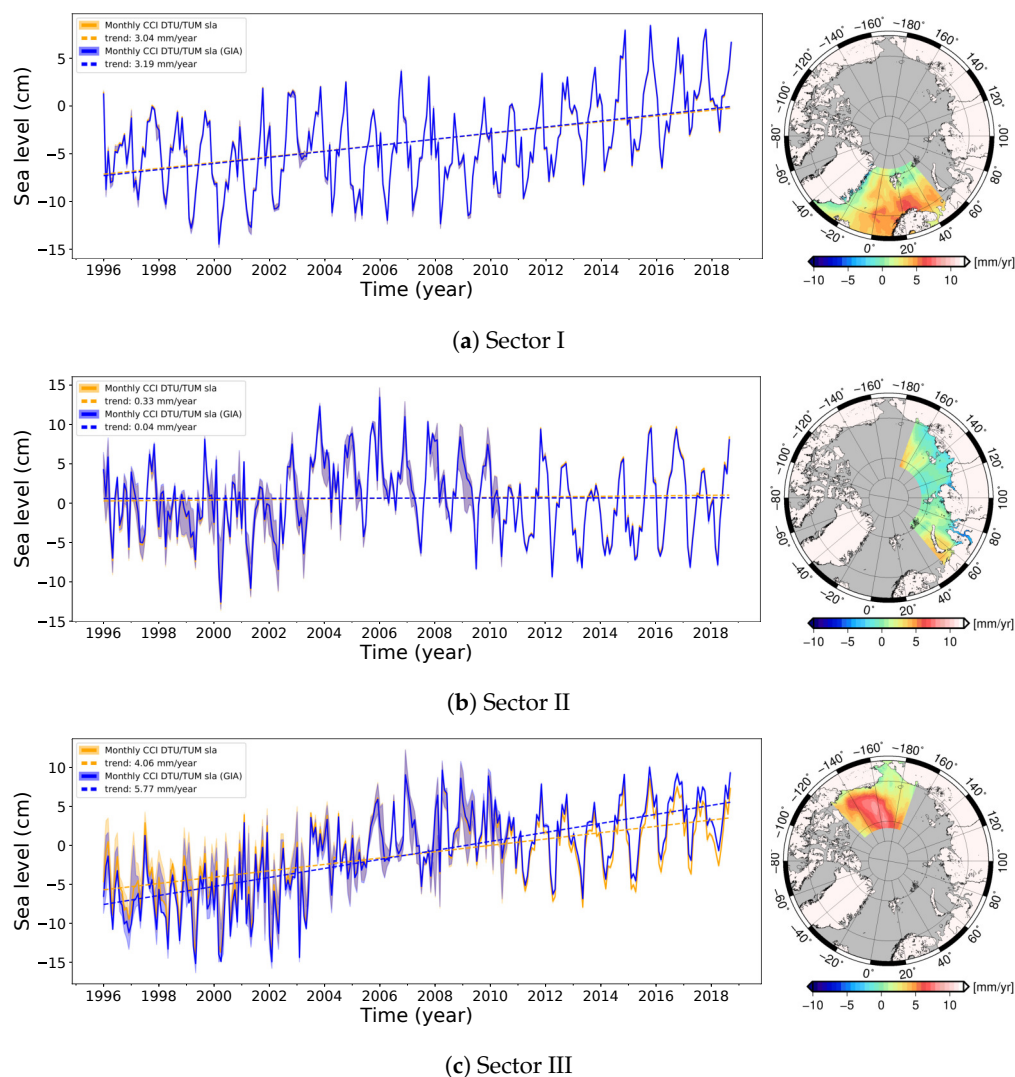
Figure 7. *Cont.*
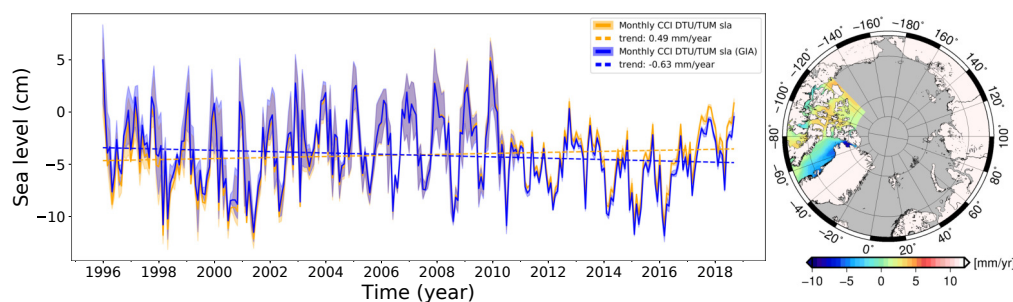
(**d**) Sector IV

Figure 7. Regional changes of sea level in the different sectors shown in Figure 1. Blue is the monthly CCI DTU/TUM SLA in meters and the red line is the estimated trend in mm/year for the given sector. The 95% confidence level is given by the blue and yellow shadows with GIA and without GIA, respectively.

4.5. Validation

Tide gauges (Section 2.3) in the Arctic are sparsely distributed and gauges with long time series are rare. The six tide gauges used in this study (Figure 1) are chosen due to their geographical distribution in the region, their time span covering most possible of the altimetry era and their continuity in time.

The tide gauges are mounted on land and do not account for GIA effects nor the atmospheric loading. Consequently, in the comparison, the atmospheric loading is not applied to the altimetry data. There is a large GIA signal in the Arctic, with large variations over the region, but GIA models are very uncertain [59,60]. The most direct method for determining the local vertical displacement is by GPS measurements. The GPS vertical displacement includes both the GIA and the elastic signal, whereas the elastic displacement comes from present displacements as mass changes from ex. outlet glaciers or ground water depletion. The elastic displacement is very small if the tide gauge is far from the large mass changes. A vertical GPS displacement is provided when available, or else the closest grid point from the Caron et al. [58] GIA model (given with two times standard deviation) is used (See Table 4).

Table 4. Vertical displacement from from GPS and the Caron et al. [58] GIA model.

Tide Gauge	Vert. Disp. mm/year	GIA mm/year
Ny Ålesund	7.98±0.49 [1]	0.47 ± 0.67
Honningsvåg	1.9±0.3 [2]	1.344 ± 0.42
Prudhoe bay	-	−1.51 ± 0.095
Vise Ostrov	-	1.96 ± 0.38
Golomianyi Ostrov	-	1.99 ± 0.33
Sannikova Proliv	-	−0.48 ± 0.21

[1] Obtained dec. 2018 from www.sonel.org [61]; [2] [62].

The results of the comparison between the CCI DTU/TUM Arctic SLA and the tide gauge data are shown in Figure 8 and in Table 5 and described with more details in Appendix D. We are using an inverse distance weighted average of data in a radius of 350 km from the tide gauge station. Using a radius of 350 km is also done in [24].

Figure 8 compares each satellite relative to the tide gauge. The tide gauge is shown with an orange curve, while the altimetry data are shown with different colors depending on the satellite: ERS-1 (red), ERS-2 (blue), Envisat (green) and CryoSat-2 (Grey). Also trend lines for each satellite are shown for both tide gauges and altimetry data. In Figure A2, Appendix D, the total time series is shown together with the corresponding trend line for every tide gauge station. The trend differences between the altimetry and tide gauge data for Sannikova Proliv (Figure A2e) and Prudhoe Bay (Figure A2f) are large.

(**a**)

(**b**)

(**c**)

(**d**)

Figure 8. *Cont.*

(**e**)

(**f**)
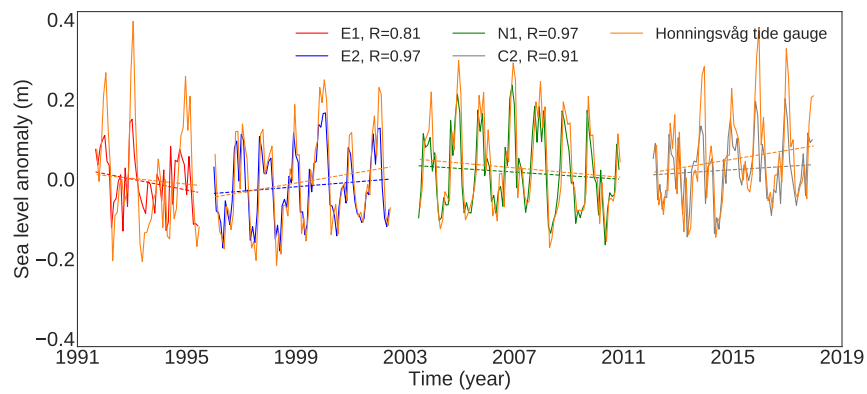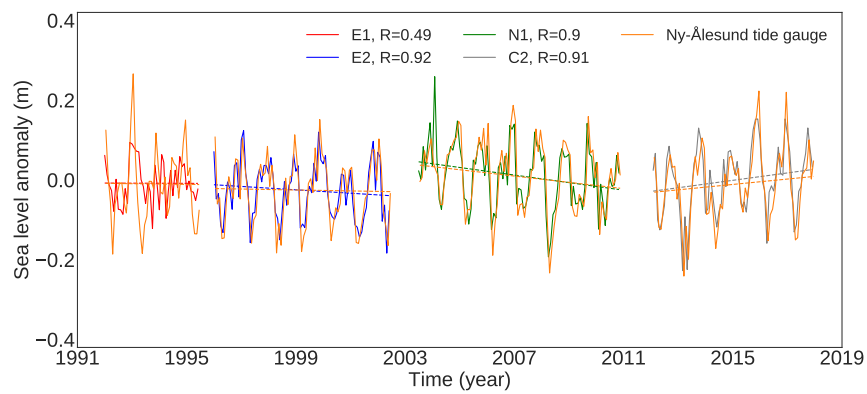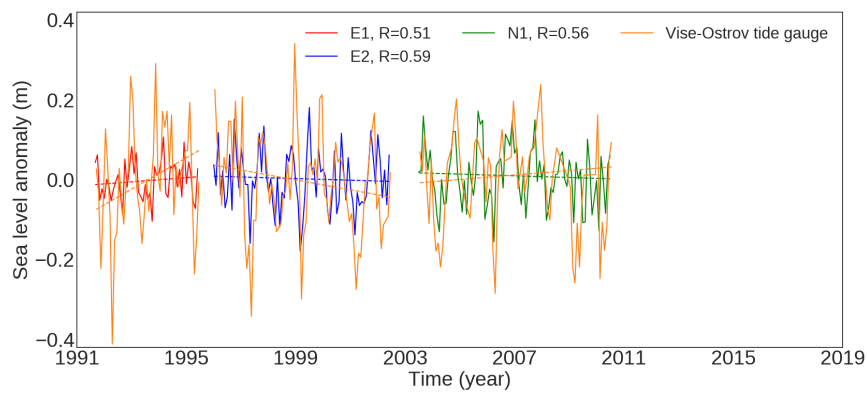
Figure 8. Tide gauge comparison of the six tide gauges for each satellite period, where red (ERS-1), blue (ERS-2), green (Envisat) and grey (CryoSat-2) are the altimetric data and orange is the tide gauge data. The tide gauges are evaluated relative to each individual satellite and accordingly a gap appear in betwee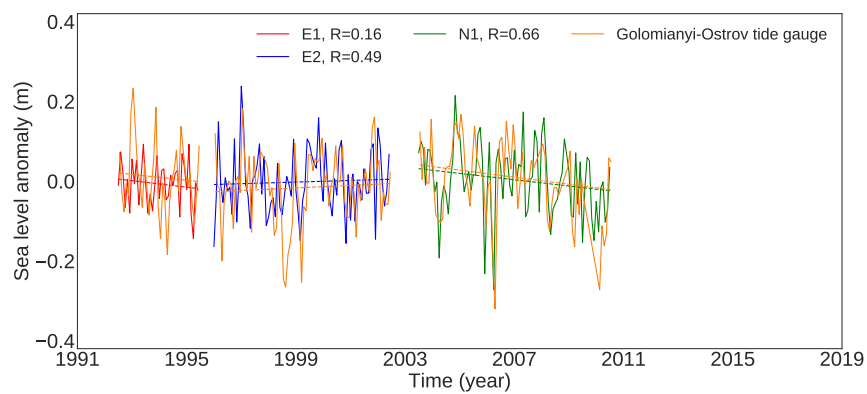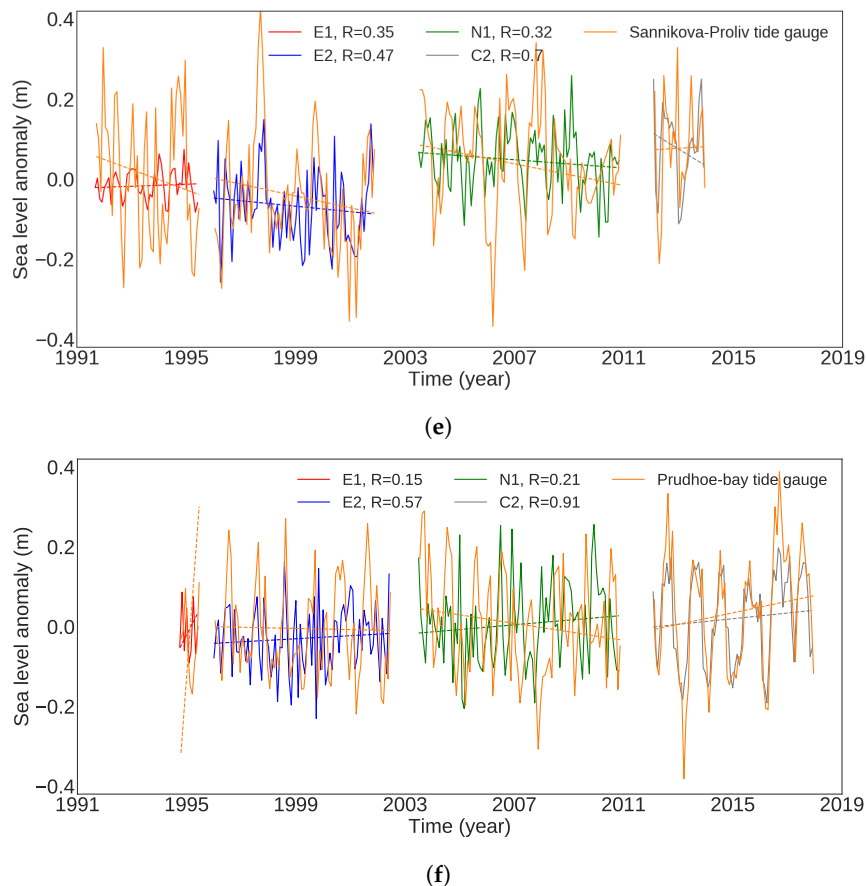n the satellites where data overlaps. Also trend lines are shown on the figures. (**a**) Honningsvåg. (**b**) Ny Ålesund. (**c**) Vise Ostrov. (**d**) Golomianyi Ostrov. (**e**) Sannikova Proliv. (**f**) Prudhoe bay.

Table 5. Tide gauge comparisons. The second column shows the number of months analyzed. The second part of the table summarizes the tide gauge comparison given as the RMSE (in meters) with Persons' correlation coefficient in parenthesis for ERS-1 (E1), ERS-2 (E2), Envisat (N1), CryoSat-2 (C2), before GIA correction, in the period starting from 1996 (without ERS-1) and for the total time period.

Tide Gauges	No. of Month	RMSE (R)						
		E1	**E2**	**N1**	**C2**	**Pre GIA**	**1996–**	**Total**
Ny Ålesund	312	0.080 (0.49)	0.031 (0.92)	0.034 (0.90)	0.038 (0.91)	0.072 (0.70)	0.042 (0.88)	0.050 (0.81)
Honningsvåg	316	0.089 (0.81)	0.037 (0.97)	0.032 (0.97)	0.060 (0.91)	0.057 (0.91)	0.047 (0.94)	0.055 (0.92)
Prudhoe bay	273	0.11 (0.15)	0.099 (0.57)	0.15 (0.20)	0.072 (0.91)	0.12 (0.53)	0.11 (0.57)	0.12 (0.53)
Vise Ostrov	221	0.12 (0.51)	0.10 (0.59)	0.097 (0.55)	-	0.11 (0.52)	0.098 (0.57)	0.10 (0.53)
Golomianyi Ostrov	202	0.099 (0.16)	0.086 (0.49)	0.077 (0.66)	-	0.085 (0.53)	0.081 (0.59)	0.081 (0.53)
Sannikova Proliv	244	0.16 (0.35)	0.13 (0.47)	0.13 (0.32)	0.092 (0.70)	0.14 (0.36)	0.14 (0.37)	0.14 (0.36)

Table 5 summarizes the results of the comparison. The altimetric SLAs are compared for each satellite and for the entire time series available by the Root Mean Square Error (RMSE) and the Persons correlation coefficient. ERS-1 shows a very good correlation for the Honningsvåg tide gauge, where

there is ice free year round and a good data coverage; a good correlation for Ny Ålesund, fair correlation for Vise Ostrov, weak correlation for Sannikova Proliv and no correlation for Golomianyi Ostrov. In the later tide gauges, we know that the ERS-1 data are very sparse and the tide gauges are placed in a region where sea-ice is changing from season to season. There is a better correlation in the Summer data than in the Winter data, where the ocean is ice free. The correlation for ERS-2, Envisat and CryoSat-2 is excellent for Ny Ålesund and Honningsvåg. For Prudehoe Bay in the Canadian sector the results are also good, except for Envisat where we get a correlation of only 0.21. This is due to loss of data in this area in the Envisat period. Data from the Russian sector are generally having a moderate correlation. There are some very large variation in the tide gauge data ($>\pm 0.4$ m), which are not captured by the altimetry. This will be discussed in Section 5.3. In Table 5, the last two columns represent the comparisons for the time series without ERS-1 (1996–) and the total time series with ERS-1 (Total). The results improve when the ERS-1 data are ignored.

5. Discussion

In this section the results are examined and evaluated.

5.1. The SLA Record

ERS-1 was the first radar satellite measuring in the Arctic, and the quality of useful data are sparse, especially in the Beaufort Gyre area. Consequently, several grid cells in this period where empty or close to and therefore not included in the analysis.

It is difficult to assign the quality of the classification in conventional altimetry. In conventional altimetry it is not possible to identify the leads with the same accuracy as in SAR or SARIn. A wrong classification could give a bias with respect to SAR/SARIn. In the transition to SAR/SARIn this could give negative trends and thus an underestimation of the actual Arctic SLA trend. This concern is partly supported by the fact that we generally observe smaller sea level trends in the combined Envisat and CryoSat-2 period compared with the individual Envisat and CryoSat-2 periods and particularly in regions with seasonal sea-ice cover.

In Figure 3, the mean SLA for each satellite were shown. The ice-edge is visible in the subfigures to the East of Svalbard. It is a delicate compromise to keep measurements from conventional satellites in the ice-covered regions or not, as it is impossible to discriminate between reflections from the top of the ice or from leads, causing the average for these satellites to be too high. The chosen PP threshold values may be too loose, but it is a trade-off of either removing some of the signal or getting too many false-positives. We have chosen to go with the second option, and hopefully removing the faulty values in a strict outlier detection. Despite our careful editing, we still find this to be a problem that needs further attention. Getting a more strict PP threshold would lead to areas with very low data coverage, not being able to get a region wide SLA record relaying on data and not only extrapolation. An other option could be to use more advanced classification schemes and machine learning to get a better control of the leads in the sea-ice cover similar to [63–65].

There is an agreement between the four satellites in Figure 3 on positive averaged SLA values in the region (80–82, 0E–100E) north of Svalbard. This might indicate that the DTU18 MSS used to reference the average SLA is too low. CryoSat-2 again shows slightly different signal to the other satellites. This is suspected to be a consequence of the merger of lead data retracked with LARS and open ocean data retracked with RADS. Any discrepancies/offset between these two data sets might cause such a mean signal.

The correlation between ERS-1 and ERS-2 (Figure 2) was moderate. This maybe due to the fact that the ERS-1 satellite's data coverage is poor in both time and space or it could be that the overlapping time period is shorter for this comparison. On the other hand it is very reassuring how well the remaining satellites are matching in the overlapping periods (Figure 2). Especially, it is interesting how well the ERS-2 and Envisat data are correlating when they are processed with the same retracker. Errors in the inter-satellite bias estimation would propagate into the final trend estimation. If the

inter-satellite bias would be wrong, it would also have shown up in the total time series of the tide gauge comparison (See Table 5 and Figure A2 in Appendix D).

Gridded satellite data are very sensitive to the coverage of satellite tracks. In the Arctic, the data distribution is much more dense in the high latitudes when using a constant area grid. Furthermore, the collocation method we are using is very sensitive to missing data and tends to extrapolate data towards zero. Therefore, using this gridding method where there is no or very little data coverage, should be done with caution.

5.2. Error Analysis Evaluation

In order to avoid a troublesome error analysis, where the risk of forgetting some error propagation in the process, a bootstrap analysis was carried out. The advantage with bootstrapping is that we do not need to know all the error sources and the size of the uncertainties. The concern with block bootstrapping is to determine the right block size, such that data are independent. The bootstrap method fails if the blocks are too small and we do not get the right variation of data if the blocks are too large. This was tested on trail and error.

Data were not normal distributed (Appendix C). This means that a normal standard deviation evaluation of the uncertainty is not a proper evaluation. In Figure 6, the 95% confidence level was shown. The uncertainty decreases with time with the largest error in the ERS-1 period and smallest for the CryoSat-2 measurements. This is not surprising with the large improvements in the satellites payload giving more data with higher quality.

There is a higher uncertainty in the interior of the Arctic Ocean, than in areas without permanent or seasonal sea-ice cover (Figure 4). Looking at the standard deviation (not shown here—for comparison only) of the bootstrapping realizations the level is between about 2 cm in the interior and about 5 cm outside. This may indicate, that some data are tracked as sea-ice, but the results look similar to Poisson et al. [65] (only using Envisat data) which get a transition between the open ocean and the interior of the Arctic Ocean of about 2 to 4 cm, and much better than the former DTU data set by Cheng et al. [24].

In Figure 7 (Section 4.4), it is striking how low the uncertainty in Sector I is compared to the other sectors. This is the only area with very good satellite coverage, large areas with no sea-ice year round, and with only a little seasonal sea-ice in the northern parts of the sector. The figures clearly indicate that conventional altimetry in the interior of the Arctic Ocean (Sector II, III, IV) before 2010 is more noisy than SAR altimetry from Cryosat-2.

5.3. Regional and Seasonal Variability

In the Arctic Ocean a sea level rise of 1.54 mm/year with a 95% confidence interval of 1.16–1.81 mm/year from September 1991 to September 2018 is found. Ignoring the ERS-1 data, a linear trend of 2.22 mm/year with a 95% confidence interval of 1.67–2.54 mm/year from January 1996 to September 2018 is found. These results correspond well with other studies: Cheng et al. [24] used reprocessed RADS data to make the Arctic DTU SLA record V2 and found a SLA trend of 2.1 ± 1.3 mm/year in the period 1993–2011. Andersen and Piccioni [26] made an update of the Cheng et al. [24] data and found a trend of 2.2 ± 1.1 mm/year in the period 1993–2015. Both studies used data from the sea-ice cover that was processed with an ocean retracker and sampled to 1 Hz. Prandi et al. [23] made an update to the SSALTO/DUACS product from 1993–2009 and found a higher SLA trend of 3.6 ± 1.3 mm/year, but they have a very low data coverage in the area corresponding to Sector III.

In Figure 9, the SLA trends are derived by cutting the total time series with five years at a time. Up to 2007 we see an almost constant sea level trend around 1–2 mm/year, but an increased trend can be seen after 2004. There is also evidence, that the loss of multi-year ice is stable up to 2007 where after a steepened loss of multi-year ice is seen [66]. Also the Greenland ice sheet did experience an accelerating ice mass loss already from 2004 [67].
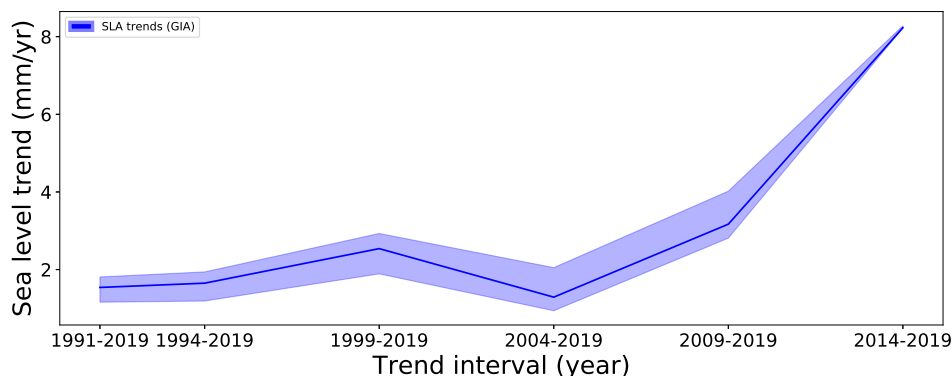
Figure 9. Sea level trends in the CCI DTU/TUM SLA period in steps of eliminating five years at a time. The light blue color shows the 95% confidence interval.

In general, the tide gauges show slightly higher sea level variability than the altimetry data (Figures 8 and A2). However, in a few of the tide gauges we suspect that the combination of seasonal sea-ice cover and the location of the tide gauge in sheltered environment away from the harsh Arctic conditions (i.e., up a river) causes the gauge to measure a signal which is smaller than in the open ocean. The local GIA signal can be large, and in Table 4, for the Ny Ålesund tide gauge, we saw how large the difference between the GPS uplift versus the GIA model could be. We also know [59,60] how uncertain the GIA model can be, so applying the GIA correction can be associated with large errors. Sector II was examined in Section 4.4 (Figure 7), Section 4.5 (Figure 8c–e), Appendix D (Figure A2c–e) and Table 5 and found to be the most difficult sector for the altimetry with the worst correlation to the tide gauges.

Inspecting the seasonal variability for the Arctic Ocean in the different sectors (Figure 7), the mean SLA for each month (1996–2019) is plotted (Figure 10) for the entire Arctic Ocean (All) and for each of the geographical sectors (Sector I to IV). We see a maximum SLA for the entire region in October and a minimum in April. This is similar to [25].

There is a minor difference in the seasonal signal in particularly in Sector IV (Figure 7d) which can be explained from the fact that conventional altimetry did not have that many observations in the Canadian Archipelagos, so the seasonal variation was dominated by the seasonal variation in the Baffin Bay and the Beaufort Gyre. This is not the case with the Cryosat-2 data.
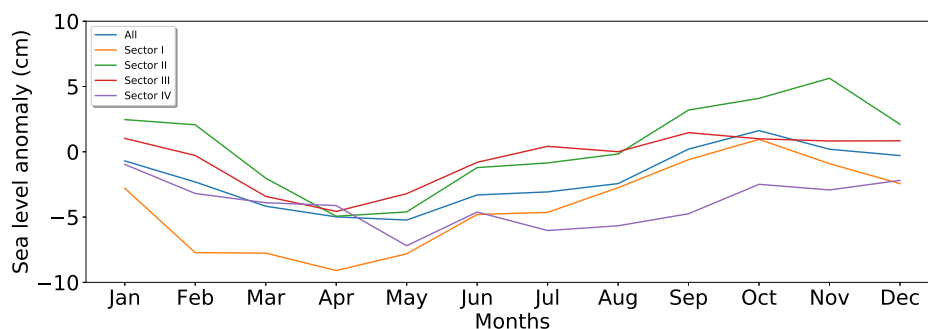
Figure 10. The mean value for all months in the interval 1996–2019 for the entire Arctic Ocean (blue) and the different regions outlined in Figure 1: Sector I (orange), II (green), III (red), IV (purple).

The trend pattern in Sector I (Figure 7a) is similar to other studies [23,24,26] with exceptions of the area near the Greenlandic coast, where [26] has a very high SLA trend. For Sector I, we see a maximum SLA in October and a minimum in April, but as described in Volkov et al. [68], the seasonal minimum and maximum can change within small regions. Volkov et al. [68] studied the causes for the sea level variability in this region. The region was divided into smaller areas, and they found a difference in the maximum amplitude (September to December) depending on the area in question (and minimum

in (March to May)). The Barents Sea had a phase lag of 1–3 months compared to the Norwegian and Greenland Sea. This was due to mass changes caused by wind forcing, a varying bottom topography and dissipation. The annual cycles did not change over different time spans.

Sector II (Figure 7b), the Russian Arctic, has a insignificant trend of 0.04 mm/year with a confidence interval of −0.86–1.00 mm/year. This is a product of negative trends particular in the Laptev Sea and positive trends in the Kara Sea and in the East Siberian Sea. In the period before the satellite era 1954–1989 a trend of 1.85 mm/year was found in the Russian sector from in-situ measurements [69], where also negative trends in the inner Kara Sea and in the Laptev Sea were found. 35% of the sea level rise was determined to originate from the ocean expansion, 30% from the atmospheric pressure, 10% from wind forcing and about 25% from increasing ocean mass from melting land ice. A more recent study by Henry et al. [17] covering 1950–2009, also using in-situ observations agrees on these observations. Furthermore, they studied the GIA effect and found that the GIA signal is large in this region and models do not agree well. We do not see the large GIA signal in Figure 7b, but we are looking at a much larger area, where the local effects can vary a lot (see ex. Table 4). The annual SLA variation (Figure 10, green curve) is highest in November and lowest in April.

Sector III (Figure 7c), the Beaufort Gyre region, is the sector with the largest trend (5.77 mm/year with confidence interval 4.12–6.42 mm/year) and with a local maximum trend of 8.45 mm/year. The large trend is due to increasing fresh water accumulation caused by anti-cyclonic winds and Ekman transport [70,71]. There is evidence that the Beaufort Gyre SLA trend has decreased from 1995 to 2003 (−5.9 ± 1.3 mm/year) and steepened from 2003 to 2011 (18.8 ± 0.9 mm/year) [71]. The steepening could also be visible in Figure 7b. Our maximum is smaller, but we are also looking at a different time interval and a larger geographical region. This region has a maximum annual SLA peak (Figure 10, red curve) already in September, a second peak in July and a minimum in April. In a study using moorings [70] from 2003–2007, the authors also find a seasonal cycle with two maximums in June–July and in November–January. They explain the two maximums as originating from the largest yearly sea-ice melt and from the largest wind curl when the salt from sea-ice formation has not jet reached its highest level. Armitage et al. [25] have also studied this area, and evaluated the steric height from 2003–2014. They found a maximum in November, a second peak in June and a minimum in May. This is shifted compared to this study, but it is seen before [68] that the steric and altimetric height not necessarily have the same annual cycle. The GIA effect in this area is large (Figure 7b).

Sector IV (Figure 7d), is an area with very different conditions, having both the archipelagos and the flow through the Baffin Bay. In the archipelagos there are few observations from conventional altimetry. The main signal comes from the Baffin Bay and the CryoSat-2 satellite. There is a seasonal SLA peak in January and a low in May (Figure 10, purple). It is also a region with high GIA values, probable due to melt from the large outlet glaciers in the area. The trend pattern is similar to Carret et al. [72].

6. Conclusions

The Arctic Ocean is warming faster than ever, nevertheless the Polar Oceans are not included in global sea level studies due to the uniqueness of the regions and with the associated large errors. In this study, we have presented the CCI DTU/TUM Arctic SLA record including data from four ESA radar altimeter satellites, which is (to current date) the longest time series available. We have carefully combined data from different processings including L2 measurements and state-of-the-art retracking. This can be troublesome, and a lot of cautions have to be taken in combining different time series. Data are validated against six tide gauges spread along the coast in the Arctic Ocean. We found a very good correlation of data in the Fram Strait and a less good correlation in the Russian Arctic due to a bad data coverage. The GIA estimation is uncertain, but when applying the correction, the sea level rise gets larger. A sea level rise of 1.54 mm/year with a 95% confidence interval of 1.16–1.81 mm/year is found in the total time period from September 1991 to September 2018. Ignoring the ERS-1 data and looking

at the period from 1996 to 2018, we get a linear trend of 2.22 mm/year with a 95% confidence interval of 1.67–2.54 mm/year. We handled the troublesome error analysis by a bootstrapping method allowing us to get an uncertainty estimate without keeping track of all the uncertainties in the processing chain.

The trends are associated with relatively large uncertainties. Our trends are likely underestimated in the ice-covered regions of the Arctic, which is a combination of several factors currently under investigation. We had to be tolerant in the editing of the conventional altimetry data in order to get data at all during the ERS-1/ERS-2/Envisat period. The risk is here, that we allow for reflections from the top of the ice, biasing the first part of the time series too high. Vice versa the SAR altimetry from Cryosat-2 over the sea-ice cover is also associated with uncertainties, because we only have SAR data and not SARIn data. This way we are unable to detect off-nadir reflections, which will cause the sea level estimate to be too low in the last part of the time series, and hence the estimated trend will be too low. This could also explain why the altimeteric trend for several stations north of Russia were lower than that observed at the tide gauge.

In several of our results we do seem to see small effects (i.e., Figure 3) related to the behavior of the retracker in the presence of partly to full sea-ice coverage. Biases between data sets processed from different missions and retrackers shall be resolved by cross-calibration, as shown in this study. For Cryosat-2 the merger between RADS used in the open ocean and LARS (in-house gaussian retracker) used in the sea-ice seems to result in smaller seasonal SSH effects. The latter effect is particularly hard to tackle as the data are disjoint to each other. This is currently work in-progress to improve the consistency among the different retrackers.

Monthly gridded SLA maps from September 1991 to September 2018 is available at https://ftp.space.dtu.dk/pub/ARCTIC_SEALEVEL/DTU_TUM_V3_2019/ and at ESA SL_CCI (cci.esa.int/data).

Abbreviations

The following abbreviations are used in this manuscript:

ALES	Adaptive Leading Edge Subwaveform
AO	Arctic Oscillation
DAC	Dynamic Atmosphere Correction
DTU	Technical University of Denmark
ECMWF	European Centre for Medium-Range Weather Forecasts
ESA	European Space Agency
ERS	European Remote Senesing satellite
GIA	Glacial Isostatic Ajustment
IBE	Inverse Barometer Effect
IPCC	Intergovernmental Panel on Climate Change
LRM	Low Resolution Mode
MAD	MediAn Deviation
MSS	Mean Sea Surface
PP	Pulse Peakiness
PSMSL	Permanent Service for Mean Sea Level
RADS	Radar Altimetry Database System

REAPER　　　　　Reprocessing of Altimeter Product for ERS
SSH　　　　　　　Sea Surface Height
SAR　　　　　　　Synthetic Aperture Radar
SARIn　　　　　　SAR Interferometry
SGDR　　　　　　Sensor Geophysical Data
SLA　　　　　　　Sea Level Anomaly
SLBC_CCI　　　　Sea Level Budget Closure Climate Change Initiative
SL_CCI　　　　　 Sea Level Climate Change Initiative
TUM　　　　　　　Technical University of Munich

Appendix A. Satellite Specific Processing Details

Appendix A.1. ERS-1

ERS-1 was launched in July 1991 carrying among other instruments a pulse-limited single frequency K_u band (13.8 GHz) Radar Altimeter (RA). RA measured with a footprint of 16–20 km spatial resolution and with an accuracy of 10 cm over the ocean. It was the first Earth observing ESA satellite with a Sun-synchronous polar orbit (inclination: 98.52°) allowing measurements up to about 81.5°. ERS-1 had a repeat cycle of: 3-days, 35-days and 176-days. The mission failed in March 2000, but already in 1996 the ERS-2 satellite (launched April 1995) took over the operational services [73]. For ERS-1 we use the Reprocessing of Altimeter Products for ERS (REAPER) [34] L2 data set.

There are known orbital errors for the ERS satellites as a consequence of lacking accuracy of gravity data and International Terrestrial Reference Frame (ITRF) realizations. It was found necessary to correct for orbital errors even though one of the REAPER project scopes was to make a better orbit solution [34]. For ERS-1, we use a orbit correction scheme similar to [74], described in more details in Cheng et al. [24]. This study is deviating from [74] by not aligning data to the TOPEX/Jason-1/2 SLA because the coverage of the satellites only reached up to 66°N. To get rid of the most noisy measurements, abnormal outliers (>10 m) are removed and a median deviation (MAD) outlier detection is applied to each track before further analysis.

Appendix A.2. ERS-2

ERS-2 was launched in the same orbital plan as ERS-1, but with a one day lag allowing for tandem measurements. ERS-2 was launched with almost identical instruments as ERS-1 with a few improvements. ERS-2 was sending valuable measurements back to the ground station till June 2003 and failed entirely in 2011 [73]. For ERS-2 we use the ESA Sensor Geophysical Data Records (SGDR) of ERS-2 REAPER [34] covering the period from September 1995 to July 2003.

Appendix A.3. Envisat

Envisat is ERS-2's successor. It was launched in March 2002, as the largest ever built satellite with 10 different instruments aboard. ESA lost contact to Envisat in May 2012. The radar altimeter on-board (RA-2) was a pulse-limited dual-frequency radar operating in the K_u (13.575 GHz) band and S bands. Only the K_u band is used here. The spatial resolution is 2–10 km [11] with an accuracy better than 4.5 cm. The satellite's turning latitude was 82° [73]. Envisat had a repeat cycle of 35-days [73]. The SGDR Envisat version 2.1 is used. For Envisat the entire duration of the phase 2 (May 2002—October 2010) and phase 3 (November 2010–May 2012) is used.

The ERS-2 and Envisat satellites are processed with the ALES+ retracker [35]. It is an upgraded version of the Adaptive Leading Edge Subwaveform (ALES) Retracker [75] that is a retracker adapted to coastal ocean areas, without lowering the quality of the results in the open ocean. ALES+ is developed to improve retrievals of peaky waveforms such as echos from leads in the sea-ice cover. Particularly, one large advantage of this retracker is the seamless transitions between leads and open ocean waveforms. For unknown reasons data is missing in ERS-2 covering the weeks: 15 April 2000 to 7 May 2000, 2 July 2000 to 9 July 2000, 21 January 2001 to 4 February 2001,

10 March 2002 to 17 March 2002. For Envisat data are missing in the weeks: 16 March 2003 to 23 March 2003 and 22 March 2011 to 29 March 2011.

Appendix A.4. CryoSat-2

Cryosat-2 was launched on April 2010 and is still active. CryoSat-2 is a dedicated cryosphere satellite with a coverage up to 88° latitude measuring more of the Arctic than ever before. It has a 369-day repeat cycle. The main instrument of CryoSat-2 is the K_u (13.6 GHz) band SIRAL-2 (SAR/Interferometric Radar Altimeter-2). SIRAL is able to measure in one of three modes; LRM over ocean and flat surfaces such as the interior of the ice sheets; SAR mode mainly over sea-ice covered ocean; SARIn over steep terrain and coastal areas. We will be using data from all three modes. The conventional LRM is a pulse-limited footprint, in SAR mode the Doppler principle results in a narrow along-track footprint which can be seen as a beam-limited footprint. The SARIn mode utilizes the two antennas on CryoSat-2 forming an across-track interferometer. The echoes received by each antenna undergo Doppler beam processing as in SAR mode, but the number of waveforms averaged is lower due to the longer interval between the bursts. Processing with multi-looks results in a waveform with a more sharpened leading edge and stronger peak power [73]. For SAR and SARIn baseline C Ice level 1B data are used.

The CryoSat-2 data contains LRM, SAR and SARIn. For LRM and SAR the 1 hz Radar Altimetry Database System (RADS) [38] are used. The specular lead returns from the 20 hz SAR and SARIn are retracked using the Lars Advanced Retracking System (LARS) [37] using a Gaussian fitting routine similar to [13]. Off-nadir SARIn data are processed as SAR data. For unknown reasons almost one month of SAR/SARIn data is missing from 12 August 2010 to 16 September 2010.

Appendix B. The Ice Concentration Grid

In each ice concentration (Section 2.2) grid cell a percentage of the ice concentration is given. A threshold greater than 15% is defined as a cell with sea-ice, and if the cell is below 15% the cell is classified as open ocean. The ice concentration masks are also used to remove CryoSat-2 RADS data from the ice cover, such that the RADS data is only used over the open ocean.

Every satellite point is tracked in the sea-ice concentration grid and evaluated in terms of its location with respect to the sea-ice cover. The satellite coordinate is tracked by a *k*-dimensional (kd)-tree for quick nearest-neighbor lookup for the closest coordinate.

Appendix C. SLA Distributions and Uncertainty Estimates

For each monthly data set, 1000 new bootstrap realizations are generated by splitting data in *n* non-overlapping blocks as done in the making of the SLA (Section 3.6). The bootstrapping blocks need to be independent from each other, hence the size of the blocks was tested. This test was done as a trial and error. When the block sizes were too small the bootstrapping failed. Furthermore, it was a wish to get so much variation in the data as possible, hence the block size should be as small as possible. The final block sizes are three times the size of the first averaging i.e., $0.6° \times 0.6°$ in the latitude and longitude direction. The bootstrapping is carried out by randomly drawing *n* blocks with replacements from the SLA data set. In practice, this means that some blocks are appearing more times and some are not represented at all. For each monthly grid cell, for all 1000 bootstrap realizations, a new SLA is calculated as done in the previous section, and a 95% confidence level is estimated for every grid cell.

The SLAs in each grid cell in the Arctic Ocean is not normal distributed. Figure A1 shows the monthly SLA distribution of the median of the 1000 bootstrap realizations for selected grid cells distributed in the Arctic Ocean. It is only valid to show results with a standard deviation if the results are normal distributed. The Arctic SLA distributions are not normal distributed for all grid cells in the Arctic Ocean, therefore the uncertainty is expressed in a 95% confidence level. This was also verified by q-q plots (not shown here). Therefor we use 95% confidence level as the uncertainty estimate.
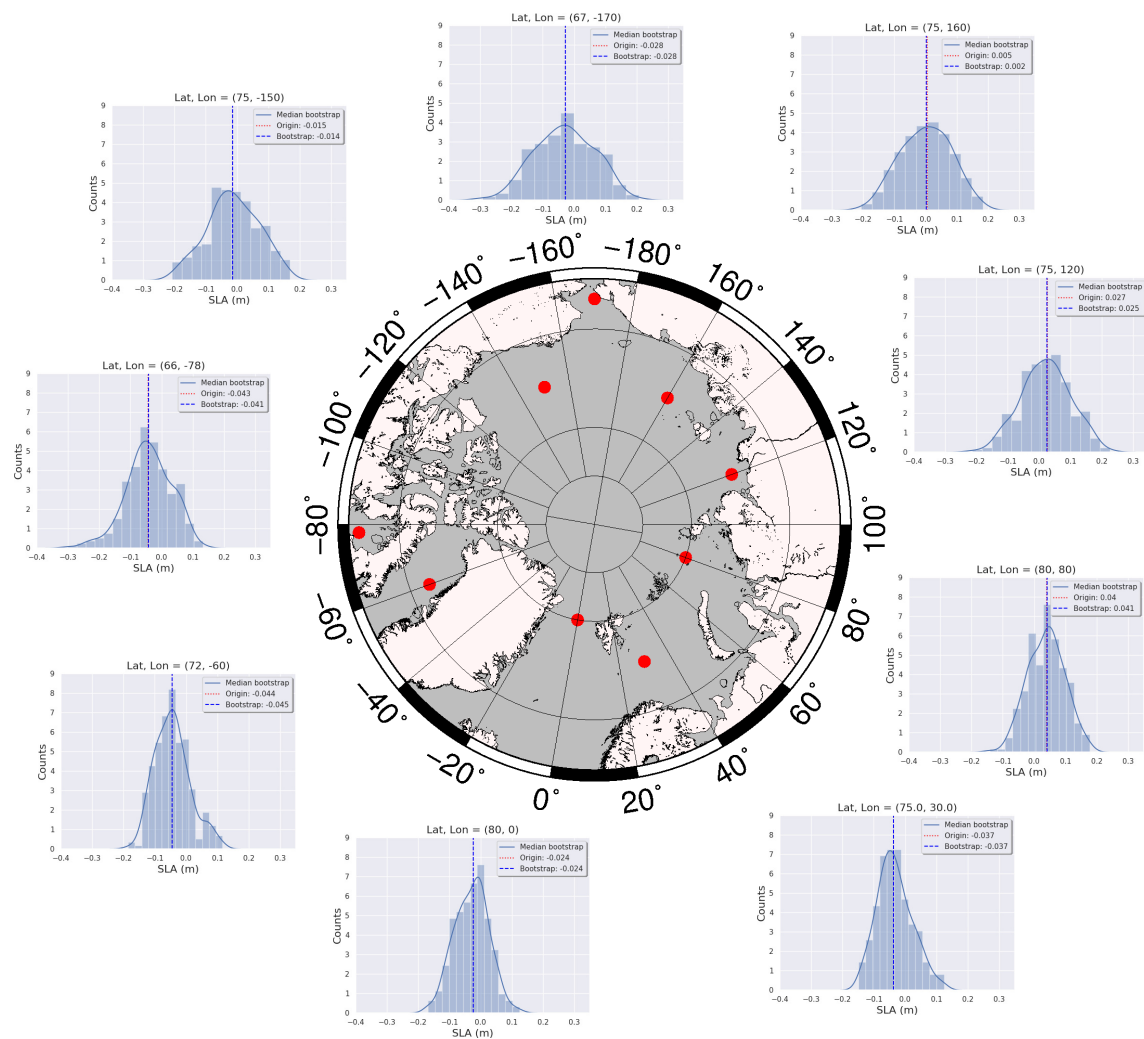
Figure A1. Examples of median bootstrap SLA distribution from January 1991 to September 2018 for various grid points. The vertical lines represent the median of the original SLA (red) and the median bootstrap realizations (blue).
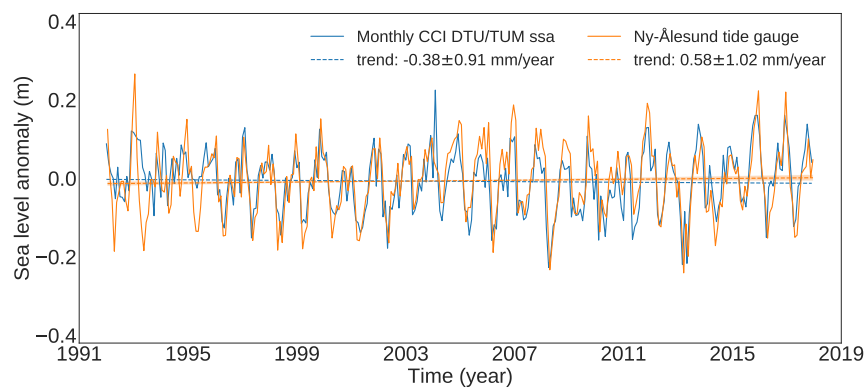
Appendix D. Tide Gauge Comparison

The altimetry data were average with a radius of 350 km around te tide gauge with an inverse distance weighted function. Various radii around the tide gauges and a simple median average were tested, but this method showed the best results for the overall result. For all tide gauges, except for Ny Ålesund, the inverse distance weighting of data (not shown) improves the results. This may indicate that there is control of the outliers. The reason why Ny Ålesund does not improve by the inverse distance weighting, could be due to the fact that the tide gauge is situated on an island, where there are a lot of coastal area with many fjords. To make this point stronger it is also ERS-1 and ERS-2 that suffer the most when doing the weighted mean. The worse performance of ERS-1 and ERS-2 near the coast are due to the lower pulse repetition frequency of the satellites. A simple median average of the data would give a better solution in areas with little data ex. for ERS-1 and in the Russian Arctic. The amplitude of the altimeter data gets larger for the weighted solution and also the trends get closer. The tide gauge in the Laptev Sea (Sannikova Proliv) performs best when eliminating data with an interpolation error >0.10 (not shown). This is normal an indicator of missing or very low data coverage.
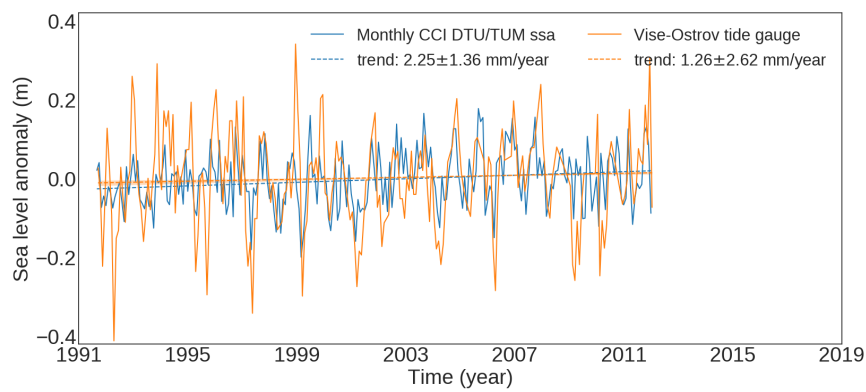
In Figure A2 the total altimetry time series (blue) within 350 km of the tide gauge is compared with the tide gauge data (orange). Also the trend lines are shown and the different trends are written in the figure caption. The uncertainties are given by three times the standard deviation.
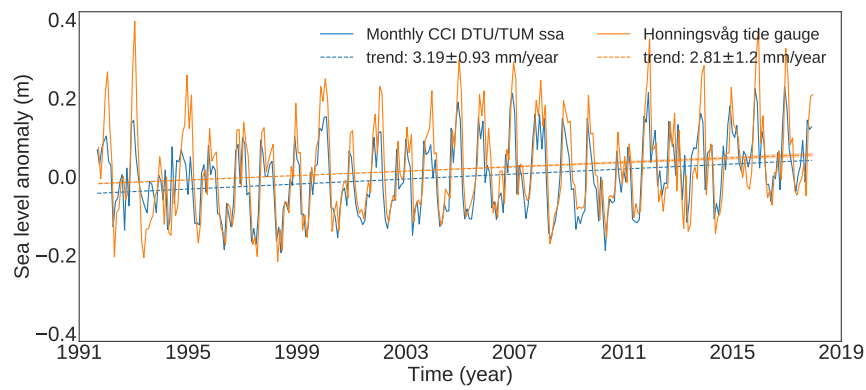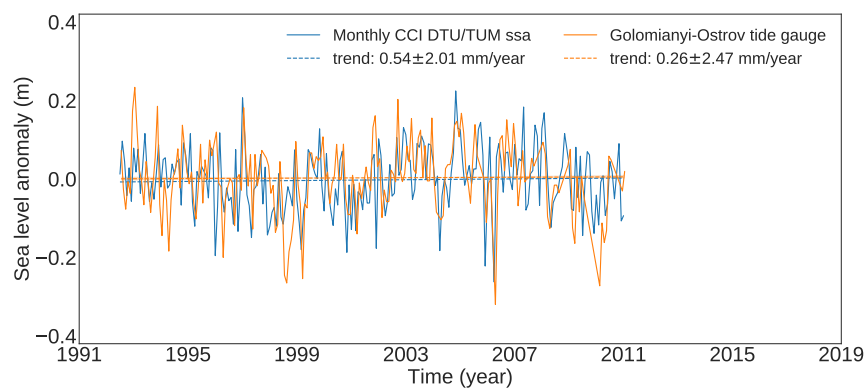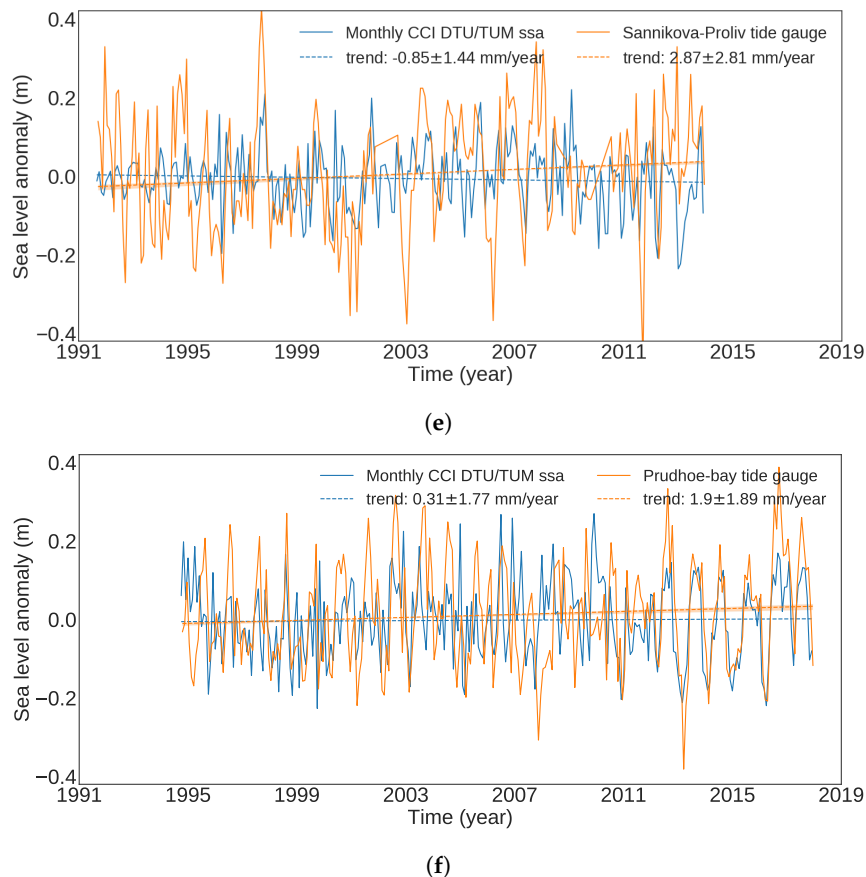
(**a**)

(**b**)

(**c**)

(**d**)

Figure A2. *Cont.*

(**e**)

(**f**)

Figure A2. Tide gauge comparison of the continued altimetry time series from the six tide gauges in the period from 1991 to 2019, where blue is the altimetry data and orange is the tide gauge data. The vertical lines are the trend lines colored like the time series. The various trends are written in the captions. (**a**) Honningsvåg. (**b**) Ny Ålesund. (**c**) Vise Ostrov.(**d**) Golomianyi Ostrov.(**e**) Sannikova Proliv.(**f**) Prudhoe bay.

References

1. Serreze, M.C.; Stroeve, J.C. Arctic sea ice trends, variability and implications for seasonal ice forecasting. *Philos. Trans. R. Soc. A Math. Phys. Eng. Sci.* **2015**, *373*, 20140159.

2. Church, J.; Clark, P.; Cazenave, A.; Gregory, J.; Jevrejeva, S.; Levermann, A.; Merrifield, M.; Milne, G.; Nerem, R.; Nunn, P.; et al. Sea level change. In *Climate Change 2013: The Physical Science Basis*; Contribution of Working Group I to the Fifth Assessment Report of the Intergovernmental Panel on Climate Change; PM Cambridge University Press: Cambridge, UK , 2013; pp. 1137–1216, doi:10.1017/CB09781107415315.026.

3. Wigley, T.M.L.; Raper, S.C.B. Thermal expansion of sea water associated with global warming. *Nature* **1987**, *330*, 127–131, doi:10.1038/330127a0.

4. Cheng, L.; Abraham, J.; Hausfather, Z.; Trenberth, K.E. How fast are the oceans warming? *Science* **2019**, *363*, 128–129, doi:10.1126/science.aav7619.

5. Lettenmaier, D.; Milly, P. Land waters and sea level. *Nat. Geosci.* **2009**, *2*, 452–454, doi:10.1038/ngeo567.

6. Rignot, E.; Velicogna, I.; Van Den Broeke, M.R.; Monaghan, A.; Lenaerts, J. Acceleration of the contribution of the Greenland and Antarctic ice sheets to sea level rise. *Geophys. Res. Lett.* **2011**, *38*, 1–5, doi:10.1029/2011GL046583.

7. Moon, T.; Joughin, I.; Smith, B.; Howat, I. 21st-century evolution of Greenland outlet glacier velocities. *Science* **2012**, *336*, 576–578, doi:10.1126/science.1219985.

8. Yang, Q.; Dixon, T.H.; Myers, P.G.; Bonin, J.; Chambers, D.; van den Broeke, M.R. Recent increases in Arctic freshwater flux affects Labrador Sea convection and Atlantic overturning circulation. *Nat. Commun.* **2016**, *7*, 10525, doi:10.1038/ncomms10525.

9.   Ricker, R.; Hendricks, S.; Beckers, J.F. The impact of geophysical corrections on sea-ice freeboard retrieved from satellite altimetry. *Remote Sens.* **2016**, *8*, 317, doi:10.3390/rs8040317.

10. Fetterer, F.M.; Drinkwater, M.R.; Jezek, K.C.; Laxon, S.W.; Onstott, R.G. Sea ice altimetry. In *Microwave Remote Sensing of Sea Ice*; Carsey, F.D., Ed.; DTIC Document; American Geophysical Union: Washington, DC, USA,1992.

11. Connor, L.N.; Laxon, S.W.; Ridout, A.L.; Krabill, W.B.; McAdoo, D.C. Comparison of Envisat radar and airborne laser altimeter measurements over Arctic sea ice. *Remote Sens. Environ.* **2009**, *113*, 563–570.

12. Chelton, D.B.; McCabe, P.J. A review of satellite altimeter measurement of sea surface wind speed: With a proposed new algorithm. *J. Geophys. Res.* **1985**, *90*, 4707, doi:10.1029/JC090iC03p04707.

13. Armitage, T.; Davidson, M. Using the Interferometric Capabilities of the ESA CryoSat-2 Mission to Improve the Accuracy of Sea Ice Freeboard Retrievals. *IEEE Trans. Geosci. Remote Sens.* **2013**, *52*, 529–536.

14. Stammer, D.; Ray, R.D.; Andersen, O.B.; Arbic, B.K.; Bosch, W.; Carrère, L.; Cheng, Y.; Chinn, D.S.; Dushaw, B.D.; Egbert, G.D.; et al. Reviews of Geophysics Accuracy assessment of global barotropic ocean tide models. *Rev. Geophys.* **2014**, *52*, 243–282, doi:10.1002/2014RG000450.Received.

15. Scharroo, R.; Visser, P. Precise orbit determination and gravity field improvement for the ERS satellites. *J. Geophys. Res. Ocean.* **1998**, *103*, 8113–8127, doi:10.1029/97JC03179.

16. Perovich, D.K.; Tucker, W.B.; Eicken, H.; Tucker, W.B.; Perovich, D.K. Indirect measurements of the mass balance of summer Arctic sea ice with an electromagnetic induction technique. *Ann. Glaciol.* **2001**, *33*, 194–200.

17. Henry, O.; Prandi, P.; Llovel, W.; Cazenave, A.; Jevrejeva, S.; Stammer, D.; Meyssignac, B.; Koldunov, N. Tide gauge-based sea level variations since 1950 along the Norwegian and Russian coasts of the Arctic Ocean: Contribution of the steric and mass components. *J. Geophys. Res. Ocean.* **2012**, *117*, 1–23, doi:10.1029/2011JC007706.

18. Rose, S.; Skourup, H.; Forsberg, R. Arctic tides from GPS on sea-ice. *J. Geodyn.* **2013**, *63*, doi:10.1016/j.jog.2012.09.002.

19. Cazenave, A.; Lombard, A.; Llovel, W. Present-day sea level rise: A synthesis. *C. R. Geosci.* **2008**, *340*, 761–770, doi:10.1016/j.crte.2008.07.008.

20. Laxon, S.; Peacock, N.; Smith, D. High interannual variability of sea ice thickness in the Arctic region. *Nature* **2003**, *425*, 947–950. doi:10.1038/nature02063.1.

21. Laxon, S.W.; MacAdoo, D. Arctic ocean gravity field derived from ERS-1 Satellite Altimetry. *Science* **1994**, *265*, 621–624.

22. Peacock, N.R.; Laxon, S.W. Sea surface height determination in the Arctic Ocean from ERS altimetry. *J. Geophys. Res.* **2004**, *109*, C07001, doi:10.1029/2001JC001026.

23. Prandi, P.; Ablain, M.; Cazenave, A.; Picot, N. A New Estimation of Mean Sea Level in the Arctic Ocean from Satellite Altimetry. *Mar. Geod.* **2012**, *35*, 61–81, doi:10.1080/01490419.2012.718222.

24. Cheng, Y.; Andersen, O.B.; Knudsen, P. An Improved 20-Year Arctic Ocean Altimetric Sea Level Data Record. *Mar. Geod.* **2015**, *38*, 146–162, doi:10.1080/01490419.2014.954087.

25. Armitage, T.W.K.; Bacon, S.; Ridout, A.L.; Thomas, S.F.; Aksenov, Y.; Wingham, D.J. Arctic sea surface height variability and change from satellite radar altimetry and GRACE, 2003–2014. *J. Geophys. Res. Ocean.* **2016**, *121*, 4303–4322, doi:10.1002/2015JC011579.

26. Andersen, O.B.; Piccioni, G. Recent Arctic Sea Level Variations from Satellites. *Front. Mar. Sci.* **2016**, *3*, 76, doi:10.3389/fmars.2016.00076.

27. Schaeffer, P.; Faugére, Y.; Legeais, J.F.; Ollivier, A.; Guinle, T.; Picot, N. The CNES_CLS11 Global Mean Sea Surface Computed from 16 Years of Satellite Altimeter Data. *Mar. Geod.* **2012**, *35*, 3–19, doi:10.1080/01490419.2012.718231.

28. Andersen, O.B.; Knudsen, P. DNSC08 mean sea surface and mean dynamic topography models. *J. Geophys. Res. Ocean.* **2009**, *114*, 1–12, doi:10.1029/2008JC005179.

29. EUMETSAT. *EUMETSAT Ocean and Sea Ice Satelite Application Facility. Global Sea Ice Concentration Continuous Reprocessing Online Product*; Norwegian and Danish Meteorological: Darmstadt, Germany, 2018.

30. EUMETSAT. *EUMETSAT Ocean and Sea Ice Satellite Application Facility. Global Sea Ice Concentration Climate Data Record 1979–2015 (v2.0, 2017)*; Norwegian and Danish Meteorological Institutes: Darmstadt, Germany, 2017.

31. Holgate, S.J.; Matthews, A.; Woodworth, P.L.; Rickards, L.J.; Tamisiea, M.E.; Bradshaw, E.; Foden, P.R.; Gordon, K.M.; Jevrejeva, S.; Pugh, J. New Data Systems and Products at the Permanent Service for Mean Sea Level. *J. Coast. Res.* **2013**, *288*, 493–504, doi:10.2112/JCOASTRES-D-12-00175.1.

32. PSML. Permanent Service for Mean Sea Level, Tide Gauge Data. Available online: http://www.psmsl.org/data/obtain (accessed on 20 December 2018).

33. European Space Agency (ESA); University College London (UCL). *CryoSat Product Handbook*; Technical Report; ESRIN-ESA and Mullard Space Science Laboratory—University College London: London, UK, 2013.

34. Gilbert, L.; Baker, S.; Dolding, C.; Vernier, A.; Brockley, D.; Martinez, B.; Gaudelli, J. REAPER Product Handbook for ERS Altimetry Reprocessed Products. Available online: https://earth.esa.int/web/guest/document-library/browse-document-library/-/article/reaper-product-handbook-for-ers-altimetry-reprocessed-products (accessed on 20 December 2018).

35. Passaro, M.; Rose, S.; Andersen, O.; Boergens, E.; Calafat, F.; Dettmering, D.; Benveniste, J. ALES+: Adapting a homogenous ocean retracker for satellite altimetry to sea ice leads, coastal and inland waters. *Remote Sens. Environ.* **2018**, *211*, 456–471, doi:10.1016/j.rse.2018.02.074.

36. European Space Agency (ESA). *ENVISAT RA2 / MWR Product Handbook*; European Space Agency: Paris, France , 2007.

37. Stenseng, L.; Andersen, O.B. Preliminary gravity recovery from CryoSat-2 data in the Baffin Bay. *Adv. Space Res.* **2012**, *50*, 1158–1163, doi:10.1016/j.asr.2012.02.029.

38. Scharroo, R.; Leuliette, E.; Lillibridge, J.; Byrne, D.; Naeije, M.; Mitchum, G. RADS : Consistent multi-mission products. In Proceedings of the Symposium on 20 Years of Progress in Radar Altimetry (ESA SP-710), Venice, Italy, 24–29 September 2012; pp. 5–8.

39. Dee, D.P.; Uppala, S.M.; Simmons, A.J.; Berrisford, P.; Poli, P.; Kobayashi, S.; Andrae, U.; Balmaseda, M.A.; Balsamo, G.; Bauer, P.; et al. The ERA-Interim reanalysis : Configuration and performance of the data assimilation system. *Q. J. R. Meteorol. Soc.* **2011**, *137*, 553–597, doi:10.1002/qj.828.

40. Scharroo, R.; Smith, W. A GPS-based climatology for the total electron content in the ionosphere. *J. Geophys. Res.* **2010**, *115*, doi:doi:10.1029/2009JA0014719.

41. Jee, G.; Lee, H. B.; Kim, Y. H.; Chung, J. K.; Cho, J. Assessment of GPS global ionosphere maps (GIM) by comparison between CODE GIM and TOPEX/Jason TEC data: Ionospheric perspective. *J. Geophys. Res. Space Phys.* **2010**, *115*, doi:doi:10.1029/2010JA015432.

42. Llewellyn, T.S.; Bent, R.B. *Documentation and Description of the Bent Ionospheric Model*; Atlantic Science Corp Indian Harbour Beach: Brevard, FL, USA , 1973.

43. Carrere, L.; Faugère, Y.; Ablain, M. Major improvement of altimetry sea level estimations using pressure-derived corrections based on ERA-Interim atmospheric reanalysis. *Ocean Sci.* **2016**, *12*, 825–842, doi:10.5194/os-12-825-2016.

44. Carrère, L.; Lyard, F. Modeling the barotropic response of the global ocean to atmospheric wind and pressure forcing Comparisons with observations. *Geophy. Res. Lett.* **2003**, *30*, 4, doi:10.1029/2002GL016473.

45. Carrere, L.; Lyard, F.; Cancet, M.; Guillot, A. FES 2014, a new tidal model on the global ocean with enhanced accuracy in shallow seas and in the Arctic region. In Proceedings of the EGU General Assembly Conference Abstracts, Vienna, Austria, 12–17 April 2015; Volume 17, p. 5481.

46. Cartwright, D.E.; Edden, A.C. Corrected tables of tidal harmonics. *Geophys. J. Int.* **1973**, *33*, 253–264, doi:10.1111/j.1365-246X.1973.tb03420.x.

47. Wahr, J.M. Deformation induced by polar motion. *J. Geophys. Res.* **1985**, *90*, 9363–9368, doi:10.1029/JB090iB11p09363.

48. Passaro, M.; Nadzir, Z.A.; Quartly, G.D. Improving the precision of sea level data from satellite altimetry with high-frequency and regional sea state bias corrections. *Remote Sens. Environ.* **2018**, *218*, 245–254, doi:10.1016/j.rse.2018.09.007.

49. Andersen, O.B.; Stenseng, L.; Piccioni, G.; Knudsen, P. The DTU15 MSS (Mean Sea Surface) and DTU15LAT (Lowest Astronomical Tide) reference surface. In Proceedings of the ESA Living Planet Symposium 2016 (SP-740), Prague, Czech Republik, 9–13 May 2016.

50. Fernandes, M.J.; Lázaro, C.; Ablain, M.; Pires, N. Improved wet path delays for all ESA and reference altimetric missions. *Remote Sens. Environ.* **2015**, *169*, 50–74, doi:10.1016/j.rse.2015.07.023.

51. Laxon, S.; Rapley, C. Radar altimeter data quality flagging. *Adv. Space Res.* **1987**, *7*, 315–318, doi:10.1016/0273-1177(87)90332-2.

52. Ricker, R.; Hendricks, S.; Helm, V.; Skourup, H.; Davidson, M. Sensitivity of CryoSat-2 Arctic sea-ice freeboard and thickness on radar-waveform interpretation. *Cryosphere* **2014**, *8*, 1607–1622, doi:10.5194/tc-8-1607-2014.

53. Knudsen, P.; Andersen, O.B.; Tscherning, C.C. Altimetric gravity anomalies in the Norwegian-Greenland Sea-Preliminary results from the ERS-1 35 days repeat mission. *Geophys. Res. Lett.* **1992**, *19*, 1795–1798.

54. Laxon, S. Sea ice extent mapping using the ERS-1 radar altimeter. *EARSeL Adv. Remote Sens.* **1994**, *3*, 112–116.

55. Andersen, O.B. Shallow water tides in the northwest European shelf region from TOPEX/POSEIDON altimetry. *J. Geophys. Res.* **1999**, *104*, 7729–7741.

56. Ablain, M.; Cazenave, A.; Valladeau, G.; Guinehut, S. A new assessment of the error budget of global Mean Sea Level rate estimated by satellite altimetry over 1993–2008. *Ocean Sci.* **2009**, *5*, 193–201, doi:10.5194/os-5-193-2009.

57. Lahiri, S. *Resampling Methods for Dependent Data*; Springer Science & Business Media: Berlin/Heidelberg, Germany , 2013; p. 374.

58. Caron, L.; Ivins, E.R.; Larour, E.; Adhikari, S.; Nilsson, J.; Blewitt, G. GIA Model Statistics fro GRACE Hydrology, Cryosphere, and Ocen Science. *Geophy. Res. Lett.* **2018**, *45*, 2203–2212, doi:10.1002/2017GL076644.

59. Barletta, V.R.; Sabadini, R.; Bordoni, A. Isolating the PGR signal in the GRACE data: Impact on mass balance estimates in Antarctica and Greenland. *Geophys. J. Int.* **2008**, *172*, 18–30, doi:10.1111/j.1365-246X.2007.03630.x.

60. Barletta, V.R.; Sørensen, L.S.; Forsberg, R. Scatter of mass changes estimates at basin scale for Greenland and Antarctica. *Cryosphere* **2013**, *7*, 1411–1432, doi:10.5194/tc-7-1411-2013.

61. Santamaría-Gómez, A.; Gravelle, M.; Collilieux, X.; Guichard, M.; Míguez, B.M.; Tiphaneau, P.; Wöppelmann, G. Mitigating the effects of vertical land motion in tide gauge records using a state-of-the-art GPS velocity field. *Glob. Planet. Chang.* **2012**, *98–99*, 6–17, doi:10.1016/j.gloplacha.2012.07.007.

62. Sato, T.; Okuno, J.; Hinderer, J.; MacMillan, D.S.; Plag, H.P.; Francis, O.; Falk, R.; Fukuda, Y. A geophysical interpretation of the secular displacement and gravity rates observed at Ny-Ålesund, Svalbard in the Arctic—Effects of post-glacial rebound and present-day ice melting. *Geophys. J. Int.* **2006**, *165*, 729–743, doi:10.1111/j.1365-246X.2006.02992.x.

63. Lee, S.; Im, J.; Kim, J.; Kim, M.; Shin, M.; Cheol Kim, H.; Quackenbush, L.J. Arctic Sea Ice Thickness Estimation from CryoSat-2 Satellite Data Using Machine Learning-Based Lead Detection. *Remote Sens.* **2016**, *8*, 698, doi:10.3390/rs8090698.

64. Paul, S.; Hendricks, S.; Ricker, R.; Kern, S.; Rinne, E. Empirical parametrization of envisat freeboard retrieval of arctic and antarctic sea ice based on CryoSat-2: Progress in the ESA climate change initiative. *Cryosphere* **2018**, *12*, 2437–2460, doi:10.5194/tc-12-2437-2018.

65. Poisson, J.C.; Quartly, G.D.; Kurekin, A.A.; Thibaut, P.; Hoang, D.; Nencioli, F. Development of an ENVISAT altimetry processor providing sea level continuity between open ocean and arctic leads. *IEEE Trans. Geosci. Remote Sens.* **2018**, *56*, 5299–5319, doi:10.1109/TGRS.2018.2813061.

66. Maslanik, J.; Stroeve, J.; Fowler, C.; Emery, W. Distribution and trends in Arctic sea ice age through spring 2011. *Geophys. Res. Lett.* **2011**, *38*, 2–7, doi:10.1029/2011GL047735.

67. Velicogna, I.; Wahr, J. Acceleration of Greenland ice mass loss in spring 2004. *Nature* **2006**, *443*, 329–331, doi:10.1038/nature05168.

68. Volkov, D.L.; Landerer, F.W.; Kirillov, S.A. The genesis of sea level variability in the Barents Sea. *Cont. Shelf Res.* **2013**, *66*, 92–104, doi:10.1016/j.csr.2013.07.007.

69. Proshutinsky, A.; Ashik, I.M.; Dvorkin, E.N.; Häkkinen, S.; Krishfield, R.A.; Peltier, W.R. Secular sea level change in the Russian sector of the Arctic Ocean. *J. Geophys. Res. Ocean.* **2004**, *109*, 1–19, doi:10.1029/2003jc002007.

70. Proshutinsky, A.; Krishfield, R.; Timmermans, M.L.; Toole, J.; Carmack, E.; McLaughlin, F.; Williams, W.J.; Zimmermann, S.; Itoh, M.; Shimada, K. Beaufort Gyre freshwater reservoir: State and variability from observations. *J. Geophys. Res.* **2009**, *114*, 1–25, doi:10.1029/2008jc005104.

71. Giles, K.A.; Laxon, S.W.; Ridout, A.L.; Wingham, D.J.; Bacon, S. Western Arctic Ocean freshwater storage increased by wind-driven spin-up of the Beaufort Gyre. *Nat. Geosci.* **2012**, *5*, 194–197, doi:10.1038/ngeo1379.

72. Carret, A.; Johannessen, J.A.; Andersen, O.B.; Ablain, M.; Prandi, P.; Blazquez, A.; Cazenave, A. Arctic Sea Level During the Satellite Altimetry Era. *Surv. Geophys.* **2017**, *38*, 251–275, doi:10.1007/s10712-016-9390-2.

73. European Space Agency (ESA). *ESA Earth Observation Missions*; ESA: Paris, France, 2018.

74. Knudsen, P.; Brovelli, M. Collinear and cross-over adjustment of Geosat ERM and Seasat altimeter data in the Mediterranean Sea. *Surv. Geophys.* **1993**, *14*, 449–459.

75. Passaro, M.; Cipollini, P.; Vignudelli, S.; Quartly, G.D.; Snaith, H.M. ALES: A multi-mission adaptive subwaveform retracker for coastal and open ocean altimetry. *Remote Sens. Environ.* **2014**, *145*, 173–189, doi:10.1016/j.rse.2014.02.008.

Check for updates

OPEN

DATA DESCRIPTOR

Coastal sea level anomalies and associated trends from Jason satellite altimetry over 2002–2018

The Climate Change Initiative Coastal Sea Level Team*

Climate-related sea level changes in the world coastal zones result from the superposition of the global mean rise due to ocean warming and land ice melt, regional changes caused by non-uniform ocean thermal expansion and salinity changes, and by the solid Earth response to current water mass redistribution and associated gravity change, plus small-scale coastal processes (e.g., shelf currents, wind & waves changes, fresh water input from rivers, etc.). So far, satellite altimetry has provided global gridded sea level time series up to 10–15 km to the coast only, preventing estimation of sea level changes very close to the coast. Here we present a 16-year-long (June 2002 to May 2018), high-resolution (20-Hz), along-track sea level dataset at monthly interval, together with associated sea level trends, at 429 coastal sites in six regions (Northeast Atlantic, Mediterranean Sea, Western Africa, North Indian Ocean, Southeast Asia and Australia). This new coastal sea level product is based on complete reprocessing of raw radar altimetry waveforms from the Jason-1, Jason-2 and Jason-3 missions.

Background & Summary

Since the early 1990s, sea level is routinely measured globally and regionally by high-precision altimeter satellites. The first high-precision altimetry measurements from space started with the launch in 1991 of ERS-1 by the European Space Agency (ESA), and in 1992 with the joint NASA (National Aeronautics and Space Administration) - CNES (Centre National d'Etudes Spatiales) satellite Topex/Poseidon (T/P). Since then, several altimetry missions have followed: Jason-1 (2001), Jason-2 (2008) and Jason-3 (2016), the successors of T/P with similar orbital characteristics. ESA also developed ERS-2 (1995), Envisat (2002), CryoSat (2010) and Sentinel-3A/3B (2016/2018). SARAL/AltiKa (2013), a joint Indian-French mission, operates in the Ka-band, allowing a smaller radar footprint on ground than other missions (T/P, the Jason series, ERS and Envisat being equipped with Ku-band radars). Cryosat and Sentinel-3A/3B use new technology, i.e. Synthetic Aperture Radar (SAR) altimetry. The T/P and Jason series have an orbital cycle of 10 days but a large spacing between satellite tracks (~300 km at equator). They cover the 66°S-66°N latitude domain. The orbital cycle of the ESA missions and SARAL/AltiKa is 35 days, but the spacing between tracks is smaller and the latitudinal coverage goes up to 82°, allowing a large portion of the Arctic Ocean to be covered.

When combined, the current satellite altimetry record, 28-year long at the time of writing, shows that the global mean sea level is rising and even accelerating. Over the 1993–2019 time span, the mean rate and the acceleration amount to 3.3 +/− 0.3 mm/yr and ~0.1 mm/yr^2 respectively[1–4]. Satellite altimetry also shows important regional variability in sea level trends, with rates up to 3 times the global mean in some regions[2,5,6]. While we now have precise sea level data sets from multi mission altimetry, at global and regional scales, this is not yet the case for coastal zones. This is because in classical altimetry sea level products, the amount of valid data strongly decrease within 10–15 km from the coast. An example is shown in Fig. 1 for data located in the Western Tropical Pacific. Classical criteria for declaring a data as invalid are: data on land, lack of one or more geophysical corrections, sea surface height (SSH) >1 m[7,8].

This loss in valid sea level data close to the coast first results from land contamination within the footprint of Ku-band nadir altimeters (hereinafter called LRM for 'Low Resolution Mode'). When the satellite approaches the coast, the radar signal reflected from the sea surface is modified in a complex way and differs from the standard Brown-type ocean waveform (the magnitude and shape of the radar altimetry return echo after reflection on the sea surface), preventing accurate estimation of the altimeter range (the distance between the satellite and the Earth surface measured by the onboard radar) used to estimate the sea surface height (also called sea level). This

---

*A full list of authors and their affiliations appears at the end of the paper.
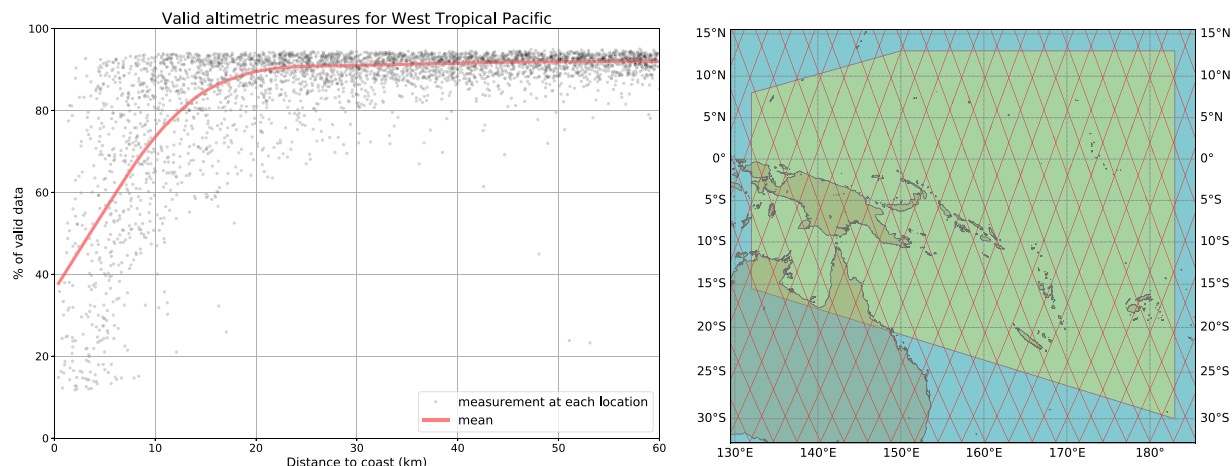
Fig. 1 Percentage of valid range data for standard LRM altimetry missions, as a function of distance to the coast (left panel). Region (Western Tropical Pacific, green polygon) where the data come from (righ panel).
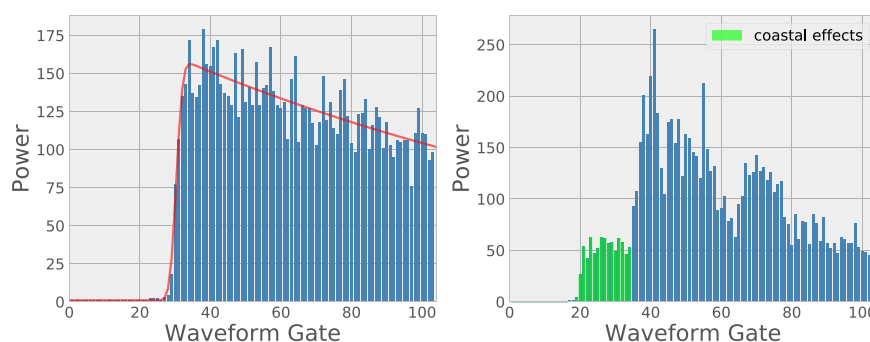

Fig. 2 Typical altimetry waveforms along a Jason track in the Mediterranean Sea. Open ocean at location 43.02°N, 4.27°E (left panel). Coastal zone at location 43.34°N, 4.54°E (right panel).

is illustrated in Fig. 2 showing a standard radar waveform over the open ocean and an example of waveform in coastal zones.

In addition, the geophysical corrections to be applied to the altimetry range measurements are usually optimized for the open ocean and not for the coastal zones. In the coastal zones, the wet tropospheric correction, based on on-board microwave radiometers is inaccurate at distances shorter than 20–50 km from land as land reflections enter the radiometer footprint. Tides and the high-frequency sea level response to wind and pressure changes need to be removed from altimetry data in order to avoid aliasing errors. However, in global models used to compute the corresponding geophysical corrections, significant errors still exist in coastal and shelf areas. The sea state bias (SSB) correction is usually estimated from models optimized for open-ocean altimetry measurements and becomes inaccurate within 10–15 km from the coast. More details can be found in[9,10]. Hence, the geophysical corrections applied to altimetry measurements remain a source of significant errors in the coastal zones. Note that the increased along-track resolution of SAR altimeters are able to provide more accurate ocean range measurements in the 0–10 km coastal zone, but even there, inadequate geophysical corrections remain a strong limitation as far as the accuracy of the sea level product is concerned.

Why is it important to precisely measure sea level in the coastal zone? Sea level rise is considered to be a major threat of current global warming to the low-lying coastal regions of the world. Coastal zones are indeed densely populated and concentrate important infrastructures such as harbors and industries. While the causes of the global and regional sea level changes are now well known and reasonably well quantified[3,4,6,11,12], additional small scale processes of oceanographic and hydrological origin, specific to coastal areas, may superimpose on the global and regional components, eventually modifying the rate of sea level rise close to the coast compared to the open ocean[13,14]. Potential coastal process able to modify sea level trends at the coast include local atmospheric effects, baroclinic instabilities, coastal trapped waves, shelf currents, waves, fresh water input from rivers in estuaries. Hence, sea level change at the coast is not necessarily an extrapolation of the regional sea level trends that are routinely provided by standard ocean altimetry products[15].

About a decade ago, the European Space Agency (ESA) implemented the Climate Change Initiative programme (http://cci.esa.int/) dedicated to provide long, accurate and stable time series of a set of Essential Climate Variables (ECVs) observable from space, including sea level. The CCI sea level project (www.esa-sealevel-cci.
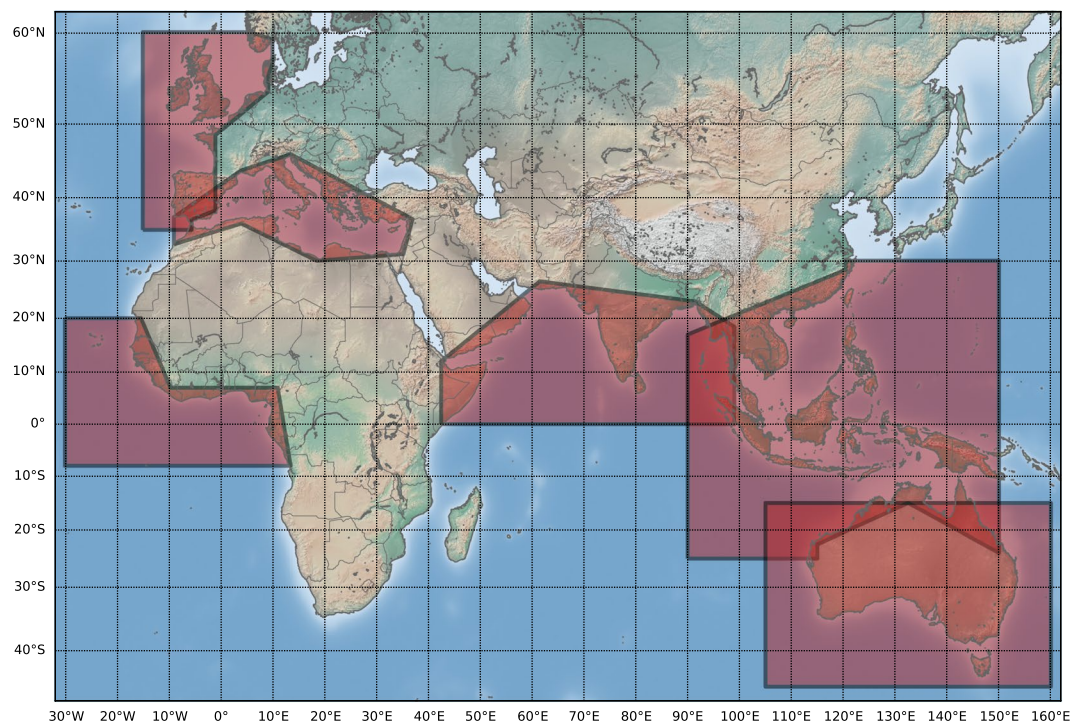
Fig. 3 The 6 regions (in red) where new coastal sea level products are presented in this study.

org/) provided monthly gridded sea level maps over 1992–2015 based on the complete reprocessing of nine different altimetry missions, using new, optimized algorithms and geophysical corrections. In the context of additional activities, the CCI + Sea Level project, has proposed to extend the processing efforts to the coastal zones, and develop a new coastal sea level product in six selected regions: Northern Europe, Mediterranean Sea, Western Africa, North Indian Ocean, Southeast Asia and Australia (Fig. 3). This is a first step selection due to limited resources. Near future work will include the whole African coastlines. In case of project extension, the North and South America coastlines will also be studied.

The reprocessing method is described in Section 3. It consists of: (1) using an adapted retracking methodology to estimate the altimeter range from waveforms collected in the coastal zone, (2) using improved geophysical corrections, and (3) applying a strict data editing procedure adapted to coastal ocean conditions. The approach has been applied to the high frequency (20-Hz, corresponding to a ground resolution of ~300 m) along-track measurements from the Jason-1, Jason-2 and Jason-3 missions. For each satellite track, the sea level data of each mission have been combined into a single record over the study period (June 2002 to May 2018), and further expressed in terms of sea level anomalies located along a theoretical mean reference track. At all 20 Hz points along the track, the original sea level anomalies at 10-day interval have been further averaged on a monthly basis. Post-validation based on severe criteria (see section 4.2) has led to retain 429 coastal sites.

The corresponding regional product available is presented in section 4. It consists of: (1) monthly sea level anomalies time series at each 20-Hz point along the track, from June 2002 to May 2018, from 20 km offshore to the coast, and (2) sea level trends estimated over the study period at each 20 Hz point along the 20 km-long track portion.

Methods

Stage 1: The ALES retracking. The fitting of the altimetric waveform (retracking) in the open ocean is performed considering the full averaged echo registered on board the satellite at the typical frequency of 20 Hz. In the coastal zone, at distances up to about 20 km from land, the echoes are often corrupted by the presence of interferences in the trailing edge of the return. These can derive from the land intruding in the reflection, but also from the presence of areas with inhomogeneities in the backscatter characteristics of the illuminated surface.

In the Adaptive Leading-Edge Subwaveform (ALES) retracker, the retracking of each waveform is performed in two passes. A first pass looks at the rising portion of the waveform and provides a rough estimate of the significant wave height (SWH) from the slope of that portion. This estimate is then entered into an algorithm that selects the sub-waveform (i.e., sets the width of the fitting window over which a fitting is performed in the second pass). The dependence on the SWH is necessary to maintain the same level of precision achievable in the open ocean using a full-waveform retracker, given the direct relationship between sea state and noise of the retrieval. Full details of the retracking procedure are given in[16].

Sea surface height and sea state are also related by the SSB correction. This correction is needed to correctly estimate the distance between the satellite and the mean surface of the illuminated area (Range). The SSB is determined by empirical models that relate SSH errors (for example differences at the intersection between two tracks)

with the measured sea state. Since the sea state is measured using the same retracking method adopted to estimate the Range, any correlated error in the estimation of these parameters falls into the modelling of the SSB. The SSB corrections in the standard products are computed at low frequency (1-Hz, equivalent to an along-track distance of about 7 km), but correlated errors in the retracking affect the measurements at 20-Hz[17].

In this study, an SSB correction is computed for every 20-Hz measurement applying the model developed by Tran et al.[18] to the sea state retrievals of the ALES retracker. This approach has been demonstrated to improve the precision of the measurement by decreasing the variance of the SSH differences at crossover points by 10 to 20% depending on the region[19]. This improvement is due to the fact that the computation of a high-frequency SSB reduces the correlated errors between the retracked parameters[20]. The general aim of future research on SSB shall be to work on a retracked dataset that is free from the retracker-related noise, in order to correct for the physical effects of the interaction between the radar signal and the waves. Meanwhile, this approach offers a first step to improve the correction currently used in the standard products of the missions considered in this study.

The advantage of the ALES retracker coupled with the recomputed SSB correction in improving the quality and quantity of the altimetric records has been studied in recent years in several regional studies. The retracked SSH time series show a strong abatement in the number of outliers in the Baltic Sea/North Sea transition zone compared to the global along-track Sea Level CCI dataset[21]. Chereskin et al.[22] have shown that the spatial spectrum of the SSH for the Jason missions retracked by ALES is comparable to the one obtained from Sentinel-3 measurements, despite the latter having an intrinsically better signal-to-noise ratio. The application of the retracker allows for a better estimation of the along-track mean sea surface profiles, as proved in the Gibraltar Strait[23], and an improvement in the computation of the tidal constants from altimetry data in the coastal zone[24].

Stage 2. XTRACK-ALES Merging; Geophysical corrections; Editing.   In this section we explain and describe the processing and post-processing system that has been implemented to derive the CCI + sea level products. The objective is to produce, from the combination of measurements provided by different altimetry missions, homogeneous long-term sea level time series and associated trends, as close as possible to the coastline (i.e. a few kilometers).

The X-TRACK/ALES processing and post-processing system is largely built on the X-TRACK software[7], developed at the LEGOS laboratory (http://www.legos.obs-mip.fr/) in order to optimize the completeness and the accuracy of the SSH derived from satellite altimetry in coastal ocean areas. It is tailored for extending the use of altimetry data to coastal ocean applications and already provides freely available 1-Hz (i.e. with a resolution of 6–7 km in the along-track direction) sea level time series covering all the coastal oceans, distributed by the AVISO + operational centre. It is based on the standard ocean MLE4 (Maximum Likelihood Estimator 4) altimeter waveform retracker. The X-TRACK system is described in detail in[7,25,26] (see also https://www.aviso.altimetry.fr/index.php?id=3047).

In the context of the ESA SL_CCI + project, X-TRACK has been extended to the processing of high-rate altimetry measurements (20-Hz in the case of Jason missions) instead of the 1-Hz data and then adapted to the ingestion of data provided by the ALES retracker. The resulting new processing system, called X-TRACK/ALES is illustrated by Fig. 4.

Like X-TRACK, the X-TRACK/ALES processing system works on a regional basis (the regional domain can be easily defined before the processing in a parameter file). It first uploads all the parameters needed to compute the product (orbit solution, altimeter ranges, instrumental, environmental and geophysical corrections), which were previously ingested and indexed in the altimetry database of the French National Observations Service for altimetry called CTOH (http://ctoh.legos.obs-mip.fr/). These parameters come from the Geophysical Data Records (GDRs) data sets distributed by the space agencies for the different altimetry missions, ALES products from TUM (Technical University Munich) and additional geophysical corrections provided by the RADS (Radar Altimetry Database System) altimeter database (http://rads.tudelft.nl/rads/rads.shtml) and the University of Porto for the GPD (GNSS-derived Path Delay) plus wet tropospheric correction[27]. In terms of altimetry corrections, the best altimeter standards defined in the ESA SL_cci project were selected in order to calculate sea level anomalies for climate studies (Table 1).

As already mentioned above, the characteristics of ocean altimetry measurements and corrections change significantly when approaching the coast, resulting in an important degradation of the corresponding sea level products (see[28] for a complete review of the technical and processing issues related to coastal altimetry). To cope with this, the X-TRACK/ALES system first selects valid ocean data through a precise land mask (based on the GSHHS -Global Self-consistent, Hierarchical, High-resolution Geography- shoreline database distributed by NOAA, http://www.ngdc.noaa.gov/mgg/shorelines/data/gshhs/version2.1.1/) and a dedicated editing strategy. The latter includes two steps. The first step is to impose editing criteria, both on the altimeter measurements and corrections, designed to be more restrictive than the standard criteria used for the open ocean (https://www.aviso.altimetry.fr/fileadmin/documents/data/tools/hdbk_L2P_all_missions_except_S3.pdf). For each cycle, the spatial behavior of each correction is analyzed along the track, taking into account its individual characteristics. Abrupt changes are assumed to be associated with erroneous data and are removed[7]. In a second step, all corrections are recomputed at the 20-Hz frequency through interpolation/extrapolation methods, based on valid data for each correction. This strategy is very efficient in recovering a significant amount of valid altimeter measurements that were flagged in the standard product because of a deficient correction[25,29]. The corrected SSHs are computed at 20 Hz along-track point using Eq. 1, and are further projected onto fixed points along a nominal ground track and converted into Sea Level Anomalies (SLA) by subtracting a precise Mean Sea Surface (MSS) height using Eq. 2. The MSS is computed at the fixed nominal points, by inversion of all the available SSH measurements along the repeated ground tracks of the considered altimetry mission. This procedure allows better solving the coastal MSS gradients than the use of a standard gridded MSS product, thus reduces the errors in coastal SLA data[25].
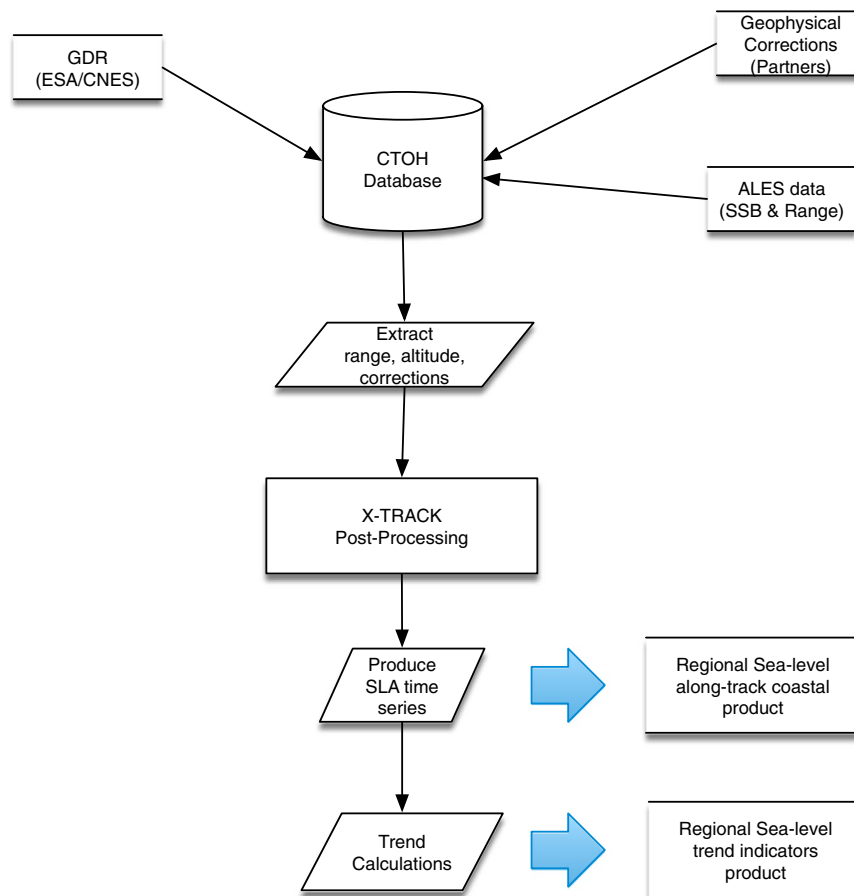
Fig. 4 Sketch of the procedures applied to derive the coastal CCI + sea level products from altimetry measurements and geophysical corrections.

$$\text{Corrected SSH} = \text{Orbit-Range-Sum corrections} \tag{1}$$

$$\text{SLA} = \text{Corrected SSH-MSS} \tag{2}$$

The corrections account for atmospheric effects (wet and dry troposphere, ionosphere, inverse barometer), geophysical phenomena (ocean tides, high frequency atmospheric effects on the ocean) and the sea-surface state (electromagnetic sea-surface bias).

At this stage of the processing, we obtain a regional dataset of SLA time series with a temporal resolution of 10 days and a spatial resolution of ~300 m along the tracks of each Jason altimetry mission. The computation of a single long-term multi-mission product requires the application of inter-mission biases in order to remove instrument and corrections biases, thus to obtain stable merged sea level time-series. Inter-mission biases are computed during the "calibration phases" between two consecutive missions (about 3 month-long between Jason-1 and Jason-2 in 2008, and between Jason-2 and Jason-3 in 2016), when both satellites measure the same sea level on the same ground track, with about 1 minute time lag. The biases are computed for each of the six studied regions, excluding altimetry points located at less than 10 km from the coast, as well as points where more than 20% of data are missing in the time series. In order to remove the high-frequency variations in the resulting 20-Hz along-track bias values, known to be associated with measurement noise, the data are low-pass filtered (with a 40-km cutoff frequency) and averaged over 1° × 1° boxes. The corresponding smoothed 1° × 1° bias values are then interpolated at the original 20-Hz along-track altimetry points and applied to the SLAs. The Jason-1/2 inter-mission bias is applied to Jason-2 SLAs first, and then the Jason-2/3 inter-mission bias to Jason-3 SLAs.

It is worth mentioning that no orbit error reduction has been applied to the coastal sea level product. This is because such a correction based on differences between ascending and descending satellites tracks due to orbit errors needs to be computed globally. However, the orbit error is supposed to be small at the coast because of its large-scale behavior.

Finally, the long-term multi-mission SLA time series are monthly averaged, and a linear trend v and associated error are derived at each 20-Hz along-track point (see section 4.2 for details on the trend calculation).

A first version of the processing system described above has been successfully evaluated and validated in[30,31]. It significantly increases the number of valid SLAs in the coastal zone. As an example, in the Mediterranean Sea,

Parameter	Source	Jason-1/Jason-2/Jason-3
Altitude	GDR	Altitude of satellite
Range	ALES	20 Hz Ku band ALES corrected altimeter range[16]
sigma0	ALES	20 Hz Ku band ALES altimeter sigma0[16]
Ionosphere	GDR	From dual-frequency altimeter range measurement
Dry troposphere	GDR	From ECMWF (European Centre for Medium-Range Weather Forecasts) model
Wet troposphere	University of Porto	GPD + correction[27]
Sea state bias	ALES	Sea state bias correction in Ku band, ALES retracking[19]
Solid tides	RADS	From tide potential model[38,39]
Pole tides	GDR	From[40]
Loading effect	RADS	From FES 2014[41]
Atmospheric correction	RADS	From MOG2D-G[42] + inverse barometer
Ocean tide	RADS	From FES 2014[41]

Table 1. List of altimetry parameters and geophysical corrections used in the computation of the SL_cci+ coastal sea level product.

80% of valid sea level data are still available at distances of <2 km from coast, compared to distances of several km in the standard X-TRACK product[30].

Data Records

Using the regional data processing system described above, the measurements of the three Jason-1, Jason-2 and Jason-3 altimetry missions are combined in single homogeneous 10-day SLA time series over the period June 2002 – May 2018. These 10-day time series at each 20-Hz point, from 20 km offshore to the coast, represents the basic SLA data set called '**Coastal Sea Level Product 1**'[32,33]. It is available to users and distributed as NetCDF files. This data set contains 628 portions of 20 km-long tracks, crossing land at different locations across all regions. The 'Coastal Sea level Product 1' is not subject to any other further editing than the one done during the X-TRACK/ALES processing. The Jason track coverage for Northeast Atlantic, Mediterranean Sea and West Africa on the one hand, and for North Indian Ocean, Southeast Asia and Australia on the other hand, is presented in Fig. 5 and Fig. 6 respectively.

We further constructed another edited product called '**Coastal Sea Level Product 2**' (delivered with this paper), that not only includes SLA time series (expressed as monthly averages), at each 20-Hz point along a track portion of 20 km from the coast, but also sea level trends and associated standard errors. This 'Coastal Sea Level Product 2' contains a much smaller number of track portions because based on a severe data selection, largely based on trend estimates (see below). The product includes monthly SLAs, simply computed by averaging available 10-day data (the monthly SLAs are based on a maximum of 4 values but sometimes only 2 or 1 value are available in the monthly interval). At each along-track 20-Hz point from 20 km offshore to the coast, annual and semi-annual signals were removed by fitting sinusoidal functions to the SLA time series. An editing was further applied by computing the mean of the deseasonalized and detrended SLA time series, and removing outliers located outside a 2-sigma threshold around the root mean squares of the time series (as in[31]). After re introducing the initial trend, a new trend and its associated 1-sigma formal error were estimated through a least-squares fit of a linear function to the edited SLA time series. Note that we do not correct the SLA time series for the regional contribution of Glacial Isostatic Adjustment. Such a correction is small (<1 mm/yr) and can be further removed from the estimated trends by the users.

The criteria considered for the selection of the monthly SLAs plus trends of the **Coastal Sea Level Product 2** are: (1) Number of valid data of the SLA time series at each 20-Hz points (missing data <50%); (2) Distribution of the valid data as uniform as possible across the three Jason missions. In a number of cases, Jason-1 data were much less numerous than the Jason-2 data. The corresponding SLA time series were then discarded; (3) Trend values in the range –15 mm/yr to +15 mm/yr (this threshold is based on occasional spurious discontinuities observed in sea level trends from one point to another, on the order of 10–15 mm/yr); (4) Standard errors on trends <2 mm/yr; (4) Continuity of trend values between successive 20 Hz points. Too abrupt changes in trends over very short distances were considered as spurious and the corresponding point was removed. This mostly occurred close to the coast but sometimes, at a larger distance from the coast.

With this selection approach, we discarded a large number of along-track 20-Hz points considered as not accurate enough to compute reliable trends. This led us to retain only 429 track portions from the initial set of 628 original track portions. We further identified them by a coastal site where the satellite track crosses land. The selected sites are named by the region and the track number to which they belong and by the site number on the track, going from north to south.

Figure 7 shows such an example, here site n°2 on track 20 in the Mediterranean Sea. From top to bottom, it shows a map of the site position on the track, the sea level trends at each 20-Hz point, expressed as a function of distance to the coast, starting from 15 km offshore, and superimposed trend error (shaded area), and finally SLA time series at the first six valid points from the coast.

The 'Coastal Sea Level Product 2' is available from the SEANOE repository website[34].

The parameters provided to users at each 20-Hz point on a selected track portion are gathered in Table 2.
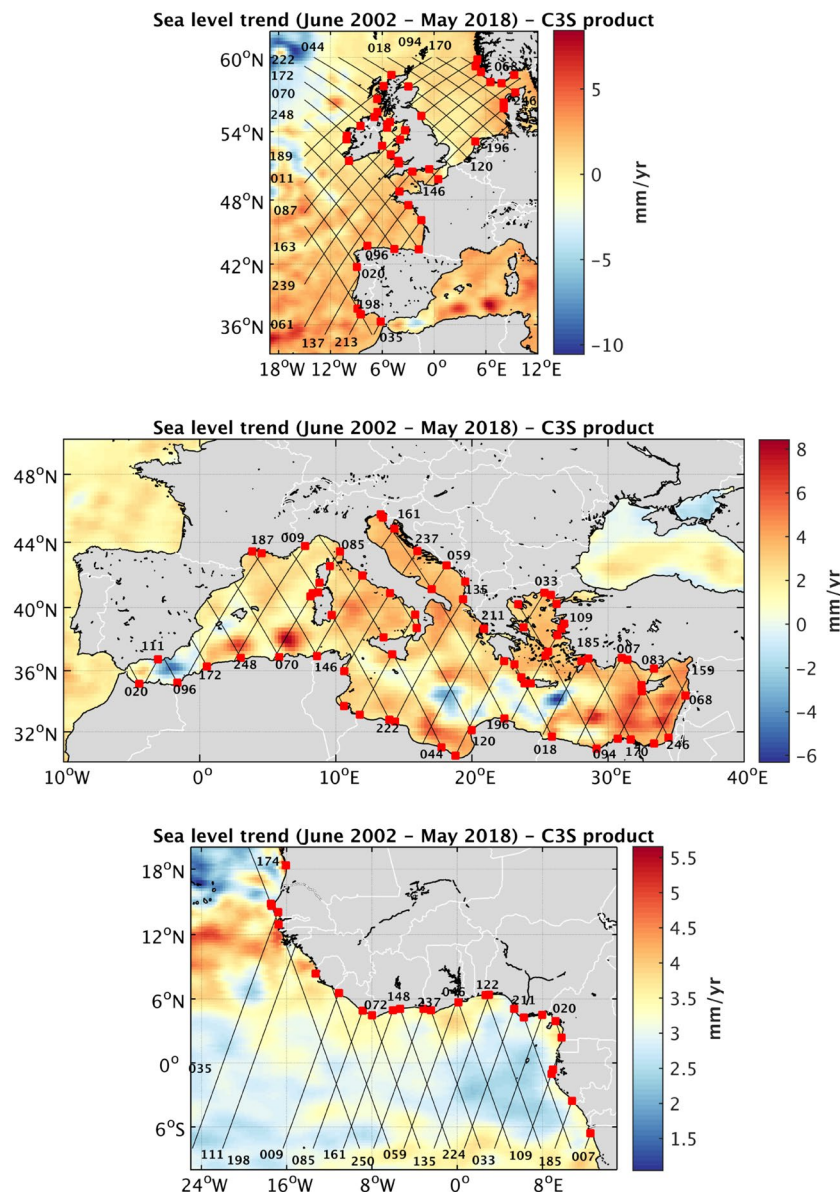
Fig. 5 Jason tracks coverage (black lines, identified by numbers) superimposed on the sea level trend patterns over June 2002 - May 2018 (from the C3S data base, https://climate.copernicus.eu/). From top to bottom: Northeast Atlantic, Mediterranean Sea, Western Africa. Red squares represent the selected sites (see text).

Technical Validation

Statistics on coastal sea level trends. In this section, we present statistics on coastal sea level trends and associated trend errors, as well on distances to the coast of the first valid point. These results are shown in the form of histograms. For coastal trends and associated errors, separate histograms are provided for ascending and descending satellite tracks, as well for 'sea to land' and 'land to sea' flying directions. The reason for looking at potential differences when the satellite flies from 'sea to land' or 'land to sea' is the following: The on-board tracking algorithm in the radar instrument suffers from some delay in adapting to the oncoming surface, therefore the radar is more efficient when it flies from a smooth surface to a harsh relief (sea to land) rather than the reverse. When it is tracking over land it needs up to one second after the land-sea transition to stabilize on the surface of the ocean.

Similarly, histograms of closest distance to the coast of the first valid point are presented for ascending and descending satellite tracks, as well as for 'sea to land' and 'land to sea' flying directions. In all cases, this is done for all six regions together and for each region individually. Results are presented in Fig. 8 for all six coastal zones.

The histograms shown in Fig. 8 display no differences between ascending and descending tracks in terms of trends distribution. Although it has to be noted that the sites where the track crosses land are different for ascending and descending tracks, the distributions looks quite similar in both cases and mean trend values are on the same order of magnitude within 0.1 mm/yr. The mean value for all tracks amount to 2.6 mm/yr. Note that
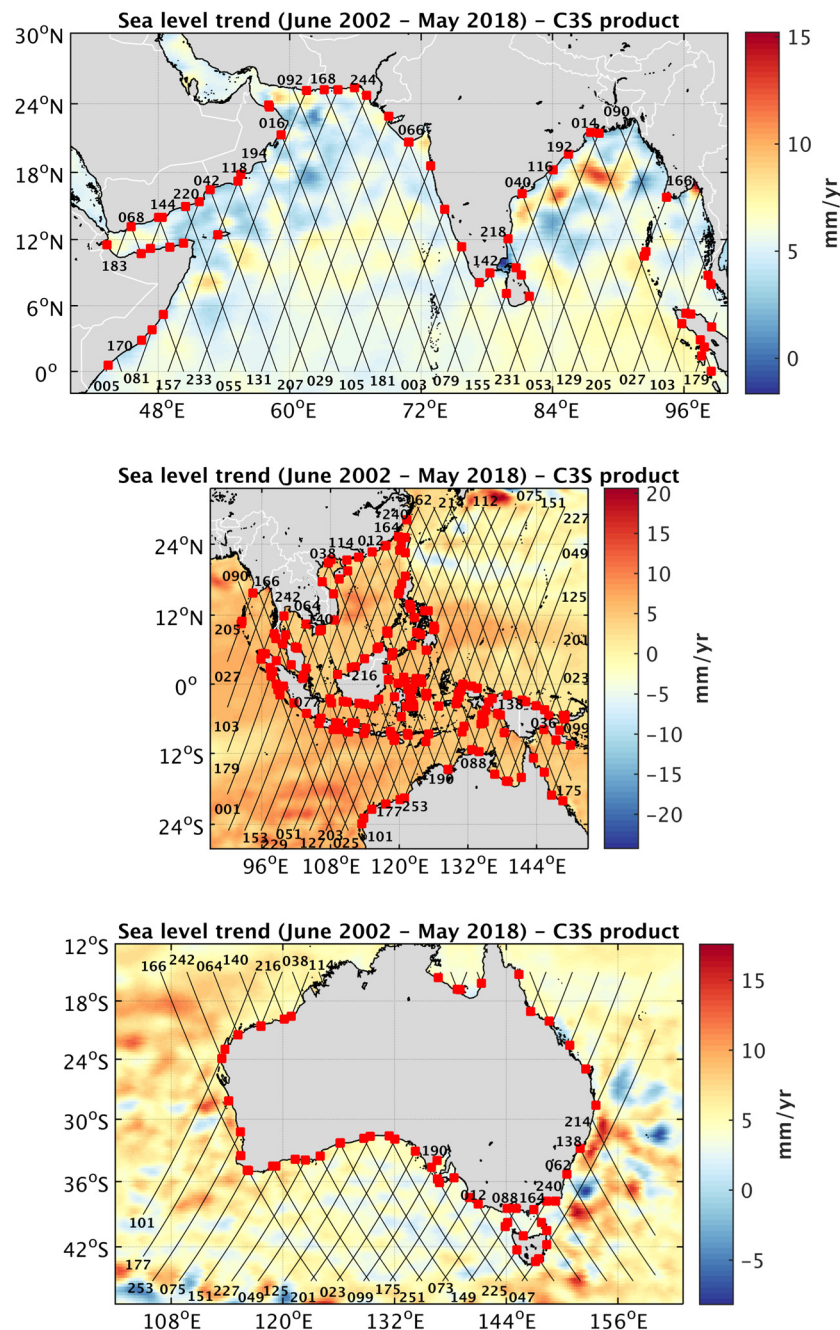
Fig. 6 Jason tracks coverage (black lines, identified by numbers) superimposed on the sea level trend patterns over June 2002 - May 2018 (from the C3S data base, https://climate.copernicus.eu/). From top to bottom: North Indian Ocean, Southeast Asia, Australia. Red squares represent the selected sites (see text).

this trend value is not GIA-corrected. Several GIA models exist and users can apply the GIA correction of their choice using available gridded GIA data sets. Because of differences between models, we prefer not to apply this correction.

The mean and median trend errors are also similar for ascending and descending tracks, and on the order of 1.1 mm/yr. Note that there is no trend error larger than 2 mm/yr, a consequence of one of our selection criteria (see section 4.2).

In Fig. 8 are also shown the distributions of the closest distance to the coast (first valid point) for the same configurations as for the trends. Again little difference is observed between ascending and descending tracks, with a mean distance of 3.5 km for all sites. On the other hand, we note better performance for the sea to land configuration (mean value of 3.2 km, more sites with closest distance to coast <2 km) than the land to sea configuration.

Similar histograms for individual regions (not shown) display some differences from one region to another. In the Mediterranean Sea, 70 sites are selected. Their mean coastal trend is 1.9 +/−1.0 mm/yr. No difference is
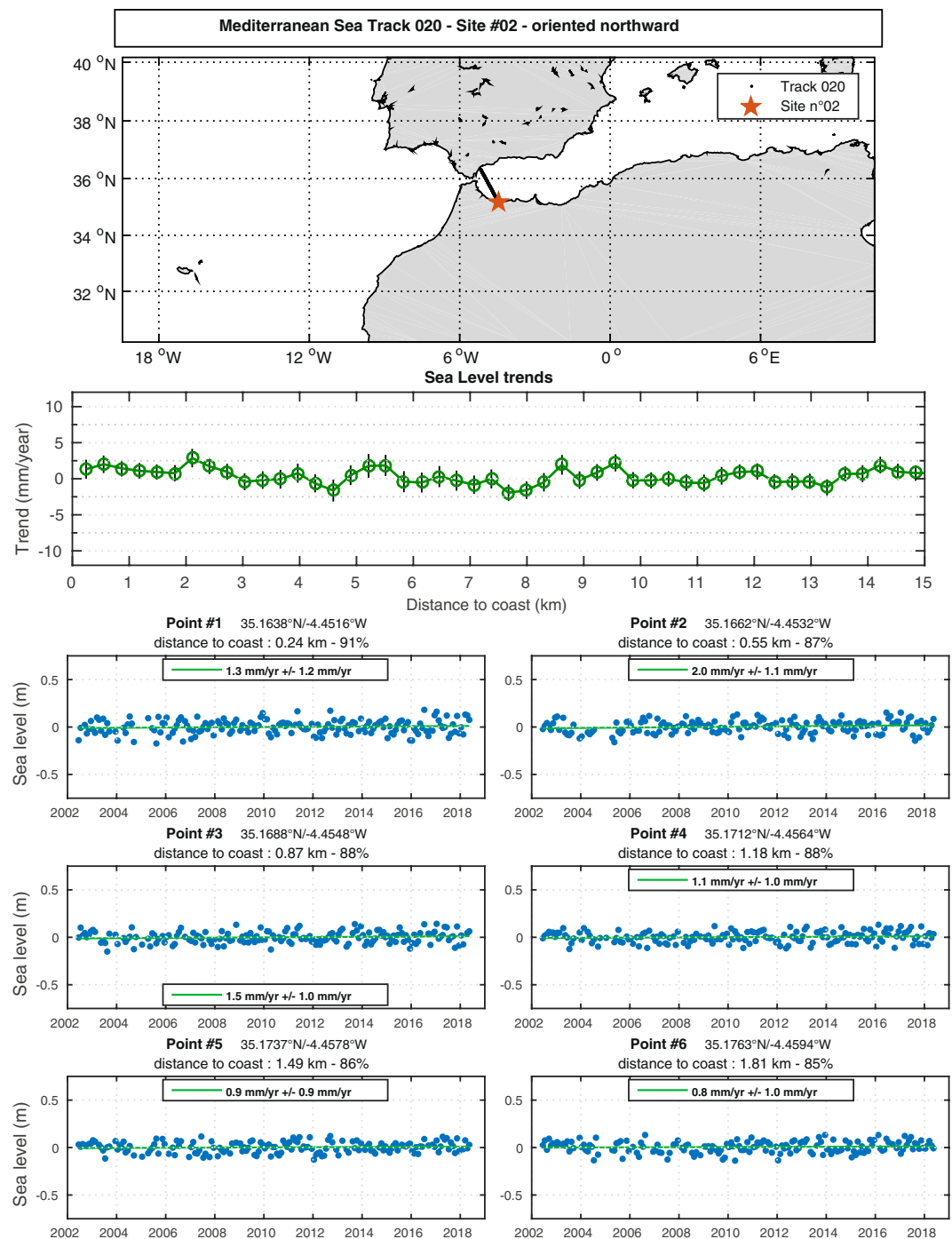
Fig. 7 Position of the site n°2 on track 20 in Mediterranean Sea (red star, top panel), along-track sea level trends and trend errors (vertical bars) against distance to the coast (middle) and sea level anomalies time series of the 6 first points closest to the coast (bottom).

noted between ascending and descending tracks. There is a smaller amount of land to sea configurations in the selected sites, with slightly smaller coastal trends (1.7 +/− 1. mm/yr) than in the sea to land case (coastal trends of 2. +/− 1. mm/yr). The distances of the first valid point to the coast are spread from <1 km to >5 km. The mean distance is in the 3–4 km range but a larger number of cases fall within less than 2 km from the coast. In the northeast Atlantic region, 44 sites are selected. The mean trend is 2. +/− 1.2 mm/yr. Only slight difference is observed between ascending (1.85 +/− 1.2 mm/yr) and descending tracks (2.05 +/− 1.2 mm/yr). Five time more measurement points are seen for the sea to land configuration than the land to sea one. The mean distance of the closest valid point is 3.5 km, with only few cases <2 km and most of the distribution lying between 2 km and 4 km.

26 sites only are selected along the Western Africa region. The mean rate of coastal sea level rise is 2.15 +/− 0.9 mm/yr. Along ascending tracks, the mean trend is 2. +/− 0.9 mm/yr while it is only 1.35 +/− 0.9 mm/yr

Variables	Description
lat	Latitude of each 20 Hz point
lon	Longitude of each 20 Hz point
distance_to_coast	Distance (m) to a reference point at the coast of each 20 Hz point
time	Time of measurements (days since 1950,0)
sla	Monthly Sea Level Anomalies (m) from X-TRACK/ALES 20 Hz
local_msl_trend	Sea level trend (mm/yr) computed from the monthly SLA
local_msl_trend_error	Sea level trend error (mm/yr)

Table 2. List of altimetry parameters included in the 'Coastal Sea Level Product 2'.

along descending tracks. But the latter concerns a much smaller number of measurement points. We also observe more sea to land cases than land to sea, due to the particular configuration of the African coast and Jason tracks. On average, the closest distance to coast distribution is in the 2–4 km range, with most of the cases included between 3 and 4 km to the coast. In the northern Indian Ocean region, 57 sites have been selected. The average distance to coast of the first valid point lies in the 3–4 km range but we observe a large spread from <1 km to >5–6 km from the coast. The mean trend is 3.5 +/− 1. mm/yr, with no noticeable difference between ascending and descending tracks nor between sea to land and land to sea directions. The Southeast Asia region displays the largest number of selected sites (177), with a mean trend of 2.7 +/− 1.2 mm/yr. As for the north Indian Ocean region, no significant difference is seen between ascending and descending tracks nor between sea to land and land to sea directions. The mean distance of the closest valid point is 3.8 km, with a maximum of the distribution between 3 km and 4 km. Finally, 55 sites are selected around Australia. The mean trend is 3.2 +/− 1.2 mm/yr. In this region, several sites display sea level trends of 5 mm/yr or larger. We note more valid points for ascending than descending tracks. The mean value of the closest distance to coast is 3.3 km, with a more or less uniform distribution between the coast and 6 km offshore.

A map of coastal trends (averaged over 2 km along-track from the first valid point) is shown in Fig. 9. The figure indicates that at a significant number of sites, over the study period, the coastal sea level rise is in general positive (with a few exceptions), with values as high as 4–5 mm/yr in some regions. This is particularly the case in the northern and eastern parts of the Indian Ocean (around Indonesia for the latter).

In Fig. 10 is shown a map of the distance to coast of the first valid point.

Figure 10 shows that in most regions, the distance to the coast of the first valid point in the 3–4 km range, but as discussed above, the closest distance to the coast can be <2 km, particularly in the Mediterranean Sea and around Australia.

In order to investigate whether the coastal trends shown in Fig. 8 differ from open ocean trends, the differences in sea level trends between an along-track portion of 2 km from the closest valid point to the coast and the 14–16 km average, offshore, have been computed. These are shown in Fig. 11.

The trend difference map presented in Fig. 11 shows an unexpected result: In most places, no significant difference (within +/−1 mm/yr) is noticed between the open ocean (here assumed ~15 km away from the coast) and the coastal zone (the first few km from the coast). However, this is not always true. At a few sites, we observe a larger trend close to the coast than offshore, but with the exception of 3 sites in the Mediterranean Sea and one site in Australia, the increase is modest, of 1–2 mm/yr only, and possibly not significant in view of the trend uncertainties. In a number of cases, we note a decrease in trend as the distance to the coast decreases (blue points on the map). But here again just a few cases may be significant. These particular sites are the object of an on-going study.

Although it had been expected that coastal processes may cause some discrepancy in coastal sea level trends compared to the open ocean[13,14], the results presented here seem to contradict this hypothesis in about 80% of our 429 selected sites. An important consequence of this observation is that it would be possible to extrapolate up to the coast, regional sea level trends computed by classical altimetry missions. More investigations using additional satellites and longer records are definitely needed to confirm such results.

Validation with tide gauges.   In this section we present a comparison of the new altimetry product with tide gauge observations. The tide gauge data used here consists of monthly mean values of sea level spanning the same period as the altimetry data and are obtained from the Revised Local Reference data archive of the Permanent Service for Mean Sea Level (http://www.psmsl.org/)[35]. To be consistent with the altimetry data, the same atmospheric correction that is applied to the altimetry data (i.e., MOG2D-G + inverse barometer) is also applied to the tide gauge data. The comparison between the two types of measurements is conducted in terms of sea-level variability (detrended and deseasoned monthly time series of sea level) and trends over the period from June 2002 to May 2018. In designing the validation strategy, a number of points merit consideration.

First, it is important to recognize that while the tide gauge data represent true monthly mean values, the altimetry monthly data are based on at most four measurements per month (due to the 10-day orbital cycle of the Jason missions) and so such data will be subject to sampling uncertainty due to variability at sub-monthly timescales. This sampling uncertainty will manifest as differences with the tide gauge observations, both in the variability and the trend. Exploratory analysis of this issue (not shown here) indicates that the effect of sampling uncertainty is fairly small when using three or more values per month, however it is more noticeable when using only one value
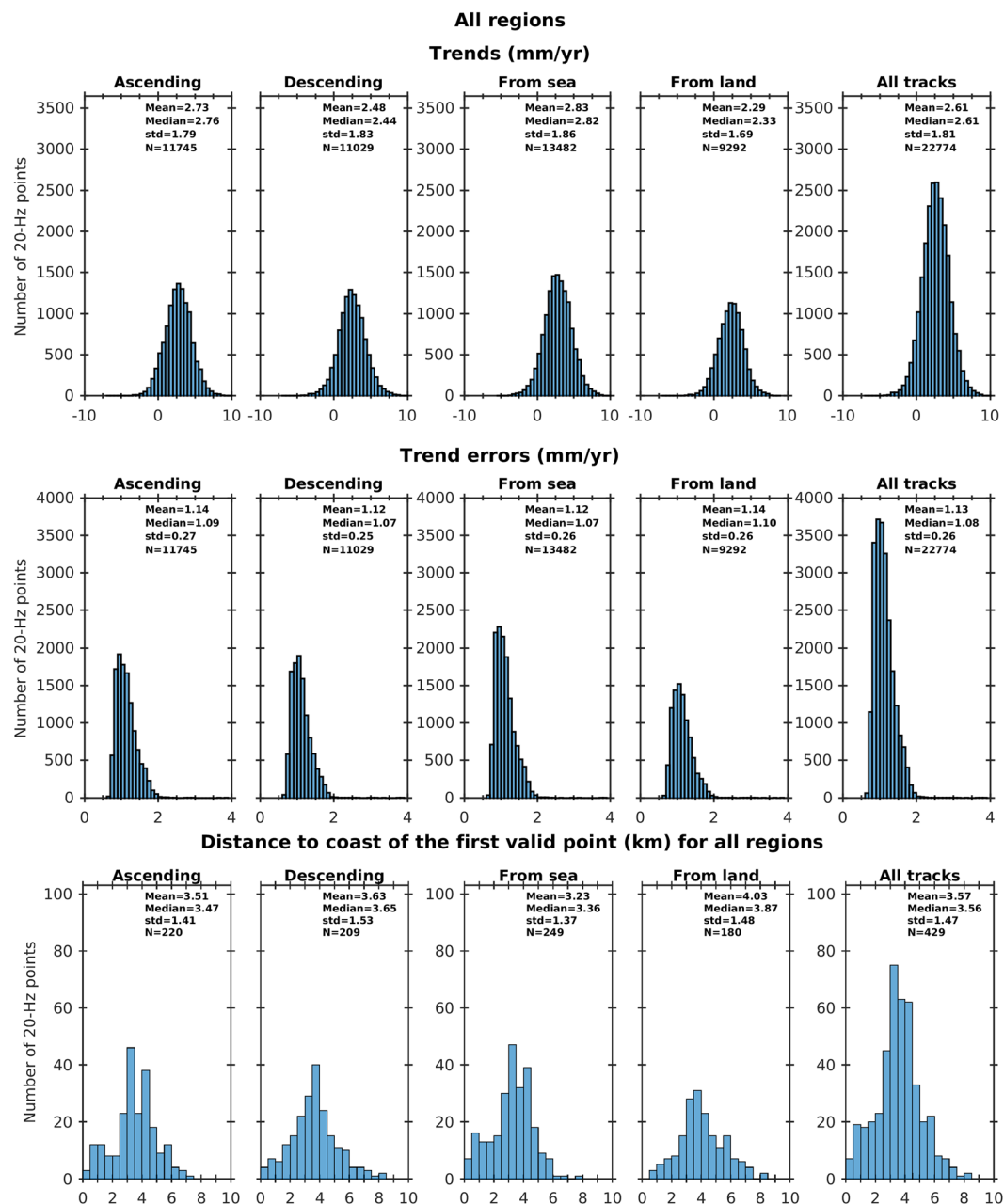
Fig. 8 Histograms of trends (mm/yr) for ascending, descending, sea to land, land to sea and all tracks (upper panel) for all regions. Histograms of associated trend errors (mm/yr) (middle panel). Histograms of distance to coast of the first valid point (km) for ascending, descending, sea to land, land to sea and all tracks (all regions) (lower panel).

per month and can degrade the correlation between the two otherwise identical time series, on average, from 1 to 0.7 and cause trend differences as large as 1.5 mm/yr. It is important to keep these effects in mind when interpreting the results of the validation against tide gauge data.

A second point to note is that, in general, altimetry measurements are not taken at tide gauge locations but at some ocean point nearby, and this spatial separation will inevitably lead to differences between the two types of data. The importance of such differences will depend on the length scales of the sea-level signals around the tide gauges and can be significant. For this comparison, we first select the closest altimetry track to each tide gauge station and then, along this track, we select the altimetry time series showing the highest correlation with the tide gauge record. This altimetry time series is the one that we use in our comparison.

A third point to consider is that tide gauges measure sea level relative to the land on which they reside and so the measurements can be strongly affected by vertical land motion (VLM), particularly on long timescales. When comparing trends from altimetry and tide gauges it is important to account for this land contribution. Here, this is done by adjusting the tide gauge rates using Global Positioning System (GPS) vertical velocities. The GPS data
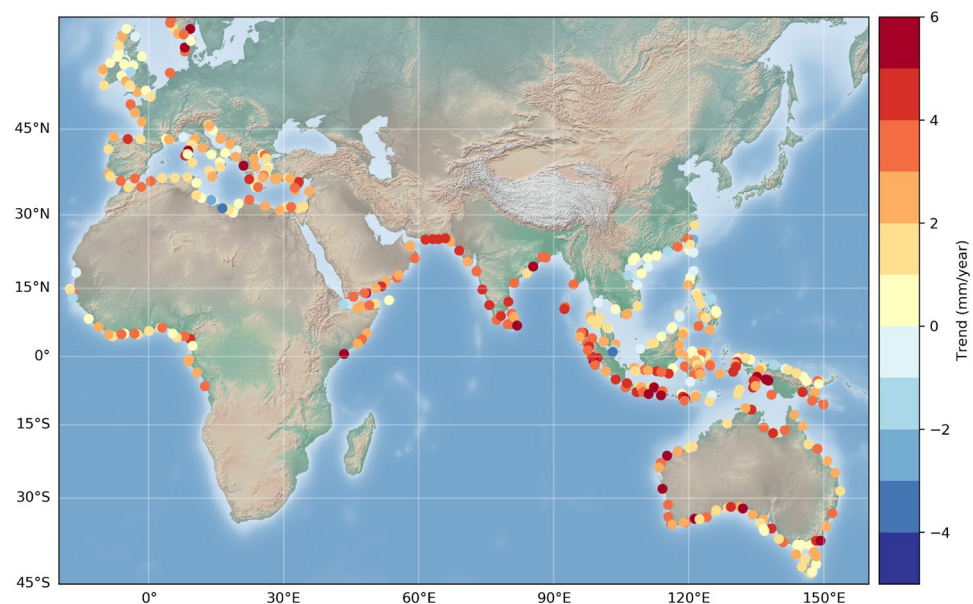
Fig. 9 Coastal sea level trends (mm/yr) at the first valid point from the coast at the 429 selected sites.
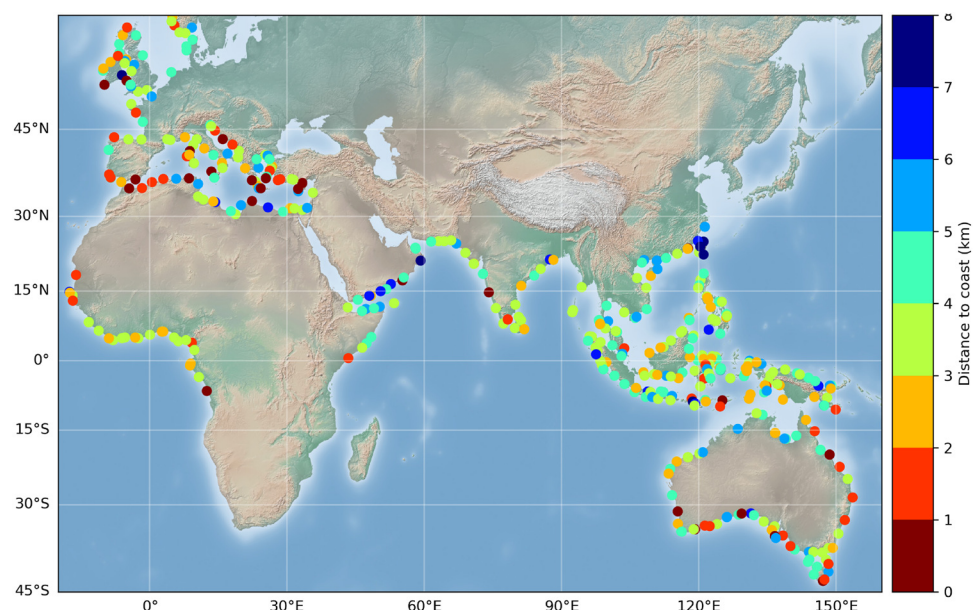

Fig. 10 Map of the closest distance (km) to the coast of the first valid point from the coast at the 429 selected sites.

consists of VLM rates from three different solutions (ULR, NGL, and JPL) and are obtained from SONEL (https://www.sonel.org). If there is a GPS station within 5 km of the tide gauge, then we use the rates from such station as our estimate of VLM (averaged over the various GPS solutions – ULR, NGL and JPL – available), otherwise we average the GPS rates over all GPS stations (and solutions) that are located within 50 km of the tide gauge. If there are no GPS stations within 50 km of the tide gauge, then we do not consider such tide gauge in the trend comparison.

The agreement between altimetry and the tide gauges in terms of trends is evaluated using fractional differences (FDs), which are defined as FD $= |\tau_d|/(1.97*SE)$, where τ_d is the trend of the time series of sea level differences between altimetry and the tide gauge, SE is the associated standard error and 1.97 is the critical value of the Student's t-distribution for the 95% confidence level. Hence, an FD value >1 means that, with 95% confidence, the two trends are statistically different. To be as rigorous as possible in the comparison of trends and obtain proper standard errors, we account for serial correlation in the estimation of the trends by using a regression model with first-order autoregressive errors. The model is analogous to that described by Chib[36].
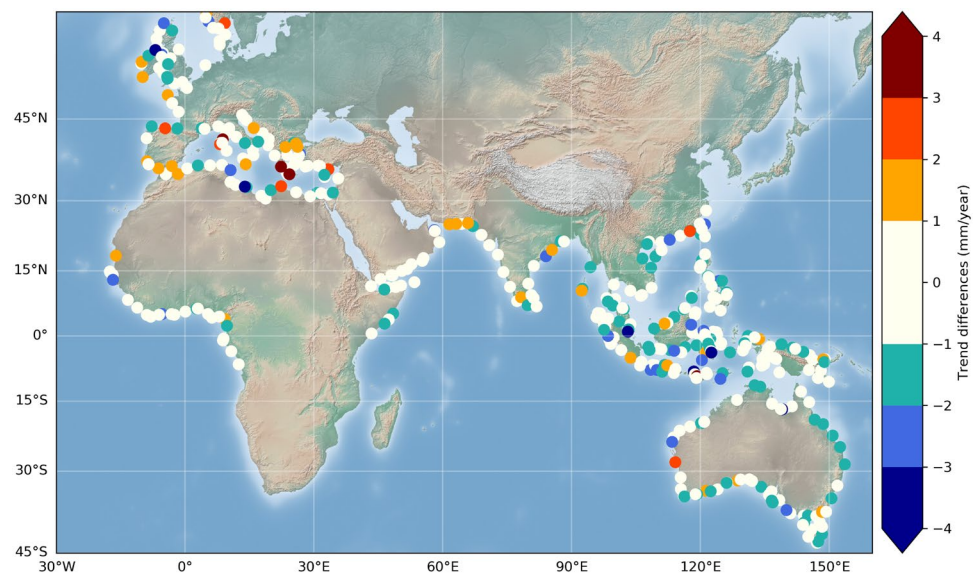
Fig. 11 Differences in sea level trends between an along-track band of 2 km from the closest valid point to the coast and the 14–16 km average, offshore. White points correspond to no significant differences (within +/−1 mm/yr) between open ocean and coast. Orange-red/blue dots correspond to coastal trend increase/decrease at the coast.
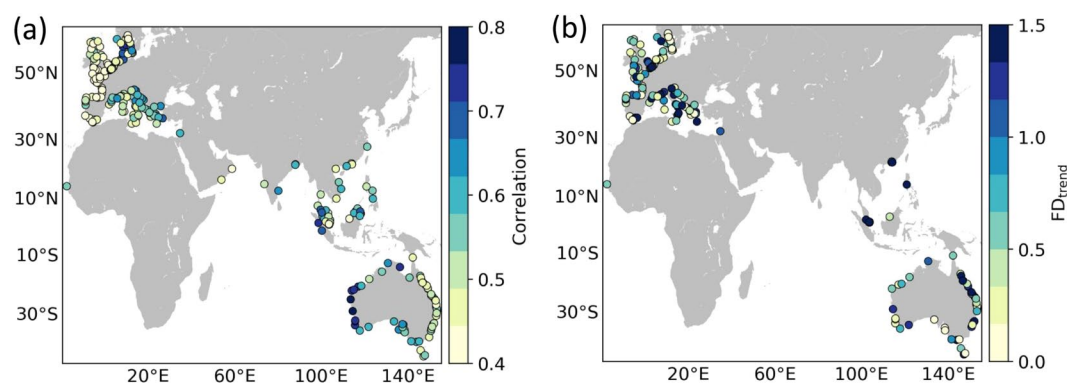

Fig. 12 Correlations (**a**) and trend FDs (**b**) for the comparison between altimetry and tide gauge observations. The correlations are for detrended and deseasoned monthly timeseries. Only tide gauges with a GPS station within 50 km are shown in (**b**).

The average correlation between the altimetry and tide gauge time series across all tide gauge stations is 0.5, indicating an overall good match, but there are clear differences in agreement between regions (Fig. 12a). These differences are most obvious along the Australian coastlines, where correlations are significantly higher along the western coast (>0.7) than on the eastern coast (~0.5). This is indicative of sea-level signals with shorter length scales along eastern Australia resulting in larger differences due to spatial separation, and thus it should not be interpreted as reflective of a difference in altimetric performance between the two coastlines. Sampling uncertainty due to variability at sub-monthly timescales present in the altimetry time series is also likely to play a role in explaining the relatively low correlations in some regions.

To place the correlations shown in Fig. 12a into a broader context, we next compare those with the correlations obtained using the SSALTO/Duacs all-sat-merged gridded product distributed by CMEMS (https://marine.copernicus.eu) at the same tide gauge stations (we compare each tide gauge with the nearest gridded point). The average correlation for the CMEMS data is 0.74 across all tide gauges, which is indeed higher than the average correlation we find for point-level measurements in our product (0.51). However, the higher correlations found with the gridded altimetry product are to be expected because the gridding process alleviates the issue of sampling uncertainty (monthly means are based on more values) and reduces the influence of both small-scale variability and measurement errors (data are 'averaged' across space and over several altimetry missions).

To illustrate this last point, we perform a second comparison with tide gauge data using an approach that merges altimetry data from different tracks based on sea-level length scales. For this, we use the SL_cci+XTRACK-ALES v1.1 along-track coastal product (available at http://www.esa-sealevel-cci.org/products),
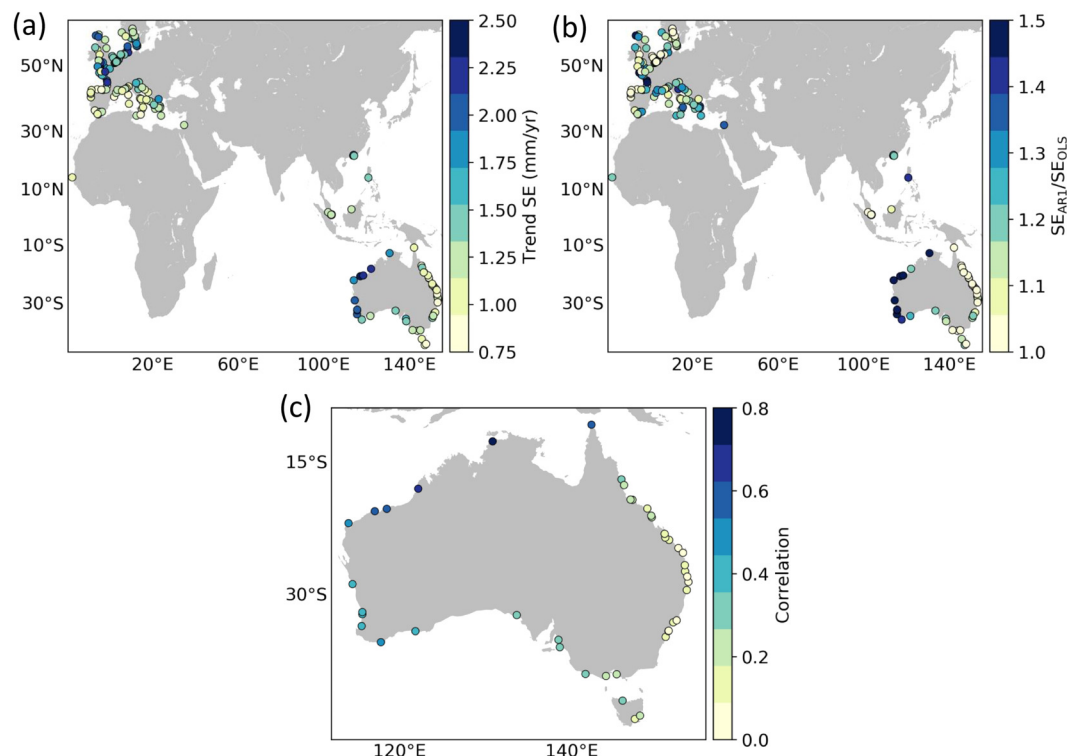
Fig. 13 Standard errors associated with the tide gauge trends as estimated by a model that accounts for serial correlation (**a**), along with the ratio between standard errors with and without consideration of serial correlation (**b**). Standard errors that ignore serial correlation are computed using ordinary least squares (i.e., assuming the residuals from the regression model are normally distributed). (**c**) Correlation between the detrended and deseasoned tide gauge records and the Southern Oscillation Index.

on which the data presented in the paper is based (this product provides data beyond 20 km from the coast, which are needed for this approach). We first estimate coherence length scales of sea level variability at each tide gauge by first correlating the deseasoned and detrended sea-level from the tide gauge record with that from along-track altimetry, and then fitting a Matérn function[37] to the vector of correlations as a function of distance to the tide gauge. Then, at each tide gauge, we merge the altimetry data from all tracks that fall within the estimated length scale into a monthly time series by averaging spatially along tracks and temporally across tracks. Using only altimetry data within a length scale from the tide gauge can reduce differences due to spatial separation. In addition, if more than one altimetry track falls within the estimated length scale, our approach allows us to compute monthly values based on many more than 4 values, alleviating the issue of sampling uncertainty. The average correlation between our merged altimetry time series and the tide gauge data is 0.78, which is slightly higher than the correlation for the CMEMS gridded product. Importantly, there are 19 tide gauge stations where our product gives significantly higher correlations (>0.2), suggesting that our product performs better at locations where sea level signals have relatively small length scales. Note that at locations where the CMEMS data performs better, the difference in correlation is smaller than 0.18 in all cases.

In regard to the trends (Fig. 12b), the median FD is 0.69 and FDs are <1 at 64% of the tide gauge stations, indicating that altimetry and tide gauge trends are in good agreement at the vast majority of stations. Again, there are regional differences such as the better agreement in western Australia compared to eastern Australia. This is again suggestive of shorter sea-level length scales along the eastern coast. There are 10 stations where FDs are >3, which reflects large trend differences. Such differences are likely due to local VLMs at the tide gauge stations that are not captured by the non-colocated GPS stations.

To get a sense of the magnitude of the trend standard errors and the effect of serial correlation on such errors, we show the values of the standard errors at all of the tide gauge stations (Fig. 13a) along with the ratio between errors with and without serial correlation adjustment (Fig. 13b). The value of the standard errors ranges from ~0.75 mm/yr to ~2.5 mm/yr, with the largest values found in regions of relatively large sea-level variability such as the North Sea and the western coast of Australia (Fig. 13a). The degree of serial correlation also varies with region, with the largest effect found in western and northwestern Australia where the true standard errors (i.e., those that account for serial correlation) can be more than 50% larger than the errors given by ordinary least squares. Interestingly, serial correlation is almost negligible along the eastern coast of Australia. This contrast between the western and eastern coasts of Australia partly reflects the much larger influence of the El Niño - Southern Oscillation on sea level along the western coast of Australia, which results in large low-frequency fluctuations there (reddening the spectrum, hence increasing serial correlation) (Fig. 13c).

Summary

In this paper, we have described a new coastal sea level product based on reprocessed satellite altimetry data from the Jason missions, available to users for a variety of applications, including studies of sea level change close to the coast and associated coastal impacts. This product is, to our knowledge, the first coastal sea level data set available at high along-track resolution (~300 m) over a time span longer than a decade. It includes validated sea level anomalies in the close vicinity of the coast (within 20 km from the coast) and associated coastal sea level trends in six regions. As shown in this study, it helps answering the question: is coastal sea level rising at the same rate as open ocean sea level? In the context of the on-going ESA CCI + project, we plan to extend in time and space this data product by updating the Jason-3 record and using additional satellites with smaller inter-track spacing (Envisat, SARAL/AltiKa, Sentinel-3A, Sentinel-3B). In this coming next phase, the data coverage will include coastlines of the whole African continent. On a longer time span, if resources permit, other regions will be studied, in particular North and South America. On the short-term, future activities will also be devoted to investigate which coastal processes cause departure of the rate of sea level change at the coast compared to the open ocean at the few sites where a trend increase/decrease has been reported (if in situ data and/or high-resolution hydrodynamical models are available). Finally, systematic comparisons with tide gauge trends will be performed at sites where the satellite tracks cross land in the vicinity of a tide gauge.

Code availability

The numerical code corresponding to the X-TRACK/ALES processing and post-processing system is not public. It is based on the merging of methodologies previously described in[7] and[16]. Further code evolutions and associated data sources are indicated in the present manuscript.

References

1. Ablain, M. et al. Altimetry-based sea level, global and regional scales. Surveys in Geophysics **38**, 7–31, https://doi.org/10.1007/s10712-016-9389-8 (2017).
2. Legeais, J. F. et al. An improved and homogeneous altimeter sea level record from the ESA Climate Change Initiative. Earth Syst. Sci. Data **10**, 281–301, https://doi.org/10.5194/essd-10-281-2018 (2018).
3. WCRP Global Sea Level Budget Group. Global sea level budget, 1993-present. Earth Syst. Sci. Data **10**, 1551–1590, https://doi.org/10.5194/essd-10-1551-2018 (2018).
4. Nerem, R. S. et al. Climate-change–driven accelerated sea-level rise detected in the altimeter era. Proceedings of the National Academy of Sciences **115**(9), 2022–2025, https://doi.org/10.1073/pnas.1717312115 (2018).
5. Stammer D., Cazenave A., Ponte R. M. & Tamisiea M. E. Causes for contemporary regional sea level changes. Annual Rev. Mar. Sci. https://doi.org/10.1146/annurev-marine-121211-172406 (2013).
6. Cazenave, A., Palanisamy, H. & Ablain M. Contemporary sea level changes from satellite altimetry: What have we learned? What are the new challenges? Advances in Space Research, https://doi.org/10.1016/j.asr.2018.07.017 (2018).
7. Birol, F. et al. Coastal applications from nadir altimetry: example of the X-TRACK regional products. Advances in Space Research **59**, 936–953, https://doi.org/10.1016/j.asr.2016.11.005 (2017).
8. Xu, X. Y., Birol, F. & Cazenave, A. Evaluation of Coastal Sea Level Offshore Hong Kong from Jason-2 Altimetry. Remote Sens. **10**, 282, https://doi.org/10.3390/rs10020282 (2018).
9. Ray, R. D., Egbert, G. D. & Erofeeva, S. Y. Tide predictions in shelf and coastal waters: Status and prospects. In Coastal Altimetry (eds. Vignudelli, S., Kostianoy, A. G., Cipollini, P. & Benveniste, J.), Springer, Berlin Heidelberg, 191–216, https://doi.org/10.1007/978-3-642-12796-0_8 (2011).
10. Vignudelli, S. et al. Satellite altimetry measurements of sea level in the coastal zone. Surveys in Geophysics https://doi.org/10.1007/s10712-019-09569-1 (2019).
11. Horwath, M. et al. ESA Climate Change Initiative (CCI) Sea Level Budget Closure (SLBC_cci) Sea Level Budget Closure Assessment Report D3.1. Version 2 (2019).
12. Hamlington, B. et al. Understanding of Contemporary Regional Sea-level Change and the Implications for the Future. Review of Geophysics https://doi.org/10.1029/2019RG000672 (2020).
13. Durand, F. et al. Impact of continental freshwater runoff on coastal sea level, Surveys in Geophysics, 40:1437–1466, https://doi.org/10.1007/s10712-019-09536-w (2019).
14. Woodworth P. et al. Forcing Factors Causing Sea Level Changes at the Coast, Surveys in Geophysics, https://doi.org/10.1007/s10712-019-09531-1 (2019).
15. Cipollini, P. et al. Satellite altimetry in coastal regions. In 'Satellite altimetry over the oceans and land surfaces', Stammer & Cazenave Edts, CRC Press, Taylor and Francis Group, Boca Raton, London, New York, pp 343-373, https://doi.org/10.1201/9781315151779-11 (2018).
16. Passaro, M., Cipollini, P., Vignudelli, S., Quartly, G. D. & Snaith, H. M. ALES: A multi-mission adaptive subwaveform retracker for coastal and open ocean altimetry. Remote Sensing of Environment **145**, 173–189, https://doi.org/10.1016/j.rse.2014.02.008 (2014).
17. Sandwell, D. T. & Smith, W. H. Retracking ERS-1 altimeter waveforms for optimal gravity field recovery. Geophysical Journal International **163**(1), 79–89, https://doi.org/10.1111/j.1365-246X.2005.02724.x (2005).
18. Tran, N., Labroue, S., Philipps, S., Bronner, E. & Picot, N. Overview and update of the sea state bias corrections for the Jason-2, Jason-1 and TOPEX missions. Mar. Geod. **33**, 348–362, https://doi.org/10.1080/01490419.2010.487788 (2010).
19. Passaro, M., Nadzir, Z. A. & Quartly, G. D. Improving the precision of sea level data from satellite altimetry with high-frequency and regional sea state bias corrections. Remote Sensing of Environment **218**, 245–254, https://doi.org/10.1016/j.rse.2018.09.007 (2018).
20. Quartly, G. D., Smith, W. H. & Passaro, M. Removing Intra-1-Hz Covariant Error to Improve Altimetric Profiles of σ0 and Sea Surface Height. IEEE Transactions on Geoscience and Remote Sensing **57**(6), 3741–3752, https://doi.org/10.1109/TGRS.2018.2886998 (2019).
21. Passaro, M., Cipollini, P. & Benveniste, J. Annual sea level variability of the coastal ocean: The Baltic Sea-North Sea transition zone. Journal of Geophysical Research: Oceans **120**(4), 3061–3078, https://doi.org/10.1002/2014JC010510 (2015).
22. Chereskin, T. K., Rocha, C. B., Gille, S. T., Menemenlis, D. & Passaro, M. Characterizing the transition from balanced to unbalanced motions in the southern California Current. Journal of Geophysical Research: Oceans **124**(3), 2088–2109, https://doi.org/10.1029/2018JC014583 (2019).
23. Gómez-Enri, J. et al. Wind-induced cross-strait sea level variability in the Strait of Gibraltar from coastal altimetry and in-situ measurements. Remote Sensing of Environment **221**, 596–608, https://doi.org/10.1016/j.rse.2018.11.042 (2019).
24. Piccioni, G. et al. Coastal improvements for tide models: the impact of ALES retracker. Remote Sensing **10**(5), 700, https://doi.org/10.3390/rs10050700 (2018).

25. Vignudelli, S. *et al*. Improved satellite altimetry in coastal systems: Case study of the Corsica Channel (Mediterranean Sea). *Geophys. Res. Let*., 32, L07608, 1029/2005GL22602 (2005).

26. Roblou L. *et al*. Post-processing altimeter data toward coastal applications and integration into coastal models. Chapter 9 In: S. Vignudelli, A.G. Kostianoy, P. Cipollini, J. Benveniste (eds.), Coastal Altimetry, Springer Berlin Heidelberg. https://doi.org/10.1007/978-3-642-12796-0_9 (2011).

27. Fernandes, M. J., Lázaro, C., Ablain, M. & Pires, N. Improved Wet Path Delays for All ESA and Reference Altimetric Missions. *Remote Sensing of Environment* **169**, 50–74, https://doi.org/10.1016/j.rse.2015.07.023 (2015).

28. Vignudelli S., A. G. Kostianoy, P. Cipollini, and J. Benveniste (Eds.), Coastal Altimetry, Springer, Berlin, https://doi.org/10.1007/978-3-642-12796-0 (2011).

29. Jebri, F., Birol, F., Zakardjian, B., Bouffard, J. & Sammari, C. Exploiting coastal altimetry to improve the surface circulation scheme over the central Mediterranean Sea. *J. Geophys. Res. Oceans* **121**, 4888–4909, https://doi.org/10.1002/2016JC011961 (2016).

30. Léger, F. *et al*. X-Track/Ales Regional Altimeter Product for Coastal Application: Toward a New Multi-Mission Altimetry Product at High Resolution, IGARSS 2019 - 2019 IEEE International Geoscience and Remote Sensing Symposium, Yokohama, Japan, 2019, pp. 8271-8274, https://doi.org/10.1109/IGARSS.2019.8900422 (2019).

31. Marti, F. *et al*. Altimetry-based sea level trends along the coasts of western Africa, *Adv. in Space Res., published online 24 May2019*, https://doi.org/10.1016/j.asr.2019.05.033 (2019).

32. Sea Level CCI+ Team. Sea Level CCI+ ECV dataset: SLCCI XTRACK/ALES Sea Level Anomalies (SLA) v1.1. *European Space Agency*, https://doi.org/10.5270/esa-sl_cci-xtrack_ales_sla-200206_201805-v1.1-202005 (2020).

33. Benveniste, J. *et al*. Coastal Sea Level Product 1. *Figshare* https://doi.org/10.6084/m9.figshare.13019813 (2020).

34. The Climate Change Coastal Sea Level Team. A database of coastal sea level anomalies and associated trends from Jason satellite altimetry from 2002 to 2018. *SEANOE*, https://doi.org/10.17882/74354 (2020).

35. Holgate, S. J. *et al*. New data systems and products at the permanent service for mean sea level. *J. Coast. Res.* **29**, 493–504, https://doi.org/10.2112/JCOASTRES-D-12-00175.1 (2013).

36. Chib, S. Bayes regression with autoregressive errors. A Gibbs sampling approach. *J. Econometrics* **58**, 275–294, https://doi.org/10.1016/0304-4076(93)90046-8 (1993).

37. Rasmussen, C. E. & Williams C. K. I. *Gaussian Processes for Machine Learning* (MIT Press, Cambridge, MA, 2006, ISBN 0-262-18253-X) (2006).

38. Cartwright, D. E. & Taylor, R. J. New computation of the tide-generating potential. *Geophysical Journal of the Royal Astronomical Society* **23**, 45–74, https://doi.org/10.1111/j.1365-246X.1971.tb01803.x (1971).

39. Cartwright, D. E. & Edden, A. C. Corrected Tables of Tidal Harmonics. *Geophysical Journal of the Royal Astronomical Society* **33**, 253–264, https://doi.org/10.1111/j.1365-246X.1973.tb03420.x. (1973).

40. Wahr, J. M. Deformation induced by polar motion. *J. Geophys. Res*. **90**(B11), 9363–9368, https://doi.org/10.1029/JB090iB11p09363 (2005).

41. Carrere, L. *et al*. FES2012: A new global tidal model taking taking advantage of nearly 20 years of altimetry,, in Proceedings of the "20 Years of Progress in Radar Altimetry" Symposium, Venice, Italy, 24–29 September 2012, Benveniste, J. and Morrow, R., Eds., ESA Special Publication SP-710, https://doi.org/10.5270/esa.sp-710.altimetry2012 (2012).

42. Carrere, L. & Lyard, F. Modeling the barotropic response of the global ocean to atmospheric wind and pressure forcing-Comparisons with observations. *Geophys. Res. Lett*. **30**(6), 1275, https://doi.org/10.1029/2002GL016473 (2003).

Acknowledgements

Author contributions

All authors contributed in different parts of the data production and validation, as well as in writing the manuscript. J.F.L. and A.C. are project manager and science leader of the CCI+ Coastal Sea Level project, respectively.

Competing interests

The authors declare no competing interests.

Additional information

Correspondence and requests for materials should be addressed to A.C.

Reprints and permissions information is available at www.nature.com/reprints.

Publisher's note Springer Nature remains neutral with regard to jurisdictional claims in published maps and institutional affiliations.

The Climate Change Initiative Coastal Sea Level Team

Jérôme Benveniste[1], Florence Birol[2], Francisco Calafat [3], Anny Cazenave [2,4 ✉], Habib Dieng[2,5], Yvan Gouzenes[2], Jean François Legeais[6], Fabien Léger[2], Fernando Niño[2], Marcello Passaro[7], Christian Schwatke [7] & Andrew Shaw[8]

[1]ESA/ESRIN, Frascati, Italy. [2]LEGOS, Toulouse, France. [3]NOC, Liverpool, UK. [4]ISSI, Bern, Switzerland. [5]OceanNext, Grenoble, France. [6]CLS, Ramonville St Agne, France. [7]TUM, Munich, Germany. [8]SKYMAT, Southampton, UK. ✉e-mail: anny.cazenave@legos.obs-mip.fr

The following manuscript is an uncorrected proof of the accepted scientific article:

Passaro M., Müller F.L., Oelsmann J., Rautiainen L., Dettmering D., Hart-Davis M.G., Abulaitijiang A., Andersen O.B., Høyer J.L., Madsen K.S., Ringgaard I.M., Särkkä J., Scarrott R., Schwatke S., Seitz F., Tuomi L., Restano M., Benveniste J.: Absolute Baltic Sea Level Trends in the Satellite Altimetry Era: A Revisit, Frontiers in Marine Science, ACCEPTED (2021)

Absolute Baltic Sea Level Trends in the Satellite Altimetry Era: A Revisit

Marcello *Passaro*[1*], Felix L. *Müller*[1], Julius *Oelsmann*[1], Laura *Rautiainen*[2], Denise *Dettmering*[1], Michael G. *Hart-Davis*[1], Adili *Abulaitijiang*[3], Ole B. *Andersen*[3], Jacob L. *Høyer*[4], Kristine S. *Madsen*[4], Ida Margrethe *Ringgaard*[4], Jani *Särkkä*[2], Rory *Scarrott*[5], Christian *Schwatke*[1], Florian *Seitz*[1], Laura *Tuomi*[2], Marco *Restano*[6] and Jérôme *Benveniste*[7]

[1] Deutsches Geodätisches Forschungsinstitut der Technischen Universität München, Munich, Germany, [2] Finnish Meteorological Institute, Uusimaa, Finland, [3] Danish Technical University, [4] Danish Meteorological Institute, Munich, Germany, [5] Department of Geography, MaREI Centre, Environmental Research Institute, University College Cork, Cork, Ireland, [6] SERCO/ESRIN, Largo Galileo Galilei, Frascati, Italy, [7] European Space Agency-ESRIN, Largo Galileo Galilei, Frascati, Italy

The absolute sea level trend from May 1995 to May 2018 in the Baltic Sea is analyzed by means of a regional monthly gridded dataset based on a dedicated processing of satellite altimetry data. In addition, we evaluate the role of the North Atlantic Oscillation and the wind patterns in shaping differences in sea level trend and variability at a sub-basin scale. To compile the altimetry dataset, we use information collected in coastal areas and from leads within sea-ice. The dataset is validated by comparison with tide gauges and the available global gridded altimetry products. The agreement between trends computed from satellite altimetry and tide gauges improves by 9%. The rise in sea level is statistically significant in all the region of study and higher in winter than in summer. A gradient of over 3 mm/yr in sea level rise is observed, with the north and east of the basin rising more than the south-west. Part of this gradient (about 1 mm/yr) is directly explained by a regression analysis of the wind contribution on the sea level time series. A sub-basin analysis comparing the northernmost part (Bay of Bothnia) with the south-west reveals that the differences in winter sea level anomalies are related to different phases of the North-Atlantic Oscillation (0.71 correlation coefficient). Sea level anomalies are higher in the Bay of Bothnia when winter wind forcing pushes waters through Ekman transport from the south-west toward east and north. The study also demonstrates the maturity of enhanced satellite altimetry products to support local sea level studies in areas characterized by complex coastlines or sea-ice coverage. The processing chain used in this study can be exported to other regions, in particular to test the applicability in regions affected by larger ocean tides.

Keywords: sea level, satellite altimetry, North Atlantic Oscillation (NAO index), Baltic Sea, coastal altimetry

1. INTRODUCTION

Coastal societies are forced to constantly adapt to changes in sea level (SL). Global SL products such as those produced by the European Space Agency's Sea Level Climate Change Initiative (SLCCI) (Legeais et al., 2018), the Integrated Multi-Mission Ocean Altimeter Data for Climate Research (Beckley et al., 2017), and the Copernicus services (Von Schuckmann et al., 2016), are proving to

be instrumental in tracking the global SL rise, one of the most severe impacts of climate change. These synoptic and objective SL products are generated using the fleet of satellite-based altimeter sensors in orbit for over two decades. However, for regional to local coastal adaptation and planning for future scenarios, regionally-tailored SL information is required.

In the Baltic Sea (BS), satellite observations are particularly important given that the network of tide gauge (TG)s, which measures relative SL, is strongly affected by Vertical Land Motion (VLM) and, in particular, due to the Glacial Isostatic Adjustement (GIA) (Ludwigsen et al., 2020). For example, relative SL trends in the northern part of the BS over the last few decades have been shown to be strongly negative, while absolute SL trends display significant positive trends (Olivieri and Spada, 2016; Madsen et al., 2019). While global altimetry products have been used to study SL in the area (Karabil et al., 2018), they are affected by data gaps that are smoothed out by the typical strong interpolation in space and time (Madsen et al., 2019). In particular, the BS includes the two main features that limited the use of satellite altimetry since the start of the "altimetry era": the presence of sea-ice and the proximity of the coast. For example, the average annual maximum extent of sea-ice in March covers up to 40% of the water surface (Leppäranta and Myrberg, 2009), and there are around 200,000 islands in almost 400,000 km^2 of water surface. However, an advantage for using altimetry in the BS is that the tidal component is limited, which mitigates the known problems of tidal modelling in areas with complex coast and bathymetry.

The advances in altimetry processing have shown that dedicated signal processing techniques are able to enhance the quality and the quantity of the retrievals (Benveniste et al., 2019). This is particularly significant when a better fitting of the radar return (retracking) is combined with a dedicated selection of corrections to the altimetric range to enhance coastal data (Benveniste et al., 2020). In the sea-ice covered areas, classification techniques are able to identify water apertures (leads), which when combined with retracking allow for the retrieval of SL. Such processing has recently driven an improved SL analysis in the Arctic Ocean (Rose et al., 2019), but has never been applied to the BS yet. This gap presented an opportunity for the European Space Agency's Baltic+ Sea Level (ESA Baltic SEAL) Project, to produce a regional gridded SL product, that incorporates observations from altimetry measurements acquired from sea-ice leads, and coastal waters.

The use of dedicated altimetry SL products, combined with external datasets, can contribute to characterise local differences in SL trend and variability (Passaro et al., 2016). The SL variability in the BS has been found to be highly correlated with the variability of westerly winds (Andersson, 2002). Wind patterns are modulated by large scale variability of the atmospheric pressure, which can be described by climate indices, and in particular by the North Atlantic Oscillation (NAO) index (Jevrejeva et al., 2005). The objective of this study, therefore, is to analyse the SL trend in the BS during the altimetry era and to characterise the relationship between wind patterns, NAO and variability in absolute SL at a sub-basin scale. To do so, we use the ESA Baltic SEAL monthly gridded SL, summarising the methodology followed to create this

dataset and assessing its performances against *in-situ* data and global gridded SL products. Subsequently, trends are computed providing statistical uncertainty that takes into account the serial correlation in the time series.

2. METHODS

2.1. Altimetry Data Processing

This study is based on the analysis of the ESA Baltic SEAL project, whose documentation is freely available from http://balticseal.eu/outputs/. In the context of this project, along-track data from most of the altimetry missions operating in the last two decades are reprocessed to generate a dedicated monthly gridded product from May 1995 to May 2018. In particular the following conventional Low Resolution Mode (LRM) altimetry missions are used: TOPEX-Poseidon (TP, from May 1995), Jason-1 (J-1), Jason-2 (J-2), ERS-2, Envisat, SARAL. Considering the latest Delay-Doppler (DD) altimetry technology, data from the following missions were acquired: Cryosat-2 (CS-2), Sentinel-3A, and Sentinel-3B (S3-A/B).

High-frequency data are downloaded, i.e., distributed at 20-Hz rate for most of the missions, except 10-Hz for TP, 40-Hz for SARAL, and 18-Hz for Envisat. A detailed list of the data source and the version of the altimetry data acquired for the reprocessing is provided in Ringgaard et al. (2020).

The overall process from radar pulse to SSH estimate delivered as a gridded product is outlined in **Figure 1**. Also outlined are the enhancements which the ESA Baltic SEAL Project implements to tailor the data produced to BS regional stakeholders, and further develop best practice for coastal altimetry globally. These enhancements are summarised in the following sections and build on the overall pulse-to-SL process.

2.1.1. Classification

In the winter months, parts of the BS especially the regions Bay of Bothnia and Gulf of Finland, as defined in **Figure 2** are covered by a dynamic changing sea-ice cover, which makes continuous, gapless SL estimations difficult. Moreover, observations during the winter season are limited to leads (i.e., narrow cracks within the sea-ice) enabling only brief spatially limited opportunities for open water measurements.

The behaviour of the reflected radar signals is used to classify lead returns and to identify open water areas within the sea-ice. The applied open water detection is based on unsupervised, artificial intelligence machine-learning algorithms. The algorithm used in this study has been described in Müller et al. (2017) for LRM altimetry and its versatility to be applied also to DD missions has been shown in Dettmering et al. (2018).

In order to group the reference datasets automatically into a specific number of clusters representing different waveforms types, the waveforms samples from a training set are introduced to a K-medoids clustering algorithm (Xu and Wunsch, 2008; Celebi, 2014). In principle K-medoids searches for hidden similarities within the data based on a given input feature space by minimizing the distance between the individual features and most centrally positioned features (medoids) from the feature space itself. At first the algorithm defines randomly K-medoids
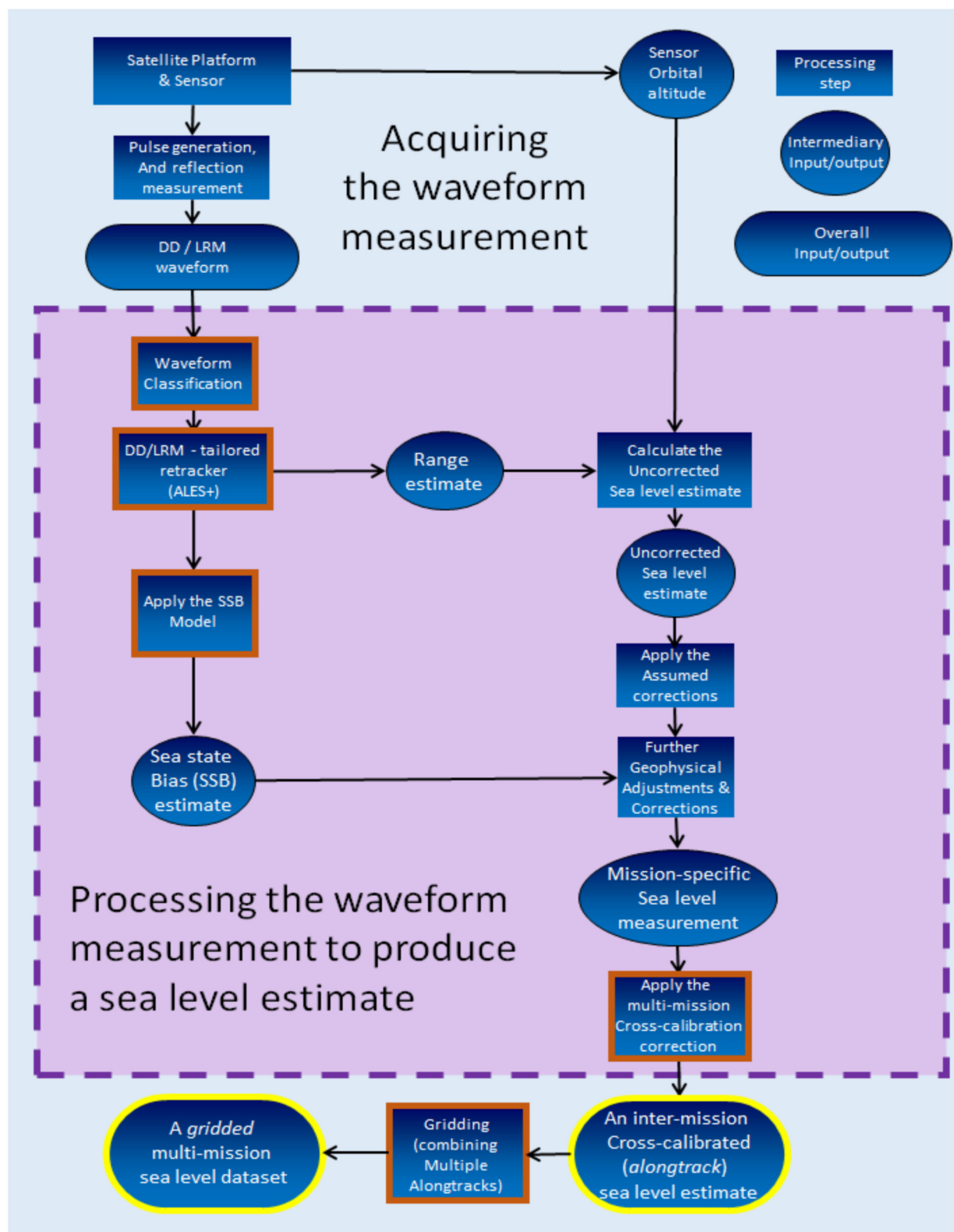
FIGURE 1 | From measurement to corrected sea level estimates delivered as along-track and gridded datasets. A simple flowchart of the origins of the waveform data, and how it is processed to produce the ESA Baltic SEAL estimate of sea level. Process steps which are enhanced and tailored for use in BS, are highlighted in orange.

FIGURE 2 | The area of study divided in different boxes representing major sub-basins. Color shades display the bathymetry.
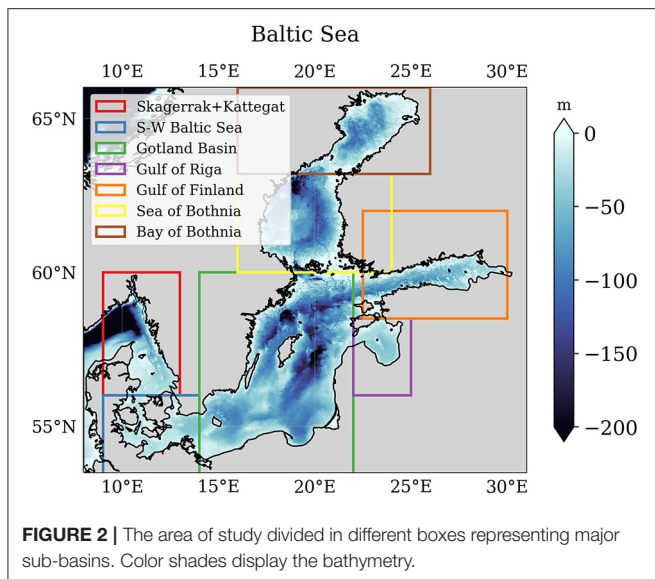
followed by the computation of the distance between all features and the initially selected K centres. In the next steps K-medoids rearranges the location of the medoids as long as there is no motion among the features. K-medoids belongs to the "partitional" clustering algorithms, which require a pre-defined number of clusters K.

After clustering, the clusters are assigned manually to the different surface types, by using background knowledge about the physical backscattering properties of the individual surface conditions and feature statistic per each cluster.

The waveform features considered are the usual ones describing the shape of the echo: waveform maximum, trailing edge decline (an exponential function fitted to the trailing edge of the waveform), waveform noise, leading edge slope, trailing edge slope. The features are applied to all required satellite missions and altimetry datasets.

The second part of the classification is related to the classification of the remaining waveforms. Therefore, a K-Nearest Neighbour (KNN) classifier is applied. KNN searches for the closest distance between the reference model and the remaining waveforms (Hastie et al., 2009). The majority of clusters among the K nearest neighbours defines which class has to be assigned to the waveform.

As a final result of the classification, each high-frequency waveform is classified as open water or sea-ice. Waveforms classified as sea-ice returns are flagged and not considered for the generation of the gridded product.

2.1.2. Retracking

All the waveforms from the altimetry missions used in this study, except for TP, are re-fitted by means of dedicated algorithms (retrackers) that are able to track the signal in open ocean, coastal, and sea-ice covered conditions.

ALES+ is the retracker that has been further developed and extended to all the missions considered in this project. ALES+

is based on the Brown-Hayne functional form that models the radar returns from the ocean to the satellite. The Brown-Hayne theoretical ocean model is the standard model for the open ocean retrackers and describes the average return power of a rough scattering surface (i.e., what we simply call waveform) (Brown, 1977; Hayne, 1980). A full description of ALES+ retracker for LRM missions is provided in Passaro et al. (2018a).

In the case of the DD waveforms, the correspondent version called ALES+ SAR adopts a simplified version of the Brown-Hayne functional form as an empirical retracker to track the leading edge of the waveform. The model simplification is achieved by assigning a fixed decay of the trailing edge, instead of a dependency with respect to antenna parameters (beamwidth, mispointing) as in the LRM case. A full description of ALES+ SAR retracker is provided in Passaro et al. (2020a). Data from CS-2, S3-A/B can be reprocessed with ALES+ SAR using the ESA Grid Processing On Demand (GPOD) service (https://gpod.eo.esa.int/, Passaro et al., 2020b).

By means of a leading edge detection, ALES+ and ALES+ SAR retrack only a subwaveform whose width is dependent on the wave height in LRM and fixed in DD. In this way, it is possible to avoid considering signal perturbations typical of the coastal zone when fitting the echoes. In the case of peaky waveforms, typical of leads within sea-ice, both algorithms perform a direct estimation of the trailing edge slope.

Together with the retracking, a dedicated sea state bias (SSB) correction is computed. The SSB correction is computed at 20-Hz rate. This guarantees a better precision of the range retrieval, since it decreases the impact of correlated errors in the retracked parameters (Passaro et al., 2018b).

For the LRM missions, the SSB correction is derived by using the same 2D map from Tran et al. (2010), but computed for each high-frequency point using the high-frequency wind speed and significant wave height (SWH) estimations from ALES+.

In the original DD altimetry products, the SSB correction is either missing (Cryosat-2) or computed using the Jason model. Here instead, a first model is computed specifically for the ALES+ SAR retracker. As a reference parameter on which the model is built, we take the rising time of the leading edge, which is taken as a proxy for the significant wave height.

The corrections are derived by observing the SL residuals (with no correction applied) at the points of intersections between satellite tracks (crossover points). A wider region covering the North Sea and the Mediterranean Sea is used in order to have more open ocean crossover points, which are scarce in the BS. The residuals are modelled with respect to the variables influencing the sea state (here the rising time of the leading edge) in a parametric formulation.

In particular, at each crossover m:

$$\Delta SL_m = \hat{\alpha}\sigma_{c_o} - \hat{\alpha}\sigma_{c_e} + \epsilon \qquad (1)$$

where o and e stand for odd and even tracks (indicating ascending and descending tracks respectively), ϵ accounts for residual errors, σ_c is the rising time of the leading edge. We have therefore a set of m linear equations, which is solved in a least square sense. The chosen α is the one that maximises the variance explained

TABLE 1 | Altimeter corrections/parameter applied to the along-track processing.

Correction	Missions								
	TP	J-1[a]	J-2	J-3	ERS-2	Envisat	SARAL	CS-2	S3-A/B
Wet Trop. (WT)	GPD/GPD+ (Fernandes et al., 2015; Fernandes and Lazaro, 2016)			VFM3 Landskron and Böhm (2018)	GPD/GPD+ (Fernandes et al., 2015; Fernandes and Lazaro, 2016)		VMF3 (Landskron and Böhm, 2018)		
Dry Trop. (DT)	ERA-Interim for Vienna Mapping Functions (VMF3) (Landskron and Böhm, 2018)								
Ionosphere (IONO)	NOAA Ionosphere Climatology (NIC09) (Scharroo and Smith, 2010)								
Dynamic Atmosphere Corr. (DAC)	DAC (inverse barometric (ECMWF), (MOG2D)HF) (Collecte Localisation Satellites , CLS)								
Solid Earth Tide (SET)	IERS Conventions 2010 (Petit and Luzum, 2010)								
Pole Tide (PT)	IERS Conventions 2010 (Petit and Luzum, 2010)								
Sea State Bias (SSB)	MGDR	ALES+ (Passaro et al., 2018a)							
@l Radial Orbit Errors (ROC)	Multi-mission cross calibration (MMXO) Vers. 18 (Bosch et al., 2014)								

[a]No GPD/GPD+ (Fernandes et al., 2015; Fernandes and Lazaro, 2016) is available for J-1 geodetic mission phase. Instead, VMF3 Landskron and Böhm (2018) is used.

at the crossovers, i.e., the difference between the variance of the crossover difference before and after correcting for the SSB using the computed model.

2.1.3. Choice of Range Corrections

Once the ranges have been obtained by retracking the waveforms, the following altimeter equation is implemented to derive the sea surface height (SSH):

$$SSH = H_{orbit} - (R + WT + DT + IONO + SSB + DAC$$
$$+SET + PT + ROC) \qquad (2)$$

The atmospheric and geophysical corrections applied are listed in **Table 1**. H_{orbit} and R stands for the orbital height above the TOPEX/POSEIDON ellipsoid and the retracked range between the satellite and the sea surface. To generate the gridded product, the SSH is also corrected for ocean tide and load tide using the FES2014 tidal model (Carrere et al., 2015).

2.1.4. Multi-Mission Cross-Calibration

In order to ensure a consistent combination of all different altimetry missions available, a cross-calibration is necessary. We follow the global multi-mission crossover analysis (MMXO) approach described by Bosch et al. (2014) in order to produce a harmonized dataset and a consistent vertical reference for all altimetry missions.

For all crossover locations, a radial correction for the observations of both intersecting tracks is estimated by a least squares approach based on crossover differences without the application of any analytic error model. These corrections are later interpolated to all measurement points of all missions included in the analysis.

The approach was developed for global calibration and is adapted for regional applications within ESA Baltic SEAL. This comprises the following points of change in comparison to (Bosch et al., 2014):

1. The maximum acceptable time difference for the crossover computations is increased from 2 to 3 days, in order to ensure enough crossover differences in the BS region.
2. For the same reason, all crossover points are used, including coastal areas.
3. For the computation of crossover differences, high frequency data are used. This is realised by changing the interpolation of along-track heights to crossover locations from point-wise to distance-wise.
4. All missions are equally weighted. The weighting between crossover differences and consecutive differences is adapted in order to account for the smaller region.

2.1.5. Gridding

After the multi-mission cross-calibration, the along-track SL estimates undergo an outlier detection whose consecutive steps are listed in Passaro et al. (2020a). After this flagging, the observations are interpolated on an unstructured triangular grid (i.e., geodesic polyhedron). The grid has a spatial resolution of 6–7 km.

The gridded monthly SL estimates are obtained by fitting an inclined plane to each grid node by means of weighted least square interpolation, considering SSH along-track information within 100 km radius around the grid node centre. Distance-based Gaussian weights are defined in a diagonal matrix W. The median absolute deviation of the along-track

SSH observation within an area in the open sea without complex topographic features is computed per mission and used as an estimation of the uncertainty. This is placed as variance on the main diagonal of the uncertainty matrix Q_{bb}. The uncertainty information and W are combined to form the least-squares weighting matrix P_{bb}, following the equation:

$$P_{bb} = W * (\frac{1}{Q_{bb}}) \qquad (3)$$

In order to eliminate still existing outliers among the along-track data within the cap-size, the weighted least square estimation is performed iteratively. At each iteration, the difference between the monthly average and all along-track SSH values is evaluated. The along-track estimates whose residual exceeds 3 times the standard deviation of all residuals (3-sigma criterion) are flagged as outliers and the weighting matrix P_{bb} is consequently updated, before a new least-squares adjustment is performed.

Finally, an additional outlier rejection based on a Student distribution is performed: the standardised residuals of each remaining observations within the search radius are tested against quantiles of the Student distribution (t), setting the 99th percentile as boundary condition. If a standardised residual is smaller than the value of the t distribution, the corresponding observation is used in a last iteration of the least-squares adjustment.

2.2. Validation of the Altimetry Product

To validate the gridded SL product from altimetry, we perform a comparison against SL data from TGs. The main source of data is the Copernicus Marine Environment Monitoring Service (CMEMS) service and some data are complemented from the national datasets of the Danish Meteorological Institute (DMI), the Finnish Meteorological Institute (FMI) and the Swedish Meteorological and Hydrological Institute (SMHI). A full list of TG data sources used in this study is available in Ringgaard et al. (2020).

To avoid gaps in the time series, we consider only grid points with at least 250 months of valid data. We also divide the BS in different sub-basins whose naming and geographical extensions are provided in **Figure 2**.

The TG and altimeter SL measurements are not equivalent and hence both data sets were further processed before they were compared. In particular, to allow the comparison, the DAC was added back to the altimetry data, since TG data is not corrected for it.

The SL reference frame of the altimeter SL height is tied to the TOPEX ellipsoid, while TG SL height data are referred to the Normaal Amsterdams Peil (NAP) reference frame. To allow for comparison of the TG-altimetry pairs, the mean of the gridded SL was removed and set equal to the mean of the corresponding TG.

In order to validate the gridded dataset, the grid points within 20 km from every TG are considered. As the gridded dataset has a frequency of a month, the TG data are monthly averaged. TGs measure relative SL and altimeters measure absolute SL, hence the effect of land uplift is removed from the TG data using the GIA model NKG2016LU (Vestøl et al., 2019). NKG2016LU is

the latest GIA model for the BS. The closest absolute land uplift values are located for each TG and used for trend removal.

The root mean square error (RMSE) and the Pearson correlation coefficient (r) are computed for all TG-grid pair time series and the results are displayed in **Figure 3**. Out of 67 TGs and gridded altimetry pairs, 62 show a correlation higher than 0.6 and 61 have a RMSE lower than 9 cm. The lowest performing area is located north of the Danish straits. A possible reason lies in the performances of the tide corrections, which are much more important north of the straits, than in the BS.

The results of the validation considering the sub-basin division used in this study are summarised in **Table 2**. For this purpose, TG and altimetry gridded data are averaged in space across each sub-basin and in time every 3 months. The comparison shows that the correlation is never lower than 0.75 and the RMSE is never higher than 0.10 m.

## 2.3. Methods for SL Analysis
2.3.1. Trend Computation

We estimate the seasonal cycle, the linear trend and the parameter uncertainties by fitting multi-year monthly averages (to approximate the seasonality) and a linear trend to the monthly gridded data. In terms of formulation, this means fitting the time series $d(t)$ with the model $y(t)$, which for every monthly step t is defined as:

$$y(t) = o + at + m_i + \epsilon \qquad (4)$$

Where o is an offset term, a is the linear trend, m_i is the multiyear monthly mean for the month i corresponding to the time step t and ϵ is the residual noise. The trend estimate is found solving the fitting by linear least squares. The standard error σ of the least square solution would be nevertheless unrealistic, since it would not consider the autocorrelation of the time series. Therefore, to account for the autocorrelation, σ is found by an iterative maximum likelihood estimation (MLE), as described in [6]. This requires the definition of an appropriate covariance matrix of the observations, including a formulation of the residual noise. In particular, we investigate the fit of a variety of different stochastic noise model combinations as done in e.g., Royston et al. (2018): These are an autoregressive AR(1) noise model, a power law plus white, a generalized Gauss Markov (GGM) plus white, a Flicker noise plus white and an auto-regressive fractionally-integrated moving-average (ARFIMA) model. For the considered domain we find that on average the AR(1) has the lowest mean (or median) values of the Akaike Information Criterion (AIC, Akaike, 1998) and the Bayesian Information Criterion (BIC, Schwarz, 1978). Finally, the uncertainties provided in this study are scaled as $1.96 * \sigma$ to obtain a 95% confidence interval.

2.3.2. Principal Component Analysis

We perform a Principal Component Analysis (PCA) (Preisendorfer, 1988) to investigate the major modes of SL variability in the BS. For this purpose, we consider a set of multiple SL anomalies $x_k(t)$, where k and t describe the dimensionality of the data in space and time, respectively. To identify the maximum modes of joint space and time variations,
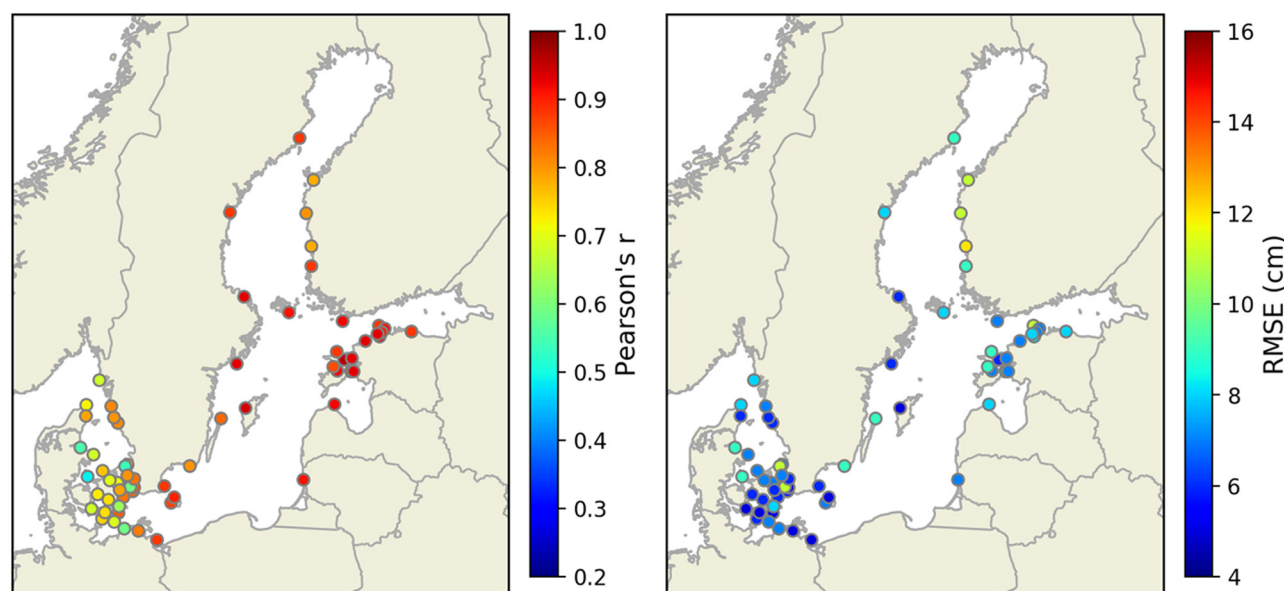
FIGURE 3 | Correlation coefficient and root mean square error between every TG considered and the altimetry grid points used for trend computation which are located within 20 km. The circles showing the statistics are co-located with the TGs.

TABLE 2 | Pearson Correlation Coefficient and RMSE between TGs and gridded altimetry averaged in space over the sub-basins considered in this study and in time every 3 months.

Sub-basin	r	RMSE (m)	Num of samples
Skagerrak+Kattegat	0.75	0.08	1,698
S-W Baltic Sea	0.76	0.07	3,367
Gotland Basin	0.91	0.07	1,336
Gulf of Riga	0.92	0.08	145
Gulf of Finland	0.91	0.08	1,318
Sea of Bothnia	0.84	0.10	1,612
Bay of Bothnia	0.88	0.09	112

we determine a set of linear combinations in form of Principal Component (PC) $u_m(t)$ and associated eigenvectors or Empirical Orthogonal Function (EOF) e_{km}. The linear combinations, or the modes are arranged such that the higher-order modes $m = 1, 2, 3, \ldots$ explain the highest variance fractions of the data. The PCs $u_m(t)$ are equal to the projection of the data vector onto the mth eigenvector $e_k m$ (e.g., Wilks, 2006):

$$u_m(t) = \sum_{k=1}^{K} e_{km} x_k(t), m = 1, \ldots, M \qquad (5)$$

In this manner the data is explained by a set of PCs, which represent time series (which are uncorrelated or independent from each other), as well as the EOFs (or eigenvectors) which represent the geographical coherence of the individual modes.

We compute the EOF and their PC from monthly gridded deseasoned SL. The latter is called sea level anomaly (SLA)

in this description, since it is the anomaly with respect to a monthly-based average (for example, based on the average for all Januaries in the period of record at a particular grid point). In this way we capture the "full-year" monthly variability and no seasonal variations. Because monthly SL variability is generally most pronounced in winter, the derived full year EOF-pattern are very similar to the once derived only over the winter season (DJF). EOF patterns are given as point-wise correlations of their PCs with SLAs.

2.3.3. Regression Analysis

We use a simple statistical approach to understand the relation of surface winds and SL trends: We compute point-wise linear regressions of the deseasoned, monthly and basin-averaged surface winds (horizontal U component and vertical V component) and SLAs by solving for: $SLA(t) = aU(t) + bV(t) + \eta$, where a and b are the first order partial regression coefficients to be estimated and η is the residual (e.g., Storch and Zwiers, 1999; Dangendorf et al., 2013). Based on these point-wise linear regressions we estimate a linear trend (without seasonal component) which is explained by the individual wind components as well as the explained variance of SL variability by the components (as for example in Dangendorf et al., 2013).

3. RESULTS AND DISCUSSION

3.1. Absolute Sea Level Trends

Figure 4 shows the map of SL trends estimated using the ESA Baltic SEAL dataset. Superimposed in circles along the coast are the estimations of the TGs, which are corrected for GIA. In accordance to previous studies based on the altimetry era (e.g., Madsen et al., 2019), it is found that the absolute SL has been rising throughout the region. The rate of SL rise increases from

FIGURE 4 | SL trends **(A)** and corresponding uncertainties **(B)** estimated by altimetry (shading) and TGs (circles) from May 1995 to May 2018. TGs are corrected for the GIA using the NKG2016 model. Uncertainties are reported as 95% confidence interval.
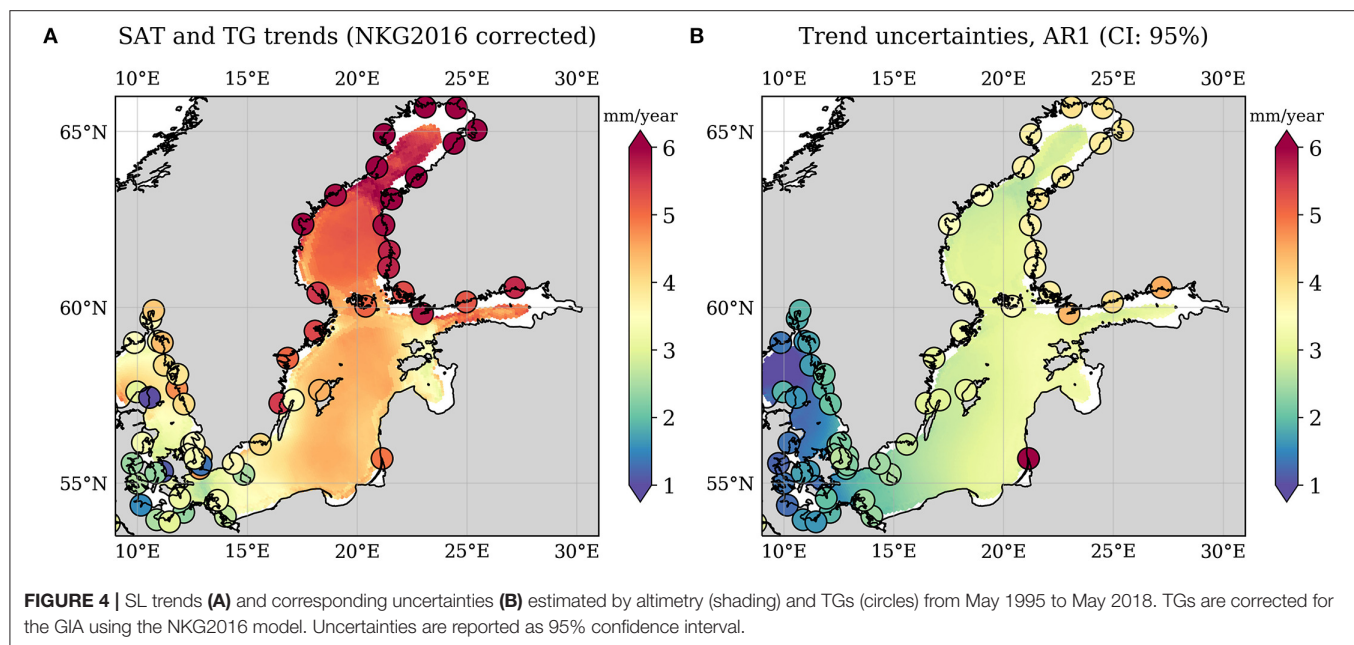
the South West of the Baltic Sea (S-W) to the Gotland Basin, and from the Gotland Basin to the Bay of Bothnia and the Gulf of Finland.

By retrieving the SL information from the leads within sea-ice in winter, we are able to extend the analysis to areas characterised by seasonal sea-ice coverage, i.e., Bay of Bothnia and Gulf of Finland. Nevertheless, gaps are still present in such regions along the coast. Other remaining gaps involve locations in the Danish Archipelago, where the predominant presence of land within the search radius of each grid point hinders to find enough data in particular during years in which few altimeters were in orbit. Finally, our SL analysis does not provide results in some parts of the Turku Archipelago (south-western Finnish coast). The presence of numerous islets in this area means that the vast majority of SL retrieval are located at distances below 1 km from the nearest land. This is well below the possibilities of any LRM altimeter, even using a coastal retracking to avoid land contamination.

These data gaps could be artificially mitigated by means of heavier interpolation and different weighting in the gridding process, nevertheless the choice in this study is to avoid generating information that is indeed not available. The comparison of the agreement between the SL trends from different altimetry dataset and TGs presented in **Figure 5** is a proof of the validity of our solution. In the histograms, the SL trend estimates from the TGs are compared with the closest estimates from altimetry using data from this study (**Figure 5A**) and data from CMEMS (**Figure 5B**, Taburet et al., 2019). In **Figure 5C**, the length of the time series of this study is May 1995–December 2015, to enable the comparison with the gridded product of the SLCCI (**Figure 5D**, Legeais et al., 2018). In both pairs of comparison, the comparability between trends from altimetry and from TGs improves by 9% using the Baltic+ data

in terms of root mean square of the differences. All the altimetry dataset show a median of the trends that is about 0.2 mm/yr lower than in the TG records. We acknowledge that the nonlinear elastic uplift from present day deglaciation, which is not taken in consideration by the GIA model, may affect the bias, although GIA has been shown to be the dominating source of vertical deformation in the region (Ludwigsen et al., 2020).

Figure 4B also shows the uncertainty of the computed trends. This is a purely statistical function of the number of samples in the time series and their SL variability, taking in consideration the serial correlation. The same method is used also to estimate the uncertainty of the trend estimated from TGs, which also do not have an uncertainty value associated to each measurement. This is in line with most of the studies estimating trends from altimetry measurements, for example (Benveniste et al., 2020). The possibility to associate an uncertainty to the single altimetry measurement has been explored by (Ablain et al., 2016) and analysed in the BS by Madsen et al. (2019), but requires a large amount of assumptions concerning every single correction added to the altimetric range. Nevertheless, our statistical uncertainties show a similar pattern and range of the ones shown in Madsen et al. (2019).

By grouping the grid points according to their location, **Figure 6** displays the averaged SL trends of each sub-basin with their statistical uncertainty. In **Figures 6B,C**, the monthly time series for the Bay of Bothnia and the S-W are shown as examples, since they present the largest discrepancies in the linear trend estimations. The rise in SL is statistically significant in all sub-basins. The spatial variation of the best estimate of the linear trend is confirmed, although the uncertainties due to the larger variability of the SL time series in most of the sub-basins cannot ensure statistical significance to this assertion yet.
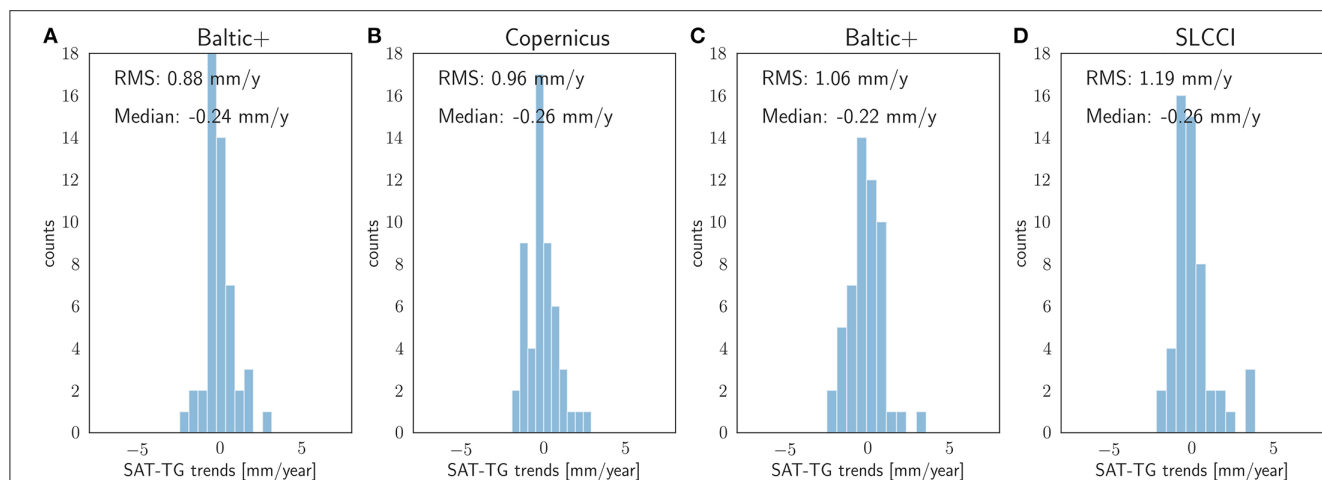
FIGURE 5 | Histograms of the differences in estimated SL trends from gridded altimetry (SAT) and TGs, compared using the closest point. Each panel correspond to different SAT dataset: the altimetry dataset from May 1995 to May 2018 developed in this study (**A**, Baltic+), the altimetry dataset from May 1995 to May 2018 CMEMS (**B**, Copernicus), the altimetry dataset from May 1995 to December 2015 developed in this study (**C**, Baltic+), the altimetry dataset from May 1995 to December 2015 of the SLCCI (**D**, SLCCI).
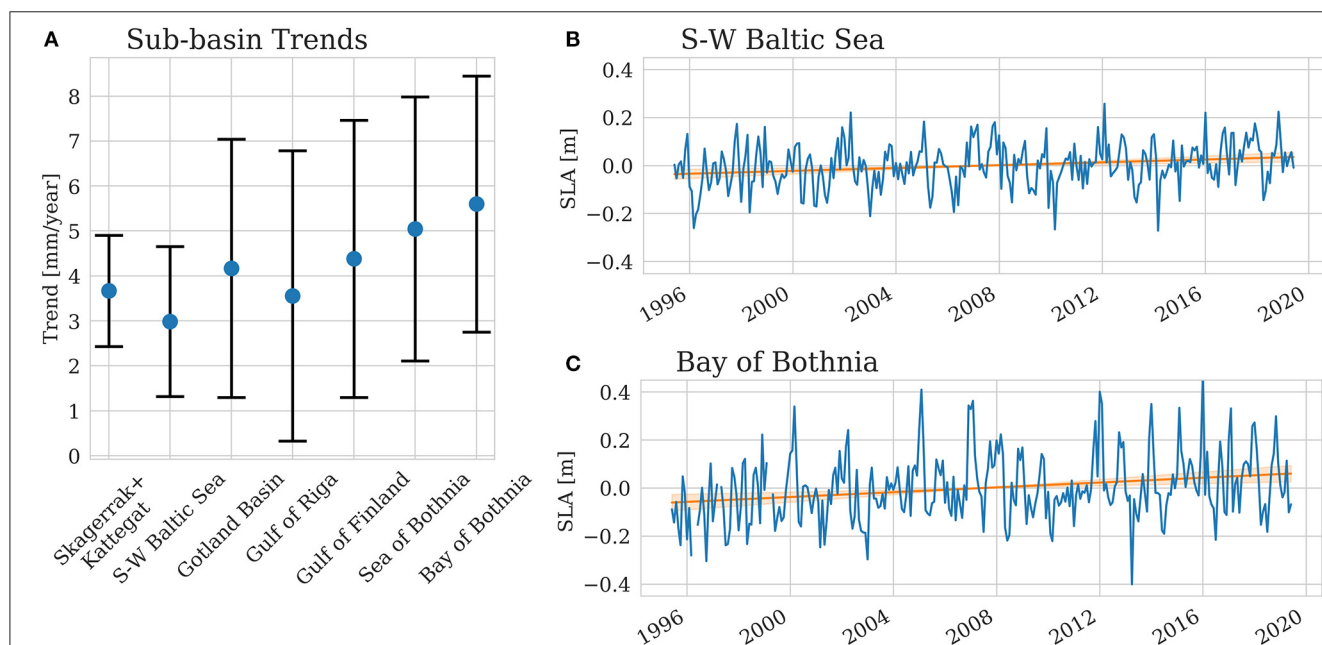
FIGURE 6 | SL trends from gridded altimetry averaged across different sub-basins of the BS from May 1995 to May 2018. Corresponding uncertainties are reported as black error bars. **(B,C)** Monthly SL time series of the S-W Baltic Sea and the Bay of Bothnia. The linear trend is shown as a red line, with the shading representing its uncertainty.

Figure 7 shows the trends in SL considering only the winter months (**Figures 7A,C**) and only the summer months (**Figures 7B,D**). Positive trends are found in the winter SL, with a difference of over 4 mm/year comparing the winter trends in their minimum and maximum values. A similar gradient in SL trend estimates is seen for the full time series in **Figure 4A**. This spatial variation in the trend is less pronounced in summer. Due to the relatively short duration of the time series, the seasonal

trend uncertainties are comparatively large. Thus, we investigate whether a similar pattern can also be found in TG records, which spans much longer periods than the altimetry time series.

Figures 8A–D report the best estimate of the linear trends in SL from the longest TG time series in the region, spanning from 1920 to 2020 at intervals of 25 years. Indeed, the same gradient of about 4 mm/yr in SL trend estimates from altimetry across the basin is observed in the most recent TG record (**Figure 8A**). It
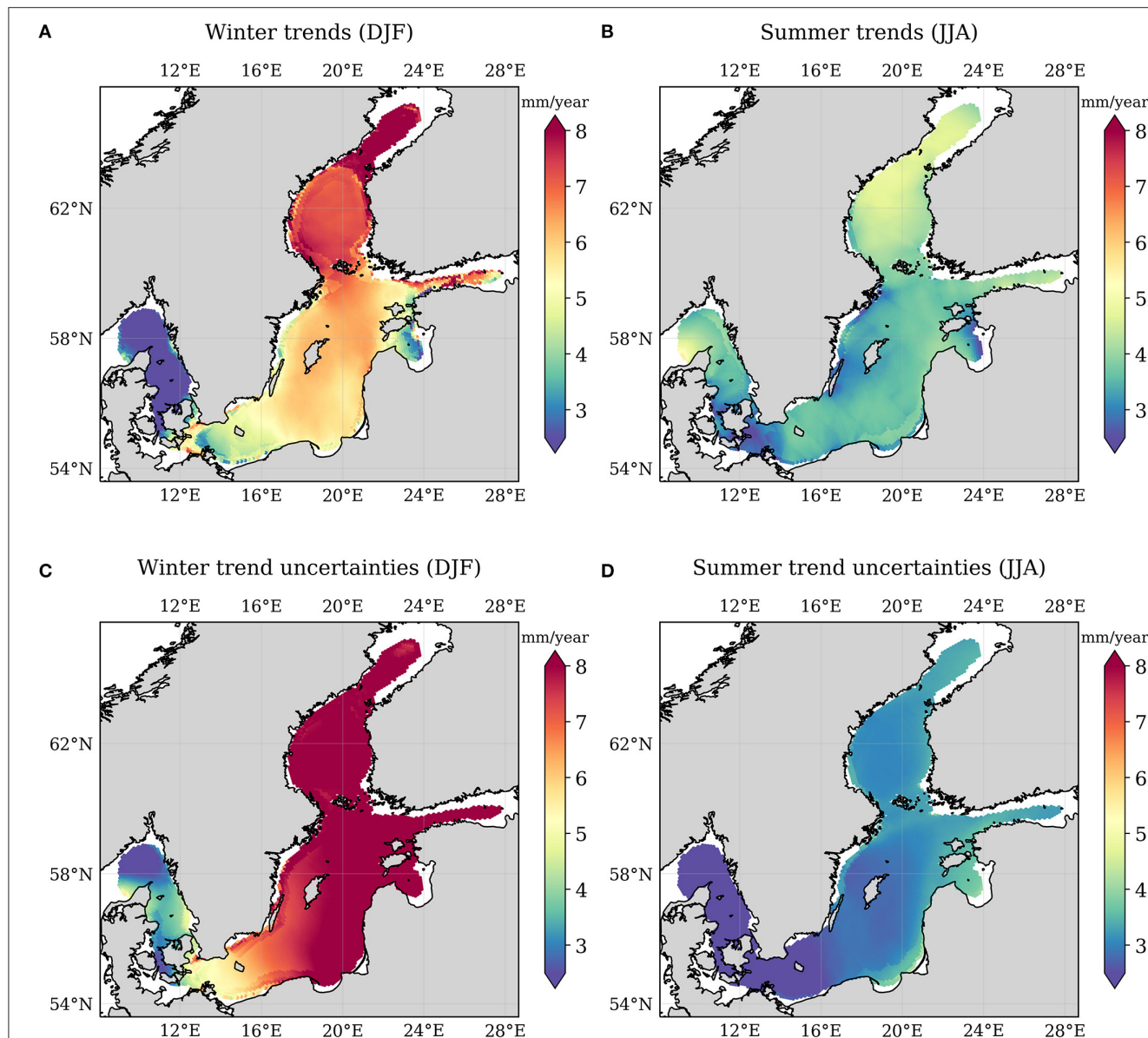
FIGURE 7 | SL trends with uncertainties from gridded altimetry computed using only the winter months (December, January, and February, **A,C**) and the summer months (June, July, and August, **B,D**).

is observed not only that the SL rise in the BS is evident in the last 50 years, but also that the spatial gradient in trends has been increasing in time.

In the next section, we analyse the possible role of wind patterns and the NAO in shaping this spatial gradient.

3.2. Discussion
3.2.1. Relationships With Wind Pattern
To analyse the spatial and temporal pattern of SL variability and how they differ locally across the basin, we perform an EOF analysis on the deseasoned altimetry time series at each grid point (as described in section 2.3.2). **Figures 9A,D** show the spatial patterns of the first and second EOFs. We find that 87.4% of

the variance in the entire domain is explained by the first EOF, which is associated with a uniform SL pattern across the basin. The second EOF, while representing 3.1% of the variance, is connected to a SL variability with a strong gradient from S-W toward Bay of Bothnia and Gulf of Finland, generating SL anomalies of opposite sign.

To characterise these two modes, we correlate the accompanying PC to the zonal (U) and meridional (V) components of the surface wind from the ERA5 reanalyses (Hersbach et al., 2020). The results displayed in **Figures 9B,C,E,F**, show that the PC1 is correlated with U in the South of the basin, with the correlation degrading toward North. The predominance of the zonal component in shaping the SL

FIGURE 8 | SL trends from TGs computed at 25-year intervals from 1920 to 2020. **(A)** Linear trends 2020–1995, **(B)** linear trends 1995–1970, **(C)** linear trends 1970–1945, **(D)** linear trends 1945–1920.

FIGURE 9 | (A,D) Empirical orthogonal functions of SL variability expressed as correlation of their corresponding PC against the SL time series at each grid point. **(B,C)** Correlation between the first PC of SL variability and the zonal (U) and meridional (V) component of the surface winds. **(E,F)** Same for the second PC.

variance of the region is in accordance with previous studies, for example Johansson et al. (2014). PC2 is instead well described by the variability of V, with correlation values over 0.5 in all our region of study.

To further study how the wind variability may affect the estimates of SL trend during the altimetry era, we perform a multiple regression analysis of the SL time series using the U and V wind components (as described in section 2.3.3). We consider the large scale wind field by spatially averaging the monthly wind speed over the entire domain. The results are shown in **Figure 10**, in which the explained trend for each component of the wind and for the sum of the two components is presented, with its uncertainty. The average variance explained

is 31% by U and 2% by V, but the latter explains over 15% of the variance in the Bay of Bothnia (not shown). Despite the high variance explained, the U regression shows a very small, homogenous trend in the whole BS, while V is responsible for a gradient of over 1 mm/yr from South to North. Although a conclusive statement with statistical relevance cannot be drawn, given the uncertainties, both EOF and regression analysis point out to the same role of the meridional wind component to shape a North-South imbalance in the SL anomalies. Recently, spatial gradients of the SL trend within the BS have been attributed, based on circulation models, to an increase in the days of westerly winds, which increase transport toward the east (Gräwe et al., 2019). Our analysis suggests that the meridional
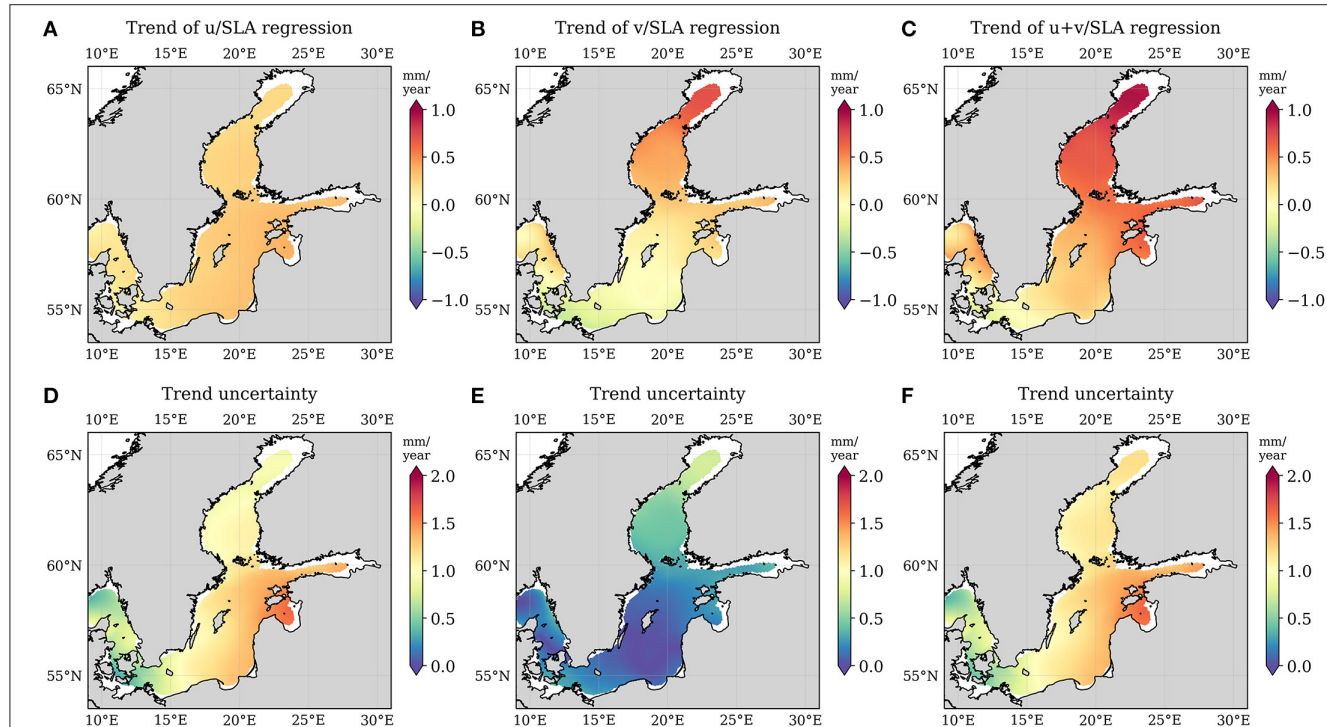
FIGURE 10 | Trends (and corresponding uncertainties) resulting from the regression of the zonal (U, **A**) and meridional (V, **B**) component of the surface winds on the SL time series. **(C)** Shows the trend obtained summing the two components of the regression.

wind component also affects the differences in SL trend among the sub-basins.

3.2.2. Relationships With North-Atlantic Oscillation

The large scale variability of both SL and wind patterns in our area of study can be well-described using teleconnections. There is a strong agreement that the NAO is the leading mode of atmospheric circulation in the region (Andersson, 2002; Jevrejeva et al., 2005). Interconnections with other climate patterns and the corresponding indices have been shown to play a role in the area, such as the East Atlantic (EAP) pattern, Scandinavian (SCAN) pattern (Chafik et al., 2017) and the BS and North Sea Oscillation index (BANOS) (Karabil et al., 2018).
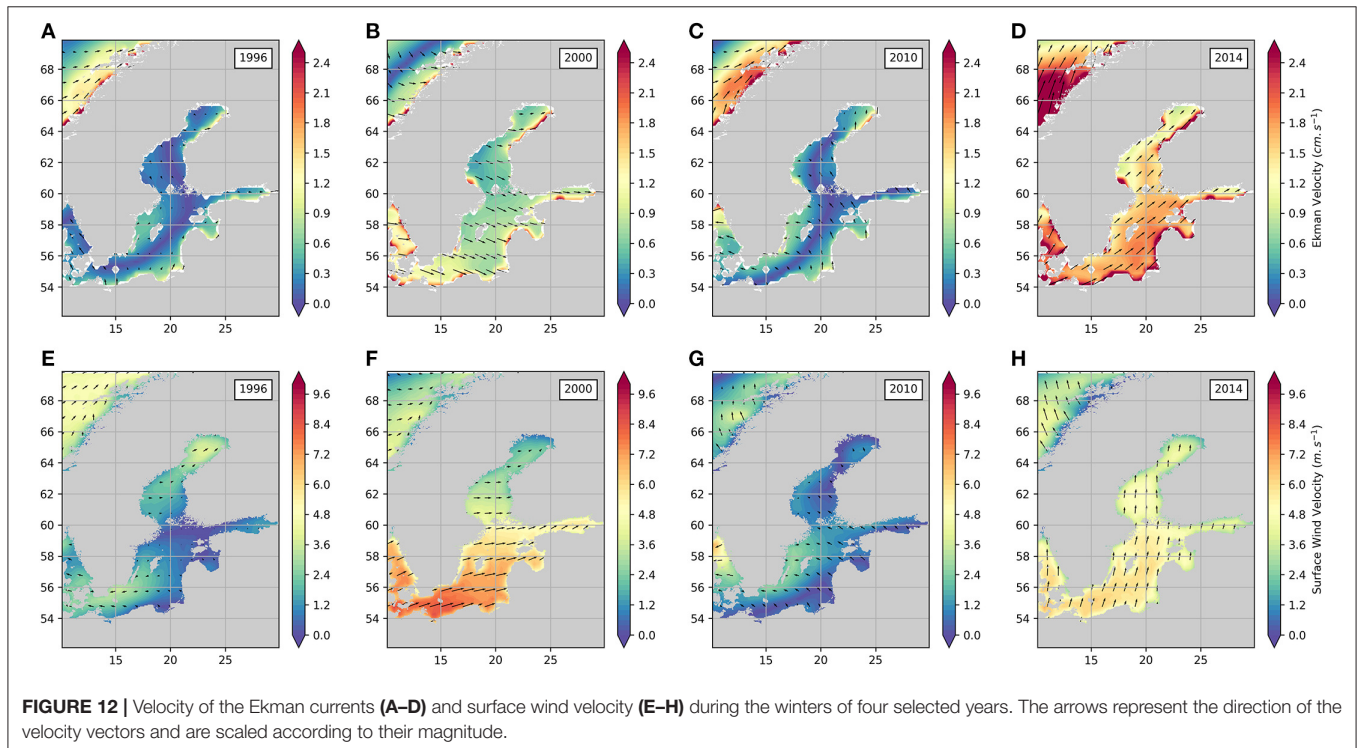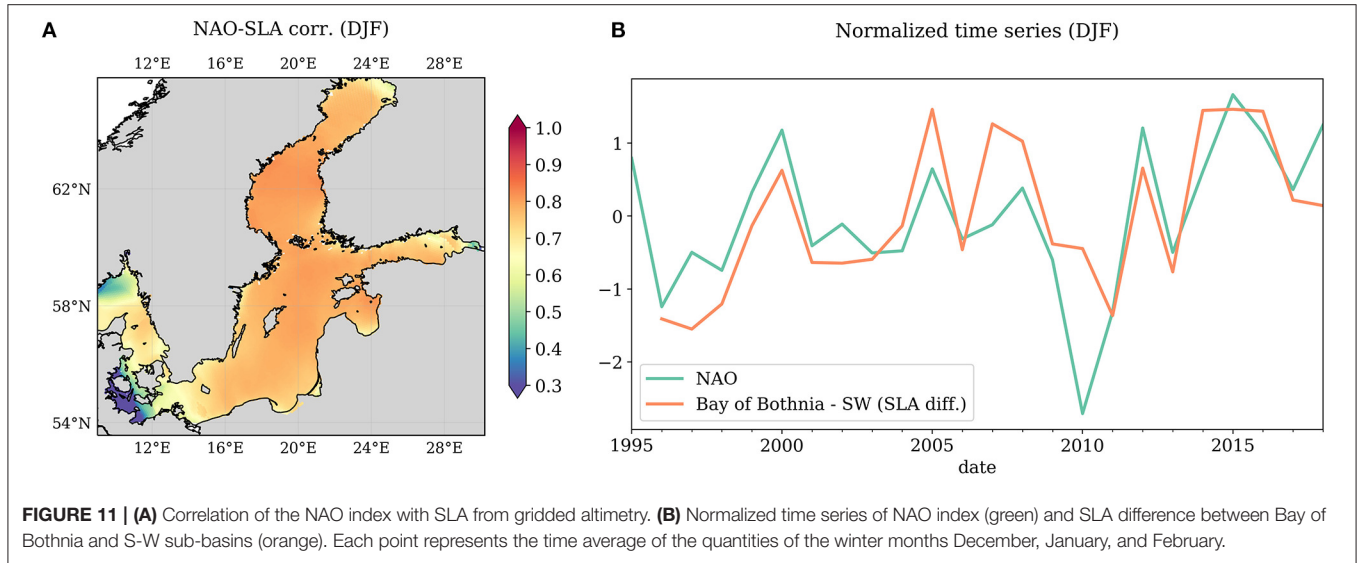
We focus on the local effects of NAO variability, since the relationship of NAO to the Baltic SL variability has been previously reported to be spatially heterogeneous (Jevrejeva et al., 2005 with TG observations, Stephenson et al., 2006 with global models). **Figure 11A** shows that in the altimetry era the correlation between the SL variability and the NAO index is dominant in winter, as expected, and uniform in all domain except for the S-W.

The possibility given by our dataset to observe local SL changes in winter in the sea-ice covered areas allow a basin-wide comparison of the Bay of Bothnia against the S-W, which present the largest discrepancies in the linear trend estimations. In **Figure 11B**, the difference in SL (Bay of Bothnia–S-W) in the winter months is plotted against the NAO index. The correlation between the two curves is 0.71. From the comparison it is seen

that positive NAO phases are related to winters in which the SLA are higher in Bay of Bothnia than in S-W. As seen in the next section, this is linked to the action of stronger southerlies and westerlies winds during positive NAO phases, which push the water north and east of the basin through Ekman transport. The intensity of the NAO phase, which is linked to the wind forcing (Dangendorf et al., 2013), is here shown to drive differences of SLA at a sub-basin scale in the BS, with interannual variations that have an effect on the linear trend of the SL estimated on time series spanning two decades of observations. In particular, as seen in **Figure 10**, the effect of the positive NAO phases in our period of observation results in a wind-related SL trend increasing toward north.

3.2.3. Ekman Currents

Winds affect the surface circulation of water masses through Ekman transport. We show in **Figure 12** the average winter wind speed direction (**Figures 12E–H**) and the resultant Ekman currents (**Figures 12A–D**) in selected winter seasons to observe the mechanism that may regulate the SL differences among different sub-basins within the BS. The years are chosen based on the highest and lowest differences between the winter SLA of Bay of Bothnia and the S-W as reported in **Figure 11B**. We analyse the Ekman transport at 15 m depth from GlobCurrent (Rio et al., 2014). The Ekman currents are distributed on a 1/4 of a degree grid and they are derived using wind stress from ECMWF, Argo floats and *in-situ* surface drifter data.

FIGURE 11 | (A) Correlation of the NAO index with SLA from gridded altimetry. (B) Normalized time series of NAO index (green) and SLA difference between Bay of Bothnia and S-W sub-basins (orange). Each point represents the time average of the quantities of the winter months December, January, and February.

FIGURE 12 | Velocity of the Ekman currents (A–D) and surface wind velocity (E–H) during the winters of four selected years. The arrows represent the direction of the velocity vectors and are scaled according to their magnitude.

When considering these results, we are dropping the hypothesis of a fully developed Ekman spiral, in which case the transport would be perpendicular to the wind direction. Nevertheless, given the low depths of the S-W of the BS, the 15 m-depth Ekman transport should be a good approximation at least in this sub-basin. Since the Bay of Bothnia is covered by sea-ice for most of the winters, which hinders formation of an Ekman spiral, and since sea-ice is not taken into account in the GlobCurrent product, we are mostly interested in the effect of the Ekman currents in the southern part of the domain. The results

are consistent with the Ekman transport pushing the surface waters to the right of the wind direction.

Winters with SLA higher in Bay of Bothnia than in S-W (e.g., 2000, 2014) are either characterised by strong westerlies in S-W whose intensity decrease toward the North (e.g., 2000), or by a marked southerly component of the wind (e.g., 2014). Years in which the differences are very low, or even flip (e.g., 1996, 2010) are characterised by much lower wind speed.

In conclusion, the years in which the winter SLA in the Bay of Bothnia are higher than in the S-W are characterised by a

strong Ekman transport, which affects the sea-ice free part of the domain. This mechanism fails during the negative NAO phases, directly affecting the SL difference between the two sub-basins.

4. CONCLUDING REMARKS

This study analysed the SL trend in the BS during most of the altimetry era (1995–2018). A new reprocessing in the framework of the ESA Baltic SEAL project enables the retrieval of more data in the coastal zone and among sea-ice. A trend analysis based on this dataset improves the agreement with trends estimated using GIA-corrected TGs (**Figure 5**). The information retrieved from the leads among sea-ice covered areas enhances the possibility to study SL variability and its differences across the basin during winter, which is the season with the largest SL rise in our observation period (**Figure 7**).

The absolute SL rise is statistically significant in the entire domain, since the uncertainties are lower than the trend estimates (**Figure 4**). Differences in trends among the different sub-basins are not statistically significant, but are seen in both the TGs and the altimetry dataset (**Figure 6**).

The absolute SL rise is a year-round phenomenon, although trends are higher in winter than in summer. The gradient in SL rise across the basin mainly occurs during winter (**Figure 7**). SL differences between the North and the South West of the BS are shown to be well-correlated with the NAO index in winter (**Figure 11**). In particular, winter positive NAO phases trigger lower SL anomalies in the S-W, as strong south-westerly winds transport surface water away from the sub-basin (**Figure 12**).

The NAO drives not only the SL in the entire domain, but is shown to also affect internal sub-basin gradients. A part of it can be explained by wind forcing, which accounts on average for about 40% of the SL variability. Other factors can contribute to the observed spatial gradient of the SL trend, which we plan to consider in a future study. Karabil et al. (2018) for example observes that a possible driver can be the freshwater flux, but this would be particularly pronounced in summertime, therefore would not explain the larger trend differences found in winter. The increasing use of GRACE data to compute mass SL changes at a regional scale (Kusche et al., 2016) and the availability of sea surface temperature and salinity datasets can be combined with measurements from the Argo floats (Guinehut et al., 2004; Boutin et al., 2013) (particularly in a low-depth basin like the BS). This suggests that a regional SL budget based on observational data shall be the subject of a future study and the next step to increase our knowledge of the Baltic SL variability and drivers.

This study highlights the value of developing regionalised SL products, using satellite altimetry measurements. It has improved the efficacy of retrieving meaningful SL observations from areas featuring complex coastlines, and those affected by sea-ice contamination of the altimeter footprint. While current efforts in the exploitation of altimetry in the coastal zone are focused on the analysis of along-track data, this work for the first time employs a coastal-dedicated reprocessing to produce gridded sea level data. Moreover, we have demonstrated that such techniques are able to obtain reliable sea level time series also in areas and seasons interested by sea-ice coverage. The BS has proved to be an excellent region to explore these issues concerning coastal altimetry. Using the best practice advances developed here, comparative analyses can be conducted in more tide-prone regions to test the further applicability of our approach.

DATA AVAILABILITY STATEMENT

The datasets presented in this study can be found in online repositories. The names of the repository/repositories and accession number(s) can be found at: http://balticseal.eu/data-access/.

AUTHOR CONTRIBUTIONS

MP designed the study, wrote the manuscript, and was the principal investigator of the research group. He was also the author of the retracking algorithm and of the sea state bias correction developed for this study. FM was responsible for the classification and the gridding. He was the main responsible for the altimetry database organisation, with CS and DD. FM also contributed in the coordination of the activities of the research group. JO was responsible for the trend and sea level variability estimation and interpretation. DD was responsible for the multi-mission calibration. AA and OA were responsible for the mean sea surface used to obtained the sea level anomalies. MH-D contributed in the interpretation of the sea level trends. FS provided the basic resources making the study possible and coordinates the activities of the research group at TUM. RS helped in the coordination of the research group and reviewed the manuscript. JH, KM, and IR contributed to the interpretation of the results. LR, JS, and LT were responsible for the validation of the along-track data. MP, MR, and JB conceptualized the research project. MR and JB reviewed the manuscript and all deliverables of the research project and supported the validation activities of the ALES+ SAR retracking algorithm. All authors read, commented, and reviewed the final manuscript.

ACKNOWLEDGMENTS

The following manuscript is the accepted version of the scientific article:

Passaro M., Hemer M., Quartly G.D., Schwatke C., Dettmering D., Seitz F.: Global coastal attenuation of wind-waves observed with radar altimetry, Nature Communications, Under Review, ACCEPTED (2021)

Abstract

Coastal studies of wave climate and evaluations of wave energy resources are mainly regional and based on the use of computationally very expensive models or a network of in-situ data. Considering the significant wave height, satellite radar altimetry provides an established global and relatively long-term source, whose coastal data are nevertheless typically flagged as unreliable within 30 km of the coast. This study exploits the reprocessing of the radar altimetry signals with a dedicated fitting algorithm to retrieve several years of significant wave height records in the coastal zone. We show significant variations in annual cycle amplitudes and mean state in the last 30 km from the coastline compared to offshore, in areas which were up to now not observable with standard radar altimetry. Consequently, a decrease of the average wave energy flux is observed. Globally, we found that the mean significant wave height at 3 km off the coast is on average 22% smaller than offshore, the amplitude of the annual cycle is reduced on average by 14% and the mean energy flux loses 38% of its offshore value.

Global coastal attenuation of wind-waves observed with radar altimetry

Marcello Passaro[1], Mark A. Hemer[2], Graham D. Quartly[3], Christian Schwatke[4], Denise Dettmering[5], and Florian Seitz[6]

[1]Deutsches Geodätisches Forschungsinstitut der Technischen Universität München, marcello.passaro@tum.de

[2]Commonwealth Scientific and Industrial Research Organisation Oceans and Atmosphere, Hobart, Tasmania, Australia, Mark.Hemer@csiro.au

[3]Plymouth Marine Laboratory (PML), Plymouth, UK, gqu@pml.ac.uk

[4]Deutsches Geodätisches Forschungsinstitut der Technischen Universität München, christian.schwatke@tum.de

[5]Deutsches Geodätisches Forschungsinstitut der Technischen Universität München, denise.dettmering@tum.de

[6]Deutsches Geodätisches Forschungsinstitut der Technischen Universität München, florian.seitz@tum.de

May 3, 2021

1 Introduction

The height of the wind waves in the ocean, together with their period, direction and speed, is a fundamental parameter to describe the sea state and more generally to study the ocean climate and interactions with the atmosphere [Cavaleri et al., 2012]. The significant wave height (SWH), defined as four times the standard deviation (std) of the surface elevation [Ardhuin et al., 2019], is an integral parameter that is extensively used as reference to quantify both extremes and mean sea states. In particular, the relevance of a SWH climatology is manifold, from the optimisation of shipping routes [Padhy et al., 2008] to the quantification of the impact of sea level rise at the coast [Melet et al., 2018, Ponte et al., 2019]. Such a climatology is also fundamental to assess the wave energy resources of a particular area and planning

the exploitation of a potential source of renewable energy [Rusu, 2009].

Despite the overwhelming importance of measuring waves in the coastal zone, our knowledge of coastal wave climate and coastal wave energy resources is limited in data availability, accuracy and resolution [Ardhuin et al., 2019]. In-situ data are collected by buoys, whose records are sparse in time and space. Ocean models work very well in the open ocean, but a nested high resolution model needs to be used in order to correctly simulate the coastal features that modify wave parameters.

Satellite altimeter measurements of SWH, collected along repeating ground tracks, extend from 1985 through to present [Ribal and Young, 2019]. The principle is based on the shape of the returned radar echo and in particular on its stretch being proportional to the wave height [Chelton et al., 2001]. Such estimation has the advantage of being independent from atmospheric corrections that are needed to estimate the range (distance between the satellite centre of mass and the sea level). This technique has been used to quantify global open ocean mean wave climate, seasonality [Young, 1999, Stopa, 2019], energy flux resources [Reguero et al., 2015] and global historical trends [Young and Ribal, 2019]. Nevertheless, these studies cannot see small scale variability of coastal processes, given the large grid-points of over 1° spacing in latitude and longitude. Other studies identified the potential of using along-track measurements to locally observe variations in the sea state [Goddijn-Murphy et al., 2015, Queffeulou and Bentamy, 2007], but efforts have been restricted to specific regions and were limited by the unreliability of standard altimetry data in the coastal strip. This is due to the influence of land and areas with different backscattering characteristics within the satellite footprint [Passaro et al., 2014], which can negatively affect SWH measurements within about 20 km of the coast [Passaro et al., 2015].

In recent years, coastal altimetry has been the focus of several improvements [Cipollini et al., 2017]. In particular, specific algorithms (retrackers) have been designed to fit the returned echo while avoiding spurious coastal reflections that degrade the quality of the estimated parameters. This, coupled with a conservative strategy to detect outliers, has brought strong improvements to the quality and the quantity of SWH retrievals.

Here, we exploit these improvements to provide, based on reprocessed along-track satellite altimetry data, an assessment of the average global coastal wave climate in the coastal zone in terms of SWH, and to highlight the differences with respect to the climatology of previously presented offshore conditions [Young, 1999, Stopa, 2019]. The results presented are based on the reprocessing of satellite altimetry data from Jason-1 and Jason-2 missions, from July 2001 to January 2016, following the methodology described in Section 4. We are able to quantify the progressive attenuation of the average wave climate towards the coast, even focusing on the differences in the last 30 km. These differences are finally quantified in terms of wave energy flux. The coastal proximity and resolution, as well as the global character of these observations is unprecedented and verified by comparison with buoys and a regional

3

₇₃ high-resolution nested wave model.

2 Results

₇₅ The terminology referring to coastal oceanography as compared to the variability further away from the
₇₆ coast differs significantly in the literature. In this study, we define coastal along-track locations and
₇₇ compare their variability against offshore along-track locations, using the following definition:

₇₈   Coastal wave measurement points are taken as the location of the 1-Hz sample point nearest to the
₇₉ coast (noting points within 3km of the coast are excluded to avoid outliers). Offshore wave measurement
₈₀ points are taken as the first 1-Hz sample point located more than 30km from the coast. In order to
₈₁ ease comparison between offshore and coastal points, we consider only along-track sections with a single
₈₂ ocean-land or land-ocean transition.

2.1 Mean Significant Wave Height

₈₄ Figure 1 displays maps of the mean SWH according to offshore and coastal definitions, and the difference
₈₅ between these measured along the same track. For each altimetry track, the circles of panel b and c are
₈₆ centred on the coordinates of the coastal location being compared. The highest mean coastal SWHs are
₈₇ registered along the Chilean Patagonian coast, with up to about 4 meters of average wave height (Figure
₈₈ 1b), This is a notable distinction to the well understood climatology of offshore wave heights (Figure 1a),
₈₉ where the highest mean SWHs are observed in the Indian Ocean sector of the Southern Ocean [Young,
₉₀ 1999]. This maxima corresponds with the position of the southern extratropical winds, and contribution
₉₁ of the eastward propagating swell on westward facing coastlines. The mid-latitudes and eastern coasts
₉₂ are instead characterised by smaller values.

₉₃   Several wave processes exist in the nearshore zone that can contribute to differences in SWH between
₉₄ our defined offshore and coastal points. These processes can attenuate wave heights nearer to shore, via
₉₅ sheltering and depth effects. Wave heights may also increase in between offshore and coastal locations
₉₆ owing to local wind generated growth or shoaling effects. Wave-wave interactions and refractive processes
₉₇ may also modulate wave heights in this zone. Figure 1c shows that almost exclusively, coastal SWH are
₉₈ less than the offshore SWH, with varying degrees of coastal attenuation. To summarise and quantify
₉₉ the results, Table 1 shows the regional average attenuation of SWH between the defined offshore and
₁₀₀ coastal points. Most regions show a coastal attenuation of about 20%. The highest attenuation is seen
₁₀₁ in Greenland and Iceland (26%), characterised by stormy seas, but also very jagged coastline where
₁₀₂ sheltering effects will influence coastal wave climate. Only the western coast of North America and the
₁₀₃ Hawaiian archipelago show an attenuation of less than 10%.

4

Region	SWH offshore (m)	SWH coastal (m)	Diff (%)
North America (E)	1.43	1.11	22.01
North America (W)	2.56	2.37	7.48
South America (W)	2.76	2.21	19.99
South America (E)	1.66	1.30	21.67
Hawaii	2.21	2.16	1.96
Greenland and Iceland	2.87	2.12	26.09
Europe (N&W)	2.23	1.78	22.41
Africa (W)	1.66	1.47	11.22
Africa (E)	1.63	1.46	10.53
Madagascar	1.61	1.28	20.68
Asia (S)	1.20	0.98	18.78
Polynesia	1.30	1.07	18.05
Asia (E)	1.90	1.56	18.02
Australia and New Zealand	1.908	1.49	21.87

Table 1: Regional comparison of the mean SWH between offshore and coast. The regional boundaries are reported in section 4.6.

We isolate a group of case studies in Figure 2, where each subplot illustrates a different response between the offshore and coastal mean SWH values. Knowledge of the dominant wave direction is invaluable to best interpret the relevant acting processes. Since altimetry data do not contain information on the wave direction, we average the monthly values of wave direction available from the ERA5 reanalysis onto a 0.5°x0.5° grid [Hersbach et al., 2020]. For each case study, we overlay the mean SWH obtained from altimetry (colour scale) with vectors displaying the mean wave direction.

In Figure 2a, showing a section of the Alaska's coast, we can now resolve the sheltering effect of the island, either as a full or partial barrier, resulting in smaller SWH nearshore relative to the landward propagating swell observed on the up-wave (windward) side of the island(s). Attenuation of SWH due to the sheltering effect of islands is also seen on the global scale, where the attenuation effects from island sheltering can have influence over very large distances. For example, Ponce de León and Guedes Soares [2005], report the broad scale effects of sheltering from the Azores Archipelago on the Atlantic wave climate. In Figure 2b, we are able to discern the depth induced dissipation of wave energy, seen as a reduction in the altimeter measured wave height as the waves propagate across the continental shelf towards the south coast of the Australian continent. An associated refraction of wave direction is seen with small anticlockwise changes in reanalysis derived mean wave direction between the off-shelf and on-shelf locations (represented by an average 5.2° change in direction of black arrows in the corresponding locations).

As in Figure 2a, our case study presented in Figure 2c also displays higher mean SWH offshore. However in contrast to Figure 2a, we see the waves are propagating offshore, suggesting the higher offshore SWH are attributable to local wind-generated growth in fetch-limited conditions.

Few locations in our dataset show no change of mean SWH between offshore and the coast, or a slight increase. One example is provided in Figure 2d, located in Eastern Australia in the region of the

Great Barrier Reef. Here, the SWH attenuation caused by the reef (visible by the bathymetric contour at -20 m depth) is counteracted by additional growth on the landward side of the reef. Shallow-water interactions may also drive an increase in SWH, whether via shoaling or convergence of wave energy, as for example via refraction around headlands.

While our observations show that on average the attenuation of SWH from offshore up to 3 km from the coast is prevalent, this does not exclude that locally the average SWH can increase in the last 3 km. This limitation might be overcome in the next years, when Delay-Doppler altimeters on repeated tracks will have acquired time series that are long enough to observe a mean behaviour. These altimeters are characterised by a better signal-to-noise ratio and along-track resolution, which could enable to fill the remaining coastal gap.

2.2 Amplitude of the annual cycle

Figure 3 shows the amplitude of the annual cycle of SWH in the global ocean, its coastal value found in this study and the difference between coastal and offshore estimations (offshore-coast). Open ocean features (Figure 3a) resemble what has been previously described by Young [1999] and [Stopa, 2019] with a gridded dataset, even if the use of along-track measurements provides less observations on a single location and no spatial interpolation with neighbouring tracks is performed in this study.

In Figure 3b and c the amplitude of the annual cycle in the coastal regions and the difference between the offshore and the coastal estimate of the amplitude are shown.

26% of the locations show a statistically significant (black outline in figure) attenuation of the seasonality. This attenuation is largely consistent with a proportional attenuation of the mean SWHs presented in Section 2.1. While there are also areas showing an amplification of seasonality in the coastal sites, the values are not statistically significant.

2.3 Average wave energy flux

Figure 4a provides a global view of the average wave energy flux computed with our dataset, exhibiting the expected spatial variability consistent with the mean SWH (Fig 1a). The results agree also with the estimations of Gunn and Stock-Williams [2012] and Reguero et al. [2015], which were generated using the WaveWatch3 model [Tolman, 2008].

Figure 4b shows the average coastal wave energy flux and Figure 4c the difference between coastal and offshore estimations (offshore-coast). A direct comparison can be made with Krogstad and Barstow

[1999], which used altimetry measurements spanning over two years to evaluate global wave resources along the coast. Their estimations are much higher and closer to the open ocean ones, due to the fact that they relied on an average of 3 along-track points (i.e. over 20 km along-track) and they could not exploit data in the last kms within the coastline. Largest differences between the offshore and coastal estimates of wave energy flux are found along the Chilean coast, on the southern tip of New Zealand, along the South East coast of Australia and in the North West coast of Europe. Distinction between the offshore and coastal energy flux representations is well observed also along the Western US Coastline. Some areas that showed offshore high energy flux in previous studies are shown here to be affected by a strong reduction of the energy flux within few kms: examples are several locations in Iceland, in the south-west coast of Australia, and along the south east coast of South Africa.

These results are summarised in Table 2 according to the region. The most powerful waves are observed along the Pacific coast of the American continent (25.39 kW/m on the North American coast, and 24.20 kW/m along the South American coast). The high energy along the North American coast is notable in that this region displays the second smallest attenuation of wave energy flux from offshore to coastal (17%) after Hawaii (7%). In contrast, the relatively energetic wave climates off Greenland, Iceland and the NW European Shelf display high attenuation from offshore to coastal values (42% and 41% respectively).

For a further check of the reliability of our estimates, it is possible to look at regions in which high resolution wave models are available. One of the regions of high interest is the Southern Australian Margin. The Australian Wave Energy Atlas [Hemer et al., 2017, Hemer and Griffin, 2010] presents the wave climate around the Australian continent at a resolution of approximately 4 km and is based on a global implementation of the WAVEWATCH III (v4.08) hindcast, with a series of nested high-resolution computational grids in the Australian and South Pacific region. This dataset enables comparison of the cross-shelf gradients of wave energy flux in this region. The agreement between these model results and our derivation from the coastal altimetry data, shown in Figure 5a, is quantified in Figure 5b, where the mean and standard deviation of the differences between altimetry-derived and model-derived results is plotted with respect to the distance to coast, binned every 3 km. The mean bias is below 1 kW/m in the first 60 km from the coast, with a maximum standard deviation of about 5 kW/m close to the coast. Further away, altimetry tends to slightly overestimate the flux, but the mean bias is on average below 4 kW/m regardless of the distance to coast, i.e. less than 13% of the modelled wave energy flux.

Region	WEF offshore (kW/m)	WEF coastal (kW/m)	Diff (kW/m)
North America (E)	8.11	4.81	3.30
North America (W)	30.62	25.39	5.24
South America (W)	37.10	24.20	12.91
South America (E)	9.34	5.93	3.40
Hawaii	19.75	18.61	1.14
Greenland and Iceland	42.15	24.58	17.57
Europe (N&W)	28.44	16.87	11.57
Africa (W)	12.29	10.10	2.20
Africa (E)	11.60	8.66	2.95
Madagascar	11.00	7.48	3.52
Asia (S)	6.10	4.09	2.00
Polynesia	7.16	5.27	1.88
Asia (E)	16.46	11.76	4.70
Australia and New Zealand	19.50	12.61	6.89

Table 2: Regional comparison of the average wave energy flux (WEF) between offshore and coast. The regional boundaries are reported in Section 4.6.

Mean SWH – Offshore (m)

(a)

Mean SWH – Coast(m)

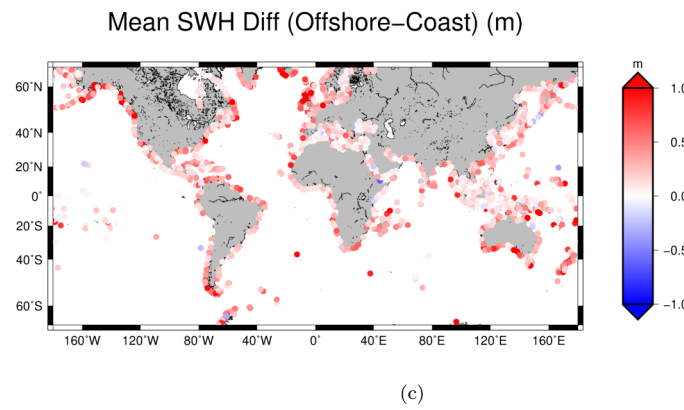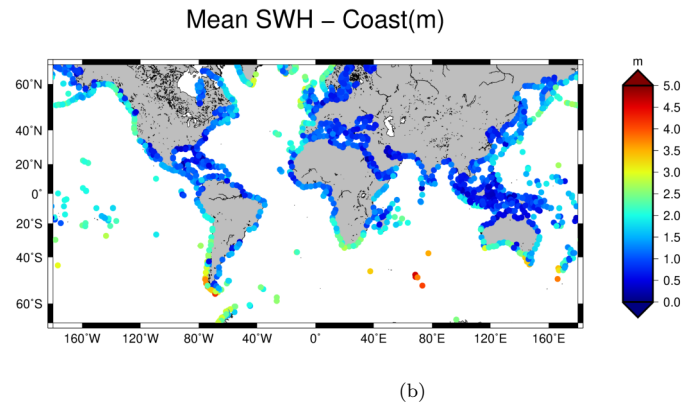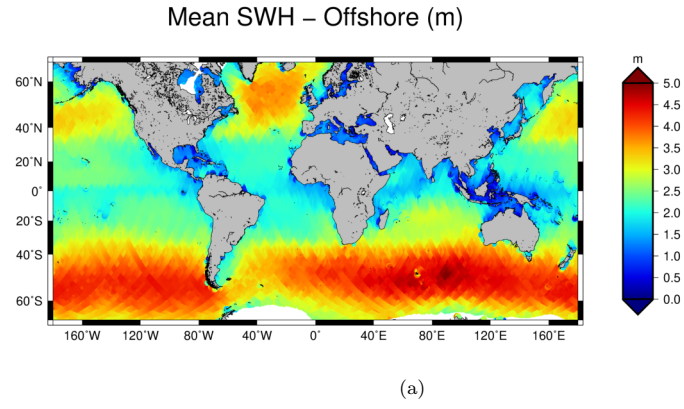

(b)

Mean SWH Diff (Offshore−Coast) (m)

(c)

Figure 1: Mean Significant Wave Height (SWH). Mean SWH from along-track satellite altimetry over the global ocean (a) and along the coastline (b). (c) shows the difference between the offshore and the coastal estimates.
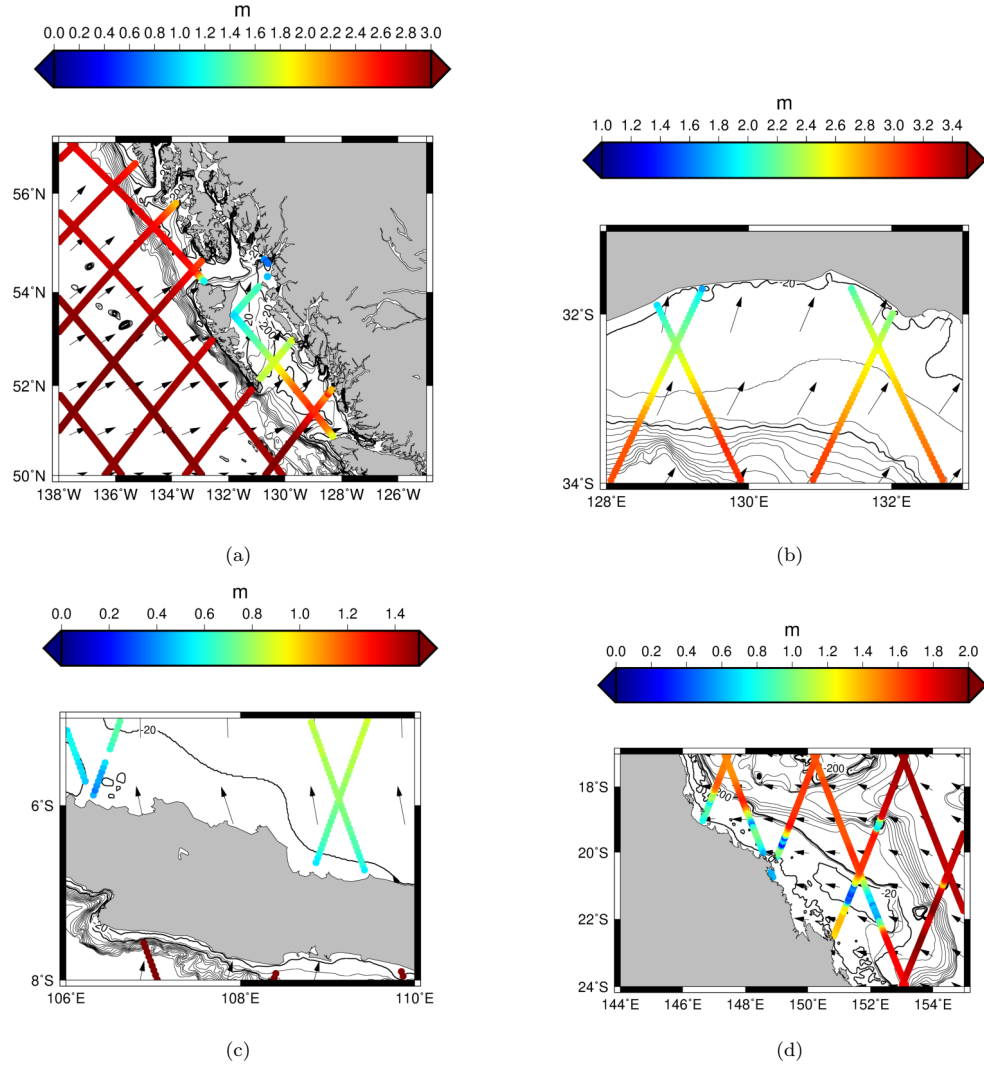
Figure 2: Coastal changes of mean Significant Wave Height (SWH). Examples of coastal changes of mean SWH along the altimetry tracks (colour scale) in Alaska (a), South Australia (b), the island of Java in Indonesia (c) and in Great Barrier Reef region of East Australia (d). Bathymetry contours are plotted at intervals of 60 m from -20 m until -200 m depth and every 200 m until -2000 m depth. The mean wave direction computed from the ECMWF ERA5 reanalysis is shown with black arrows.

SWH Annual Cycle Amplitude – Offshore (m)

(a)

SWH Annual Cycle Amplitude – Coast (m)

(b)

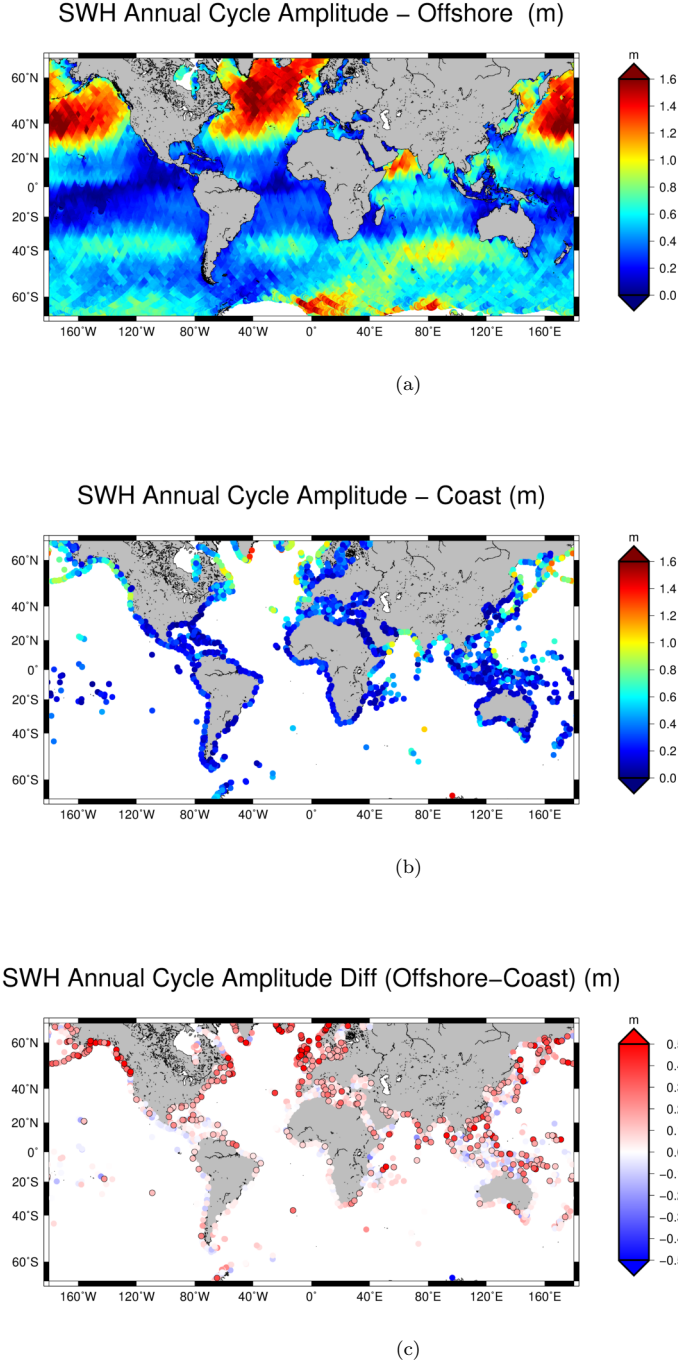SWH Annual Cycle Amplitude Diff (Offshore–Coast) (m)

(c)

Figure 3: Amplitude of the annual cycle. Amplitude of the annual cycle computed for Significant Wave Height (SWH) time series from along-track satellite altimetry over the global ocean (a) and along the coastline (b). (c) shows the difference between the offshore and the coastal estimate of the amplitude. Statistically significant differences are marked with a black contour. The point is marked as significant if the absolute value of the difference between the offshore and the coastal amplitude is higher than its uncertainty. Uncertainties are computed as described in section 4.2

Average Wave Energy Flux – Offshore (kW/m)

Average Wave Energy Flux – Coast (kW/m)
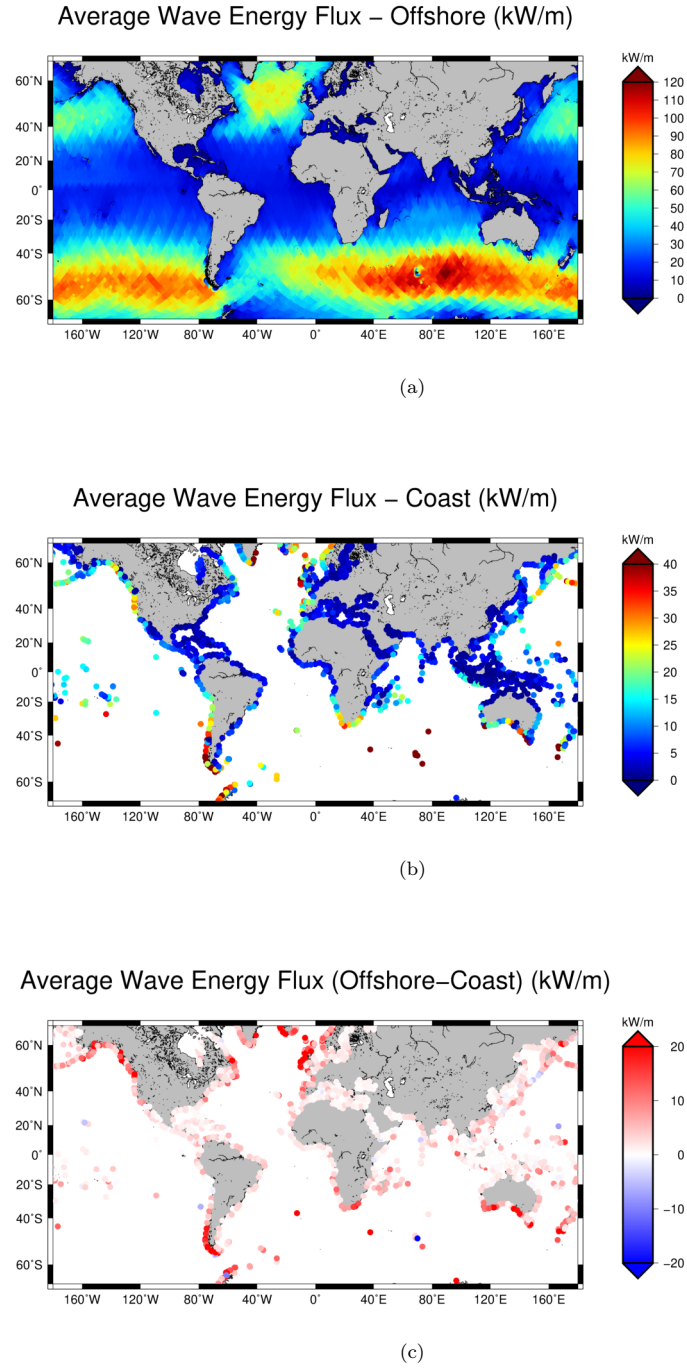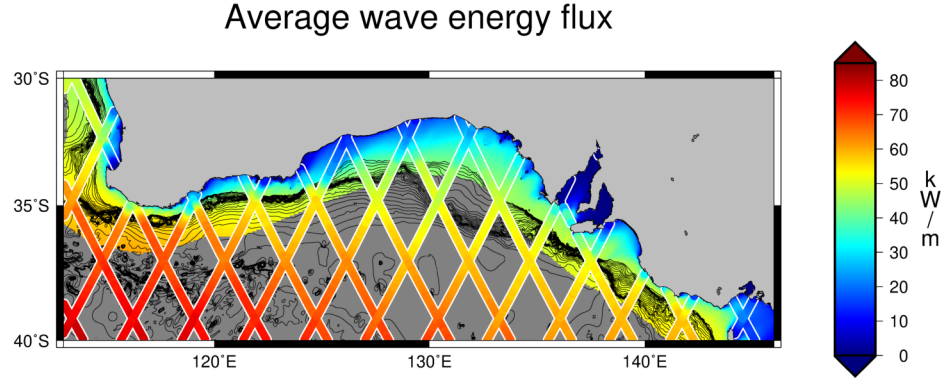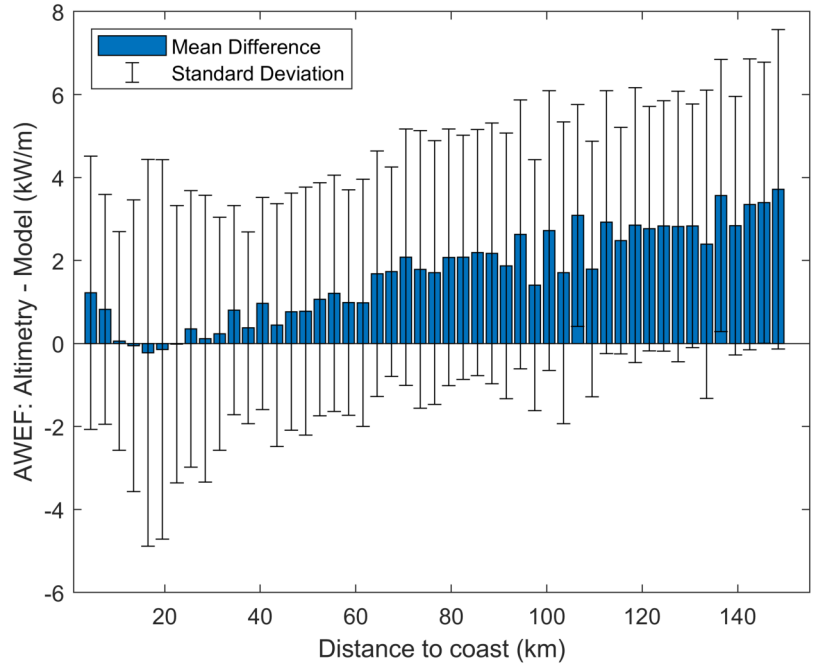
Average Wave Energy Flux (Offshore−Coast) (kW/m)

Figure 4: Average wave energy flux. Average wave energy flux from along-track satellite altimetry over the global ocean (a) and along the coastline (b). (c) shows the difference between the offshore and the coastal estimates.

Average wave energy flux

(a)

(b)

Figure 5: Coastal average wave energy flux in South Australia. Average wave energy flux (AWEX) along the altimetry tracks in South Australia superimposed over the 50th percentile of wave energy flux computed using model data [Hemer et al., 2017] (a). Mean difference (blue bars) and standard deviation of the differences (error bars) between colocated altimetry and model locations with respect to the distance to coast binned every 3 km (b).

13

3 Discussion

The use of reprocessed time series of coastal altimetry data provide the chance to observe the interaction between waves, bathymetry, and coastlines in terms of SWH. Besides the common understanding that SWH is decreased in the coastal zone, the study quantifies the attenuation of mean state, seasonality, and wave energy flux at an unprecedented resolution that could so far only been achieved using dedicated high-resolution models for regional and local downscalings [Perez et al., 2017].
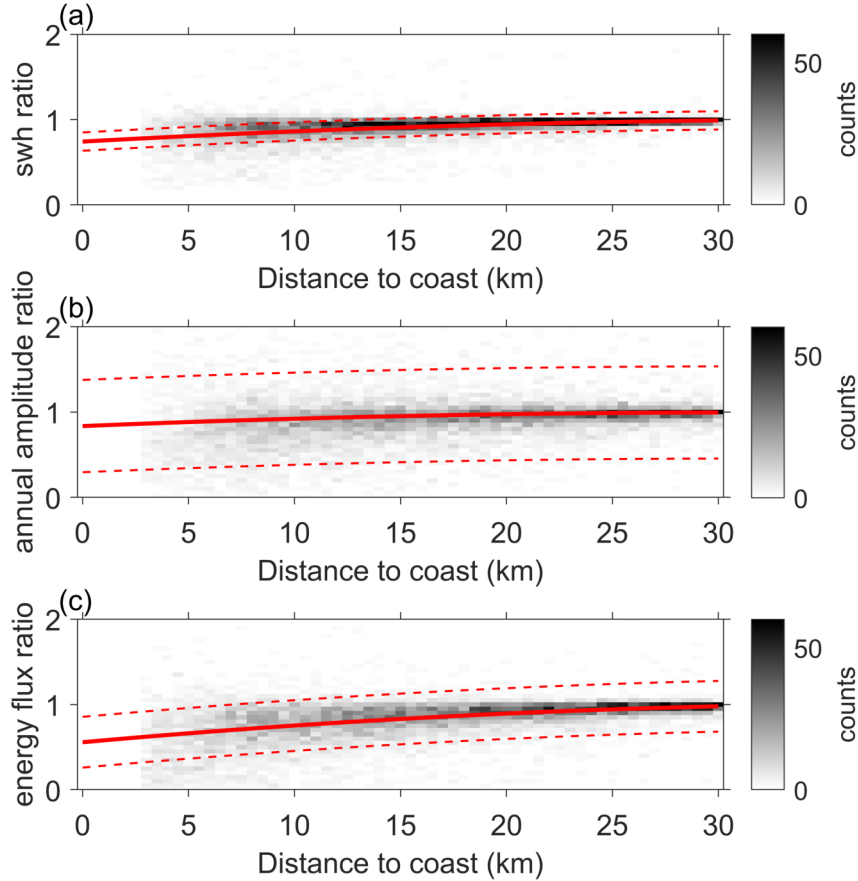

Figure 6: Global coastal attenuation. Density plots of the ratios between wave parameters computed in the coastal zone over the globe and the corresponding parameter computed offshore. The parameters considered are the mean Significant Wave Height (SWH) (a), the amplitude of the annual cycle (b) and the average wave energy flux (c). A second-degree polynomial is fitted to the data and plotted in red. The 95% confidence interval of the fit is shown with red dashed lines.

The results are summarised in their global statistics in Figure 6, where the parameters are shown as a ratio against the value at 30 km from the coast (defined as offshore in this study). The polynomial fit indicates that the mean SWH at 3 km from the coast is on average 22% smaller than offshore, the amplitude of the annual cycle is reduced in the same distance on average by 14% and the average energy flux loses 38% of its offshore value. The global coastal attenuation is verified with a confidence level of 95% for both mean SWH and average energy flux. This is not true for the amplitude of the annual cycle,

whose difference between coastal and offshore values has a wider spread.

While dedicated regional high-resolution models are able to take into account the attenuation seen with satellite altimetry, studies of global wave power up to now, including the assessment of the World Energy Council [World Energy Council, 2010] have typically been defined using models or reanalysis with validation relative to offshore satellite altimetry data. The resolution of these models may be high for regional applications (e.g., of order hundreds of metres, [Losada et al., 2010]). At global scale, the resolution of these models is typically in the range of 0.25 ° [Perez et al., 2017] to 0.5 ° [Reguero et al., 2015]. The wave energy generation systems are typically planned to be placed near the shore or in depth ranges of 30-50 m in the offshore cases [Hemer and Griffin, 2010]. Given the global observational representation of the coastal attenuation provided in this study, studies of global wave power shall be therefore updated using the latest models at higher resolution.

Finally, this study shows the level of accuracy that reprocessed satellite altimetry offers to describe the coastal wave climate in terms of SWH. Our dataset is unprecedented in presenting altimeter wave height data near to the coast at a global scale. This opens possibilities for future global analyses seeking to quantify near coastal wave transformations across a full distribution of shelf environments. The short time series with respect to the variability of this quantity still hampers the estimation of significant trends [Young and Ribal, 2019]. Future efforts in this sense, which are planned for example in the framework of the European Space Agency's Sea State Climate Change Initiative [Dodet et al., 2020], shall focus on a dedicated irregular coastal gridding in order to increase the sampling while avoiding rough interpolation with offshore data.

4   Methods

4.1   Processing of satellite altimetry data

4.1.1   High-frequency retracking

We analyse satellite altimetry data coming from the Sensor Geophysical Data Records (SGDR) of Jason-1 and Jason-2 missions, from July 2001 to January 2016. The SGDR contain returned radar echoes, called waveforms, at a 20-Hz rate (corresponding to a distance of about 350 m). Routinely in the standard product, a functional form (the Brown-Hayne model) is fitted to the waveform in a process called retracking. The SWH is directly estimated from the Brown-Hayne model [S. Brown, 1977, Hayne, 1980].

Several waveforms in the last 0 to about 20 km from the coast differ from the theoretical Brown-Hayne shape due to the inhomogeneity of the backscatter of the illuminated area in the coastal zone. For this reason, data in the coastal strip are routinely flagged or discarded. In this study we use instead SWH data that are retracked with the ALES algorithm, which only considers a portion of the waveform

15

in order to recover data in the coastal zone, while maintaining the quality of the retrieval in the open ocean as well.

In the ALES retracker, the retracking of each waveform is performed in two steps. A first step looks at the rising portion of the waveform (called leading edge) and provides a rough estimate of SWH from the slope of that portion. This estimate is then entered into an algorithm that selects the sub-waveform (i.e., sets the width of the fitting window over which a fitting is performed in the second step). The dependence on the SWH is necessary to maintain the same level of precision achievable in the open ocean using a full-waveform retracker, given the direct relationship between sea state and noise of the retrieval.

A full description of the ALES retracking procedure is provided in Passaro et al. [2014]. The SWH detection with the ALES retracker was validated against buoys in Passaro et al. [2015], which confirmed that ALES is able to extract meaningful retracked parameters up to about 3 km from the coast, which is also the limit of validity adopted in this study.

4.1.2 Low-frequency averages

In order to decrease the noise of the high-frequency retrievals, standard altimetry data are routinely averaged at a 1-Hz rate (approximately one waveform every 7 km).

We briefly recall the procedure used to average ALES retracked SWH to generate 1-Hz estimations [Passaro et al., 2015]. A check is performed in order to eliminate outliers on every block of 20 high-rate values X: the median value and the scaled median absolute deviation ($\widehat{\mathrm{MAD}}$) are computed. Each estimation x is considered valid if:

$$x < \mathrm{median}(X) + 3 \times \widehat{\mathrm{MAD}}(X) \tag{1a}$$

or

$$x > \mathrm{median}(X) - 3 \times \widehat{\mathrm{MAD}}(X) \tag{1b}$$

where

$$\widehat{\mathrm{MAD}}(X) = 1.4286 \times \mathrm{median}(|X - \mathrm{median}(X)|) \tag{1c}$$

The scaled $\widehat{\mathrm{MAD}}$ uses the factor 1.4286 and is approximately equal to the standard deviation for a normal distribution. Statistics based on the median are more robust and suitable for outliers detection and have been already applied to satellite data [Alvera-Azcárate et al., 2012]. Once the outliers have been excluded, the median of the remaining points is computed in order to generate the 1-Hz estimation.

It has to be noted that the 1-Hz SWH value along the track is nominally located at the centre of a segment of 20 20-Hz measurements and therefore is affected by the SWH retrievals located up to about 3.5 km before and after the nominal along-track point. In this study, a 1-Hz average is computed only

if after the outlier procedure there are at least six valid 20-Hz measurements in the 1-Hz block.

The SWH estimations for Jason-1 and Jason-2 are corrected using the instrumental corrections, as described in Thibaut et al. [2004] and Thibaut et al. [2010].

4.1.3 Cross-calibration of the missions

Although Jason-1 and Jason-2 were very similar missions aimed at the continuity of the records, biases in the retracked parameters between different missions are common and must be taken into account in a cross-calibration exercise [Dettmering and Bosch, 2010]. For this purpose, following previous studies focused on the standard products [Ablain et al., 2010], we exploit the Jason-1/2 tandem mission, with the altimeters flying the same track 54s apart (cycles 1-20 of Jason-2 and 240-259 of Jason-1). The bias is computed on each 20-Hz location.

We show the results in Supplementary Figure 1 for different sea states. Biases between the SWH from the two altimeters are likely to be caused by the treatment of the Point Target Response in the Brown- Hayne model, which approximates it with a Gaussian function [Thibaut et al., 2010]. Nevertheless, the bias is two orders of magnitude smaller than the SWH parameters analysed in this study (annual cycle, mean SWH), which are on the order of meters. Given the relatively small differences found in dependence with the sea state and since spurious small drifts in trends do not affect the results in this study, we limit our cross-calibration to the application of a constant bias obtained as median of the available comparisons, i.e. we subtract 0.03 cm to every SWH measurements from Jason-2.

4.2 Computation of mean SWH and annual cycle

In order to compute along-track 1-Hz averages to create a time series, data points along the satellite tracks have to be collinear: it is necessary to have measurements at the same geographical location for each cycle. Nominal tracks are therefore created for this study using the reference orbits, neglecting the across-track displacement of different passes along the same track, which is normally less than 1 km. Each interval between consecutive 1-Hz data points is divided in order to obtain 20 equidistant nominal locations, along which the SWH data for each cycle is then linearly interpolated. As a result of this process, at each lat-lon couple corresponds a time series with a record per each cycle. The mean SWH field is then simply the mean SWH of each of this time series.

To estimate the annual cycle, once the cycle-by-cycle time series are adapted into monthly averages, a harmonic analysis of the time series is performed. The analysis consists of modelling the sea level variability as the sum of a constant, a linear term and a sinusoid wave with an annual frequency. The unknowns (parameters) of this model are the constant term, the slope of the linear term and the amplitude and phase of the sinusoid. Amplitude and phase of the annual frequency are not independent parameters, since they are estimated through the same fit, according to the following model:

$$y = A + Bx + C \cos 2\pi xf + D \sin 2\pi xf \tag{2}$$

where A-D are the coefficients to be estimated and f is the annual frequency. The amplitude (Am) and phase (Ph) of the annual signal are then computed as follows:

$$\text{Am} = \sqrt{C^2 + D^2} \tag{3a}$$

$$\text{Ph} = \begin{cases} \arctan\left(\frac{D}{C}\right) & \text{if } C < 0 \\ \arctan\left(\frac{D}{C}\right) + \pi & \text{if } C > 0 \end{cases} \tag{3b}$$

Since we are dealing with geophysical time series, in order to correctly express the uncertainty on the estimated annual cycle it is necessary to account for autocorrelation and therefore Feasible Generalised Least Square (FGLS) methods are used instead of the standard Ordinary Least Squares. We use the Prais-Winsten (PW) estimator [Prais and Winsten, 1954], which applies a transformation to the dependent and independent variables in order to transform the problem into one that respects the Gauss-Markov hypothesis. The PW estimator is applied in the present study iteratively. Given a set of independent variables X, observations Y, error ϵ and parameters to be estimated β, the method finds the term ρ that expresses the correlation of the residuals. The steps followed are:

1. Ordinary least squares estimation of the model $Y = \beta X + \epsilon$

2. Ordinary least squares estimation of the model $\epsilon_t = \rho \epsilon_{t-1} + e$ in order to estimate the parameter ρ, which is related to the first order autocorrelation of the residuals

3. Ordinary least squares estimation of the transformed model $Q = \beta Z + e$, in which

$$Q_t = \begin{cases} Y_t \sqrt{1 - \rho^2} & t \equiv 1 \\ Y_t - \rho Y_{t-1} & t \equiv 2 : \text{end} \end{cases} \tag{4}$$

and

$$Z_t = \begin{cases} X_t \sqrt{1 - \rho^2} & t \equiv 1 \\ X_t - \rho X_{t-1} & t \equiv 2 : \text{end} \end{cases} \tag{5}$$

where t is the time index of the observations. The procedure is iterated until ρ converges to a value close to zero and therefore the errors of the transformed model are no longer autocorrelated.

4.3 Validation of the mean parameters against buoys

We use the global network of buoys provided by the Copernicus Marine Environment Monitoring Service (CMEMS, marine.copernicus.eu) to validate satellite altimetry data. Along a track, altimetry data are available every 10 days, as opposite to the sub-daily measurements from buoys. A validation is therefore necessary to test quality of the estimation of mean parameters despite this sampling. The validation is performed by comparing the time series of SWH along consecutive satellite passes with the time series generated by buoy measurements. Overlapping time periods between buoys and altimetry are used. Buoys containing less than 2 years of data are discarded.

We compare the performances of the ALES SWH against the standard geophysical data records (GDR) in terms of Pearson correlation coefficient with respect to the buoys. We select all altimetry points between between 30 and 3 km from the coast and within 30 km from a buoy. Given corr(buoy,ALES) the correlation between SWH time series from ALES and buoys, and corr(buoy,standard) the correlation between SWH time series from GDR and buoys, Supplementary Figure 2 shows the difference corr(buoy,ales) - corr(buoy,standard) with respect to the distance to coast of the along-track location. In 85% of the cases the dataset used in this study has a higher correlation than the one achieved by a standard product. This confirms previous regional validation efforts of the ALES SWH estimations [Passaro et al., 2015].

Secondly, we check the suitability of using along-track data to derive mean SWH and annual cycle. The standard procedure followed in the previous literature consists in gridding the data to average more tracks together within boxes of at least 1° spacing in latitude and longitude. This strategy is not suitable for this study, since doing so would smooth the differences at the coastal scales that we want to study. Therefore, we compare mean SWH and amplitude of the annual cycle computed with the data from the buoys with the same variables computed using the closest point of the satellite track, provided it is not located further than 30 km from the buoy. Given that in the coastal proximity the SWH changes much more rapidly, as shown in this study, we restrict this distance to 15 km for buoys located closer than 30 km to the coastline. Using these criteria, 51 altimetry-buoy couples were found, out of which 11 featuring coastal buoys.

The results show values of correlation and slope close to 1 in both mean and annual cycle amplitude of SWH (see Supplementary Figure 3). Notably, the performances of the coastal data (i.e. using buoys located closer than 30 km of the coast, highlighted in red) do not differ from the data offshore. Despite the short overlap of some altimetry-buoy couples, only 12% show a significant difference in the amplitude of the annual cycle.

4.3.1 Regional validation against coastal buoys

A downside of our global validation approach is that the comparison between the buoy and the satellite

track points may not always be valid, because the buoy and altimeter measurements could be in very different coastal environments (see Figure 3 of Quartly and Kurekin [2020]), leading to significant SWH spatial gradients as the coast is approached. For this reason, we provide a further regional validation adopting the approach of Nencioli and Quartly [2019] in using hindcast outputs from a high-resolution wave model to assess the contribution due to spatial variation in the wave field.

As hindcast, we use the NWSHELF_REANALYSIS_WAV_004_015 product from CMEMS. As indicated in the product, this is a reanalysis based on the WaveWatch3 model and the North-West Shelf configuration is based on a two-tier Spherical Multiple Cell grid mesh (3 and 1.5 km cells). The product is further referred to as WW3 in this section. As a buoy database we use the Channel Coastal Observatory containing data from 50 platforms around the English coast, of which we identified 13 as being within 50 km of a Jason track and having several years of overlap with the Jason-2 record on those tracks. We then identify all the nominal 1-Hz altimeter points within 50 km of the in situ measurements, and compared both the GDR and the ALES-retracked values against the reference.

The fine-resolution grid of WW3 enables us to use reanalysis data within ∼11km of the locations of buoy and altimeter measurements (Figure 7). A linear regression analysis is performed between WW3 fields at the two locations (Figure 8) to give the best-fit line with correlation, r and the root mean square difference (RMSD).

Similar regression analysis is then performed for the buoy and altimeter observations, first considering all the matchups within 50 km (Figure 8). The RMSD for these accepted pairings is partitioned into distance from coast using 5 km wide bins. The values for ALES (∼0.6 m in blue) are only slightly greater than the spatial variation seen within WW3, whereas those for the GDR (∼0.8 m, in red) are significantly larger and increase markedly within 15 km of the coast. Restricting the selection to buoy-altimeter pairings for which WW3 values at the two locations are highly coherent (r ≥0.95 and RMSD≤0.3 m) decreases the number of matchups from 160 to 44, and leads to a further reduction in the RMSD values for ALES to ∼0.4 m until within 8 km of the coast, but has little impact on the perceived accuracy of the GDR values. We also note that the median value of the RMSD for ALES is 0.35 m even for the bin 3-8 km and the mean in the plot has a larger RMSD due to three matches with a higher discrepancy. Therefore we conclude that the ALES-derived estimates are significantly more accurate than those on the GDR, with the RMSD for the former being dominated by the spatial changes in wave height rather than error in the retracker algorithm.

4.4 Computation of the average wave energy flux

Wave energy flux has a dependency on wave period and wave heights. Altimeters have limited ability to provide estimates of wave period [Badulin, 2014], and consequently we follow the approach of others (e.g., Young et al. [2010].) by supplementing the altimeter derived wave heights with reanalysis derived
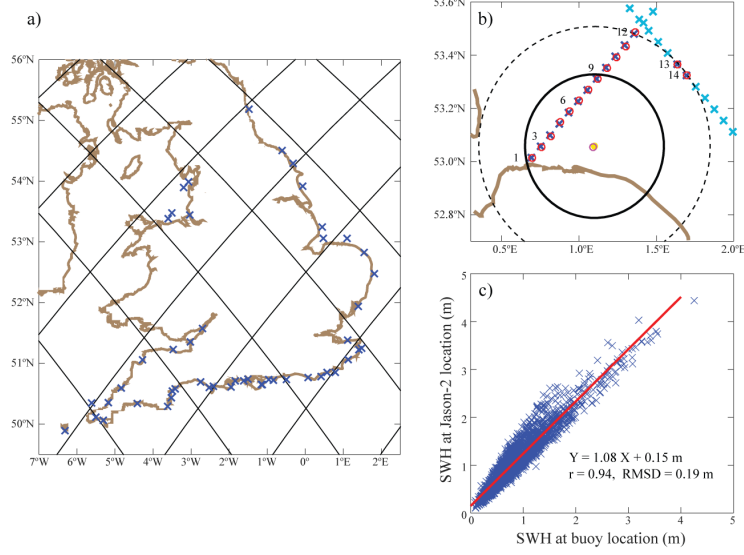
Figure 7: Regional validation against coastal buoys. a) Jason-2 tracks overlaid on map of the 50 coastal wave platforms curated by the Channel Coastal Observatory. b) Zoom over region of Blakeney Overfalls buoy (orange star) off East Anglia, with nominal points along two Jason-2 tracks shown by light blue crosses. The concentric circles indicate 50 km and 30 km from the buoy, with dark blue crosses indicating those within 50 km. The red and magenta circles indicate the centres of the corresponding model points. c) Linear regression of Significant Wave Height (SWH) values from reanalysis at altimeter point 9 (y-axis) against reanalysis values at the buoy location

wave periods to determine the wave energy flux. Here, zero-crossing wave periods are obtained from the ERA5 reanalysis at a time resolution of 3 hours and spanning the same time period as the altimetry observations.

We first compute the instantaneous wave energy flux for each satellite cycle at each location, using the following relationship [Mackay, 2012]:

$$P = \frac{\rho g^2}{64\pi}\text{SWH}^2 T_e \qquad (W/m) \qquad (6)$$

where ρ is the sea water density ($1025 kg/m^3$). The energy period T_e can be derived from the zero-crossing period using the relationship:
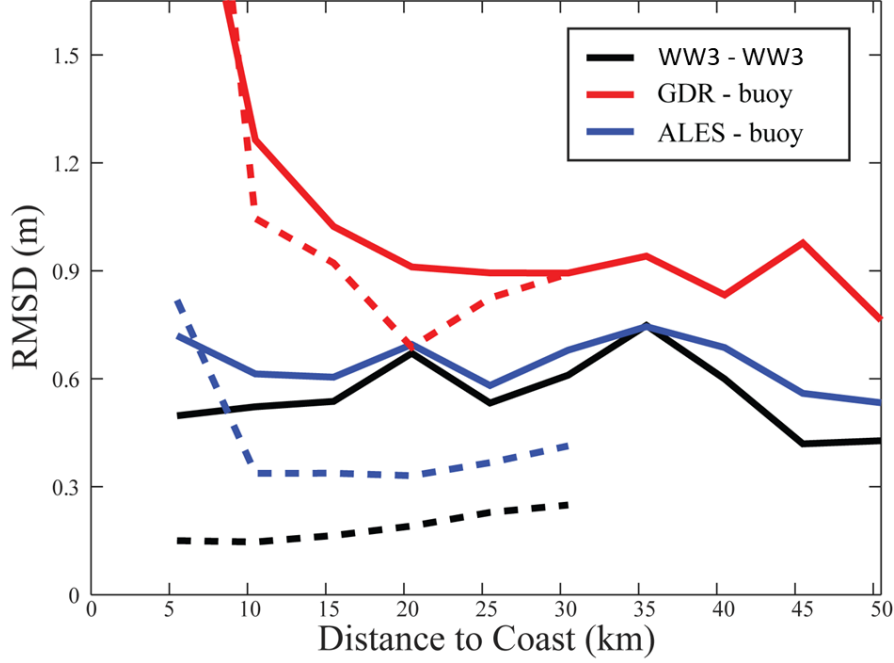
$$T_e = \alpha T_z \qquad (7)$$

21

Figure 8: Coastal comparison between buoys, altimetry and reanalysis. Root Mean Square Difference (RMSD) of observations at altimeter point and at buoy location, with respect to the distance to coast binned every 5 km. Black lines indicate comparison of reanalysis at the two locations; red and blue are for standard Geophyisical Data Records (GDR) and this study (ALES) respectively compared with the buoys. Solid line shows all comparisons; dashed line shows results for pairings deemed highly coherent i.e. for which the reanalysis comparison has r≥0.95 and RMSD≤0.3m.

384   as a value for α we use 1.18, in accordance to [Cahill and Lewis, 2014]. We thus accept the assumption

385 of a constant spectral shape, which introduces some uncertainty. Its effect is nevertheless negligible,

386 because the error, when estimating α, is an order of magnitude smaller than that for the effects of T_z

387 and SWH [Goddijn-Murphy et al., 2015].

388   By using Equation 6, we accept the following assumptions:

389 • The equation is valid with a deep-water assumption, which might not be true for our definition of

390   coastal zone, particularly for swells

391 • Given that statistics are based on reanalysis data on a 0.5° x 0.5° grid, we are assuming that the

392   wave period remains constant when approaching the coast. While the waves conserve their period

393   when approaching shallow water, waves can be also generated locally.

394   Even if small changes in the period in the shallow waters can occur, their influence is much smaller

395 than the changes in SWH also in quantitative terms in the equation [Reguero et al., 2019]. After an

396 estimation of the mean wave energy flux is computed at each collinear 1-Hz location for each satellite

397 cycle, the mean of each time series is then computed, as for the SWH.

398   A verification of this computation in absolute terms is provided regionally against model data in

Figure 5.

4.5 Errors due to deep water assumption

The adoption of equations adapted for intermediate and shallow water requires knowledge of the wave lengths and the bathymetry. In order to understand the error that we are committing in using the deep water assumption, we use the bathymetry from GEBCO2020 and the wave period from ERA5 to derive an estimation of the wavelength L following the parameterisation of Guo [2002].

Following the linear wave theory and considering a complete spectrum, the wave energy flux is:

$$P = Ec_g \qquad (8)$$

where c_g is the group velocity and:

$$E = \frac{1}{16}\rho g \text{SWH}^2 \qquad (9)$$

Using the parameterized mean wavelength L and considering the depth d, we distinguish between deep ($\frac{d}{L} >= 0.5$), shallow ($\frac{d}{L} <= 0.04$) and transitional ($0.04 < \frac{d}{L} < 0.5$) waters and compute the corresponding group velocity c_g following Reeve et al. [2012].

We notice that a downside of this approach is that, by using Equation 8, we are associating a group velocity to a single characteristic period of an irregular wave field, although the group velocity is a function of a specific frequency of regular waves. This is a commonly applied simplification used where available wave information is limited to bulk wave parameters (such as SWH and mean wave periods) [Guillou et al., 2020].

Supplementary Figure 4 shows the 98th percentile of the differences between the computation of the average energy flux using the deep water assumption and the approximate solution considering shallow and intermediate waters. The data are binned every km according to their distance to the coast. We conclude that by extending the deep water assumption in all our domain of study we are committing an error that does not exceed 1.1 kW/m.

4.6 Subdivision of coastal ocean

In order to provide regional estimates of mean SWH and average wave energy flux, we aggregate the coastal and offshore locations of the altimetry tracks according to several sub-regions, following the grouping proposed by [Reguero et al., 2015]. The regions and their naming are reported in Supplementary Figure 5.

23

Data availability

The processed data that support the findings of this study are available in SEANOE with the identifier doi:10.17882/80341.

All dataset used in this study to produce the results are freely available as indicated in this section.

Sensor Geophysical Data Records (SGDR) for Jason-1 and Jason-2 missions were downloaded from the following sources:

`ftp://avisoftp.cnes.fr/AVISO/pub/jason-1/sgdr_e/`

`ftp://avisoftp.cnes.fr/AVISO/pub/jason-2/sgdr_d/`

1-Hz significant wave height data reprocessed with ALES used in this study are stored in `https://openadb.dgfi.tum.de/en/data_access/`

Data from the ECMWF ERA5 reanalysis were obtained from `https://cds.climate.copernicus.eu/cdsapp#!/dataset/reanalysis-era5-single-levels?tab=overview`.

Data from the Australian wave energy atlas model along the Southern Australian coast are extracted from the following: `https://www.nationalmap.gov.au/renewables/#share=s-sTv1VCxfENCdHe2g`

Reanalysis data for the North West European Shelf are available from the Copernicus Marine Environment Monitoring Service (CMEMS). The product name is `NWSHELF_REANALYSIS_WAV_004_015`.

Data from the Channel Coastal Observatory were provided by the National Network of Regional Coastal Monitoring Programmes of England via `www.coastalmonitoring.org`

The code developed to provide the results presented in this study is stored and available on request.

Acknowledgements

Author Information

Contributions

M.P. conceptualised and designed the study and wrote the manuscript. M.H. contributed in writing the manuscript concerning the interpretation of the results and is supported by the Australian Commonwealth National Environmental Science Program Earth Systems and Climate Change Hub and the

Integrated Marine Observing System. G.D.Q. performed the regional validation against coastal buoys. M.P. is the author of the full software code used in this study, except for the code used for Section 4.3.1, and of the ALES retracking algorithm. D.D. initiated and coordinated the collection and organisation of the altimetry dataset. C.S. and D.D. are responsible for the altimetry database organisation and the data structure used by ALES. F.S. provided the basic resources making the study possible and coordinates the activities of the research group at DGFI-TUM. All authors read and commented on the final manuscript.

Competing interests

The Authors declare no competing interests.

Transparent peer review

The Authors wish to opt in to the publication of the reviewer reports.

References

M. Ablain, S. Philipps, N. Picot, and E. Bronner. Jason-2 Global Statistical Assessment and Cross-Calibration with Jason-1. *Marine Geodesy*, 33(sup1):162–185, 2010. doi: 10.1080/01490419.2010.487805.

A. Alvera-Azcárate, D. Sirjacobs, A. Barth, and J.-M. Beckers. Outlier detection in satellite data using spatial coherence. *Remote Sens. Environ.*, 119:84–91, 2012.

F. Ardhuin, J. E. Stopa, B. Chapron, F. Collard, R. Husson, R. E. Jensen, J. Johannessen, A. Mouche, M. Passaro, G. D. Quartly, V. Swail, and I.an Young. Observing sea states. *Frontiers in Marine Science*, 6:124, 2019. ISSN 2296-7745. doi: 10.3389/fmars.2019.00124.

S.I. Badulin. A physical model of sea wave period from altimeter data. *J. Geophys. Res. Oceans*, 119: 856–869, 2014. doi: 10.1002/2013JC009336.

G. S. Brown. The average impulse response of a rough surface and its applications. *IEEE Transaction on Antennas and Propagation*, 25(1):67–74, 1977.

B. Cahill and T. Lewis. Wave periods and the calculation of wave power. *Proceedings of the 2nd Marine Energy Technology Symposium, April 15-18, 2014, Seattle, WA*, 2014.

L. Cavaleri, B. Fox-Kemper, and M. Hemer. Wind Waves in the Coupled Climate System. *Bulletin of the American Meteorological Society*, 93(11):1651–1661, 2012.

D. B. Chelton, J. C. Ries, B. J Haines, L. Lueng Fu, and P. S Callahan. Satellite altimetry. In L. Lueng Fu and A. Cazenave, editors, *Satellite Altimetry And Earth Sciences: A Handbook Of Techniques And Applications*, volume 69, pages 1–131. Academic Press, 2001.

P. Cipollini, J. Benveniste, F. Birol, M.J. Fernandes, E. Obligis, M. Passaro, P.T. Strub, G. Valladeau, S. Vignudelli, and J. Wilkin. *Satellite altimetry in coastal regions*, pages 343–380. CRC Press, New York, 2017.

D. Dettmering and W. Bosch. Global calibration of Jason-2 by multi-mission crossover analysis. *Mar. Geod.*, 33(S1):150–161, 2010.

G. Dodet, J.F. Piolle, Y. Quilfen, S. Abdalla, M. Accensi, F. Ardhuin, E. Ash, J.R. Bidlot, C. Gommenginger, G. Marechal, M. Passaro, G. Quartly, J. Stopa. B. Timmermans, I. Young, P. Cipollini, and C. Donlon. The Sea State CCI dataset v1: towards a Sea State Climate Data Record based on satellite observations. *Earth Syst. Sci. Data Discuss.*, doi: 10.1016/j.renene.2016.08.039. , 2020.

L. Goddijn-Murphy, B. Martín Míguez, J. McIlvenny, and P. Gleizon. Wave energy resource assessment with AltiKa satellite altimetry: A case study at a wave energy site. *Geophysical Research Letters*, 42 (13):5452–5459, 2015.

N. Guillou, G. Lavidas and G. Chapalain. Wave Energy Resource Assessment for Exploitation—A Review. *Journal of Marine Science and Engineering*, 8(9):705, 2012.

K. Gunn and C. Stock-Williams. Quantifying the global wave power resource. *Renewable Energy*, 44: 296–304, 2012.

J. Guo. Simple and explicit solution of wave dispersion equation. *Coastal Engineering*, 45(2):71–74, 2002. doi: https://doi.org/10.1016/S0378-3839(02)00039-X.

G. S. Hayne. Radar altimeter mean return waveforms from near-normal-incidence ocean surface scattering. *IEEE Transaction on Antennas and Propagation*, 28(5):687–692, 1980.

M.A. Hemer and D.A. Griffin. The wave energy resource along australia's southern margin. *Journal of Renewable and Sustainable Energy*, 2(4):043108, 2010.

M. A. Hemer, S. Zieger, T. Durrant, J. O'Grady, R. K. Hoeke, K. L. McInnes, and U. Rosebrock. A revised assessment of Australia's national wave energy resource. *Renewable Energy*, 114:85–107, 2017. ISSN 0960-1481. doi: 10.1016/j.renene.2016.08.039. Wave and Tidal Resource Characterization.

H. Hersbach, B. Bell, P. Berrisford, S. Hirahara, A. Horányi, J. Muñoz-Sabater, J. Nicolas, C. Peubey, R. Radu, D. Schepers, A. Simmons, C. Soci, S. Abdalla, X. Abellan, G. Balsamo, P. Bechtold, G. Biavati, J. Bidlot, M. Bonavita, G. De Chiara, P. Dahlgren, D. Dee, M. Diamantakis, R. Dragani, J. Flemming,

R. Forbes, M. Fuentes, A. Geer, L. Haimberger, S. Healy, R. J. Hogan, E. Hólm, M. Janisková, S. Keeley, P. Laloyaux, P. Lopez, C. Lupu, G. Radnoti, P. de Rosnay, I. Rozum, F. Vamborg, S. Villaume, and J. Thépaut. The ERA5 global reanalysis. *Quarterly Journal of the Royal Meteorological Society*, 2020. doi: 10.1002/qj.3803.

P. A. Hwang. Duration- and fetch-limited growth functions of wind-generated waves parameterized with three different scaling wind velocities. *Journal of Geophysical Research: Oceans*, 111(C2), 2006. doi: 10.1029/2005JC003180.

H.E. Krogstad and S. F. Barstow. Satellite wave measurements for coastal engineering applications. *Coastal Engineering*, 37(3-4):283–307, 1999.

I. J. Losada, F. J. Mendez, C. Vidal, P. Camus, and C. Izaguirre . Spatial and temporal variability of nearshore wave energy resources along Spain: methodology and results. *OCEANS'10 MTS/IEEE Seattle*, 2010.

E.B.L. Mackay. Resource assessment for wave energy. In Ali Sayigh, editor, *Comprehensive Renewable Energy*, page 11-77. Elsevier, Oxford, 2012. doi: 10.1016/B978-0-08-087872-0.00803-9.

A. Melet, B. Meyssignac, R. Almar, and G. Le Cozannet. Under-estimated wave contribution to coastal sea-level rise. *Nature Climate Change*, 8(3):234, 2018.

F. Nencioli and G.D. Quartly. Evaluation of Sentinel-3A Wave Height observations near the coast of Southwest England *Remote Sensing*, 11(24):2019. doi: 10.3390/rs11242998.

C. P.Padhy, D. Sen, and P. K. Bhaskaran. Application of wave model for weather routing of ships in the north indian ocean. *Natural Hazards*, 44(3):373–385, Mar 2008. ISSN 1573-0840. doi: 10.1007/s11069-007-9126-1.

M. Passaro, P. Cipollini, S. Vignudelli, G.D. Quartly, and H.M. Snaith. ALES: A multi-mission sub-waveform retracker for coastal and open ocean altimetry. *Remote Sensing of the Environment*, 145: 173–189, 2014.

M. Passaro, L. Fenoglio-Marc, and P. Cipollini. Validation of significant wave height from improved satellite altimetry in the German Bight. *IEEE Transactions on Geoscience and Remote Sensing*, 53 (4):2146–2156, April 2015.

J. Perez, M. Menendez, and I. J Losada. GOW2: A global wave hindcast for coastal applications. *Coastal Engineering*, 124:1–11, 2017.

S. Ponce de León and C. Guedes Soares. On the sheltering effect of islands in ocean wave models. *Journal of Geophysical Research: Oceans*, 110(C9), 2005. doi: 10.1029/2004JC002682.

R. M. Ponte, M. Carson, M. Cirano, C. M. Domingues, T. Ezer, and X. Zhang. Towards comprehensive observing and modeling systems for monitoring and predicting regional to coastal sea level. *Frontiers in Marine Science*, 6(437), 2019.

S. J. Prais and C. B. Winsten. Trend estimators and serial correlation. Technical report, Cowles Commission discussion paper, 1954.

G.D. Quartly and A.A. Kurekin. Sensitivity of altimeter wave height assessment to data selection. *Remote Sensing*, 12(16):2020. doi: 10.3390/rs12162608.

P. Queffeulou and A. Bentamy. Analysis of wave height variability using altimeter measurements: Application to the mediterranean sea. *Journal of Atmospheric and Oceanic Technology*, 24(12):2078–2092, 2007. doi: 10.1175/2007JTECH0507.1.

D. Reeve, A. Chadwick, and C. Fleming. *Coastal engineering: processes, theory and design practice*. CRC Press, 2012. ISBN 9781138060432.

B. G. Reguero, I. J. Losada, and F. J. Méndez. A global wave power resource and its seasonal, interannual and long-term variability. *Applied Energy*, 148:366–380, 2015. ISSN 0306-2619. doi: 10.1016/j. apenergy.2015.03.114.

B. G Reguero, I. J. Losada, and F. J. Méndez. A recent increase in global wave power as a consequence of oceanic warming. *Nature communications*, 10, 2019.

A. Ribal and I. Young. 33 years of globally calibrated wave height and wind speed data based on altimeter observations. *Scientific Data*, 6(77):2019. doi: 10.1038/s41597-019-0083-9.

E. Rusu. Wave energy assessments in the black sea. *Journal of Marine Science and Technology*, 14(3): 359–372, Sep 2009. ISSN 1437-8213. doi: 10.1007/s00773-009-0053-6.

J. E. Stopa. Seasonality of wind speeds and wave heights from 30 years of satellite altimetry. *Advances in Space Research*, 2019. ISSN 0273-1177. doi: 10.1016/j.asr.2019.09.057.

P. Thibaut, L. Amarouche, O.Z. Zanife, N. Steunou, P. Vincent, and P. Raizonville. Jason-1 altimeter ground processing look-up correction tables. *Mar. Geod.*, 27(3-4):409–431, 2004.

P. Thibaut, JC. Poisson, E. Bronner, and N. Picot. Relative performance of the MLE3 and MLE4 retracking algorithms on Jason-2 altimeter waveforms. *Mar. Geod.*, 33(S1):317–335, 2010.

H. L. Tolman. A mosaic approach to wind wave modeling. *Ocean Modelling*, 25(1):35-47, 2008. ISSN 1463-5003. doi: 10.1016/j.ocemod.2008.06.005.

P. Wessel, J.F. Luis, L. Uieda, R. Scharroo, F. Wobbe, W.H.F. Smith and D. Tian. The Generic Mapping Tools Version 6. *Geochemistry, Geophysics, Geosystems*, 20(11): 5556-5564, 2019. doi: 10.1029/2019GC008515.

World Energy Council. 2010 survey of energy resources. *Available at https://www.worldenergy.org/assets/downloads/ser_2010_report_1.pdf (accessed 14.12.2019)*, 2010.

I. R. Young and A. Ribal. Multiplatform evaluation of global trends in wind speed and wave height. *Science*, 364(6440):548–552, 2019. ISSN 0036-8075. doi: 10.1126/science.aav9527.

I. R. Young, A.V. Babanin and S. Zieger. The Decay Rate of Ocean Swell Observed by Altimeter. *J. Phys. Oceanogr.*, 43:2322–2333, 2010. doi: 10.1175/JPO-D-13-083.1.

I.R. Young. Seasonal variability of the global ocean wind and wave climate. *International Journal of Climatology: A Journal of the Royal Meteorological Society*, 19(9):931–950, 1999.
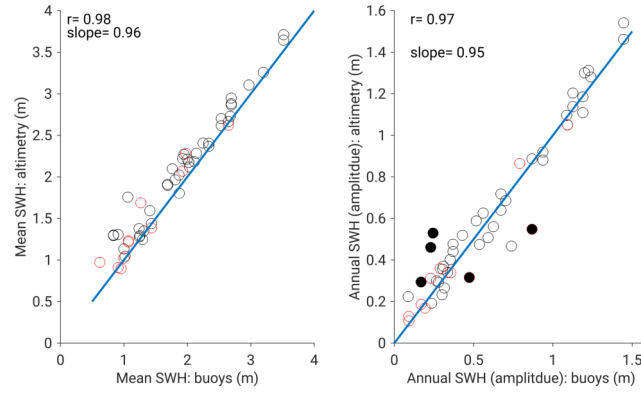
Supplementary figures
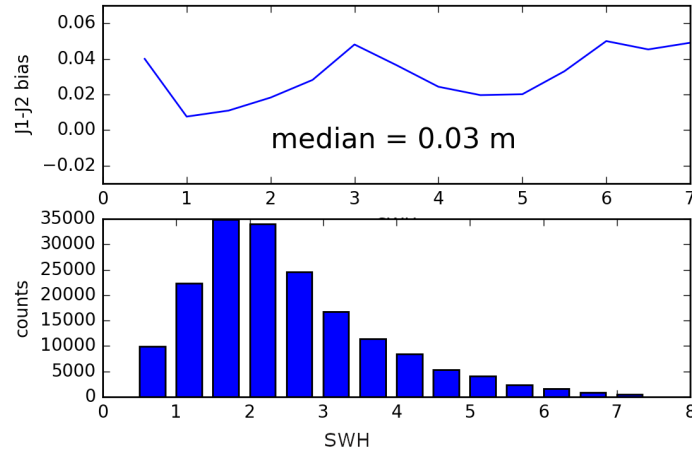
Supplementary Figure 1: Difference of SWH between Jason-1 and Jason-2 measurements as function of the average SWH in bins of 0.5 m and number of available measurements
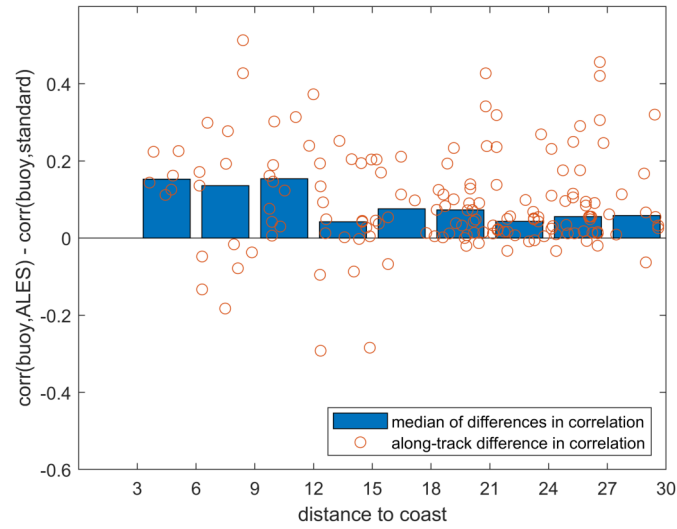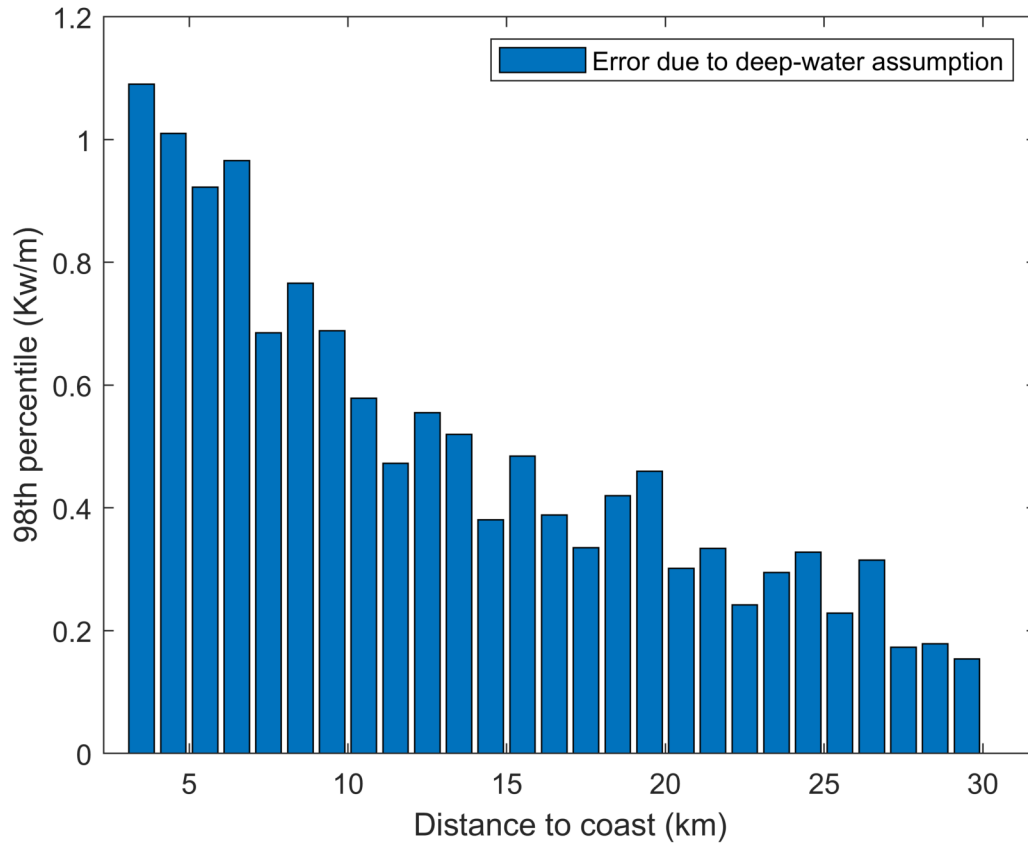

Supplementary Figure 2: Difference in correlation between altimetry and buoy time series when considering the ALES dataset or the standard GDR dataset, with respect to the distance to the coast of the altimetry point location. Positive numbers indicates a higher correlation using ALES data. Values at the single along-track locations are shown in circles, while a median of the differences is shown in 3-km-long bins.

Supplementary Figure 3: Left: Scatter plot of mean SWH from buoys and altimetry. Right: Scatter plot of the amplitude of the annual cycle from buoys and altimetry. Coastal buoys are highlighted in red. Filled circles correspond to couples in which the difference of the estimated amplitudes is statistically significant. Value of Pearson's correlation coefficient (r) and slope of the linear regresssion are reported on the top left of each plot.

Supplementary Figure 4: 98th percentile of the differences between the computation of the average energy flux using the deep water assumption and the approximate solution considering shallow and intermediate waters.
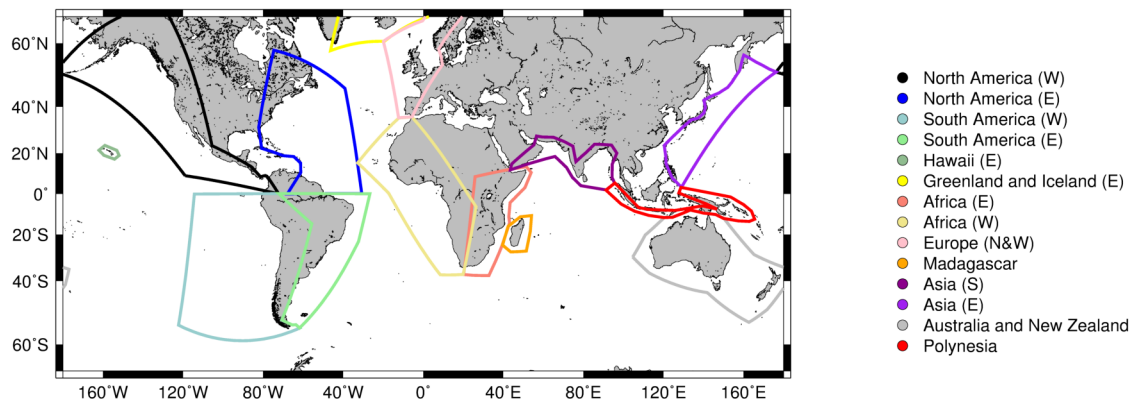
Supplementary Figure 5: Subdivision of the global coastal ocean adopted in this study.

Concluding Remarks

The work performed in these years have represented a further step towards the improvement in the use of altimetry data in areas of high societal importance and their combination and analysis in the framework of a synergetic ocean observing system. The publications here shown are nevertheless surely not an isolated effort, but generated networking and significant heritage.

The work done in (Passaro et al., 2018a) raised strong interest among the planners of the Cryosat-2 mission. Indeed the parameter developed in the paper has been now officially adopted in the new Baseline and I was invited to participate to the work presenting it (Meloni et al., 2020). The study of the bidimensional waveform of Delay-Doppler altimetry paved the way for the current strategy I am following in my research team to develop and validate innovative fitting algorithms for present and future altimetry missions in the context of the ESA Sea State Climate Change Initiative (Schlembach et al., 2020).

The development of ALES+ was rapidly recognised as a very important step in extending the application of altimetry in the coastal zone and in the polar ocean as highlighted in recent review papers of my discipline that I was invited to co-author (Ardhuin et al., 2019; Quartly et al., 2019b; Dodet et al., 2020). Besides the mentioned sea level studies, the technique has already been employed to improve the derivation of currents in the polar ocean and its comparability with the ocean models (Müller et al., 2019a,b). The further expansion of this very adaptable fitting strategy and of the findings concerning sea state bias is leading to the reprocessing of the full altimetric era in the context of the ESA Sea Level Climate Change Initiative (Birol et al., 2021), in which I lead the Algorithm Development Team. Among the most promising applications of the ALES-suite of algorithms, besides the ones featured in the preface, it is worth citing the improvements in coastal tidal modelling (Piccioni et al., 2018, 2019; Hart-Davis et al., 2021; Lago et al., 2017), coastal mean sea level (Gómez-Enri et al., 2019), and spectral representation of the ocean variability (Chereskin et al., 2019), all of which are a key element the success of future altimetric missions such as SWOT.

My research on sea level time series at the coast is fostering new analysis in the framework of the ESA Sea Level Climate Change Initiative, in particular the derivation of more accurate and dense maps of coastal vertical land

motion (Oelsmann et al., 2020) and case studies where the sea level trend measured at the coast differs from the offshore due to local effects (Marti et al., 2019; Gouzenes et al., 2020).

Finally, the work on the coastal mean wave climate shall be merged with the progresses in the analysis of local sea level for a future research focused on their combined impact for the global coastal monitoring in the context of both climatic and operational studies.

Bibliography

M. Passaro, F. L. Müller, and D. Dettmering, "Lead detection using cryosat-2 delay-doppler processing and sentinel-1 SAR images," *Advances in Space Research*, vol. 62, no. 6, pp. 1610–1625, 2018.

M. Passaro, S. Rose, O. Andersen, E. Boergens, F. Calafat, D. D, and B. J, "ALES+: Adapting a homogenous ocean retracker for satellite altimetry to sea ice leads, coastal and inland waters," *Remote Sensing of Environment*, vol. 211, pp. 456–471, 2018.

M. Passaro, Z. Nadzir, and G. D. Quartly, "Improving the precision of sea level data from satellite altimetry with high-frequency and regional sea state bias corrections," *Remote Sensing of Environment*, vol. 218, pp. 245 – 254, 2018. [Online]. Available: http://www.sciencedirect.com/science/article/pii/S0034425718304188

G. D. Quartly, W. H. Smith, and M. Passaro, "Removing intra-1-hz covariant error to improve altimetric profiles of σ_0 and sea surface height," *IEEE Transactions on Geoscience and Remote Sensing*, vol. 57, no. 6, pp. 3741–3752, 2019.

S. K. Rose, O. B. Andersen, M. Passaro, C. A. Ludwigsen, and C. Schwatke, "Arctic ocean sea level record from the complete radar altimetry era: 1991–2018," *Remote Sensing*, vol. 11, no. 14, p. 1672, 2019.

M. Passaro, F. Müller, J. Oelsmann, L. Rautiainen, D. Dettmering, M. Hart-Davis, A. Abulaitijiang, O. Andersen, J. Hoyer, K. Madsen, I. Ringgaard, J. Särkkä, R. Scarrott, C. Schwatke, F. Seitz, L. Tuomi, M. Restano, and J. Benveniste, "Absolute baltic sea level trends in the satellite altimetry era: A revisit," *Frontiers in Marine Science (In Press)*, 2021.

J. Benveniste, F. Birol, F. Calafat, A. Cazenave, H. Dieng, Y. Gouzenes, J. Legeais, F. Leger, F. Niño, M. Passaro, C. Schwatke, and A. Shaw, "(The Climate Change Initiative Coastal Sea Level Team) Coastal sea level anomalies and associated trends from jason satellite altimetry over 2002–2018," *Scientific Data*, vol. 7, 2020.

M. Passaro, M. Hemer, G. Quartly, C. Schwatke, D. Dettmering, and F. Seitz, "Global coastal attenuation of wind-waves observed with radar altimetry," *Nature Communications, ACCEPTED*, 2021.

M. Meloni, J. Bouffard, T. Parrinello, G. Dawson, F. Garnier, V. Helm, A. Di Bella, S. Hendricks, R. Ricker, E. Webb, B. Wright, K. Nielsen, S. Lee, M. Passaro, M. Scagliola, S. Simonsen, S. Sandberg, D. Brockley, S. Baker, S. Fleury, J. Bamber, L. Maestri, H. Skourup, and R. a. Forsberg, "Cryosat ice baseline-d validation and evolutions," *The Cryosphere*, vol. 14, no. 6, pp. 1889–1907, 2020.

F. Schlembach, M. Passaro, G. D. Quartly, A. Kurekin, F. Nencioli, G. Dodet, J.-F. Piollé, F. Ardhuin, J. Bidlot, C. Schwatke, F. Seitz, P. Cipollini, and C. Donlon, "Round robin assessment of radar altimeter low resolution mode and delay-doppler retracking algorithms for significant wave height," *Remote Sensing*, vol. 12, no. 8, p. 1254, 2020.

F. Ardhuin, J. E. Stopa, B. Chapron, F. Collard, R. Husson, R. E. Jensen, J. Johannessen, A. Mouche, M. Passaro, G. D. Quartly, V. Swail, and I. Young, "Observing sea states," *Frontiers in Marine Science*, vol. 6, p. 124, 2019. [Online]. Available: https://www.frontiersin.org/article/10.3389/fmars.2019.00124

G. D. Quartly, E. Rinne, M. Passaro, O. B. Andersen, S. Dinardo, S. Fleury, A. Guillot, S. Hendricks, A. A. Kurekin, F. L. Müller *et al.*, "Retrieving sea level and freeboard in the arctic: A review of current radar altimetry methodologies and future perspectives," *Remote Sensing*, vol. 11, no. 7, p. 881, 2019.

G. Dodet, J.-F. Piolle, Y. Quilfen, S. Abdalla, M. Accensi, F. Ardhuin, E. Ash, J.-R. Bidlot, C. Gommenginger, G. Marechal *et al.*, "The sea state cci dataset v1: towards a sea state climate data record based on satellite observations," *Earth System Science Data*, vol. 12, no. 3, pp. 1929–1951, 2020.

F. L. Müller, C. Wekerle, D. Dettmering, M. Passaro, W. Bosch, and F. Seitz, "Dynamic ocean topography of the northern Nordic seas: a comparison between satellite altimetry and ocean modeling," *The Cryosphere*, 2019.

F. L. Müller, D. Dettmering, C. Wekerle, C. Schwatke, M. Passaro, W. Bosch, and F. Seitz, "Geostrophic currents in the northern nordic seas from a combination of multi-mission satellite altimetry and ocean modeling," *Earth System Science Data*, vol. 11, no. 4, pp. 1765–1781, 2019.

F. Birol, F. Léger, M. Passaro, A. Cazenave, F. Niño, F. M. Calafat, A. Shaw, J.-F. Legeais, Y. Gouzenes, C. Schwatke *et al.*, "The X-TRACK/ALES multi-mission processing system: New advances in altimetry towards the coast," *Advances in Space Research*, vol. 67, no. 8, pp. 2398–2415, 2021.

G. Piccioni, D. Dettmering, M. Passaro, C. Schwatke, W. Bosch, and F. Seitz, "Coastal improvements for tide models: the impact of ALES retracker," *Remote Sensing*, vol. 10, no. 5, p. 700, 2018.

G. Piccioni, D. Dettmering, C. Schwatke, M. Passaro, and F. Seitz, "Design and regional assessment of an empirical tidal model based on FES2014 and coastal altimetry," *Advances in Space Research*, 2019.

M. G. Hart-Davis, G. Piccioni, D. Dettmering, C. Schwatke, M. Passaro, and F. Seitz, "Eot20: A global ocean tide model from multi-mission satellite altimetry," *Earth System Science Data Discussions*, pp. 1–23, 2021.

L. S. Lago, M. Saraceno, L. A. Ruiz-Etcheverry, M. Passaro, F. A. Oreiro, E. E. D'Onofrio, and R. A. González, "Improved sea surface height from satellite altimetry in coastal zones: A case study in southern patagonia," *IEEE Journal of Selected Topics in Applied Earth Observations and Remote Sensing*, vol. 10, no. 8, pp. 3493–3503, 2017.

J. Gómez-Enri, C. González, M. Passaro, S. Vignudelli, O. Álvarez, P. Cipollini, R. Mañanes, M. Bruno, M. López-Carmona, and A. Izquierdo, "Wind-induced cross-strait sea level variability in the strait of gibraltar from coastal altimetry and in-situ measurements," *Remote sensing of environment*, vol. 221, pp. 596–608, 2019.

T. K. Chereskin, C. B. Rocha, S. T. Gille, D. Menemenlis, and M. Passaro, "Characterizing the transition from balanced to unbalanced motions in the southern California Current," *Journal of Geophysical Research: Oceans*, vol. 124, no. 3, pp. 2088–2109, 2019.

J. Oelsmann, M. Passaro, D. Dettmering, C. Schwatke, L. Sanchez, and F. Seitz, "The Zone of Influence: Matching sea level variability from coastal altimetry and tide gauges for vertical land motion estimation," *Ocean Science (ACCEPTED MANUSCRIPT)*, pp. 1–32, 2020.

F. Marti, A. Cazenave, F. Birol, M. Passaro, F. Léger, F. Niño, R. Almar, J. Benveniste, and J. F. Legeais, "Altimetry-based sea level trends along the coasts of western africa," *Advances in Space Research*, 2019.

Y. Gouzenes, F. Léger, A. Cazenave, F. Birol, P. Bonnefond, M. Passaro, F. Nino, R. Almar, O. Laurain, C. Schwatke *et al.*, "Coastal sea level rise at Senetosa (Corsica) during the Jason altimetry missions," *Ocean Science*, vol. 16, no. 5, pp. 1165–1182, 2020.